Laser Technologies for Applications in Quantum Information Science

Lasertechnologien für Anwendungen in der Quanteninformationsverarbeitung
Zur Erlangung des Grades eines Doktors der Naturwissenschaften (Dr. rer. nat.)
Genehmigte Dissertation von Tilman Preuschoff aus Gelnhausen
Tag der Einreichung: 24. Januar 2023, Tag der Prüfung: 13. Februar 2023

1. Gutachten: Prof. Dr. Gerhard Birkl
2. Gutachten: Prof. Dr. Thomas Walther
Darmstadt, Technische Universität Darmstadt

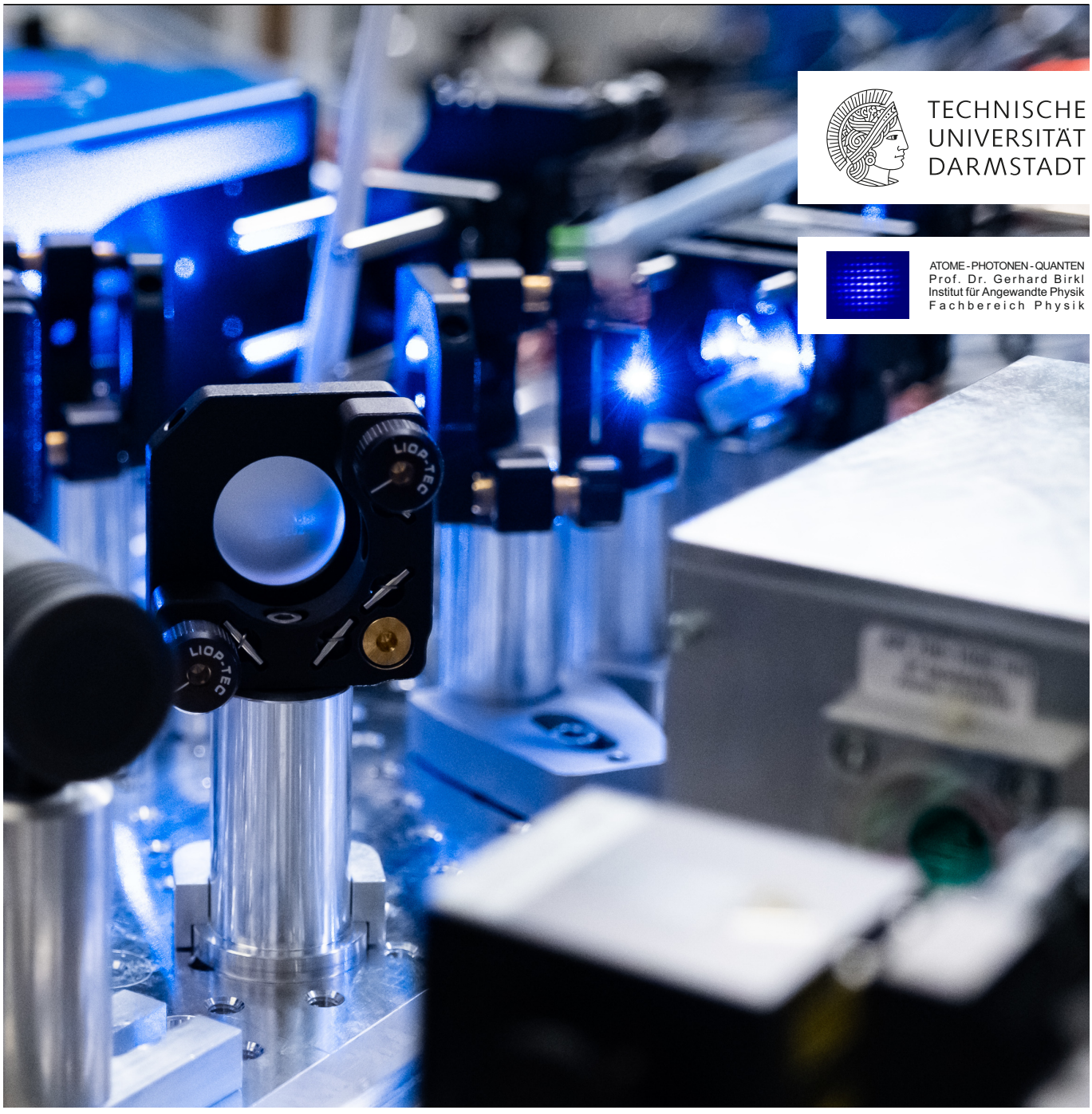

Laser Technologies for Applications in Quantum Information Science

Lasertechnologien für Anwendungen in der Quanteninformationsverarbeitung

Accepted doctoral thesis by Tilman Preuschoff

Date of submission: January 24, 2023
Date of thesis defense: February 13, 2023

Darmstadt, Technische Universität Darmstadt

Jahr der Veröffentlichung der Dissertation auf TUprints: 2023

Bitte zitieren Sie dieses Dokument als:
URN: urn:nbn:de:tuda-tuprints-232421
URL: http://tuprints.ulb.tu-darmstadt.de/23242

Dieses Dokument wird bereitgestellt von tuprints,
E-Publishing-Service der TU Darmstadt
http://tuprints.ulb.tu-darmstadt.de
tuprints@ulb.tu-darmstadt.de

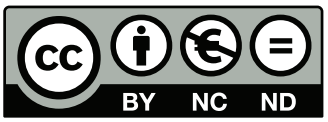

Cover picture: Close-up photograph of the Rydberg laser system developed in this work. Credit: Christian Schuller

Abstract

Scientific progress in experimental physics is inevitably dependent on continuing advances in the underlying technologies. Laser technologies enable controlled coherent and dissipative atom-light interactions and micro-optical technologies allow for the implementation of versatile optical systems not accessible with standard optics.

This thesis reports on important advances in both technologies with targeted applications ranging from Rydberg-state mediated quantum simulation and computation with individual atoms in arrays of optical tweezers to high-resolution spectroscopy of highly-charged ions.

A wide range of advances in laser technologies are reported: The long-term stability and maintainability of external-cavity diode laser systems is improved significantly by introducing a mechanically adjustable lens mount. Tapered-amplifier modules based on a similar lens mount are developed. The diode laser systems are complemented by digital controllers for laser frequency and intensity stabilisation. The controllers offer a bandwidth of up to 1.25 MHz and a noise performance set by the commercial STEMlab platform. In addition, shot-noise limited photodetectors optimised for intensity stabilisation and Pound-Drever-Hall frequency stabilisation as well as a fiber based detector for beat notes in the MHz-regime are developed. The capabilities of the presented techniques are demonstrated by analysing the performance of a laser system used for laser cooling of ^{85}Rb at a wavelength of 780 nm. A reference laser system is stabilised to a spectroscopic reference provided by modulation transfer spectroscopy. This spectroscopy scheme is analysed finding optimal operation at high modulation indices. A suitable signal is generated with a compact and cost-efficient module. A scheme for laser offset-frequency stabilisation based on an optical phase-locked loop is realised. All frequency locks derived from the reference laser system offer a Lorentzian linewidth of 60 kHz (FWHM) in combination with a long-term stability of 130 kHz peak-to-peak within 10 days. Intensity stabilisation based on acousto-optic modulators in combination with the digital controller allows for real-time intensity control on microsecond time scales complemented by a sample and hold feature with a response time of 150 ns.

High demands on the spectral properties of the laser systems are put forward for the coherent excitation of quantum states. In this thesis, the performance of active frequency stabilisation is enhanced by introducing a novel current modulation technique for diode lasers. A flat response from DC to 100 MHz and a phase lag below 90° up to 25 MHz are achieved extending the bandwidth available for laser-frequency stabilisation. Applying this technique in combination with a fast proportional-derivative controller, two laser fields with a relative phase noise of 42 mrad$_{rms}$ for driving rubidium ground state transitions are realised. A laser system for coherent Rydberg excitation via a two-photon scheme provides light at 780 nm and at 480 nm via frequency-doubling from 960 nm. An output power of 0.6 W at 480 nm from a single-mode optical fiber is obtained . The frequencies of both laser systems are stabilised to a high-finesse reference cavity resulting in a linewidth of 1.02 kHz (FWHM) at 960 nm. Numerical simulations quantify the effect of the finite linewidth on the coherence of Rydberg Rabi-oscillations. A laser system similar to the 480 nm Rydberg system is developed for spectroscopy on highly charged bismuth.

Advanced optical technologies are also at the heart of the micro-optical generation of tweezer arrays that offer unprecedented scalability of the system size. By using an optimised lens system in combination with an automatic evaluation routine, a tweezer array with several thousand sites and trap waists below 1 µm is demonstrated. A similar performance is achieved with a microlens array produced in an additive manufacturing process. The microlens design is optimised for the manufacturing process. Furthermore, scattering rates in dipole traps due to suppressed resonant light are analysed proving the feasibility of dipole trap generation using tapered amplifier systems.

Zusammenfassung

Der wissenschaftliche Fortschritt in der Experimentalphysik beruht maßgeblich auf technologischem Fortschritt. Lasertechnologien ermöglichen kohärente und dissipative Wechselwirkung von Lichtfeldern und Atomen. Mikrooptische Technologien bieten einen Zugang zu vielseitigen, neuartigen optischen Systemen, die nicht mit herkömmlichen Optiken realisiert werden können. In dieser Arbeit werden relevante Weiterentwicklungen dieser beiden Technologien vorgestellt. Die Anwendungen reichen von Quantencomputern und Quantensimulatoren auf Basis von neutralen Rydberg-Atomen bis hin zur hochauflösenden Spektroskopie von hochgeladenen Ionen.

Eine Vielzahl von neuartigen Lasertechnologien werden vorgestellt: Die Verwendung eines justierbaren Linsenhalters ermöglicht eine erhöhte Langzeitstabilität und reduziert den Wartungsaufwand deutlich. Weiterhin werden Module für Trapezverstärker entwickelt, die auf einem ähnlichen Linsenhalter basieren. Digitale Regler ermöglichen eine aktive Stabilisierung der Laserfrequenz und Laserintensität. Die Regler erreichen eine Bandbreite von $1{,}25$ MHz. Ihr Rauschverhalten wird von der verwendeten kommerziellen STEMlab-Plattform bestimmt. Darüber hinaus werden Photodetektoren für Intensitätsstabilisierung und Frequenzstabilisierung mit dem Pound-Drever-Hall-Verfahren, sowie ein glasfasergekoppelter Photodetektor zur Aufnahme von Schwebungssignalen im MHz-Bereich vorgestellt. Die Leistungsfähigkeit der Systeme wird durch die Realisierung eines Lasersystems zur Laserkühlung von ^{85}Rb bei 780 nm demonstriert. Eine präzise Frequenzreferenz wird mittels Modulationstransfer-Spektroskopie verwirklicht. Die Wahl eines großen Modulationsindex bietet ein optimiertes Fehlersignal. Ein kompaktes Modul zur Signalerzeugung wird vorgestellt. Zur Stabilisierung anderer Lasersysteme relativ zu dem Referenzsystem wird eine Phasenregelung herangezogen. Alle abgeleiteten Frequenzstabilisierungen weisen eine Halbwertsbreite von 60 kHz und Frequenzfluktuationen unter 130 kHz innerhalb von 10 Tagen auf. Der Einsatz der digitalen Regler ermöglicht die Kontrolle von Laserintensitäten auf Mikrosekunden-Zeitskalen. Auf kürzeren Zeitskalen wird ein Sample-und-Hold-Verfahren mit einer Reaktionszeiten von 150 ns verwendet.

Für die kohärente Manipulation von Quantenzuständen werden Lasersysteme mit einer besonders hohen spektralen Güte benötigt. In dieser Arbeit wird eine neuartige Technik zur Strommodulation von Diodenlasern vorgestellt, durch welche eine hohe Bandbreite zur aktiven Frequenzstabilisierung zu Verfügung steht. Mit dem Verfahren wird ein glattes Transferverhalten bis 100 MHz und eine Phasenverzögerung unter $90°$ bis zu 25 MHz erreicht. Durch Einsatz der Technik ist es möglich, zwei Laserfelder zur kohärenten Kopplung der Rubidium-Grundzustände mit einem relativen Phasenrauschen von 42 mrad$_{rms}$ zu erzeugen. Zur kohärenten Anregung von Rydberg-Zuständen wird ein frequenzverdoppeltes 960 nm-Lasersystem in Kombination mit einem 780 nm-System verwendet. Es stehen 0.6 W optische Leistung bei 480 nm zur Verfügung. Beide Lasersystem werden auf einen optischen Referenzresonator hoher Güte stabilisiert. Dabei wird eine Linienbreite von $1{,}02$ kHz bei 960 nm erreicht. Ein ähnliches Lasersystem zur Spektroskopie von hochgeladenen Bismut-Ionen wird vorgestellt.

Die Erzeugung von Quantenregistern mit Hilfe von Mikrooptiken ermöglicht eine ausgezeichnete Skalierbarkeit der Systemgrößen. Register mit mehreren tausend Fallenplätzen und Strahltaillen unter 1 µm werden durch Einsatz eines optimierten Objektives realisiert. Die additive Fertigung von Mikrolinsenregistern erlaubt es, Quantenregister ähnlicher Güte mit einer flexiblen Geometrie herzustellen. Das Mikrolinsendesign wird auf diese Anwendung optimiert. Darüber hinaus werden resonante Streuprozesse in Dipolfallen analysiert. Die Ergebnisse zeigen, dass es möglich ist ein eigens entwickeltes Trapezverstärkersystem zu diesem Zweck einzusetzen.

Contents

1. Introduction

Even a hundred years after its formulation, the theory of quantum mechanics remains fascinating and puzzling. A fascination also stemming from the fact that the counter-intuitive effects evoked by a quantum mechanical world became observable in laboratories. The genuine quantum mechanical concept of entanglement, once considered spooky [1], is now believed to be a valuable resource. The prospering field of quantum information has brought up a multitude of applications using entanglement as a resource, among them the concept of a general purpose quantum computer [2]. This device consists of two-level quantum systems called qubits in analogy to the bits of a classical computer. It is able to perform arbitrary algorithms on the states of these qubits. A mere theoretical concept at the first glance, it has fostered active research putting forth famous quantum algorithms that proof its advantages over classical computers [3–5]. Today, a great variety of isolated quantum systems are available as an experimental resource ranging from trapped atoms, ions, or molecules to more complex systems such as superconducting circuits, nitrogen-vacancy centers in diamonds, or quantum dots. [6–11] Nevertheless, all experimental approaches have not succeeded in realising a universal quantum computer so far. The systems realised are noisy intermediate scale quantum computers (NISQ). [12] David Divincenco has established five specific criteria necessary for an experimental realisation of a quantum computer. [13] Among them, the scalability of the system size is often considered the most challenging. In this aspect, neutral atoms are advantageous since they are inherently identical. [6, 14] The basic feasibility of neutral atom quantum computing has been demonstrated. [6, 15, 16] The challenges in the NISQ era are constructing error prone, scalable platforms on the one hand and more hardware efficient algorithms and interfaces on the other hand. [12, 17] For many related experimental platforms, we are currently witnessing the transition from fundamental quantum physics to quantum technology.

Another application of controllable, stationary quantum systems is based on Richard Feynman's seminal idea of taming the complexity of quantum mechanics by employing a different type of quantum mechanical systems [18]: the field of quantum simulation. An artificial quantum many-body system is engineered to mimic another quantum system with respect to its states and interactions. In this way, it is possible to study the behaviour of complex quantum many-body system, such as solid state or spin systems. Governing the full dynamics of such a many-body systems is not feasible with a classical computer for system sizes exceeding a few tens of particles. Experiments based on neutral atoms in optical tweezers have reported on substantial advances in the field of quantum simulation during the last few years. [19–25]

It is noteworthy, that the success of the neutral atom platform is enabled by the invention of groundbreaking technologies, such as laser cooling [26] or optical tweezers [27] both awarded with a Nobel prize in physics. Without these techniques, the isolation of individual neural atoms for quantum information science would remain inconceivable. The ongoing developments of the platform are still carried by advances in technology. As the scientific frontiers lie in

increasing system sizes and interconnectivity, improving fidelities, and reducing error rates, the systems grow increasingly complex. In this situation, robust and reliable technological solutions become inevitable. The scientific focus moves from proof-of-principle setups dedicated to specific problems to versatile platforms that are able to realise an optimal environment for quantum computing and quantum simulation. The author believes that the work presented here provides a significant contribution to this path. For the most part, we will restrict the discussion to a platform based on individual rubidium atoms in optical tweezers where the interaction is mediated by Rydberg-Rydberg interactions. [28–30] However, most of the results are also relevant in a more general context. Thus, generic findings and techniques are separated from results specific to our platform, if possible.

This work is organised in the following way:

Chapter 2 gives a short introduction to the physical concepts used throughout this work. This chapter also defines the requirements for the systems and techniques discussed here.

Chapter 3 presents technologies optimised for quantum information systems and high-resolution spectroscopy. Primary, this includes diode laser systems and associated electronics. The following chapters rely on the concepts developed in this chapter.

Chapter 4 describes laser systems optimised for creating a cloud of ultra-cold atoms. This includes a high-precision spectroscopic reference system and techniques for laser frequency and intensity stabilisation.

Chapter 5 is dedicated to the generation of optical tweezer arrays using microlens arrays. In particular, an imaging system allowing for creating larger arrays and a 3D-printing technique for manufacturing arrays with almost arbitrary geometries are discussed. Additionally, a trapping-light source based on diode laser systems is presented compliment by a theoretical analysis of the spectral properties required for efficient atom trapping.

Chapter 6 contains results characterising the laser systems used for coherent excitation of Rydberg states as required to introduce interactions between atoms in the tweezer array. The linewidths of the systems are analysed. Numerical simulations link the obtained laser linewidths to decoherence effects in the coherent dynamics of the atoms. Spectroscopy on highly charged bismuth is discussed as an alternative application of the laser systems characterised in this chapter.

Chapter 7 summarises and discusses the results and techniques found in this work. A brief outlook on possible improvements and future developments is given.

2. Fundamental concepts for Rydberg-atom quantum simulation and computation

Individual atoms in arrays of optical tweezers are a promising platform for quantum information processing. The platform relies on laser cooled neutral atoms that are loaded in arrays of tightly focussed laser beams, so called optical tweezers. For quantum information science, an interaction between the trapped atoms is required. The distance of adjacent array sites is on the order of several micrometer enabling single-site addressing and read-out. Between laser-trapped neutral atoms in the ground state, there is typically no significant interaction at these distances. Interactions mediated by Rydberg states, i.e. states with a high principle quantum number n, are utilised. The physical concepts underlying this platform are discussed in this chapter. While rigours derivations are omitted, the relevant equations are stated quoting suitable literature for details. To some extent, also state-of-the-art optical tweezer platforms and latest results are covered. An extensive review on this matter can be found in [31]. In this work, the rubidium isotope ^{85}Rb is used. If necessary, we will restrict the discussion to this atom species for simplicity.

This chapter contains a description of the interaction between atoms and light fields underlying most of the phenomena discussed in the following. Techniques for efficient trapping of individual atoms in optical tweezer are presented and are complemented by schemes for preparation of deterministically filled structures. Several alternative schemes for the excitation of rubidium Rydberg states are compared in this chapter. A discussion on the properties of Rydberg states and interactions between them is added.

2.1. Atom-light interactions

At the heart of almost all techniques providing isolated neutral atoms for quantum information experiments lies the interaction of atoms with laser light fields. In this section, fundamental approximations and basic equations are summarised. The notation used throughout this work is introduced. We will follow the text books [32–34] in this matter.

Consider a classical light field

$$\mathbf{E}(t, \mathbf{r}) = \boldsymbol{\epsilon} E_0 \cos(\omega_L t + \mathbf{kr}) \tag{2.1}$$

with unit polarisation vector $\boldsymbol{\epsilon}$, angular frequency ω_L, and wave number $|\mathbf{k}| = 2\pi/\lambda$ defined by the wavelength λ. The classical field is a suitable description for the strong laser fields considered here. The size of the atom in the ground state is estimated by $n^2 a_0$ where n is the principle quantum number of the ground state and a_0 is the Bohr radius. Typically, this size is negligible as compared to the wavelength such that the phase $\mathbf{kr}$ can be considered constant. Applying this *long-wavelength approximation* and choosing the Göppert-Mayer gauge of the electrical field [32, Chap. 2] yields the well-known *electric dipole Hamiltonian*

$$\hat{H}_{dip} = -\hat{\mathbf{d}}\mathbf{E} \tag{2.2}$$

governing the atom-light interaction. In this expression,

$$\hat{\mathbf{d}} = e\hat{\mathbf{r}} \tag{2.3}$$

is the *electric dipole operator* where e denotes the elementary charge.

In the following, we consider a two-level model for the atom with a ground state $|g\rangle$ and an excited state $|e\rangle$. The excitation energy is given by $\hbar\omega_0$. The Hamiltonian of the atom is given by

$$\hat{H}_0 = \hbar \begin{pmatrix} \omega_0 & 0 \\ 0 & 0 \end{pmatrix} \tag{2.4}$$

as denoted in the standard basis $\{|e\rangle, |g\rangle\}$. The dynamics of the system are described by the Hamiltonian

$$\hat{H} = \hat{H}_0 + \hat{H}_{dip} = \hbar \begin{pmatrix} \omega_0 & \Omega\cos(\omega_L t) \\ \Omega\cos(\omega_L t) & 0 \end{pmatrix} \tag{2.5}$$

where the Rabi frequency

$$\Omega = -\frac{E_0}{\hbar} \langle g| \hat{\mathbf{d}}\boldsymbol{\epsilon} |e\rangle \tag{2.6}$$

is a measure for the coupling strength between $|g\rangle$ and $|e\rangle$ induced by the light field. In particular, the coupling strength is proportional to the amplitude E_0 of the light field and such to the square root of the intensity $\sqrt{I}$. The explicit time dependence of $\hat{H}$ can be eliminated by transforming in a suitable interaction picture ($|e\rangle \to |\tilde{e}\rangle := e^{i\omega_L t} |e\rangle$) and applying the *rotating wave approximation*, i.e. neglecting terms rotating at $\omega_0 + \omega_L$. The approximation is justified, if

$$\Delta := \omega_L - \omega_0 \ll \omega_L + \omega_0, \tag{2.7}$$

i.e. the detuning Δ is small as compared to the laser frequency. In the interaction picture, the Hamiltonian is given by

$$\hat{H}_{int} = \frac{\hbar}{2} \begin{pmatrix} -2\Delta & \Omega \\ \Omega & 0 \end{pmatrix}. \tag{2.8}$$

2.1.1. Rabi oscillations

In order to solve the time dependent Schrödinger equation for the Hamiltonian 2.8, we introduce the time dependent state $|\Psi(t)\rangle := c_g(t)|g\rangle + \tilde{c}_e(t)|\tilde{e}\rangle$. Where $|c_g(t)|^2$ and $|\tilde{c}_e(t)|^2$ represent the probabilities to find the atom in the ground states or in the excited state respectively for a given time t. For an atom initially prepared in the ground state, $c_g(0) = 1$ and $\tilde{c}_e(0) = 0$, the solution of the problem is given by [33, Sec. 5.2.2]

$$c_g(t) = e^{i\frac{\Delta t}{2}}\left[\cos\left(\frac{\Omega_{eff}t}{2}\right) - i\frac{\Delta}{\Omega_{eff}}\sin\left(\frac{\Omega_{eff}t}{2}\right)\right] \tag{2.9}$$

$$\tilde{c}_e(t) = -i\frac{\Omega}{\Omega_{eff}}e^{i\frac{\Delta t}{2}}\sin\left(\frac{\Omega_{eff}t}{2}\right) \tag{2.10}$$

where $\Omega_{eff} := \sqrt{\Omega^2 + \Delta^2}$ denotes the effective Rabi frequency. Thus, the probability to find the atom in the excited state

$$|\tilde{c}_e(t)|^2 = \frac{\Omega^2}{\Omega_{eff}^2}\sin^2\left(\frac{\Omega_{eff}t}{2}\right) \tag{2.11}$$

exhibits *Rabi oscillations* at a frequency Ω_{eff} with amplitude $\frac{\Omega^2}{\Omega_{eff}^2}$. On resonance ($\Delta = 0$), deterministic excitation is achieved by applying the laser field for a certain time $t = \pi/\Omega$ (π pulse). Figure 2.1 (a) shows examples of Rabi oscillations for different detunings. For larger Δ, the oscillations occur with shorter period while the maximum amplitude is reduced. In particular, deterministic excitation is not possible for $\Delta \neq 0$. The excitation probability when applying a π pulse and scanning the laser detuning is depicted in Fig. 2.1 (b). A resonance with several side peaks is observable when keeping the pulse time constant (blue). The resonance is bound by two characteristic zeros at $\Delta = \pm\sqrt{3}\Omega$. The oscillatory behaviour originates from choosing a constant pulse time. When choosing a π pulse for Ω_{eff} at every laser frequency, equivalent to the maximum excitation probability, a broad resonance with full width at half maximum 2Ω is observable (orange).

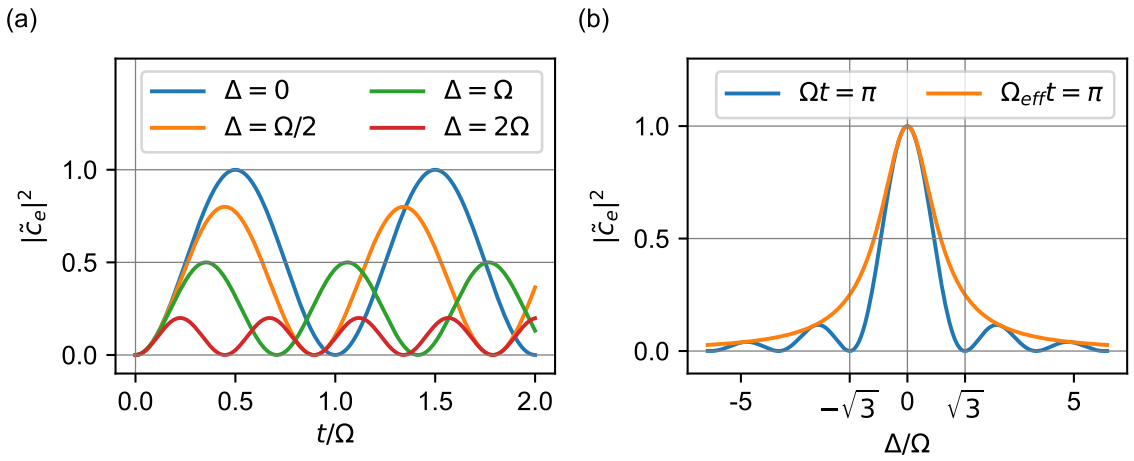

Fig. 2.1.: (a) Illustration of Rabi oscillations with different detunings. (b) Excitation probability when scanning the laser detuning (Δ) while applying a π pulse.

2.1.2. Optical dipole potentials

It is straightforward to solve the stationary Schrödinger equation for the Hamiltonian 2.8 yielding *dressed states*

$$|+\rangle = \cos(\theta)\,|e\rangle + \sin(\theta)\,|g\rangle + \tag{2.12}$$
$$|-\rangle = \cos(\theta)\,|g\rangle - \sin(\theta)\,|e\rangle \tag{2.13}$$

with the *mixing angle*

$$\tan(2\theta) = -\frac{\Omega}{\Delta}. \tag{2.14}$$

In case of a weak coupling $|\Delta| \gg \Omega$, the mixing angle is $\theta \approx 0$ such that $|-\rangle \approx |g\rangle$ and $|+\rangle \approx |e\rangle$. The corresponding eigenergies are given by

$$E_{\pm} = -\frac{\hbar\Delta}{2} \mp \frac{\hbar\sqrt{\Omega^2+\Delta^2}}{2} \tag{2.15}$$

In this case, E_- can be considered as an energy shift of the ground state

$$E_- = -\frac{\hbar\Delta}{2} + \frac{\hbar\sqrt{\Omega^2+\Delta^2}}{2} \approx -\frac{\hbar\Delta}{2} + \frac{\hbar\Delta\left(1+\frac{\Omega^2}{2\Delta^2}\right)}{2} = \frac{\hbar\Omega^2}{4\Delta}, \tag{2.16}$$

the *light shift*. The shift E_- is proportional to the intensity $I = \epsilon_0 c E_0/2$ since the Rabi frequency Ω is proportional to $\sqrt{I}$. A spatially varying intensity, e.g. a Gaussian laser beam, results in a conservative potential, the *optical dipole potential*. It is useful to express the dipole matrix element in Ω (Eq. 2.6) by the natural linewidth of the transition [34, Sec. 2.2] yielding the optical dipole potential

$$U_{dip}(\mathbf{r}) = \frac{3\pi c^2\Gamma}{2\omega_0^3}\frac{I(\mathbf{r})}{\Delta}. \tag{2.17}$$

For most species, accurate values for Γ are available, e.g. for rubidium in [35, 36], avoiding cumbersome ab initio calculation of the dipole matrix elements. The dipole potential is attractive for a negative (red) detuning and repulsive for a positive (blue) detuning, i.e. atoms are attracted to the maximum or the minimum intensity respectively. The calculations presented here are based on a simple two-level system. Alkali atoms, such as rubidium, feature strong D_1 ($|nS_{1/2}\rangle \rightarrow |nP_{1/2}\rangle$) and D_2 ($|nS_{1/2}\rangle \rightarrow |nP_{3/2}\rangle$) transitions. Assuming linearly polarised trapping light at a wavelength close to the D-lines, an accurate description of the dipole potential of the multi-level system is derived by replacing Δ with an effective detuning [37]

$$\Delta_{eff} = 3\left(\frac{2}{\Delta_2} + \frac{1}{\Delta_1}\right)^{-1} \tag{2.18}$$

where the detunings $\Delta_{1,2}$ refer to the transition from the ground state to the center of the respective D-line hyperfine structure manifold.

2.1.3. Scattering rates

While laser cooling relies on dissipative photon scattering processes, photon scattering induces undesirable decoherence in coherent dynamics such as Rabi oscillations and heating in dipole traps. In order to accurately describe photon scattering rates in the two-level system discussed in this section, spontaneous decay is introduced in the model resulting in the *optical Bloch equations* [34, Chap. 2.3]

$$\frac{d}{dt}\rho_{gg} = \Gamma\rho_{ee} + \frac{i\Omega}{2}(\tilde{\rho}_{eg} - \tilde{\rho}_{ge}) \tag{2.19}$$

$$\frac{d}{dt}\rho_{ee} = -\Gamma\rho_{ee} + \frac{i\Omega}{2}(\tilde{\rho}_{ge} - \tilde{\rho}_{eg}) \tag{2.20}$$

$$\frac{d}{dt}\rho_{ge} = -\left(\frac{\Gamma}{2} + i\Delta\right)\tilde{\rho}_{ge} + \frac{i\Omega}{2}(\rho_{ee} - \rho_{gg}) \tag{2.21}$$

$$\frac{d}{dt}\rho_{eg} = -\left(\frac{\Gamma}{2} - i\Delta\right)\tilde{\rho}_{eg} + \frac{i\Omega}{2}(\rho_{gg} - \rho_{ee}) \tag{2.22}$$

describing the time evolution of the system's density matrix $\hat{\rho} = \begin{pmatrix} \rho_{ee} & \rho_{eg} \\ \rho_{ge} & \rho_{gg} \end{pmatrix}$ where $\tilde{\rho}_{ge} = \tilde{\rho}^{\star}_{ge} := \rho_{ge}e^{-i\Delta t}$. The steady state solution $\rho_{ee}(t \to \infty)$ yields the photon scattering rate [34, Chap. 3]

$$\Gamma_{sc} = \frac{\Gamma}{2}\frac{\frac{I}{I_{sat}}}{1 + \frac{I}{I_{sat}} + \left(\frac{2\Delta}{\Gamma}\right)^2} \tag{2.23}$$

where $I_{sat} := \frac{\hbar\omega_0^3\Gamma}{12\pi c^2}$ is the *saturation intensity*. The model describes saturation effects limiting the scattering rate to $\Gamma/2$ for high intensities close to resonance. This regime is relevant for techniques such as laser cooling and quantum state preparation via optical pumping. In the regime used for optical dipole traps, the laser field is far detuned from the transition, i.e. $\Delta \gg \Gamma$. We further assume that saturation is negligible, i.e. $I/I_{sat} \ll \Delta^2/\Gamma^2$. Under these assumptions, Eq. 2.23 can be approximated by

$$\Gamma_{sc}(\mathbf{r}) \approx \frac{\Gamma}{2}\frac{\Gamma^2}{4\Delta^2}\frac{I(\mathbf{r})}{I_{sat}} = \frac{3\pi c^2}{2\hbar\omega_0^3}\frac{\Gamma^2}{\Delta^2}I(\mathbf{r}). \tag{2.24}$$

This expression shows, that Γ_{sc} scales as $1/\Delta^2$ whereas U_{dip} scales as $1/\Delta$. Hence, the scattering rate is reduced by increasing the detuning and maintaining a constant trap depth by increasing the maximum trap intensity. Note, that neglecting saturation effects is a non-trivial assumption typically justified for the traps discussed in this work. However, if significantly stronger trapping potentials or smaller detunings are required, the above expression only yields an upper bound for the scattering rate. Similarly to the dipole potential, a more accurate description for alkali atoms is derived [37] by replacing $1/\Delta^2$ by

$$\frac{1}{\tilde{\Delta}_{eff}^2} = \frac{1}{3}\left(\frac{1}{\Delta_1^2} + \frac{2}{\Delta_2^2}\right). \tag{2.25}$$

2.2. Deterministically filled tweezer arrays

The experimental platform presented in this work provides regular arrays of individual rubidium atoms for quantum information experiments. The dipole traps are loaded from a cloud of laser cooled atoms. The loading is in principle stochastic. Scalability of the system size is only guaranteed if deterministic loading of the entire array with low error rates is achieved. This section discusses briefly state-of-the-art techniques for deterministic preparation of individual atoms covering laser cooling techniques, generation of large scale tweezer arrays,

and deterministic filling of the arrays.

2.2.1. Laser cooling

Initially, laser cooled atoms are prepared in a magneto-optical trap (MOT). The atom temperature is reduced further by an optical molasses. These techniques are well documented in the literature, see e.g. [34]. The cooling transition for ^{85}Rb is the cycling transition $|5S_{1/2}, F = 3\rangle \rightarrow |5P_{3/2}, F' = 4\rangle$. [1] Additionally, repumping at $|5S_{1/2}, F = 2\rangle \rightarrow |5P_{3/2}, F' = 3\rangle$ is required to compensate for decay in the $|5S_{1/2}, F = 2\rangle$ ground state. The MOT is loaded from a rubidium beam produced by a dispenser. The divergent atom beam emitted from the dispenser is slowed using a counter propagating laser beam with a fixed frequency. Although, there are more elaborate methods such as Zeeman slowers, chirp cooling, or 2D-MOTs [38–40], most rubidium tweezer platforms rely on this simple technique since atom numbers in the MOT are typically not a limiting factor. In the MOT, atoms are cooled to the *Doppler limit*

$$T_D = \frac{\hbar\Gamma}{2k_B} = 146\,\mu\text{K} \tag{2.26}$$

defined by the heating process induced by persistent photon scattering with k_B being the Boltzman constant. The minimal temperature in an optical molasses is given by the *recoil limit*

$$T_R = \frac{h^2}{\lambda^2 m k_B} \approx 370\,\text{nK} \tag{2.27}$$

induced by the recoil of a single photon scattered in the cooling process. The atomic mass is given as m and λ is the wavelength of the cooling light field. The values stated for T_D and T_R are calculated for the ^{85}Rb D2-line. In practise, a typical temperature on the order of $10\,\mu$K is achieved in the optical molasses, sufficient for efficient loading of optical tweezer with a typical depth of $U_{dip} = 1\,\text{mK} \times k_B$.

2.2.2. Optical tweezer arrays

Optical tweezers are generated by focussing a laser beam tightly using optics with a high numerical aperture (NA). Neglecting diffractive effects, the tweezer intensity is described by a Gaussian beam [41]

$$I(x, y, z) = I_0 \frac{w_0^2}{w^2(z)}\, e^{-\frac{2x^2}{w(z)^2}} e^{-\frac{2y^2}{w(z)^2}} \tag{2.28}$$

with maximum intensity I_0 and minimum beam waist $w_0 = w(z = 0)$. The beam waist $w(z)$ along the optical axis (z) is given by

$$w(z) = w_0 \sqrt{1 + \frac{z^2}{z_R^2}} \tag{2.29}$$

where $z_R = \pi w_0^2/\lambda$ is the *Rayleigh range* with the trapping wavelength λ. It is useful to express I_0 in terms of the total laser power P used for the trap

[1] Throughout this work, the standard notation $|nL_j, F\rangle$ denotes atomic states, if not stated otherwise. In this notation, n is the principle quantum number, L denotes the atomic orbital, j is the quantum number of total electronic angular momentum, and F is the quantum number of the total angular momentum.

$$I_0 = \frac{2P}{\pi w_0^2}. \tag{2.30}$$

Atoms at low temperatures are trapped close to the maximum of $I(\mathbf{r})$. In this region, a harmonic approximation can be applied

$$I(x, y, z) \approx I_0 \left(1 - \frac{z^2}{z_R^2} - \frac{2x^2}{w_0^2} - \frac{2y^2}{w_0^2}\right). \tag{2.31}$$

In this approximation, the equipotential surfaces of the dipole potential are given by ellipsoids with an axes ratio $\sqrt{2}z_r/w_0 = \sqrt{2}\pi w_0/\lambda$. Typically, beam waists of approximately $1\,\mu\text{m}$ are achieved. Figure 2.2 shows a true-to-scale illustration of the resulting array geometry with a trap distance of $5\,\mu\text{m}$. The red ellipsoids indicate the $0.2\,U_0$ equipotential surface of the dipole traps representing the typical trapping volume. The inset shows a cross section along the optical axis.

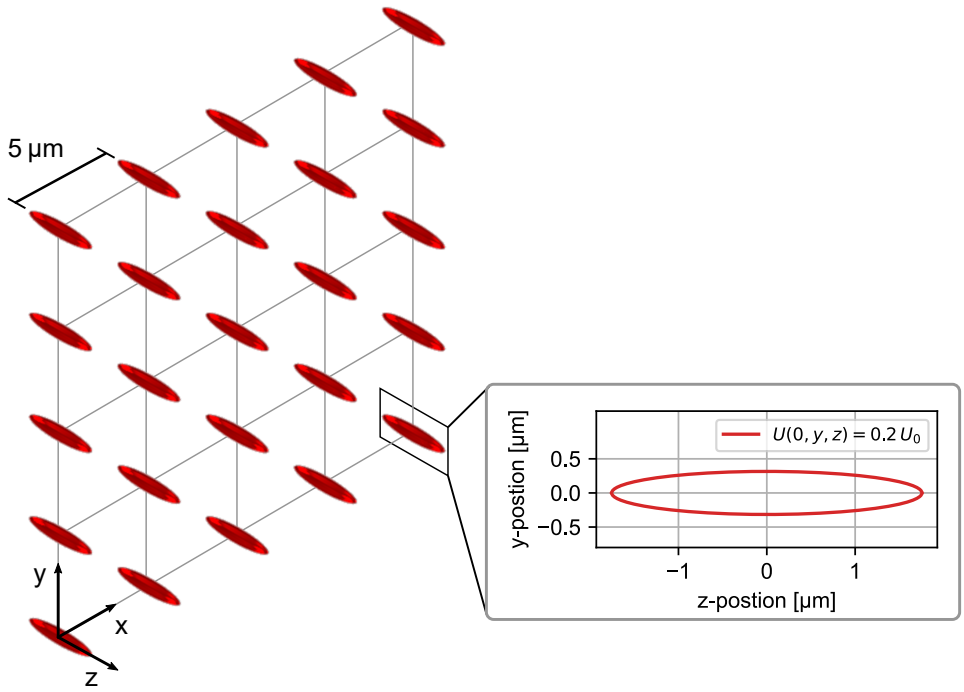

Fig. 2.2.: Illustration of the typical geometry of a tweezer array. The traps are elongated in direction of the optical axis (z). The red ellipsoids indicate the equipotential surface corresponding to $20\,\%$ of the trap depth. The inset shows a cross section in the yz-plane. All aspect ratios are to scale.

The dipole traps presented in this work are generated using micro-optics. A microlens array (MLA) produces an array of focal spots. The spots are demagnified and relayed into the vacuum chamber. The usable array size is technically limited by the total laser power available for trap generation. Hence, this approach offers an unprecedented scalability. The *Talbot effect* describes regular re-images of the focal plane along the optical axis. This effect extents the scalability even further to readily available 3D-configurations. [30] A common alternative approach is holographic trap generation based on liquid-crystal spatial light-modulators (SLMs). [42–44]

this technique offers a higher level of control regarding the parameters of individual traps and the array geometry while the scalability of the array size is limited by the resolution of the SLM. Also, trap generation based on conventional optics is typically more reliable and stable. A third approach is trap generation based on acousto-optic deflectors (AODs) operated with a multi-tone signal. [45–47]

The dipole traps are loaded during the molasses phase. In presence of the cooling light fields, light assisted collisions modify the Poissonian loading statistics. [48] The dynamics of the atom number N in a trap is governed by the differential equation

$$\frac{d\,N}{dt} = R - \gamma N - \beta N(N-1) \tag{2.32}$$

with the loading rate R, the single-atom loss rate γ, and two-body loss rate β. For a sufficiently small trapping volume and a high loading rate, the mean atom number $\bar{N}$ is dominated by two-body losses. In this regime, pairs of atoms are expelled from the trap on short time scales, such that at the end of the loading phase either $N = 0$ or $N = 1$. Both cases occur with approximately equal probability such that the mean atom number is $\bar{N} \approx 0.5$. The cooling light fields are employed for detection of the trapped atoms. Fluorescence light is captured by the high-NA optics used for generating the tweezer array. A sensitive EMCCD (electron multiplying charge-coupled device) camera detects the light with single-site resolution. The atoms remain trapped during the imaging procedure. In the obtained images, individual atoms are identified by choosing an intensity threshold in the trapping region. Depending on the camera type and the required detection fidelity, the exposure time of $30\,\mathrm{ms}$ to $100\,\mathrm{ms}$ adds a significant contribution to the total duration of an experimental cycle.

The inherently stochastic loading procedure limits the size of defect-free structures available for experiments. It is possible to guarantee defect-free structures by post selection. Even for an improved loading scheme with a success rate of up to $90\,\%$, as demonstrated recently with up to four traps [49], the probability of achieving defect free structures of more than 100 atoms $< 0.9^{100} \approx 3 \times 10^{-5}$ is prohibitively small. Thus, sorting schemes are applied that rely on the relocation of atoms from a reservoir to a target structure. These schemes are deterministic since the transport process is deterministic up to small error rates. Common transport techniques include rearranging the trap array [43, 45] or superimposing a movable optical tweezer in a static trap array [24, 29, 50]. Finding optimal transport paths between a stochastically filled reservoir and a 2D target structure is a computationally hard task. Since real-time calculations are required, fast heuristic algorithms providing close to optimal solutions are used. [29, 51–53]

Figure 2.3 shows a typical experimental sequence. In a first step, a cloud of cold atoms is prepared by a MOT phase followed by an optical molasses phase. Typically, a efficient loading of the MOT requires $0.5\,\mathrm{s}$ to $1\,\mathrm{s}$ constituting the largest timing overhead in the sequence. The duration of the molasses phase is negligible. Subsequently, the dipole traps are loaded, an image identifies occupied sites, and the target structure is filled via rearrangement. The transport time is typically on the order of $1\,\mathrm{ms}$ per target site. For small structures, the time required for rearrangement is defined by the exposure time of the imaging system. For large structures, multiple rearrangement cycle are used requiring multiple images. After assembly, the trapped atoms are prepared in a defined initial state, e.g. by optical pumping. This step is followed by the actual quantum information experiment. The results of the experiment is obtained by repeating it several hundred to several thousand times as required by the irreducible stochastic

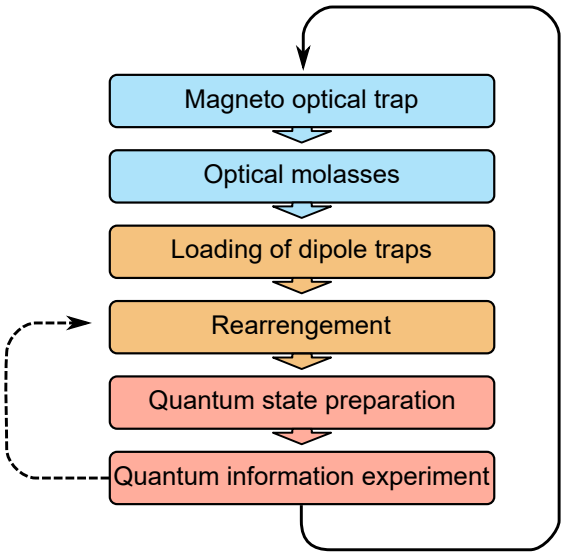

Fig. 2.3.: Overview of a typical experimental sequence conducting a quantum information experiment with individual atoms in an optical tweezer array.

nature of quantum objects. When working with a large reservoir, it is possible to reconstruct the target structure multiple times without reloading the MOT, thereby increasing the repetition rate significantly.

2.3. Rydberg atoms

Rydberg states are highly excited electronic states of atoms. In the context of this work, typically states with a principal quantum number $n \geq 30$ are considered. The excited electron is bound weakly to the ionic core of the atom. The weak bond evokes extraordinary properties distinguishing Rydberg atoms significantly from ground state atoms. These properties find an impressively wide range of applications. For quantum information experiments, especially the interaction between Rydberg atoms and their coupling to the ground state are relevant. This section discusses these aspects briefly. We will focus on alkali metal Rydberg atoms, in particular, Rydberg atoms with one Rydberg electron. An extensive review of the extraordinary properties of Rydberg atoms and their applications can be found in [54].

2.3.1. Properties of Rydberg atoms

The basic properties of Rydberg atoms arise from their electronic wavefunction. The wavefunction is described in the context of quantum defect theory where they are described as modified solutions to the well-known Hydrogen problem. [54, Chap. 2] The eigenenergy of the Rydberg state $|nlj\rangle$ is given by

$$E_{nlj} = -\frac{Ry}{(n-\delta_{nlj})^2} \tag{2.33}$$

where Ry is the Rydberg constant and δ_{nlj} is an empirical quantum defect. Exact Coulomb wavefunctions are determined by numerical integration of the radial Schrödinger equation. For accurate results, spin orbit coupling is included while the hyperfine structure, for Rydberg

atoms typically in the kHz regime [55], can be neglected. For alkali Rydberg atoms, a large database of quantum effects is available. In this work, the Python based software package *ARC* [56] is used to calculate Rydberg wavefunctions and corresponding dipole matrix elements. Figure 2.4 shows the binding energies of ^{85}Rb Rydberg states for $60 \leq n \leq 100$ and different L. The quantum defects δ_{nlj} shift the levels significantly for different L (and j). The fine structure energy is similar to the energy spacing between different n. The wavelength required for excitation of the S and D states from the $|5P_{3/2}\rangle$ hyperfine structure manifold is denoted on the right. Due to the small energy spacing of several GHz, typically a wide range of Rydberg states is accessible with a single laser system.

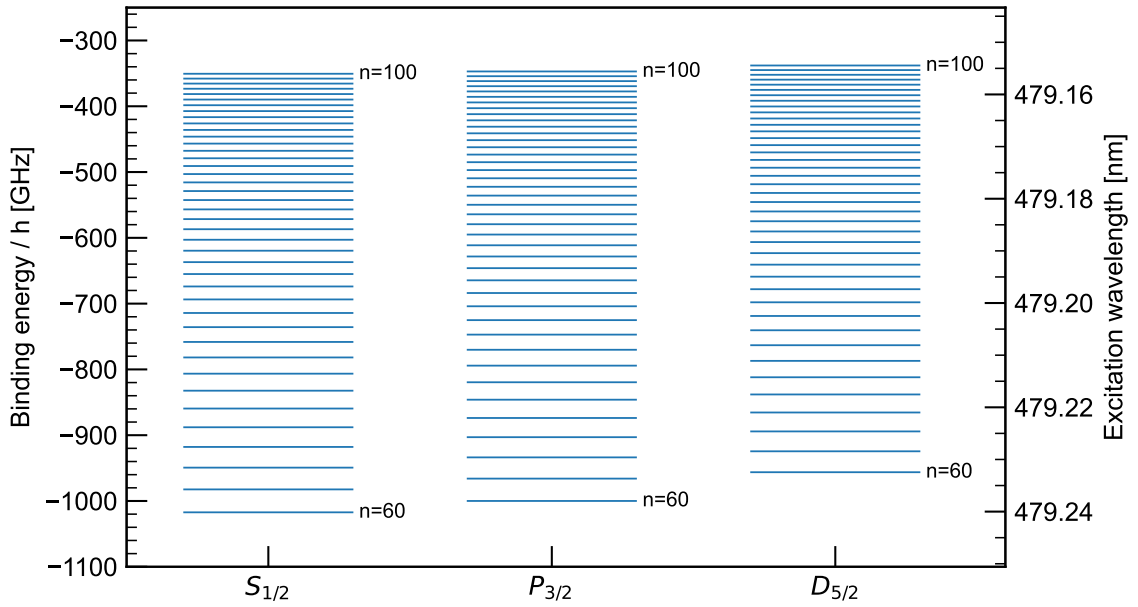

Fig. 2.4.: Binding energies of ^{85}Rb Rydberg states in units of h for different L in the range $60 \leq n \leq 100$. The values are calculated using *ARC* [56]. The wavelength required for excitation of the S and D states from the $|5P_{3/2}\rangle$ manifold is denoted on the right.

Simple scaling laws can be derived that illustrate the extraordinary properties of Rydberg atoms. In the following, we will assume $|\delta_{nlj}| \ll n$ for simplicity. According to Eq. 2.33 the binding energies scale with

$$E_{nlj} \propto n^{-2} \tag{2.34}$$

Consequently, the energy spacing $\Delta E = |E_{(n+1)l'j'} - E_{n,l,j}|$ between Rydberg states $|nlj\rangle$ and $|n+1l'j'\rangle$ scales as

$$\Delta E \propto \frac{1}{(n)^2} - \frac{1}{(n+1)^2} \approx n^{-3} \tag{2.35}$$

Due to the low binding energy, the spread of the electronic wavefunction is large. The size of the Rydberg atom is estimated in terms of the Bohr theory [54, Chap. 1]. The orbit corresponding to the energy E_{nlj} has a radius

$$r_n = a_0 n^2 \tag{2.36}$$

scaling with n^2. The quantity a_0 is the Bohr radius. Due to the quadratic scaling, the extension of a Rydberg atom is large as compared to a ground state atom. The dipole matrix element between adjacent, dipole coupled Rydberg states $\langle nl'j'|\,\boldsymbol{\epsilon}\mathbf{d}\,|nlj\rangle$ scales with r_n. Hence, a direct consequence of the large extension of the electronic wavefunction is a huge polarisability described in second order perturbation theory scaling with $|\,\langle nl'j'|\,\boldsymbol{\epsilon}\mathbf{d}\,|nlj\rangle\,|^2/\Delta E \propto n^7$. As discussed in Sec. 2.2, the central quantity describing the coupling between a Rydberg state $|nlm\rangle$ and a ground state $|g\rangle$ is the dipole matrix element $\langle g|\,\boldsymbol{\epsilon}\mathbf{d}\,|nlj\rangle$. The overlap between $|g\rangle$ and $|nlj\rangle$ is small due to the large extension of $|nlj\rangle$. The value of the relevant dipole matrix element is given by the shape of the wavefunction close to $r = 0$. The scaling behaviour in this region is dominated by the normalisation of the wavefunction scaling as $n^{-3/2}$ as long as $l \ll n$. The exact behaviour of the wavefunction is strongly influenced by the exact quantum defect of the Rydberg state. However, the coupling between Rydberg state and ground state is orders of magnitude weaker than the coupling between low lying states. Another consequence of the weak overlap between Rydberg states and ground states is an increased radiative lifetime scaling with $|\,\langle g|nlj\rangle\,|^2 \propto n^3$. Note, that the Rydberg-state lifetime observable in experiments is significantly reduced to due stimulated absorption and emission of black body radiation. Comprehensive numerical calculations of black body effects in alkali atoms can be found in [57]. Table 2.1 summarises the scaling laws discussed here. All laws should be interpreted as estimates describing the underlying behaviour, whereas the exact behaviour is determined by the atom species and the exact states involved.

Property	**Scaling law**
Binding energy E_{nlj}	n^{-2}
Energy spacing between adjacent states ΔE	n^{-3}
Orbital radius r_n	n^2
Dipole matrix element $|\,\langle g|\,\boldsymbol{\epsilon}\mathbf{d}\,|nlj\rangle\,|$	$n^{-3/2}$
Radiative lifetime τ	n^3
van der Waals coefficient C_6	n^{11}
Dipolar interaction coefficient C_3	n^4

Tab. 2.1.: Scaling laws for Rydberg atoms describing the scaling of the stated quantities with the principle quantum number n.

2.3.2. Rydberg excitation schemes

Exploiting the interaction between Rydberg atoms for quantum information experiments requires efficient coherent excitation of Rydberg states. Due to the weak coupling between the Rydberg state and the ground state, large laser intensities are necessary to achieve sufficient Rabi frequencies in the MHz regime. In this section, feasible excitation schemes for rubidium are discussed.

Figure 2.5 shows commonly used Rydberg excitation schemes for ^{85}Rb. The transition wavelength exciting Rydberg P-states directly from the $|5S_{1/2}\rangle$ ground state (a) is 297 nm. This excitation scheme is most relevant for experiments where only a small admixture of the Rydberg state, i.e. Rydberg dressing, is required. [58, 59] Working with the ultraviolet (UV) wavelength is experimentally challenging. Additionally, the laser power available limits the achievable Rabi frequencies and the required laser systems are resource intensive. Thus, most experiments

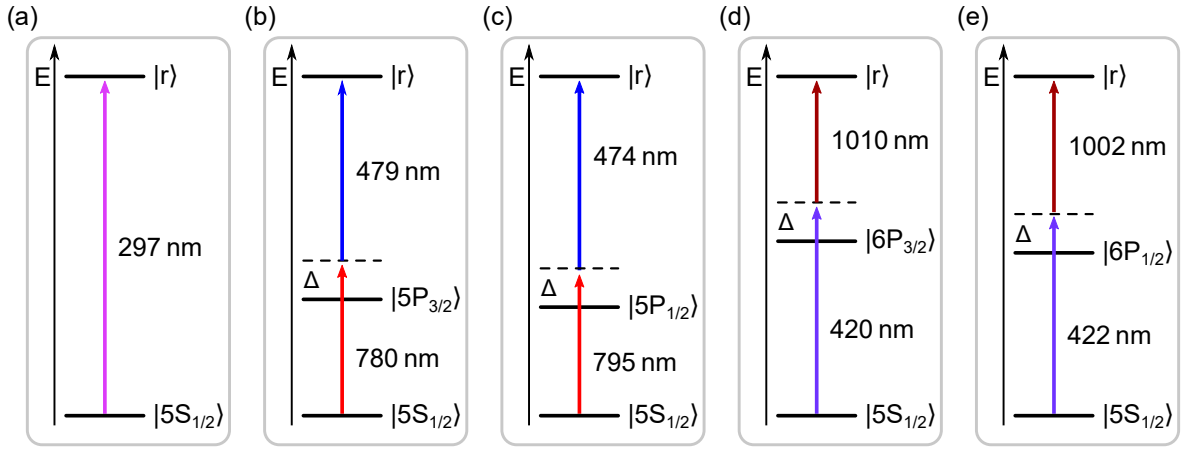

Fig. 2.5.: Commonly used Rydberg excitation schemes for ^{85}Rb. (a) shows the direct one-photon excitation while possible two-photon schemes are depicted in (b) – (e). The wavelengths stated for the transition to the Rydberg state $|r\rangle$ represent the ionisation threshold.

realise a two-photon excitation scheme. The Rydberg state $|r\rangle$ is coupled to an intermediate state $|e\rangle$ with Rabi frequency Ω_{er}. The ground state $|g\rangle$ is coupled to $|e\rangle$ with a Rabi frequency Ω_{ge} by a second laser field. A ladder scheme is realised where both laser fields are detuned by $\pm\Delta$ from their respective transition such that the sum frequency of the fields is in resonance with the transition $|g\rangle \rightarrow |r\rangle$. For $\Delta \gg \Omega_{ge}, \Omega_{er}$, the intermediate state $|e\rangle$ is not populated. Adiabatic elimination of $|e\rangle$ yields an effective two-photon Rabi frequency [60]

$$\Omega_{2p} = \frac{\Omega_{ge}\Omega_{er}}{2\Delta}. \tag{2.37}$$

When calculating Δ and the resonance condition, the light shifts induced by the light fields have to be taken into account. Additionally, residual one-photon scattering constitutes a decoherence channel. [61, 62] For a given Ω_{2p}, both effects are minimised by choosing $\Omega_{ge} = \Omega_{er}$. Their influence is reduced further by increasing Δ at the cost of lower Rabi frequencies. Figures 2.5 (b)–(e) show possible two-photon excitation schemes for ^{85}Rb. The wavelengths stated for the transition to the Rydberg state represents the ionisation threshold. The wavelengths resonant to the Rydberg states considered in this work are slightly longer. The schemes can be divided in two classes. The first class depicted in (b) and (c) uses $|e\rangle = |5P_j\rangle$. The strong coupling on the $|g\rangle \rightarrow |e\rangle$ transition allows for achieving sufficiently large Ω_{ge} with reliable standard laser systems on the D1 or D2 line. The achievable effective Rabi frequency Ω_{2p} thus depends on the laser power available at the $|e\rangle \rightarrow |r\rangle$ only. The second class employs $|e\rangle = |6P_j\rangle$. These so called inverted schemes are advantageous since the critical $|e\rangle \rightarrow |r\rangle$ transition is in the infrared regime where high-power laser systems are available. Also, the $|6P_j\rangle$ states feature a lower decay rate as compared to the $|5P_j\rangle$ states resulting in a reduction of decoherence effects due to one-photon scattering. However, the technological overhead for these schemes is significantly larger since high-power laser systems at both transitions are required. Note, that it is possible to excite Rydberg S- and D-states using the two-photon schemes while the one-photon scheme only couples P-states.

Figure 2.6 shows the dipole matrix elements for the coupling to different $|nS_{1/2}\rangle$ Rydberg states in the excitation schemes presented in Fig. 2.5 (b)–(e). The magnitude of the matrix elements shows an intuitive order in accordance with the energy of $|e\rangle$. The logarithmic scale

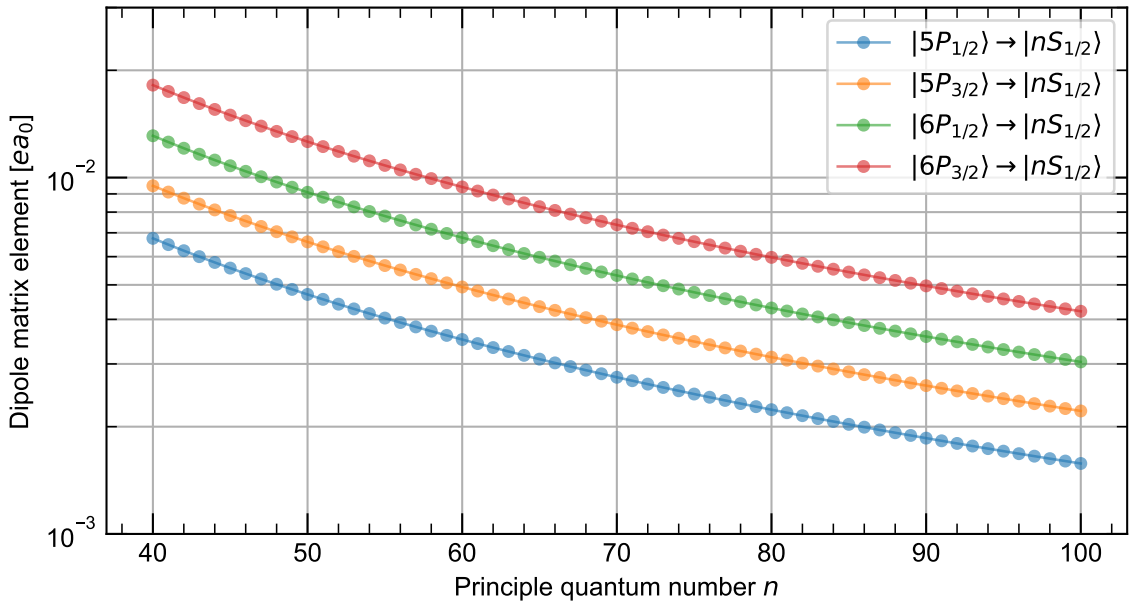

Fig. 2.6.: Dipole matrix elements for relevant couplings to a $|nS_{1/2}\rangle$ Rydberg state in the two-photon excitation schemes presented in Fig. 2.5 calculated for different principal quantum numbers n. The respective transitions are stated in the legend.

shows that the curves maintain an approximately constant ratio for all n. According to Eq. 2.6, the stated matrix elements define the (one-photon) Rabi frequency at a given laser intensity. Using the schemes involving the $j = 3/2$ states offer approximately 30 % larger Rabi frequencies than schemes using $j = 1/2$ states. This advantage may be masked by the properties of the laser systems. The schemes (d) and (e) offer a factor of $\sim$2 as compared to their counter parts (b) and (c). However, the matrix elements of the $|5S_{1/2}\rangle \rightarrow |5P_j\rangle$ transitions is almost one order of magnitude larger than the matrix elements of the $|5S_{1/2}\rangle \rightarrow |6P_j\rangle$ transitions. [35, 63] This work focusses on scheme (b) as used in our previous work. [62, 64]

2.3.3. Rydberg-Rydberg interactions

For optical tweezer experiments, Rydberg atoms are particularly interesting since they allow for introducing tunable interactions between atoms at different array sites with distances in the µm regime. [6, 14, 65] This section discusses two types of long-range Rydberg-Rydberg interactions, namely the van der Waals interaction between identical Rydberg states and the resonant dipole-dipole interaction between different Rydberg states.

Consider two atoms separated by $\mathbf{R}$ excited to a Rydberg state $|r\rangle$. Assume that the distance $|\mathbf{R}|$ is large as compared the charge distribution of the atoms, i.e. $|\mathbf{R}| =: R \gg n^2 a_0$. The dipole-dipole interaction between the atoms is given by [66]

$$\hat{V}_{dd}(\mathbf{R}) = \frac{1}{4\pi\epsilon_0}\left(\frac{\hat{\mathbf{d}}_1\hat{\mathbf{d}}_2}{|\mathbf{R}|^3} - \frac{3(\hat{\mathbf{d}}_1\mathbf{R})(\hat{\mathbf{d}}_2\mathbf{R})}{|\mathbf{R}|^5}\right) \tag{2.38}$$

where $\hat{\mathbf{d}}_1$ and $\hat{\mathbf{d}}_2$ denote the electric dipole operators acting on the respective atom. When cal-

culating interactions energies, it is convenient to transform to the pair state basis $\{|rr\rangle, |r'r''\rangle\}$, where $|r'\rangle, |r''\rangle$ are Rydberg states dipole coupled to $|r\rangle$. The dipole-dipole potential couples the pair states $|rr\rangle$ and $|r'r''\rangle$. Considering the leading order in R only, the coupling is given by $\langle rr|\,\hat{V}(\mathbf{R})\,|r'r''\rangle =: V_0/R^3$. In the pair state basis, the interaction Hamiltonian reads

$$\hat{H}_{int} = \begin{pmatrix} 0 & V_0/R^3 \\ V_0/R^3 & \Delta_F \end{pmatrix} \tag{2.39}$$

where the energy scale is defined by the Förster defect

$$\Delta_F = E_{r'} + E_{r''} - 2E_r. \tag{2.40}$$

The eigenvalues of $\hat{H}$ are given by

$$\lambda_\pm = \frac{\Delta_F \pm \sqrt{\Delta_F^2 + 4V_0^2/R^6}}{2}. \tag{2.41}$$

In general, $\Delta_F \gg V_0/R^3$ at relevant distances due to the R^{-3} dependence. In this *van der Waals* regime, the problem may be solved perturbativeley. The eigenvalue λ_- corresponds to the energy shift of the $|rr\rangle$ state, i.e. the interaction energy associated with the double excited state, while no significant state mixing occurs. The energy shift is given by $\lambda_- \approx -V_0^2/R^6$. Analogously considering all dipole coupled states $|r'r''\rangle$, yields the total energy shift ΔE_{rr} defining the van der Waals coefficient C_6 by

$$\Delta E_{rr} = -\sum_{r',r''} \frac{|\,\langle rr|\,\hat{V}(\mathbf{R})\,|r'r''\rangle\,|^2}{\Delta^2_{r',r''}} =: -\frac{C_6}{R^6}. \tag{2.42}$$

The pair state matrix elements $\langle rr|\,\hat{V}(\mathbf{R})\,|r'r''\rangle \approx \langle r|\,d_1\,|r'\rangle\,\langle r|\,d_2\,|r''\rangle$ scale as products of two dipole matrix elements in the single atom basis. Recalling that the Rydberg-Rydberg dipole matrix elements scale as n^2 and the energy spacing scales as n^{-3}, from the expression also the scaling of C_6 with n^{11} is evident. In the van der Waals regime, a *Rydberg blockade* can be realised by introducing an energy shift ΔE_{rr} that blocks the Rydberg excitation of adjacent atoms in the tweezer array by exciting one atom to $|r\rangle$. This regime is most relevant for quantum information since the famous Cirac–Zoller controlled-NOT gate is based on the blockade mechanism. [67] In the field of quantum simulation, the van der Waals interaction naturally implements quantum Ising-type Hamiltonians by identifying $|\uparrow\rangle = |r\rangle$ and $|\downarrow\rangle = |g\rangle$. [19, 24, 68, 69]

The second relevant interaction regime, is the *resonant dipole-dipole interaction* where $\Delta_F \ll V_0/R^3$. In this case, $\lambda_\pm \approx \pm V_0/R^3$. For large distances, resonant dipole-dipole interaction is realised when a pair of dipole-coupled states with a small Förster defect can be found. In this case, it is possible to tune $\Delta_f = 0$ using external electric fields such that $\Delta_F \ll V_0/R^3$ for all R. Several of these *Förster resonances* can be found for rubidium in the relevant range $40 \leq n \leq 100$. [70] Förster resonances are particularly interesting when working in the Rydberg blockade regime. Resonant dipole-dipole interactions also occur when considering two atoms in different dipole-coupled Rydberg states $|r\rangle$ and $|r'\rangle$. In this configuration, the dipole-dipole interaction $\hat{V}_{dd}$ couples the degenerate pair states $|rr'\rangle$ and $|r'r\rangle$. The interaction Hamiltonian in the basis $\{|rr'\rangle, |r'r\rangle\}$ is identical to Eq. 2.39 with $\Delta_F = 0$. Consequently, the energy shift is given by

$$\Delta E_{rr'} = \langle r'r|\,\hat{V}(\mathbf{R})\,|rr'\rangle =: C_3/R^3. \tag{2.43}$$

In other words, $\hat{V}_{dd}$ constitutes an energy associated with excitation exchange between the two atoms. This interaction naturally implements quantum XY spin models by identifying $|\uparrow\rangle = |r\rangle$ and $|\downarrow\rangle = |r'\rangle$. XY models open a wide field for quantum simulation including hard-core bosons and interacting fermions. [65] Recently, topological phases of artificial quantum matter have been realised employing XY models. [20, 21]

From an experimental perspective, in optical tweezer arrays the trap distance and the required interaction strength determine the choice of the employed Rydberg state. Larger interaction energies are achieved by choosing a larger principle quantum number n at the cost of lower Rabi frequencies for given laser intensities and detuning.

2.3.4. The ponderomotive potential

The atoms excited to Rydberg states are initially trapped in optical tweezers. The orbit size of the Rydberg electron is enormous. It is typically comparable to the waist of the tweezer. In this regime, the dipole approximation used in Sec. 2.1.2 is no longer valid. Instead, the weakly bound electron may be treated as a free electron following the electrical field in a quiver motion. [71] This approach is justified by the Born-Oppenheimer approximation since the time scales of the fast quiver motion are well separated from the time scales governing the dynamics of the Rydberg atom without the presence of the light field. The *ponderomotive energy* is the time-averaged energy corresponding to the quiver motion. It is given by [71]

$$E_{pon} = \frac{e^2 E_0^2}{4 m_e \omega_0^2} \tag{2.44}$$

for a light field $E(t) = E_0 \cos(\omega_0 t)$. For a spatially varying field, this results in a *ponderomotive potential*

$$U_{pond}(\mathbf{r}) = \frac{e^2 E_0^2}{2 m_e c \epsilon_0 \omega_0^2} I(\mathbf{r}). \tag{2.45}$$

In particular, the potential is repulsive independently on the laser frequency ω_0. Thus, red-detuned dipole traps for ground-state atoms repel Rydberg atoms. Turning off the traps while exciting ground state atoms to Rydberg states eliminates the undesired effects of the traps. However, this approach limits the observation time to typically $10\,\mu s$ due to the finite temperature of the atoms in the traps. The observation time defines a lower bound for the Rabi frequency required to observe coherent dynamics. The observation time may be extended significantly by using blue detuned traps. [72] In this configuration, a ponderomotive trap is formed for the Rydberg atom.

3. Laser technologies for quantum information science and high-resolution spectroscopy

The quantum simulation and computation experiments discussed in Chapter 2 involve a multitude of high-performance laser systems. Most of the requirements are fulfilled by state-of-the-art commercial laser systems. However, a considerable integration effort is induced by using different commercial systems in one experiment. Hence, integrability and maintainability are significantly enhanced by using specialised custom laser systems. Such systems feature a performance tailored to experimental requirements while reducing costs significantly.

In this chapter, design and specifications of our diode laser systems and optical amplifiers are discussed. In a typical application, active frequency and intensity stabilisation is applied to these laser systems. Design, characterisation, and application of optimised digital controllers for laser-frequency stabilisation as well as for laser-intensity stabilisation and control are presented. The intensity controllers are complemented by adapted low-noise wideband photodetectors. Furthermore a novel laser-current modulation technique is presented. This technique allows for achieving an optimal performance for high-bandwidth laser-frequency stabilisation.

3.1. External-cavity diode laser systems

Diode lasers are a compact, cost-efficient and robust choice for applications at a well-known wavelength that require a maximum laser power on the order of $100\,\mathrm{mW}$. The availability of efficient semiconductor materials fosters an ongoing development of high-power laser diodes for the Rubidium D1 and D2 line wavelengths of $795\,\mathrm{nm}$ and $780\,\mathrm{nm}$. In order to obtain a narrow linewidth, the laser diode is used in an external-cavity diode laser (ECDL) configuration. [73,74] The targeted applications put high demands on the spectral properties of the ECDL systems while a large mode-hop-free tuning range is not required. For these requirements a design based on interference filters as wavelength selective elements is preferable over designs using a diffraction grating. [73] The ECDL design used in this work is based on [75] and has been refined in this work. In this section, the improvements, important design details, and specifications are discussed.

Figure 3.1 shows a vertical cross section of the laser head. The laser diode is placed in an external cavity formed by a feedback mirror mounted on a piezo actuator and the rear facet of the diode. The divergent light emitted from the laser diode is collimated using an aspheric lens with a short focal length (Thorlabs C330TMD-B). The collimated light is focused on the feedback mirror by a second aspheric lens (Thorlabs A280TM-B). An additional lens of the same type collimates the output of the ECDL. This so-called cat-eye configuration increases the mechanical stability of the cavity significantly. [73,76] A narrow-band interference filter is placed in the cavity. The filter selects one of the longitudinal cavity modes by inducing a frequency dependency of the cavity finesse. The mode selection can be adjusted by tuning the

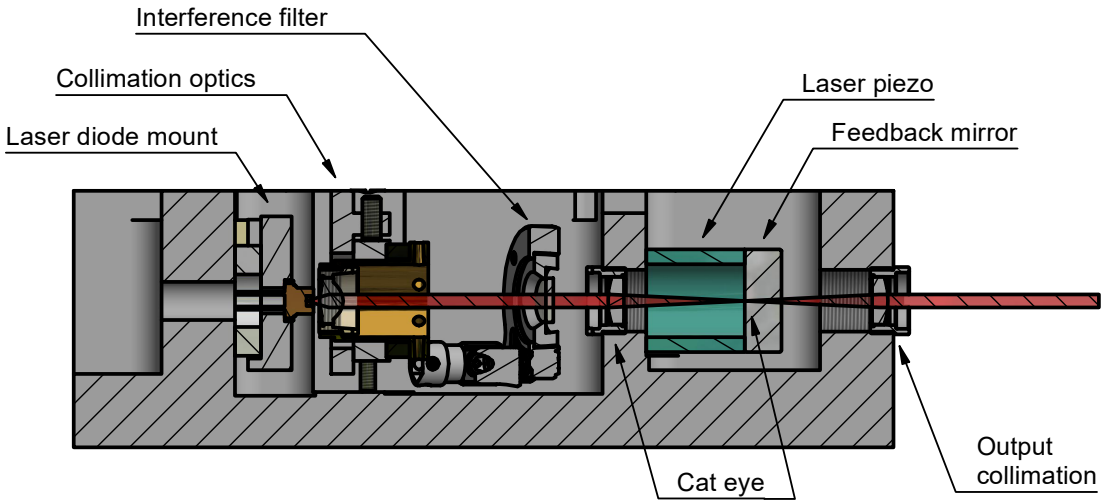

Fig. 3.1.: Cross section of the external-cavity diode laser used in this work. The depicted laser head is placed in an enclosure that contains the laser backplane and a thermo-electric cooler.

angle of incidence of the interference filter. Angle tuning of the filter does not change the laser frequency directly. It is only possible to choose between different cavity modes. Due to the high optical gain in the laser medium, even a small difference in the cavity transmission leads to a high suppression of the modes adjacent to the selected mode. For stable mode selection, the filter in use should feature a narrow linewidth in combination with a high peak transmission. A low transmission may inflict stable operation of the laser system by reducing the finesse of the external cavity. Additionally, it reduces the available output power. All interference filters used in this work have a width of approximately $0.4\,\mathrm{nm}$ (FWHM) and a peak transmission $T > 0.9$.

Nominal R_{feed}	**Coating**	**Uncertainty of R_{feed}**
4 %	uncoated	none
15 %	Laseroptik B-01438-03	± 2 %
20 %	Laseroptik	not available
30 %	Laseroptik B-01318	± 2 %
40 %	Laseroptik	not available

Tab. 3.1.: List of all available feedback-mirror types sorted by nominal reflectivity R_{feed}. For all types, laser quality fused silica substrates with an anti-reflective coating on the backside are used. The anti-reflective coating is specified to $R < 0.25\%$ at $780\,\mathrm{nm}$ (Laseroptik B-00047). See Appendix A.1 for detailed curves.

The finesse of the cavity is mainly defined by the reflectivity of the feedback mirror. The mirrors used in our laser systems are custom dielectric mirrors with a partially reflective coating on the frontside and an anti-reflective (AR) coating on the backside. The AR coating is specified to $R < 0.25\%$ at $780\,\mathrm{nm}$ (Laseroptik B-00047). An overview over available mirrors is given in Tab. 3.1. As a standard, the 15%-coating is used comprising a stable performance and decent output losses. In general, a higher feedback level is not necessary for stable perfor-

mance and reduces the maximum output power. Nevertheless, a stable operation is possible for applications that require lower laser powers. For AR-coated high-power diodes, such as Thorlabs LD785-SH300, losses are reduced further by using an uncoated mirror resulting in a $4\,\%$ feedback level. All partially reflective coatings and the AR coating feature a large bandwidth that allows for applications at wavelengths between $770\,\mathrm{nm}$ and $810\,\mathrm{nm}$ without any restrictions. Laser systems with stable operation at $960\,\mathrm{nm}$ have also been demonstrated in this work. See Appendix A.1 for detailed specifications of the coatings.

The laser head depicted in Fig. 3.1 is placed in an enclosure that contains the laser backplane with all necessary connectors. This enclosure also provides a stable mount for the ECDL and an efficient shielding against environmental influences such as acoustics and conductive heat transfer. For an additional shielding against these effects, a silicone case for the enclosure is added.

3.1.1. Laser diodes and optical power

For ECDL systems, ideally an AR-coated laser diode that does not feature an internal cavity is used. Since these diode types are only applicable to ECDL configurations, the commercial availability is limited and high costs are invoked. The ECDL systems used in this work are operated at well defined wavelengths. Hence, it is possible to use non-coated standard diodes at cost of a reduced mode-hop-free tuning range. There are laser-diode mounts for standard TO-9 and TO-56 packages available.

For most applications, a high optical output power of the laser system is desirable. The external cavity reduces the available output power of the ECDL system while increasing the optical power circulating in the diode. Thus, the optical feedback affects the maximally available power by reducing the efficiency of the laser, i.e. the output power per laser current above the threshold, and by reducing the maximum laser current at the same time. Efficiency η_0, threshold current $I_{th,0}$, and maximum current $I_{max,0}$ for the laser diode without external cavity are usually stated in the diode's data sheet. An estimate for the maximum current for safe operation in the external cavity I_{max} can be determined by measuring the efficiency η and the threshold I_{th} of the ECDL to

$$I_{max} = (I_{max,0} - I_{th,0})\frac{\eta}{\eta_0} + I_{th} \tag{3.1}$$

assuming that the change in efficiency can be attributed entirely to feedback into the laser diode.

Figure 3.2 shows the output power versus current characteristics of a typical ECDL system (blue) emitting light at $780\,\mathrm{nm}$. A high-power laser diode (Sharp GH0782RA2C) is used in the presented ECDL design with a 20%-feedback mirror. A typical feature of the wavelength selection is observable: Within one mode of the laser diode (internal mode) several modes of the external cavity can be found [76] of which one is selected by the filter. The transmission of the filter depends on the resonance frequencies of both the selected external mode and the corresponding internal mode. Both frequencies shift with the laser current (see Sec. 3.2 for details). Steps of the output power occur when an adjacent (external or internal) cavity mode is selected. Due to the larger sensitivity of the internal mode, the steps are more pronounced for a change of the internal cavity mode. The steps attributed to the change of the external cavity

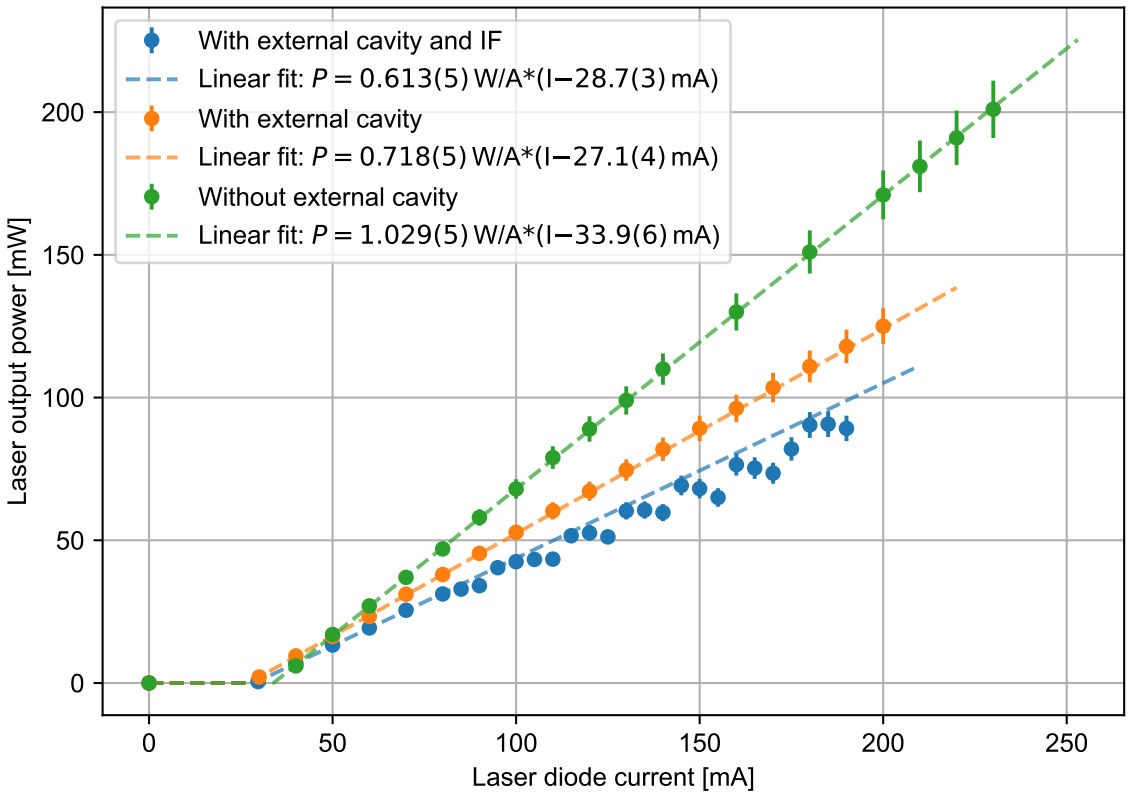

Fig. 3.2.: Typical output power versus current characteristics for different configurations of a diode laser system. The laser diode (Sharp GH0782RA2C) is placed in the ECDL configuration depicted in Fig. 3.1 equipped with a $R_{feed} = 0.2$ feedback mirror. Using an interference filter in the cavity (IF), a wavelength of 780.24 nm is selected. The markers show data points. The dashed lines indicate linear fits with the parameters stated in the legend.

mode are not resolved in this measurement. A linear fit using the first seven data points shows that the obtained power levels exhibit an linear behaviour up to the maximum laser current. For comparison, the characteristics of the ECDL without IF and the characteristics of the laser diode without external cavity are recorded in addition. The signature of the wavelength selection is not present in these cases. Linear fits to the first seven data points reveal a linear behaviour up to the maximum current. The efficiency and the threshold current is given by the slope and the I-axis intercept of the linear fit. The linear fits depicted in Fig. 3.2 represent the typical behaviour of an ECDL: The feedback of the external cavity leads to a significant drop of the threshold current. By inducing the filter in the cavity, the threshold current rises slightly (typically $\sim$1 mA) due to the finite transmission of the filter leading to a reduced feedback level. The efficiency of the laser in the external cavity is expected to be reduced by the portion of light used for feedback. [77] This effect is observable in the laser system discussed here. Typically, the reduction is larger than estimated from the reflectivity of the feedback mirror, which can be attributed to the presence of the internal cavity of the laser diode. [77, 78] Additionally, the losses on eight optical surfaces in the ECDL should be taken into account. Inducing the IF reduces the efficiency further due to the finite transmission of the filter. This effect is larger than estimated from the transmission of the IF as well. This can be attributed to the wavelength selection shifting the emission wavelength away from the optimal efficiency of the gain material.

Laser diode	Manufacturer specification			P_{ECDL}	Operational parameters		
	λ_0	P_{max}	$I_{max,0}$		I_{max}	λ	R_{feed}
Arima Laser ADL-78901TX	785 nm	90 mW	90 mA	40 mW	95 mA	785 nm	15 %
Sharp GH0782RA2C	785 nm	200 mW	230 mA	75 mW	160 mA	780 nm	15 %
Thorlabs L785H1	785 nm	200 mW	250 mA	80 mW	190 mA	780 nm	15 %
Thorlabs LD785-SH300-SP	785 nm	300 mW	450 mA	200 mW	400 mA	785 nm	4 %
Thorlabs LD808-SE500	808 nm	500 mW	800 mA	275 mW	540 mA	804 nm	4 %
JDSU SDL-5431-G1	798 nm	200 mW	270 mA	75 mW	160 mA	795 nm	15 %
JDSU SDL-6531-J1	972.5 nm	200 mW	320 mA	50 mW	190 mA	960 nm	15 %

Tab. 3.2.: List of laser-diode types used in this work. Manufacturer specification: Center wavelength λ_0, output power $P_{0,max}$ (without external cavity) at maximum forward current $I_{max,0}$. Typical output power from an ECDL system P_{ECDL} at the maximum forward current I_{max} for operation at the wavelength λ. ECDL system feedback level: R_{feed}.

In Table 3.2, laser diodes and typical operation parameters are listed. All diodes listed here are suitable for stable single frequency operation with a mode-hop-free tuning range larger than 1 GHz. All laser diodes emit light in a single transversal mode that can be coupled into a single mode optical fiber with an efficiency above 50 %. Another important criterion that has to be taken into account is the lifetime of the diode since the laser systems are typically used in continuous operation at high output powers. The standard diodes applicable for laser systems at 780 nm are Arima Laser ADL-78901TX for low-power applications and Thorlabs L785H1 for high-power applications. Sharp GH0782RA2C diodes show a similar performance as Thorlabs L785H1 while the lifetime is significantly reduced. For the maximum current derived from the data sheet, the lifetime is reduced to less than one month prohibiting permanent operation at this current. Reducing the forward current below 70 % of the maximum value extents the lifetime to approximately one year. Arima Lasers ADL-78901TX diodes have proven to feature a lifetime of several years. High-power laser diodes, such as Thorlabs LD785-SH300 and Thorlabs LD808-SE500, extend the range of possible applications of ECDL systems. [79]

3.1.2. Adjustable lens mount

In the presented ECDL design, the feedback mirror and the piezo actuator of the external cavity are assembled using adhesives. The aspheric lenses constituting the cat-eye and the output collimator are also locked using adhesives. Thus, the alignment of the external cavity cannot be readjusted. The collimation lens is used to adjust the external cavity. In the original design [75] as adapted by our group, the collimation lens is assembled using adhesives as well. Since this lens must be removed, if the laser diode is replaced, this configuration complicates maintenance significantly, especially for high-power laser diodes with a reduced lifetime. In a typical application, the output beam of the ECDL is coupled into a single-mode optical fiber at a distance of approximately 0.5 m. This setup is particularly sensitive against beam pointing instabilities. For most setups, a loss in coupling efficiency can be correlated to a change in ambient humidity. This instability can be attributed to the expansion of the adhesive defining the position of the collimation lens.

In this work, a mount for the collimation lens is introduced that features an enhanced mechanical stability and allows for readjustment as well as simple replacement of the laser

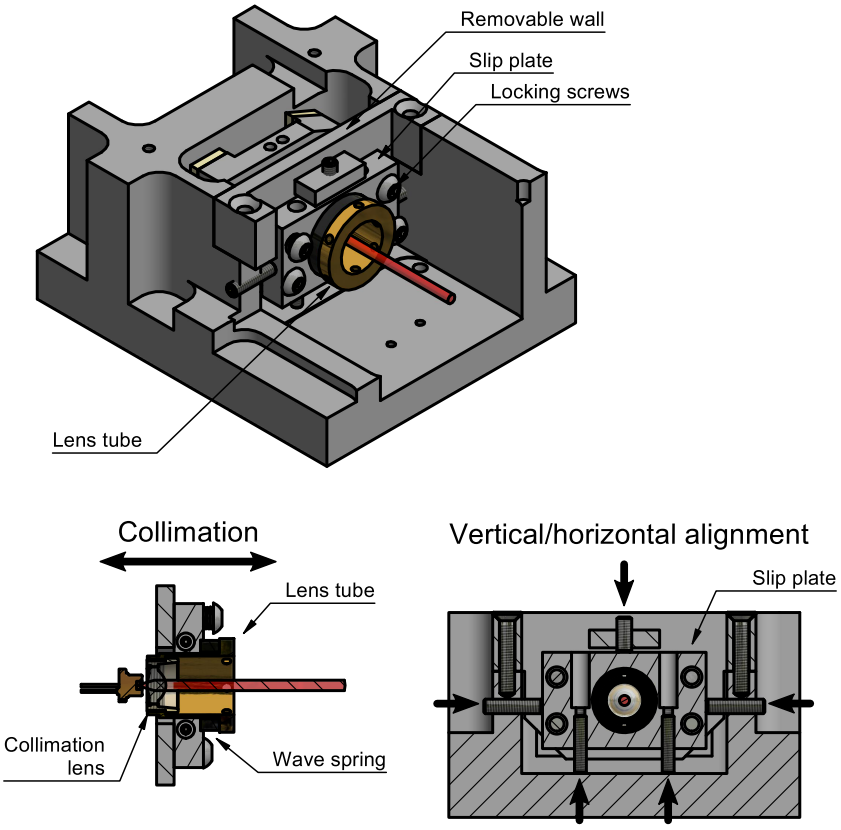

Fig. 3.3.: Schematic drawing of adjustable collimation optics for the ECDL design depicted in Fig. 3.1. The collimation unit is mounted in the laser head on a removable wall (top). A lens tube held by a wave spring allows for adjusting the collimation (bottom,left). Mounting the lens tube in an adjustable slip plate enables vertical and horizontal alignment of the collimation lens.

diode. The design of the mount is based on the design used in [80]. Figure 3.3 shows a schematic drawing of the collimation optics. All adjustable parts are mounted on a removable wall in the laser head (top). A lens tube holding the collimation lens allows adjusting the distance between laser diode and lens (bottom, left). The lens tube is held in place by a wave spring (LeeSpring LW 063 20 0180S). This spring type comprises a compact outline, a large spring rate, and a travel of approximately 3 mm. The lens tube is mounted in a slip plate that is used for centring the collimation lens (bottom, left). After adjustment, the slip plate is locked guaranteeing a higher mechanical stability. The large travel of the lens tube allows for compensating for different positions of the emitter within the lase-diode package. Thus, the collimation optics are compatible to a wide range of laser diodes with TO-9 and TO-56 packages. Existing laser heads of the earlier design can be retrofitted with this optics requiring only minor modifications.

3.1.3. Laser electronics

The ECDL system is connected to the supply and control electronics via a printed-circuit-board (PCB) backplane (see Fig. 3.10 (b) for details). A low capacitance DVI cable (Supra Cables HD5) is used to connect the laser-current driver to the laser diode. The backplane is designed to be used with our ultra-low noise current driver *DgDrive* [81, 82]. Nevertheless, it can be

used with our earlier-design current driver based on a design by Libbrecht and Hall [83] with a suitable adapter. Since laser diodes are sensitive to electro-static discharge (ESD) and reverse or over voltage due to malfunction of the current driver, the backplane also features a protection circuit (see Fig. 3.10 (a) for simplified schematics). A reverse diode protects the laser diode from fast events. Since most suitable Shottky diodes exhibit a large leakage current a fast switching transistor (ON Semiconductor 2N4401BU) is employed for that purpose. When the laser is turned-off or the cable is disconnected, the laser diode is shorted by a latching relay. The relay is controlled by the current driver or an external voltage between $9\,\mathrm{V}$ and $18\,\mathrm{V}$. In order to avoid additional noise in the laser head due to magnetic coupling of the switching current through the relay coil, the relay circuit requires only a short pulse for switching. After switching the current is turned off automatically.

The laser frequency exhibits a strong dependency on the cavity temperature and the temperature of the laser diode (see Sec. 3.2 for details). For this reason, the temperature of the laser cavity and the temperature of the laser-diode mount are stabilised actively in two cascaded control loops. The respective temperatures are measured using a $10\,\mathrm{k\Omega}$-thermistor in the cavity and a second identical thermistor close to the laser diode. A thermo-electric cooler (TEC) controls the temperature of the laser-diode mount using the laser cavity as a heat sink. A second TEC controls the cavity temperature transferring heat to the mechanical mount of the laser. TECs are sensitive to mechanical stress. For that reason, spacers matching the thickness of the TECs to $0.05\,\mathrm{mm}$ define the distance between the cooled devices and the heat sink. In a typical application, the cavity is cooled below room temperature and the laser diode is cooled below the cavity temperature. Both temperatures should remain well above the dew point since condensing moisture may damage laser diode and optics. A DSub-25 connector provides connection for two TECs each with a current rating of $10\,\mathrm{A}$ and two 4-wire connections for temperature sensing. For temperature stabilisation two independent controllers (Team Wavelength HTC1500[1]) are used.

3.2. Frequency stability of diode laser systems

In the ECDL configuration presented in Sec. 3.1, the laser frequency f_L is determined by the selected mode of the external cavity. Thus, all effects changing the optical length L of the cavity change the laser frequency. In this section, these effects are analysed. Typical values for the sensitivity of the laser frequency are given. The stated values will vary significantly over different laser systems and operating conditions. However, the given values allow for an estimate of relevant effects for a given application.

3.2.1. Influence of ambient conditions

The change of the frequency of the m-th cavity mode Δf_L due to a change in the optical length of the cavity ΔL is given by

[1]These cost-efficient devices offer a reasonable temperature stability of $\sim$1 mK, if fluctuations of the temperature of the device are kept below $0.1\,\mathrm{K}$. Typically, this temperature stability cannot be guaranteed. Also, the accuracy of the device's temperature measurement is only $\sim 10\,\mathrm{mK}$.

$$\Delta f_L = m\left(\frac{c}{2(L+\Delta L)} - \frac{c}{2L}\right) \approx -m\frac{c}{2L^2}\Delta L = -f_L\frac{\Delta L}{L}. \tag{3.2}$$

Hence, assuming a linear, isotropic expansion of the laser cavity, Δf_L can be modelled by

$$\Delta f_L = K_T \Delta T \tag{3.3}$$

for small temperature fluctuations ΔT using a linear temperature coefficient K_T . For the laser cavity, the temperature coefficient $K_{T,cavity}$ is given by

$$K_{T,cavity} = -\alpha f_L \approx -9\,\frac{\text{GHz}}{\text{K}} \tag{3.4}$$

with the thermal expansion coefficient of the cavity material $\alpha = \Delta L/L = 2.3 \times 10^{-5}\,\text{K}^{-1}$ [84] and the laser frequency $f_L = 384\,\text{THz}$.

The thermal coefficient of the laser diode is stated in the data sheet for most laser diodes. For laser-diode types emitting light between $780\,\text{nm}$ and $810\,\text{nm}$, the coefficient has a typical value of $0.3\,\text{nm/K}$ corresponding to -$150\,\text{GHz/K}$ at $780\,\text{nm}$. This coefficient includes three effects that decrease the laser frequency of the light emitted by the laser diode with increasing temperature: The change of the index of refraction, the shrinkage of the band gap, and the thermal expansion of the internal cavity. [85] In an ECDL configuration, the internal cavity does not determine the laser frequency. Hence, the latter two effects may only lead to mode-hops between different modes of the external cavity, while the first effect changes the optical Length L of the external cavity with a sensitivity reduced by the fraction L_{ld}/L where L_{ld} is the optical length of the internal cavity and L is the optical length of the external cavity. The change of the refractive index Δn_{ld} is typically [86]

$$\Delta n_{ld} = 2 \sim 5 \times 10^{-4}\,\text{K}^{-1}\Delta T \tag{3.5}$$

which corresponds to a frequency sensitivity on the same order as the typical coefficient stated for the internal cavity of laser diodes. Nevertheless, the sensitivity is reduced significantly using an ECDL configuration resulting in a sensitivity coefficient

$$K_{T,diode} = -\Delta n_{ld}\frac{L_{ld}}{L} f_L \approx -3\,\frac{\text{GHz}}{\text{K}} \tag{3.6}$$

using Eq. 3.2 assuming $\Delta n_{ld} = 5 \times 10^{-4}\,\text{K}^{-1}$, $L_{ld}/L = 1/60$,[2] and $f_L = 384\,\text{THz}$.

The residual temperature fluctuations of the laser diode are typically significantly smaller due to the cascaded temperature stabilisation. Additionally, $K_{T,diode}$ is smaller than $K_{T,cavity}$. However, as a secondary effect of temperature instabilities of the laser diode mode-hops and fluctuations of the output power occur. These effects underlie the more than one order of magnitude more sensitive thermal shift of the internal cavity.

Besides thermal effects, the barometric pressure affects the laser frequency significantly. This effect can be attributed to a change of the refractive index of air changing the optical

[2] Assuming a typical free spectral range of $150\,\text{GHz}$ for the internal cavity [76] and $L = 60\,\text{mm}$. Note, that the exact optical cavity length L depends on the length of the internal cavity of the laser diode and the index of refraction of the gain material as well as the position of the emitter within the diode package.

length of the cavity. The refractive index of air can be calculated using Ciddor's formula. [87] Since only the change in the refractive index Δn_{air} is relevant, the formula is linearised in the change of the barometric pressure Δp for a given ambient temperature T yielding [88]

$$\Delta n_{air} = 7.85 \times 10^{-5} \frac{\mathrm{K}}{\mathrm{mbar}} \times \frac{\Delta p}{T} = 2.65 \times 10^{-7}\,\mathrm{mbar}^{-1} \text{ at } T = 23\,^{\circ}\mathrm{C}. \tag{3.7}$$

With Eq. 3.2, the sensitivity coefficient K_{baro} is given by

$$K_{baro} = -\Delta n_{air} f_L = -75\,\frac{\mathrm{MHz}}{\mathrm{mbar}} \tag{3.8}$$

using the approximation $\Delta L = \Delta n_{air} L$ and $f_L = 384\,\mathrm{THz}$. Even, if the sensitivity is small as compared to the thermal effects, this effect is particularly relevant since a compensation requires a large technological overhead and is not available. Over the course of the years 2021 and 2022, a maximum change in the barometric pressure of $\Delta p = 60\,\mathrm{mbar}$ has been observed. Additionally, rapid changes of the ambient pressure can be induced by pressure waves caused by acoustics or opening and closing doors for instance. The resulting frequency change has to be compensated by a suitable active frequency stabilisation.

Quantity	**Typ. sensitivity**	**Symbol**
External-cavity temperature	-9 GHz/K	$K_{T,cavity}$
Laser-diode temperature	-3 GHz/K	$K_{T,diode}$
Barometric pressure	-75 MHz/mbar	K_{baro}
Piezo voltage	-240 MHz/V	K_{piezo}
Laser current	-150 MHz/mA	$K_{current}$

Tab. 3.3.: List of relevant factors affecting the frequency stability of an ECDL system. The stated sensitivities link a change in the corresponding quantity to a change in the laser frequency. The stated values are typical values that vary depending on the wavelength, laser-diode type, or operating and ambient conditions. The given values are calculated for a typical 780 nm-ECDL system.

3.2.2. Laser-frequency actuators

For applications that require a high long-term stability of the laser frequency or a narrow linewidth, active frequency stabilisation is employed using two actuators: the laser piezo and the laser current. A voltage V_{piezo} applied to the piezo actuator alters the optical length of the external cavity with a bandwidth of up to several kHz. A preloaded piezo ring stack (Piezomechanik HPSt150/14-10/12) allows for a bipolar operation. The piezo stack is elongated if a positive voltage is applied. In general, piezo stacks exhibit a non-linear and hysteretic elongation characteristic $\Delta L(V_{piezo})$. However, from Eq. 3.2 follows

$$\Delta f_L = \frac{f_L}{L} \Delta L\left(V_{piezo}\right). \tag{3.9}$$

Thus, the sensitivity of the piezo input K_{piezo} is proportional to f_L/L since the same type of actuator is used in all ECDL systems. In general, the function $L\left(V_{piezo}\right)$ is not known. Linearisation around a given operating voltage V_0 yields $K_{piezo}(V_0)$ relevant for the respective application.

A modulation of the laser current results in a modulation of the laser frequency. The frequency modulation is pre-dominantly caused by a modulation of the refractive index of the gain material. [86] The rate of the index change depends on the laser-diode type and the operating conditions such as forward current, feedback, and temperature. The transfer function connecting current modulation and frequency modulation may show a complex behaviour at high modulation frequencies. [89] However, for frequencies within the typical maximum control bandwidth of $1\,\mathrm{MHz}$, a flat transfer function is assumed. Analog to Eq. 3.6, the sensitivity $K_{current}$ of the laser frequency against a change in the laser current is proportional to the fraction L_{ld}/L. Note, that the sensitivity of the internal modes of the laser diode is significantly larger. Thus, mode hops occur when tuning the laser current since the wavelength selection in the external cavity is affected by the internal modes.

For laser systems with an active frequency stabilisation, the sensitivities K_{piezo} and $K_{current}$ under certain operating conditions are best determined experimentally employing the method used to create an error signal for frequency stabilisation, such as a spectroscopic reference or a beat node. Such measurements yield a typical value of

$$K_{piezo} = -240(20)\,\frac{\mathrm{MHz}}{\mathrm{V}} \quad \text{and} \quad K_{current} = -150(20)\,\frac{\mathrm{MHz}}{\mathrm{mA}} \tag{3.10}$$

for laser diodes at $780\,\mathrm{nm}$ and a cavity length of $L = 60\,\mathrm{mm}$. Note, that for the piezo actuator used in our laser systems K_{piezo} increases by approximately $30\,\%$ when the actuator is operated with a negative offset voltage of several volt.

3.3. Master-oscillator power-amplifier (MOPA) systems

The output power of ECDL systems is limited to a few hundred mW. Semiconductor laser diodes with a tapered gain region offer a high output power of several watt. [90] These diodes can be used as so-called tapered amplifiers (TA) if a high-performance AR coating is applied to the front and rear facets of the chips. Light of a seed laser system is coupled into the rear facet of the TA leading to stimulated emission thereby amplifying the seed laser light. This so-called master-oscillator power-amplifier (MOPA) system offers an output power of several watt while conserving the spectral properties of a narrow linewidth seed laser, such as an ECDL. A short ridge waveguide at the input facet guarantees emission in a single transversal mode in principle. Typically, beam quality factors $M^2 < 3$ are achieved. [91]

The MOPA systems developed in this work consist of an ECDL seed system and a separate TA setup which is supplied with seed light of the ECDL system using a single-mode, polarisation-maintaining optical fiber (PM fiber). The output of the TA is also coupled into a PM fiber after optional optics for intensity stabilisation or monitoring and optical filters. Additionally to the stimulated emission, TA chips exhibit amplified spontaneous emission (ASE) emitted at the front and rear facet of the chip. Since ECDL systems are susceptible to optical feedback, Faraday isolators are installed between seed laser and TA providing a suppression larger than $60\,\mathrm{dB}$ for the ASE at the rear facet.[3] At the output side a $30\,\mathrm{dB}$ isolation is employed to protect the chip from damage due to optical feedback.

[3] Typically, 30 dB-type isolators are placed at the output of the ECDL seed system and at the input of the TA module.

3.3.1. Tapered-amplifier beam shaping

The output facet of the tapered gain region is asymmetric with a typical aspect ration of 1:100. The divergence of the output beam is determined by diffraction on the output aperture. Hence, the asymmetric aperture results in a significantly reduced beam divergence θ_x parallel to the tapered dimension of the gain region (x-dimension) as compared to the beam divergence (θ_y) perpendicular to the tapered dimension of the gain region (y-dimension). Additionally, the beam is astigmatic. The virtual focus of the beam in the x-dimension is located within the gain material while the virtual focus of the y-dimension is approximately at the output facet. The astigmatism strongly depends on the TA forward current. Figure 3.4 shows the schematic beam shape of an tapered amplifier with suitable collimation optics producing a round and collimated beam. The basic properties of the beam are well described by simple ray tracing. The y-dimension of the output beam is collimated using a second aspheric lens with a short focal length f_{AL}. This lens determines the beam radius w_{TA} to

$$w_{TA} = \tan(\theta_y) f_{AL}. \tag{3.11}$$

Due to the astigmatism of the TA output beam, the aspheric lens produces a focus in the y-dimension reducing the beam divergence to $\theta'_x < \theta_x$. A cylindrical lens is used to collimate the beam in the x-dimension. The focal length of this lens f_{CL} is matched to

$$f_{CL} = \frac{w_{TA}}{\tan(\theta'_x)} \tag{3.12}$$

such that a round collimated beam is produced. While θ_x and θ_y are typically stated in the data sheet of the TA chip, θ'_x has to be determined experimentally at a given operation current. The input beam of the seed laser is focused on the rear facet of the TA chip using an aspheric lens with a short focal length. The mode of the seed laser is matched to the mode of the ASE emitted at the rear facet.

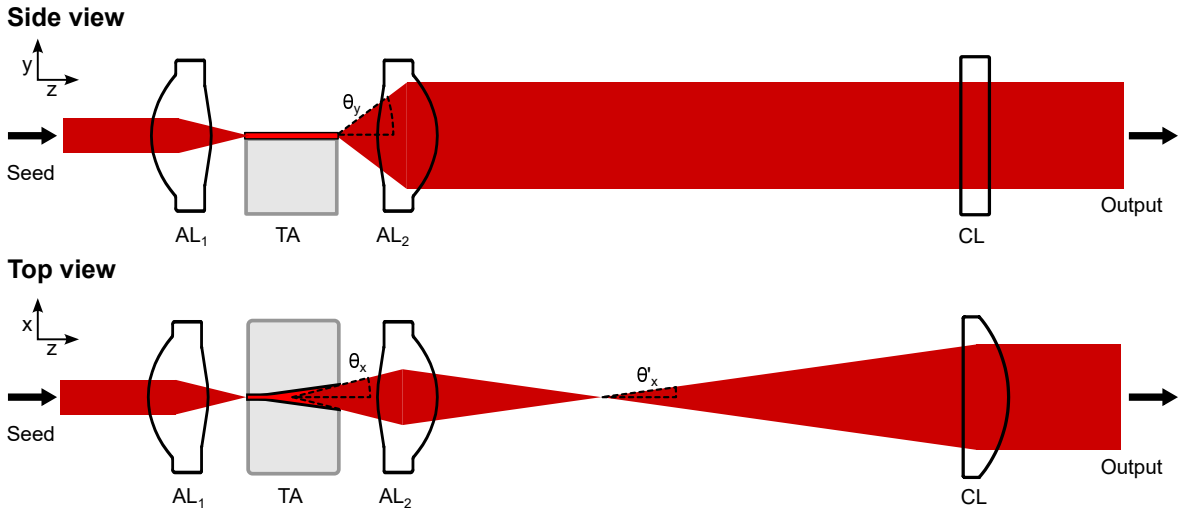

Fig. 3.4.: Schematic view of a tapered amplifier (TA) with collimation optics. The seed laser-field is coupled into the TA chip using an aspheric lens (AL). An identical lens is used to collimate the output beam in the y-dimension. The residual divergence in x-dimension is compensated using a cylindrical lens (CL).

3.3.2. Tapered-amplifier module

In this work, a tapered amplifier (TA) module is developed. The module comprises a mount for the TA chip including electrical contacts, a TEC-based temperature stabilisation, and adjustable collimation optics as depicted in Fig. 3.4.

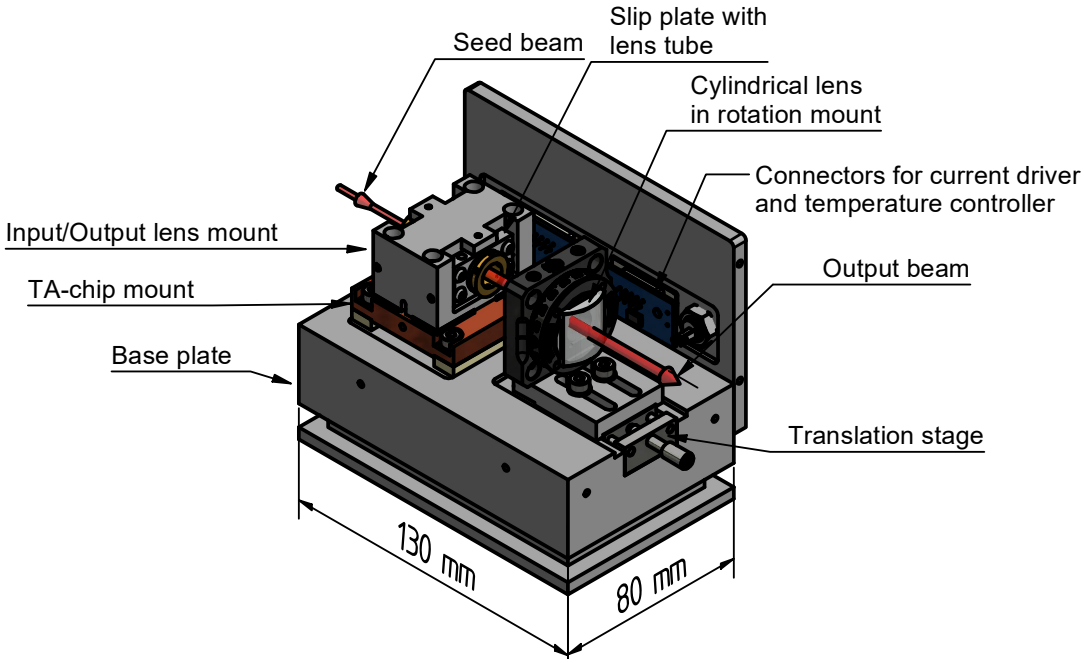

Fig. 3.5.: Schematic overview of the TA module developed in this work.

Figure 3.5 shows a schematic overview of the TA module. The TA chip is placed in a copper mount which is covered by a lens mount holding the aspheric lenses AL_1 and AL_2. Aspheric lenses with a focal length of $f_{AL} = 3.1\,\text{mm}$ are used (Thorlabs C330TMD-B). The lenses can be adjusted using lens tubes in a slip plate as described in Sec. 3.1.2 (see Fig. 3.3 for details). The cylindrical lens (*CL*) is mounted on a translation stage that is accessible from the front side of the module thereby allowing for optimisation and readjustment of the collimation, e.g. for coupling into a PM fiber. Additionally, the cylindrical lens is placed in a rotation mount that allows for fine adjustment of the lens axis to the divergent dimension of the pre-collimated output beam. Although the TA-chip mount is designed for a minimal tilt of the C-mount base, this may be necessary for chips that are not aligned exactly to the C-mount. Since the focal length of the cylindrical lens has to be matched to the astigmatism of the TA chip, the mount allows for placing the lens at a distance between approximately $25\,\text{mm}$ and $85\,\text{mm}$ from the output facet of the chip. This range is sufficient for all TA chips used in this work.

Figure 3.6 (a) shows a schematic view of the TA mount. The mount is designed for a C-mount package. The anode of the TA chip (C-mount block) is connected to the solid copper mount that also serves as a heat sink. For a better thermal contact and in order to achieve a minimal tilt of the chip, two copper clamps are used. The cathode contact is realised via a custom connector (see detail in Fig. 3.6 (a)): The C-mount tab is placed in an isolating component that holds a gold plated pin. The pin is contacted to the tab using a nylon screw. Anode and cathode of the TA chip are connected to a PCB with the connector for the TA current supply

(a) TA mount and electrical contacts

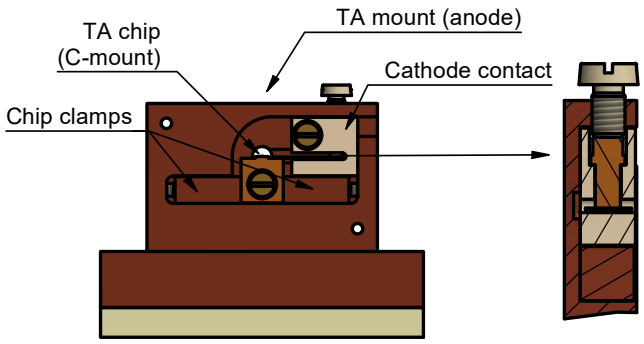

(b) Adjustable input and output collimation optics

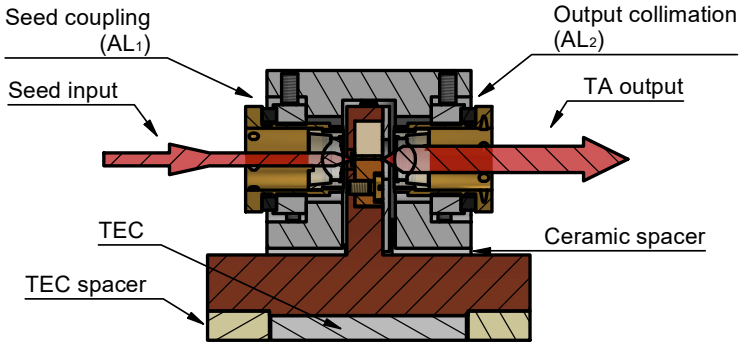

Fig. 3.6.: Details of the TA module depicted in Fig. 3.5. (a) TA chip mount. A cross section of the cathode contact is shown on the right. (b) Cross section of the fully assembled TA mount.

placed in the side panel of the TA module (compare Fig. 3.5). PCBs compatible to Thorlabs LDC8040 (4 A) and Thorlabs LDC8080 (8 A) current drivers are available. An external BNC connector is connected to the interlock channel of the current driver.

A cross section of the fully assembled TA mount is depicted in Fig. 3.6 (b). The temperature of the TA mount is stabilised using a TEC and a 10 kΩ-thermistor (not shown) placed close to the TA chip. During operation the TA chip produces a considerable heat load of several watt. Hence, a efficient operation of the TEC is essential. This is guaranteed by PEEK spacers matching the thickness of the TEC to 0.05 mm guaranteeing a good thermal contact and low mechanical stress at the same time. TEC and thermistor are connected to a second PCB in the side panel providing connections to Thorlabs TEC8040 or TEC8080 temperature controllers. The aspheric lenses for coupling of the seed laser (AL_1) and for collimation of the output beam (AL_2) in their adjustable mounts are visible in detail. Ceramic spacers are used between lens mount and TA mount. This material provides a electrical isolation while maintaining a good thermal contact. Electrical isolation of the lens mount from the TA chip avoids damage to the chip when AL_1 and AL_2 are adjusted. A good thermal contact to the temperature stabilised TA mount increases the mechanical stability of the lens alignment.

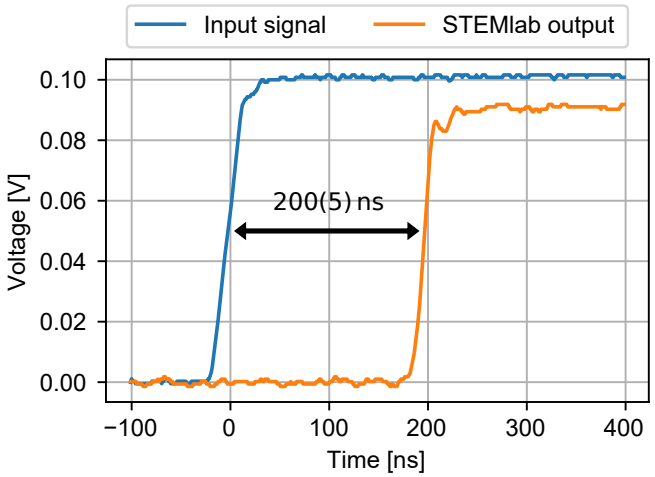

Fig. 3.7.: Delay between input and output of a digital PI controller implemented on a STEMlab 125-14 using the software package *PyRPL*.

3.4. Digital controller for laser-frequency stabilisation: RedPitaya Lockbox

Experiments with cold atoms in optical tweezers, as described in Chapter 2, utilise a multitude of laser fields at or close to an atomic transition. These applications require precise control of the laser frequency and a narrow linewidth. Typically the passive frequency stability of diode laser systems is insufficient. Hence, active frequency stabilisation to a suitable reference is employed in order to meet the requirements. The performance of the control electronics engaged in the feedback loop is crucial in order to achieve a narrow line width and stable operation of the frequency stabilised laser system. Digital controllers offer control parameters adjustable over several order of magnitude without hardware modification with a high stability and reproducibility. These features allow for a versatile application. In this work, digital controllers based on the commercial STEMlab RedPitaya 125-14 platform [92] are developed: the *Red Pitaya Lockbox* and the *Red Pitaya IntStab*. The results discussed in this section have been published in [93]. The developed hardware design is openly available. [94]

The STEMlab platform features a field programmable gate array (FPGA) that controls two 14-bit analog digital converters (ADC) as inputs and two 14-bit digital analog converters (DAC) as outputs. Both inputs and both outputs offer a $-3\,$dB-bandwidth of $50\,$MHz. The FPGA is programmed using a system on a chip (SoC) that is accessible via ethernet. The STEMlab board is controlled using the Python based open-source software package *PyRPL*. [95] It allows us to implement complex locking schemes with up to three proportional integral (PI) controllers using all inputs and outputs simultaneously. The PI controllers are implemented on the FPGA. The FPGA code provided by *PyRPL* sets a fundamental limit to the achievable control bandwidth by defining the propagation delay in the FPGA. In order to determine this delay, a PI controller with proportional gain 1 and without integral gain is implemented. Figure 3.7 shows the response at the STEMlab output (orange) when a voltage step of $0.1\,$V (blue) is applied to the STEMlab input. The delay between the depicted signals of $200(5)\,$ns can be attributed to the propagation delay on the STEMlab board. The delay corresponds to a phase lag of

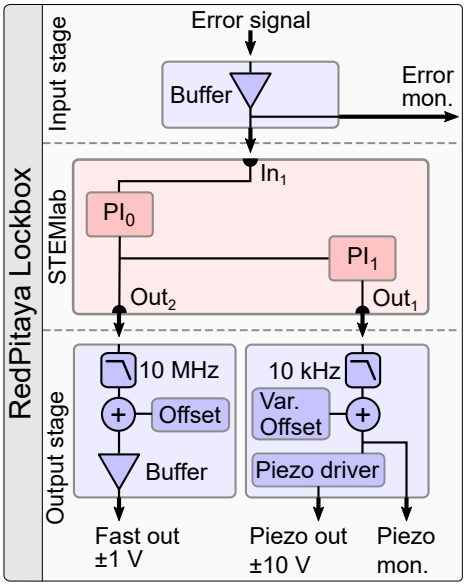

Fig. 3.8.: Block diagram of a digital controller for laser-frequency stabilisation based on the STEMlab platform (*RedPitaya lockbox*). Circuits depicted in red are provided by the STEMlab hardware. This hardware is connected to a PCB that hosts all circuits depicted in blue.

$90°$ at $1.25(3)$ MHz indicating the maximally available control bandwidth. Using the filter functions provided by *PyRPL* induces an additional delay of up to 30 ns. Otherwise, the delay is constant for all relevant configurations of the software. Note, that the internal calibration of the STEMlab ADCs can not be used with *PyRPL*. This results in a gain error of up to 3 % and a measurement offset up to ± 0.1 V for the ADCs and a gain error of up to 5 % and a DC offset up to ± 0.1 V for the DACs. For the application presented here, gain error and offset of the DAC are not relevant since the outputs are included in the control loop. Since the controller locks to the error signal zero crossing, only the measurement offset of the ADC is relevant and has to be compensated.

The controller is realised as a 19”-rack mount unit in order to facilitate integration. This unit consists of a printed circuit board (PCB) that holds the STEMlab board and a front panel with all necessary connectors. The PCB features an analog input and an analog output stage, as well as a low-noise power supply for the STEMlab board using an efficient DC/DC converter (Analog Devices LT8610). In order to utilise the full bandwidth provided by the STEMlab platform, all inputs and outputs feature a bandwidth above 10 MHz if not stated otherwise. Figure 3.8 shows a simplified block diagram of the controller. The input stage consist of an unity-gain input buffer and a buffered monitoring output for the frequency error signal. In order to match the error signal amplitude to the STEMlab input voltage range of ± 1 V, the input buffer can optionally be configured as an amplifier or attenuator. The input stage is connected to one of fast inputs of the STEMlab board (In_1). The original STEMlab 125-14 board has an output-voltage range of ± 1 V involving a noisy DC offset of -1 V. In order to reduce the output noise of the controller, these noisy offset are removed. [96] Hence, the output stage is designed for a 0–2 V output range of the STEMlab outputs. The stage consist of two parts providing an output for the laser piezo and a fast output typically acting on the laser current respectively. In the piezo stage, one of the fast outputs of the STEMlab board (Out_1) is low-pass filtered with a cut-off frequency of 10 kHz thereby reducing piezo noise

and avoiding mechanical resonances of the piezo-mirror system. Subsequently, the STEMlab output is amplified by a factor of 10. A variable offset is added to the control voltage of the STEMlab output. The offset is derived from a low-noise $10\,\mathrm{V}$-reference. It is adjustable with a precision potentiometer. This feature facilitates manual scanning of the laser frequency in order shift it into the recapture range of the control loop. The output-voltage range of the piezo stage is limited to $\pm 10\,\mathrm{V}$ by the supply voltages of $\pm 12\,\mathrm{V}$. Piezo stack actuators typically have a large capacity. In order to drive this capacitive load at frequencies up to $10\,\mathrm{kHz}$, the piezo stage features an output buffer providing currents up to $250\,\mathrm{mA}$. When calculating the bandwidth of the piezo stage, the capacity of the piezo stack forming a low pass filter with the output series resistor ($4.7\,\Omega$) has to be taken into account. For the piezo actuator used in the laser system described in Sec. 3.1 the typical capacity of $2.6\,\mu\mathrm{F}$ yields a cut-off frequency of approximately $13\,\mathrm{kHz}$. For the fast control output, the second output of the STEMlab board is used (Out_2). A low-pass filter with a cut-off frequency of $10\,\mathrm{MHz}$ is applied in order to reduce noise at frequencies above the bandwidth of the feedback loop. From the same stable voltage reference used in the piezo stage, a $-1\,\mathrm{V}$ offset is generated and added to the signal shifting the output-voltage range back to the original range of $\pm 1\,\mathrm{V}$. An additional buffer allows the fast control output to drive a $50\,\Omega$-load over the entire output-voltage range. Both, the fast output and the piezo output feature a buffered monitoring output that is used for instances for lock detection.

Figure 3.8 also shows a simplified sketch of the locking scheme implemented using the PyRPL software. The scheme is implemented in two stages: A first digital PI controller (PI_0) acting on the laser current via the fast control output is used to lock the laser frequency to the error signal zero crossing. For that purpose, the control output is connected to the modulation input of the current driver. This lock defines the performance of control loop. In order to compensate for acoustic noise mainly invoked by vibrations of the external cavity, a high PI corner frequency is chosen. For best performance, typically the quantisation noise of the STEMlab DAC is reduced by an attenuation between $6\,\mathrm{dB}$ and $20\,\mathrm{dB}$ applied to the fast control output. This reduces the dynamic range of the output. As illustrated in Sec. 3.2, the laser frequency exhibits a strong drift depending on ambient conditions. In order to avoid saturation of the fast output, a drift compensation stage is implemented: A second digital PI controller on the STEMlab FPGA (PI1) uses the (digital) output of PI_0 as an input and acts on the laser piezo actuator via the piezo output. For the controller a small integral gain is chosen and the proportional gain is set to zero such that the piezo voltage changes slowly as compared to the bandwidth of the first stage. The resulting slow change of the laser frequency is compensated by the fast control loop thereby creating feedback on the input of PI_1. In the compensation stage, this feedback is used to keep the average output of PI_1 at zero. Ideally, this stage does not change the laser frequency. However, a DAC step is performed at the full bandwidth of the piezo output ($10\,\mathrm{kHz}$) independently of the integral gain chosen for PI_1. This effect can be compensated by applying a low-pass filter with a typical cut-off frequency of $100\,\mathrm{Hz}$ to the piezo input of the laser.

The voltage noise of the controller is analysed using a low-noise pre-amplifier (Stanford Research Systems SR560) in combination with a high resolution multimeter (Keysight 34470A) for noise frequencies up to $1\,\mathrm{kHz}$, a fast oscilloscope (Keysight MSO9254A) for frequencies between $1\,\mathrm{kHz}$ and $100\,\mathrm{kHz}$, and a spectrum analyser (Tektronix RSA306) for frequencies above $100\,\mathrm{kHz}$. Figure 3.9 shows the noise spectral density (NSD) of the relevant output signals of the controller. All time domain signal are Fourier transformed using the Welsh algorithm. [98] The NSD of the STEMlab output is depicted in blue. This measurement is extended to cover the

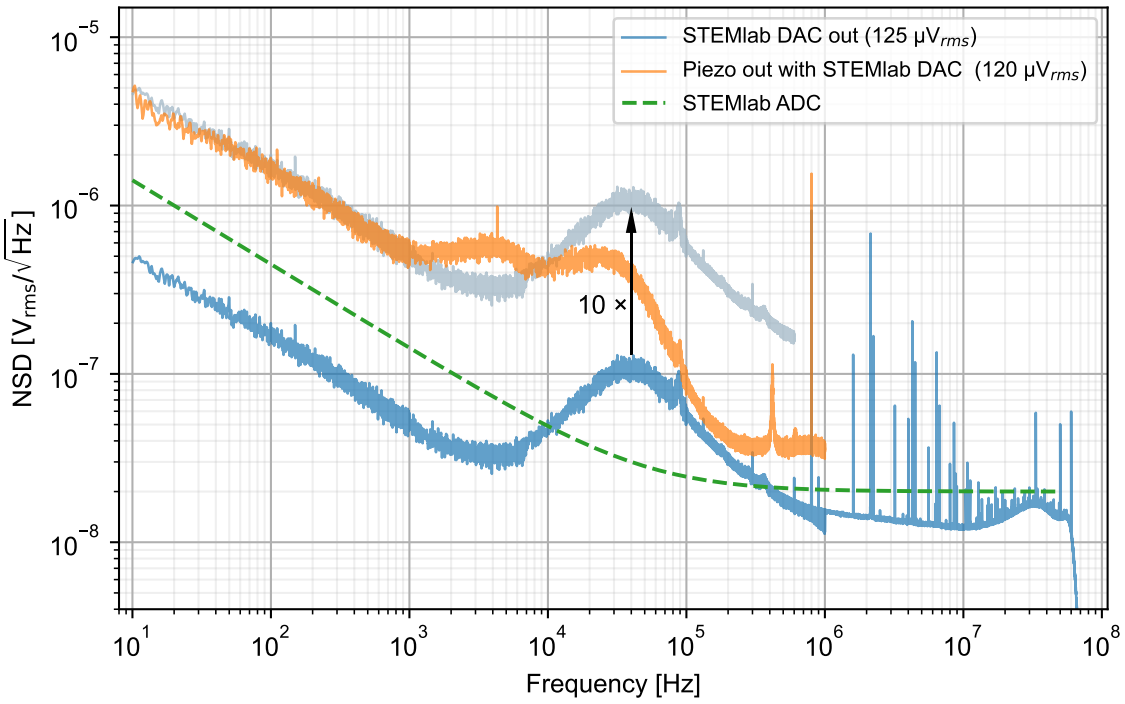

Fig. 3.9.: Noise spectral density (NSD) of the STEMlab DAC output and the piezo output of the *RedPitaya Lockbox*. Additionally, the NSD of the STEMlab DAC output scaled by a factor of 10 (light grey) and the NSD of the STEMlab ADC (dashed, green) as quoted in [97] are plotted for comparison (see text for details). The rms voltage-noise values denoted in the legend are calculated from the respective spectrum.

full bandwidth of the DAC using a wideband pre-amplifier (Mini Circuits ZFL-500LN+). The broad noise peak at $40\,\mathrm{kHz}$ and the narrow double peaks at approximately $2\,\mathrm{MHz}$ (including harmonics) are intrinsic properties of the STEMlab board. The rms voltage noise of $125\,\mu\mathrm{V}$ calculated from the recorded spectrum shows that the full 14-bit resolution corresponding to a step-size of $2\,\mathrm{V} \times 2^{-14} = 122\,\mu\mathrm{V}$ is available by removing the noisy DC offset of the STEMlab board. The NSD of the piezo output is displayed in orange. The NSD of the STEMlab output scaled up with the internal amplification of the piezo stage (grey) is plotted. Comparing it to the NSD of the piezo output (orange), shows that the latter is determined by the amplified noise of the STEMlab DAC output accounting for the additional low-pass filter at $10\,\mathrm{kHz}$. The rms noise of the piezo output of $120\,\mu\mathrm{V}$ is an order of magnitude below the 14-bit resolution of the amplified STEMlab output of $20\,\mathrm{V} \times 2^{-14} = 1.22\,\mathrm{mV}$. The voltage noise levels measured for both outputs can be linked to the frequency noise added to the laser system by the controller using the sensitivities of the actuators stated in Tab. 3.3. The noise peak at $800\,\mathrm{kHz}$ visible in all spectra depicted in Fig. 3.9 can be attributed to the DC/DC converter used to supply the STEMlab board. Its contribution to the rms noise can be neglected. If necessary, the peak can be shifted to a different frequency by replacing external components of the DC/DC converter. A separate measurement shows that the NSD of the input stage is negligible as compared to the noise of STEMlab ADC. The relevant NSD presented in [97] corresponding to a noise free resolution of 11.8 bit is plotted in Fig. 3.9 (green, dashed). The depicted noise level determines the sensitivity of the input of the digital controller. Using the properties of the error signal, the

voltage input sensitivity can be linked to the smallest detectable frequency deviation.

3.5. Wideband laser-current modulation

Commonly used techniques for laser-frequency stabilisation, such as Pound-Drever-Hall locking to high finesse cavities [99, 100] or optical phase-locked loops [101, 102], offer servo bandwidths of several MHz. In order to utilise the full potential of these techniques, a laser-frequency servo input with a large bandwidth is required. A modulation of the laser current at frequencies up to several hundreds of MHz causes a modulation of the laser frequency [89], such that a suitable servo input can be realised by modulating the laser current. For application in a control loop, the servo input should feature a flat amplitude response (gain) over the entire bandwidth and a low phase-lag. Additionally, laser-current noise and long-term stability should not be impaired by using the modulation input. In this section, a suitable technique for wideband laser-current modulation is presented. Parts of the results discussed in this section haven been published in [103]. The developed open-source hardware is available at [104].

Wideband current modulation of a laser diode is a challenging task due to the typically low AC-impedance of the laser diode and poor impedance matching between the current driver, the cable used to supply the laser diode, and the laser diode causing reflections in the cables used to supply the laser diode. In a typical application, the current modulation circuit is realised as a bipolar voltage controlled current source in the laser current driver [83] and the laser head is connected to the laser driver using a cable with a length l of several meter. Additional to the mentioned reflections, this configuration induces a delay depending on l that causes a phase-lag limiting the bandwidth of a feedback loop using this servo input. In order to achieve a higher bandwidth, the laser backplane depicted in Fig. 3.10 includes a wideband current source complemented by an impedance matching network and the laser-diode protection circuit described in Sec. 3.1.3. Simplified circuit schematics are shown on the right: The current source is realised as a *Howland Current Pump* [105, 106] using the high-speed, rail-to-rail operational amplifier U_{1B} (Analog Devices ADA4807-2). The second amplifier in the dual amplifier package U_{1A} is used as an input buffer providing a $50\,\Omega$ input set by R_1. The resistor R_2 forms a low-pass filter with the input capacitance of U_{1A} defining the roll-off of the current-modulation transfer function. For resistor R_3 to R_6 a precision resistor network (Vishay MORNTA1001AT5) network is used in order to achieve a high output impedance of the current source. [106] The transconductance gain of the source is set by the resistor network array to

$$\frac{I_{mod}}{U_{mod}} = 1\,\frac{\text{mA}}{\text{V}} \tag{3.13}$$

with an accuracy of $0.1\,\%$. The capacitor C_1 guarantees stability of the circuit. For a high bandwidth, it should be chosen as small as possible. The implemented source guarantees a high passive stability by design: The offset current of the source can be estimated from data sheet [107] of the operational amplifier to a value below $3\,\mu\text{A}$ with a low thermal drift of $10\,\text{nA/V}$. The additional current noise induced by the source is estimated likewise to be well below $30\,\text{pA}/\sqrt{\text{Hz}}$.

The operational amplifiers are supplied by two voltage regulators on the backplane (not shown) with a voltage of $\pm 5\,\text{V}$ close their maximum supply voltage. The supply is provided

by the current driver via the DVI cable. The input voltage range for V_{mod} is given by the input voltage swing of U_{1A} to $\pm 4.8\,\mathrm{V}$. The compliance voltage of the source is given by half of the output-voltage swing of U_{1B} to $V_c = 2.4\,\mathrm{V}$. When using *DgDrive*, a low compliance voltage is required for all applications due to its floating design. [81] However, when the laser-diode cathode is connected to ground, using the wideband current source limits the laser-diode forward voltage to V_c. Note, that this is the case for our earlier-design current source.

(a)

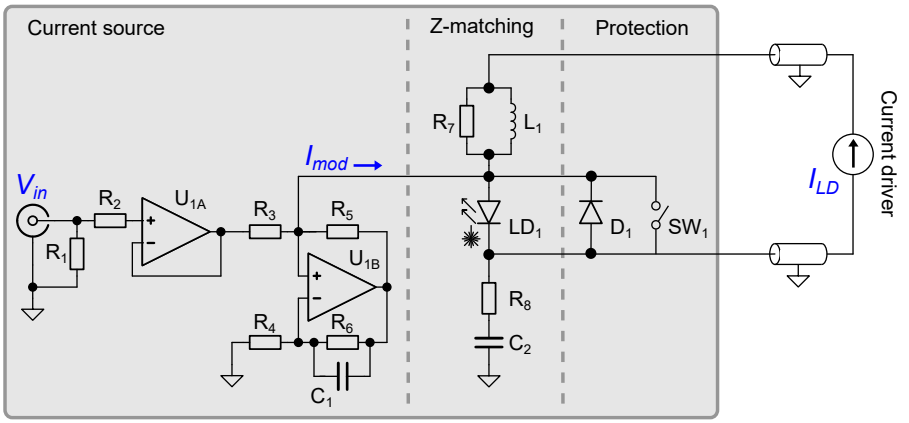

(b)

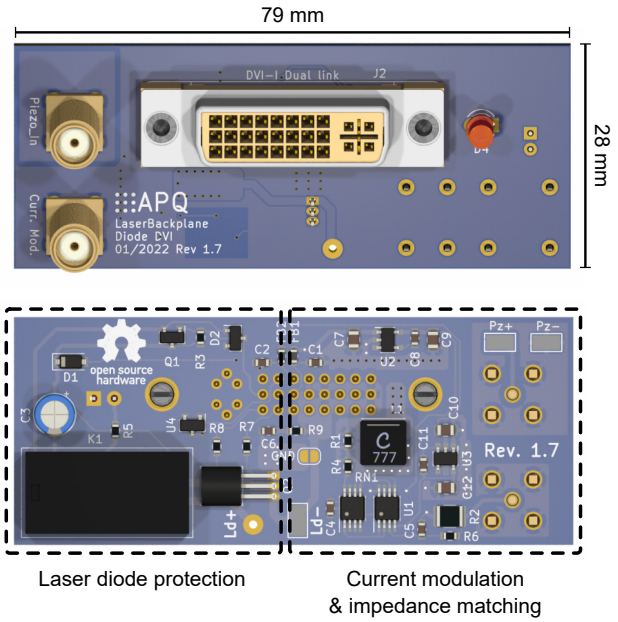

Fig. 3.10.: (a) Simplified circuit schematics of the laser backplane used in this work. The backplain comprises a wideband current source, a passive impedance matching network (Z-matching) and a laser-diode protection circuit. Dual operational amplifiers U_{1A}, U_{1B}: Analog Devices ADA4807-2. Resistors: $R_1, R_7 = 49.9\,\Omega$, R_2 to $R_6 = 1\,\mathrm{k}\Omega$, $R_8 = 4.7\,\Omega$. Capacitors: $C_1 = 1.5\,\mathrm{pF}$, $C_2 = 10\,\mathrm{nF}$. Inductor: $L_1 = 33\,\mu\mathrm{H}$. Laser diode LD_1. Latching relay SW_1: Omron G6AU-274P-ST-US-DC9. Protection diode D_1: ON Semiconductor 2N4401BU. (b) Rendered 3D-model of the laser backplane. The dashed boxes mark the approximate allocation of the circuits depicted in (a).

Although the summing point of the modulation current and the laser-diode forward current is moved close to the laser diode, reflections in the supply cable have to be considered. In a typical application, resonances in the transfer functions due to these reflection limit the bandwidth significantly (see Fig. 3.12 for details). In order to avoid this, an impedance matching network shown in Fig. 3.10 is used: The nominal impedance of the DVI cable is matched with R_7. The compact shielded power inductor L_1 bypasses R_7 for the DC current thereby reducing the required compliance voltage of the current driver and the heat dissipation in the laser head. L_1 should be chosen as large as feasible. For the return path of the current, a so-called snubber is used: The combination of C_2 and R_8 provides a low impedance node at high frequencies for the return path of the modulation current while maintaining stability of the current driver.

The performance of the developed current source is tested under realistic conditions using an ECDL system at $780\,\mathrm{nm}$ (laser diode: Thorlabs LD785-H1). For small modulation amplitudes and within the frequency range discussed here, laser-current modulation results in a proportional intensity modulation. [89] Thus, it is possible to detect a modulation of the laser current by detecting the resulting intensity modulation. For frequencies below $50\,\mathrm{MHz}$ the photodetector described in Sec. 3.8 with a bandwidth of $150\,\mathrm{MHz}$ is used. For larger frequencies a fast photodiode (Hamamatsu G4176-03) amplified by an RF amplifier with a bandwidth of $500\,\mathrm{MHz}$ (Mini Circuits ZFL500-LN) is used. A bode analyser (Omicron Lab Bode 100) allows for measurement of the magnitude and the phase of the transfer function below $50\,\mathrm{MHz}$. Above $50\,\mathrm{MHz}$ a scalar measurement of the magnitude is performed using a spectrum analyser with tracking generator (Rhode & Schwarz FPC1500).

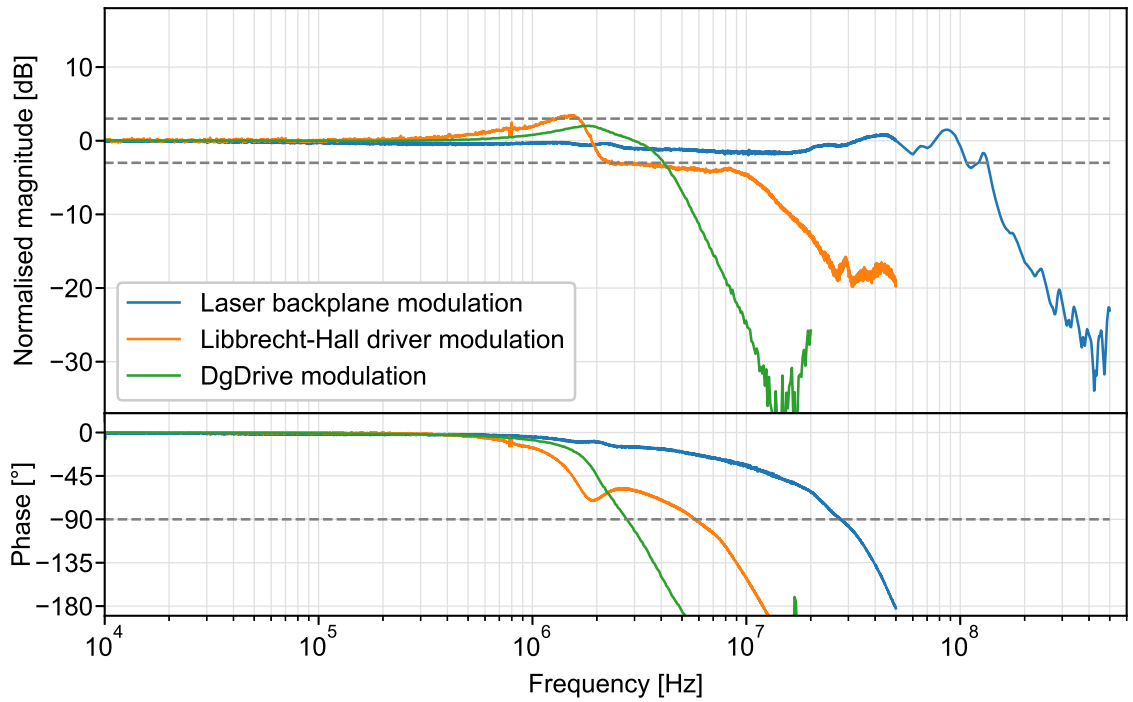

Fig. 3.11.: Bode plot of the transfer functions of different current modulation inputs. For all measurements, a cable of length $l = 2\,\mathrm{m}$ is used to connect the laser head to the current driver.

Figure 3.11 shows the transfer function of the wideband current modulation input discussed

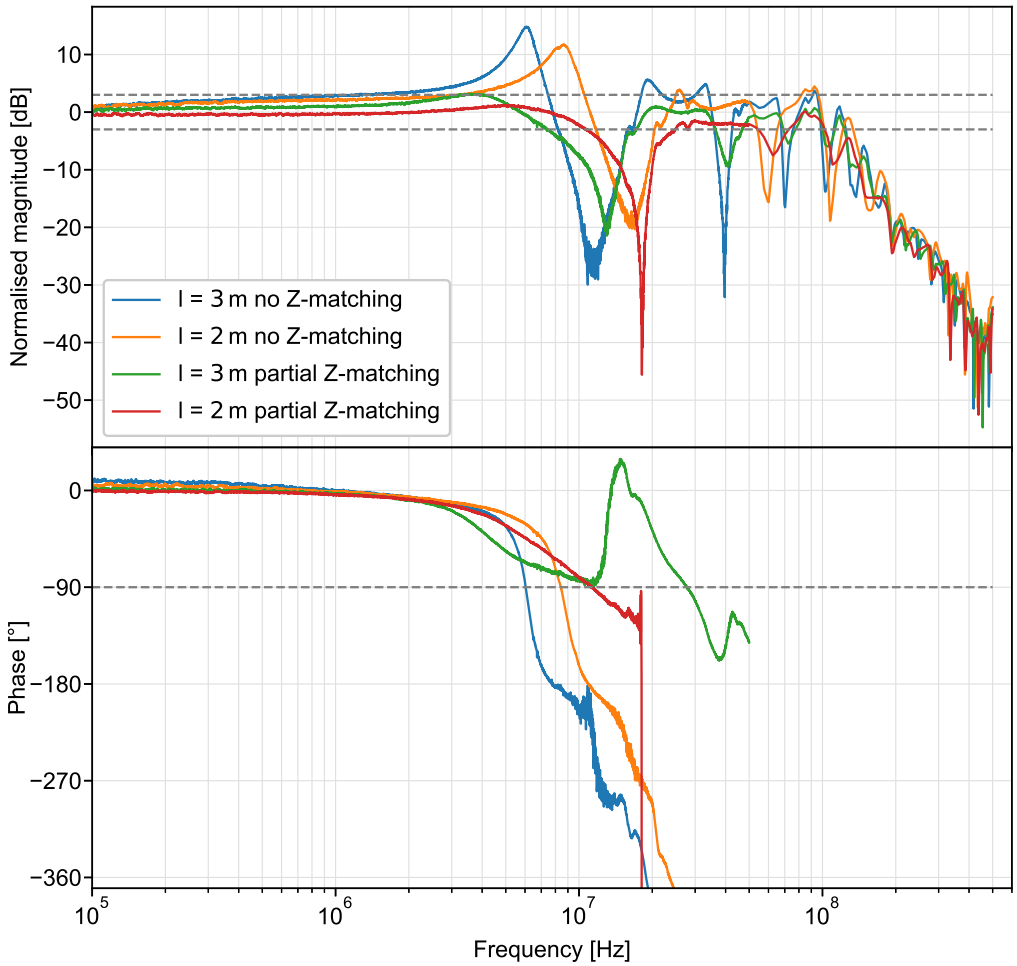

Fig. 3.12.: Bode plot of the transfer function of the current modulation input for two different cable lengths l. For this measurement, the impedance matching network depicted in Fig. 3.10 (a) is either not used (no Z-matching) by setting $R_8 = 0$ and $C_2 = 0$ or is omitted in the current return path only by setting $C_2 = 0$ (partial Z-matching).

above (blue) and the transfer function of the modulation inputs integrated in *DgDrive* [81] (green) and the Libbrecht-Hall-design [83] current driver (orange) both used in this work. For this measurement, cables with a length of $l = 2\,\mathrm{m}$ are used to connect the laser system to the driver. For the fast modulation input integrated in the laser backplane, a gain flatness of $\pm 3\,\mathrm{dB}$ is obtained in the frequency range of DC to $100\,\mathrm{MHz}$. The phase lag is below $90°$ up to $25\,\mathrm{MHz}$. The remaining influence of resonances is negligible (compare Fig. 3.12). In a separate measurement, this behaviour has been validated for cable lengths of $0.5\,\mathrm{m}$ to $4\,\mathrm{m}$. The bandwidth of the modulation input of *DgDrive* is specified to $1\,\mathrm{MHz}$. The transfer function recorded here shows a negligible gain peaking below $3\,\mathrm{dB}$ and a $-3\,\mathrm{dB}$ cut-off at approximately $4\,\mathrm{MHz}$. A phase lag below $90°$ up to $2.5\,\mathrm{MHz}$ is observed. These results suggest that the specified bandwidth of $1\,\mathrm{MHz}$ is available for all applicable cable lengths (up to $4\,\mathrm{m}$). In contrast, the modulation input of the Libbrecht-Hall driver is only specified for a $50\,\Omega$ load [108] to approximately $20\,\mathrm{MHz}$. However, under realistic operating conditions, the transfer function shows a non-trivial behaviour for frequencies above $1\,\mathrm{MHz}$ (orange). Thus, the shape of the

transfer function is expected to depend strongly on both the cable length and type. Note, that both current drivers have to be used with the impedance matching network in the laser backplane in order to achieve the performance presented in Fig. 3.11. Additionally, the modulation input of the Libbrecht-Hall driver has to be set to $50\,\Omega$ by external termination.

Figure 3.12 illustrates the influence of resonances due to reflections in the cable. For the presented measurement, the impedance matching network was removed completely by setting $R_7 = 0$ and removing C_2 and partially by removing C_2 only. In both cases, the systems exhibits pronounced resonances with a frequency and shape depending on the cable length l. Comparing the systems with completely and partially removed impedance matching, shows that the gain peaking can be attributed to reflections at the output of the current driver since it is suppressed by the impedance matching with R_7. The phase of the transfer function (Fig. 3.12 bottom) changes rapidly at the resonance frequency. The strong signature of resonances in both the magnitude and the phase limits the bandwidth a feedback loop to the first resonance frequency when using the modulation input as a servo input.

3.6. Digital controller for laser-intensity stabilisation: RedPitaya IntStab

Quantum information experiments require precise real-time control of laser intensities on sub-millisecond time scales. Fluctuating intensities are compensated by active intensity stabilisation. For that purpose the intensity is measured using a fast photodetector. An acousto-optic modulator (AOM) is used as a high-bandwidth actuator. In this work, digital controllers and photodetectors dedicated to this application are developed.

The design of the digital controller presented here is similar to the controller for laser-frequency stabilisation presented in Sec. 3.4. Parts of the results discussed in this section have also been published in [93]. A STEMlab 125-14 board [92] is integrated in a 19”-rack mount unit consisting of a PCB and a front panel. Each unit features two identical channels using one STEMlab board. The STEMlab board is configured with the Python based software package *PyRPL*. [95] The PCB contains the power supply for the STEMlab board, an input and an output stage. The hardware is designed to be used with a noise optimised STEMlab board featuring a 0–2 V output range. [96]

Figure 3.13 shows a block diagram of the controller. The input stage is used to compare the photodetector signal to an external reference level. The photodetector input features a variable attenuator. In order to achieve reproducibility, only fixed gains (1,2,4,8,16) are selectable. The reference level is subtracted from the amplified photodetector signal. The resulting error signal is connected to one of the fast ADCs of the STEMlab board (In_1). The input stage features an input voltage range of $\pm 10\,\mathrm{V}$ such that the permissible input voltage of the STEMlab input of $30\,\mathrm{V}$ is not exceeded even though the ADC input voltage range is limited to $\pm 1\,\mathrm{V}$. This design extends the input voltage range of the controller by a factor of 10 without affecting the resolution of the ADC. The input stage also features buffered monitoring outputs for the amplified photodetector signal and the error signal. The output stage consists of low-pass filter with a cut-off frequency of $10\,\mathrm{MHz}$ accounting for the maximally available control bandwidth of $1.25\,\mathrm{MHz}$ (see Sec. 3.4 for details) and an unity-gain output buffer that is able to drive a $50\,\Omega$-load. Both, cut-off frequency and gain of the output buffer may be adjusted

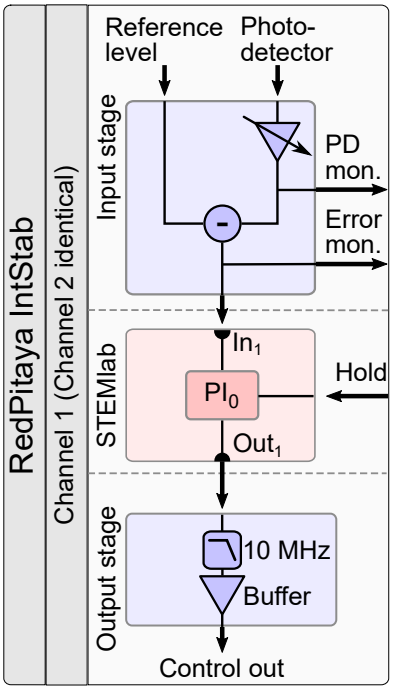

Fig. 3.13.: Block diagram of a digital controller for laser-intensity stabilisation. The device features two identical channels.

by replacing components on the PCB. The hardware design is openly available. [109] *PyRPL* implements a digital PI controller on the STEMlab board (PI_0) for intensity stabilisation. This digital controller allows for variation of the PI parameters over several orders of magnitude. It also allows for a convenient and reproducible adjustment of the parameters if the gain of the feedback loop is changed, e.g. due to an altered efficiency of the optical setup.

The noise performance of the intensity controller is evaluated using the method described in Sec. 3.4. The results are depicted in Fig. 3.14. The NSD of the input stage is measured at the interface between input stage and STEMlab board for the minimum photodiode gain (1) and for the maximum photodiode gain (16) while all inputs are shorted. For comparison, the input referred noise of the STEMlab ADC [97] is plotted. For a photodiode gain of 1 (blue), the noise of the input stage is dominated by ADC noise while the NSD of the input stage dominates for a photodiode gain of 16 (orange). However, in a typical application, the noise of the input stage is determined by shot noise of the photodetector (see Sec. 3.7 for details). The shot noise level for a typical photodetector amplifying a photocurrent of $200\,\mu A$ by a transimpedance gain of $50\,k\Omega$ is plotted in red. These values are chosen such that a realistic photocurrent is amplified to the maximum input voltage of the controller ($10\,V$).

Using the controller presented in Fig. 3.13, switching and amplitude control of light fields can be realised by changing the reference level accordingly. The achievable transient times are limited by the bandwidth of the control loop. For applications that require control of the light fields on shorter time scales, such as short light pulses, a sample and hold feature is realised, using the custom *PyRPL* version *external_pid_pause*. For each channel, a general purpose logic input of the STEMlab board is used to set the PI gains to zero while this hold input is pulled high. In order to illustrate the capabilities of the sample and hold feature, a

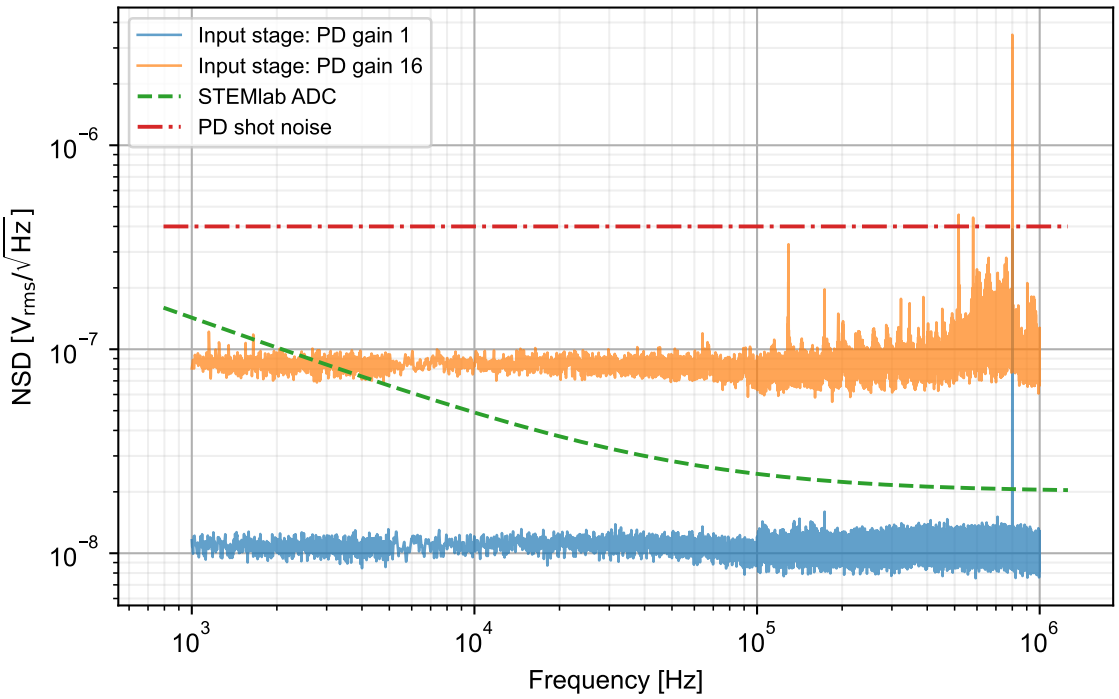

Fig. 3.14.: Noise spectral density (NSD) of the input stage of the controller depicted in Fig. 3.13. The internal photodetector (PD) gain is set to 1 (blue) and to 16 (orange). For comparison, the input referred NSD of the STEMlab ADC as quoted in [97] (dashed, green) and the shot noise level of a typical photodetector (dashed-dotted, red) are plotted.

characterisation in an open loop application is conducted. A triangular signal is applied to the input of the STEMlab board and the hold pin is triggered asynchronously. Figure 3.15 shows the response of the controller when only a proportional controller (top) or an integral controller (bottom) is implemented. All signals haven been rescaled and offset for better visualisation. The proportional controller follows the input signal. Whenever the trigger signal is pulled high the output is set to zero. The integral controller integrates the linear input signal resulting in a quadratic curve. Pulling the trigger high causes a constant output at the actual level. At transition to low (sample) the integration starts at this level. In a separate measurement the delay between the trigger signal and the according response of the controller output is determined to $150(10)$ ns. Using this digital sample and hold features combines the high precision of the digital controller with a rapid transition time between sample and hold.

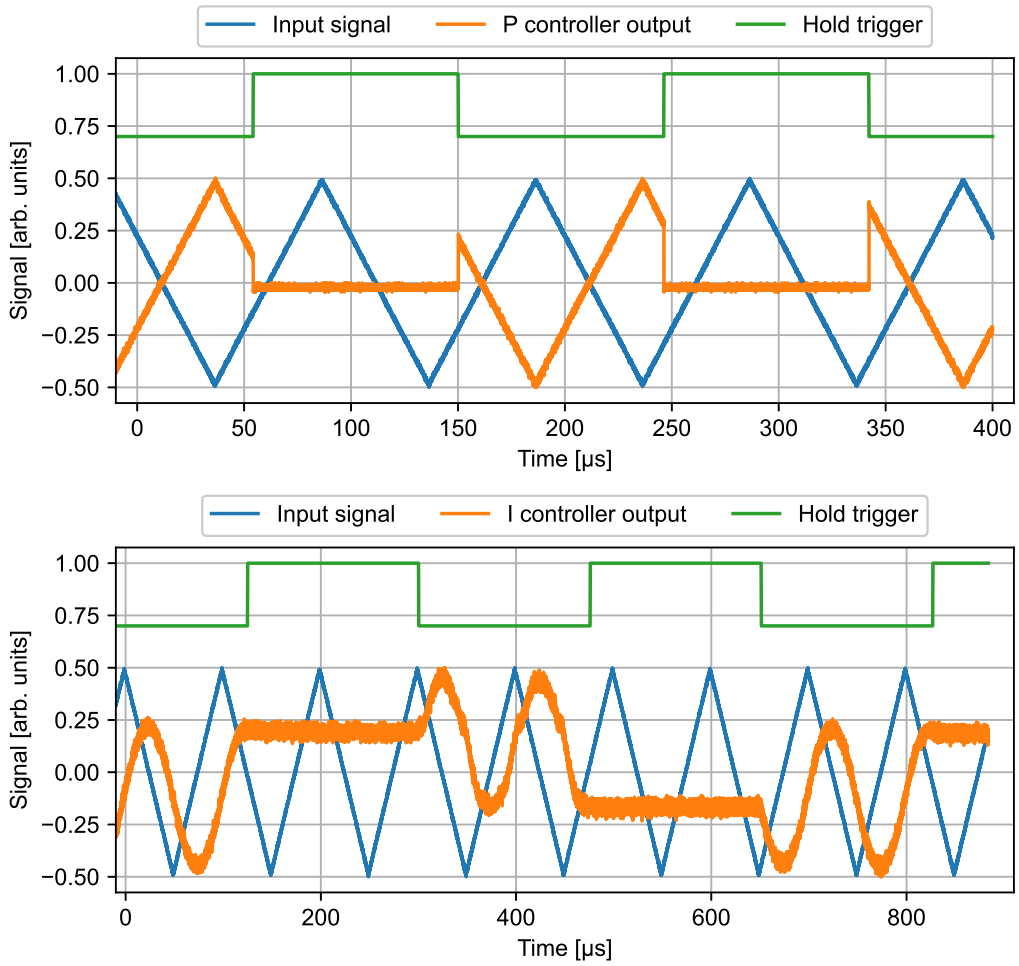

Fig. 3.15.: Illustrating application of the sample and hold feature implemented in this work. The trigger signal sets the proportional and integral gains to zero when pulled high. Top: A proportional (P) controller is implemented. Bottom: An integral (I) controller is implemented.

3.7. Low-noise photodetectors for intensity stabilisation

High-quality photodetectors are essential in order to realise high-precision intensity control. For best performance, the detectors should feature a linear response over the entire operating range, low electronic noise, and a bandwidth that does not limit the bandwidth of the feedback loop. An ideal choice combining these features is a photodiode amplified by an transimpedance amplifier. Based on this technique, a photodetector optimised for use with the digital controller described in Sec. 3.6 is developed. [110] In order to guarantee compatibility with this controller, a 0–10 V output range and a bandwidth well above the maximum control bandwidth of the STEMlab board of 1.25 MHz (see Sec. 3.4) is required. Additionally, the maximum output voltage should be accomplished by a realistic optical power below (1 mW) and the detector should be limited by photocurrent shot noise at this operating point.

Simplified schematics of a transimpedance amplifier (TIA) implemented with an operational amplifier U are depicted in Fig. 3.16. A photodiode PD is connected to the inverting input

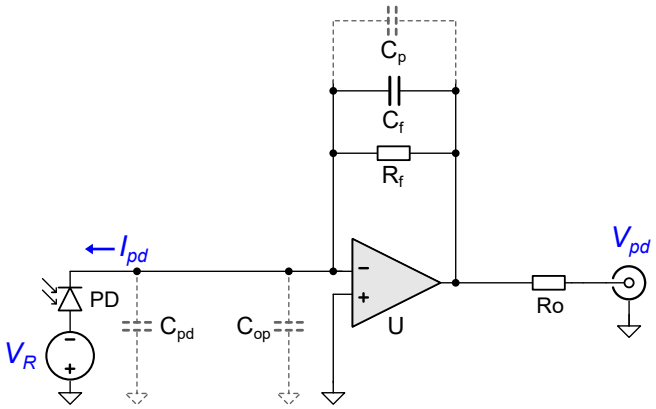

Fig. 3.16.: Simplified schematics of a photodetector based on a transimpedance amplifier. The transimpedance gain is set by the feedback resistor $R_f = 50\,\mathrm{k}\Omega$. A photocurrent I_{pd} is amplified to an output voltage $V_{pd} = R_f I_{pd}$. The photodiode PD (Osram SFH203) is biased with a reverse voltage $V_R = -12\,\mathrm{V}$. Operational amplifier: Analog Devices ADA4898-1. Feedback capacitor: $C_f = 1.5\,\mathrm{pF}$. Output series resistor $R_O = 50\,\Omega$. The dashed symbols mark relevant intrinsic capacities of the photodiode (C_{pd}), the operational amplifier input (C_{op}), and the feedback network (C_p).

of the operational amplifier producing a photocurrent I_{pd} proportional to the optical power incident on its active area P_{pd}:

$$I_{pd} = \eta P_{pd}. \tag{3.14}$$

The non-inverting input of the amplifier is connected to ground. A feedback resistor R_f provides feedback of the output to the inverting input such that a virtual ground node is formed at the inverting input, i.e. the output of the amplifier compensates all current flowing in or out of this node over R_f. Thus, the output voltage of the TIA is given by

$$V_{pd} = R_f I_{pd}. \tag{3.15}$$

In Figure 3.16, dashed symbols are used for the relevant intrinsic capacities of the components in use: the capacity of the photodiode C_{pd}, the input capacity of the operational amplifier C_{op}, and the parasitic capacities across the feedback resistor C_p. A small capacitor C_f in parallel to R_f guarantees stability of the circuit by matching the feedback bandwidth to the bandwidth of the operational amplifier. The resulting $-3\,\mathrm{dB}$-bandwidth of the photodetector f_{pd} is

$$f_{pd} = \frac{1}{2\pi R_f C_f} \tag{3.16}$$

The minimal value for C_f guaranteeing stability of the TIA is determined by the total input capacitance $C_{in} = C_{pd} + C_{op}$ and the gain-bandwidth product of the operational amplifier f_{gbw} to [111]

$$C_f \geq \sqrt{\frac{C_{in}}{2\pi R_f f_{gbw}}}. \tag{3.17}$$

For our application, this value is on the order of a few pF. In this case parasitic capacities C_p in the feedback loop are not negligible. In order to keep C_p as small as possible, a careful PCB

design employing small surface mount components and short traces is necessary. Nevertheless, the typical value of C_p is still between $0.1\,\text{pF}$ and $0.5\,\text{pF}$. Eq. 3.16 and Eq. 3.17 yield the maximal bandwidth obtainable with a TIA

$$f_{pd,max} = \sqrt{\frac{f_{gbw}}{2\pi R_f C_{in}}}. \tag{3.18}$$

Hence, a photodiode with a low input capacity and a high bandwidth operational amplifier is favourable to increase the bandwidth of the TIA. However, achieving bandwidths well above $10\,\text{MHz}$ is challenging due to the square-root scaling. In practise, substantial gain peaking and ringing may occur if the minimum value of C_f is applied. Thus, optimisation of gain flatness and transient behaviour may require a reduced bandwidth.

For the photodetector developed here, a silicon photodiode equipped with a filter blocking visible light (Osram SFH203 FA) is chosen. The filter reduces undesired effects of background light. This photodiode is suitable for detecting light at wavelengths between $750\,\text{nm}$ and $1100\,\text{nm}$. Applying a reverse bias voltage of $12\,\text{V}$, reduces C_{pd} to $2.5\,\text{pF}$. For the applications discussed here, a probe beam is focused on the active area of the photodiode. A large active area facilitates adjustment and guarantees stability. With an active area of $1\,\text{mm} \times 1\,\text{mm}$ the chosen diode provides a good trade-off between low capacitance and a large active area. The TIA is realised using a high-speed, low-noise operational amplifier that provides the required output voltage of $10\,\text{V}$ (Analog Devices ADA4898-1). The feedback resistor R_f is set to $50\,\text{k}\Omega$ such that a moderate photocurrent of $200\,\mu\text{A}$ yields the maximal output voltage. This photocurrent corresponds to an optical power of approximately $0.5\,\text{mW}$ at $780\,\text{nm}$ ($\eta \approx 0.37\,\text{A/W}$). Note, that the peak sensitivity of the photodiode at $900\,\text{nm}$ is significantly larger ($0.62\,\text{A/W}$). The value for the feedback capacitor is optimised using the design tool *Analog Devices Photodiode Wizard*. [112] A value of $C_f = 1.5\,\text{pF}$ yields a bandwidth well above $1.25\,\text{MHz}$ and negligible ringing.

An intrinsic noise limitation for detection of light intensities is shot noise. I.e. noise occurring due to the detection of discrete random events following a Possonian distribution. In average less than one electron per photon is produced in the photodiode. Hence, the lowest number of detected events leading to the largest relative shot noise level corresponds to the photocurrent. The shot-noise spectral density i_{pd} of a photocurrent I_{pd} is given by [113]

$$i_{pd} = \sqrt{2eI_{pd}} \tag{3.19}$$

In order to evaluate the noise performance of the photodetector, the shot noise level is compared to the noise spectral density (NSD) of the photodetector. For that purpose, the output-voltage noise of the photodetector is analysed using a spectrum analyser with an integrated preamplifier (Rhode & Schwarz FPC1500). From the resulting voltage NSD, an input referred NSD is calculated using the transimpedance gain $R_f = 50\,\text{k}\Omega$. For this measurement, light incident on the photodiode is blocked. The results are depicted in Fig. 3.17. The photodetector (blue) shows a constant NSD of $i_N = 1.5\,\text{pA}/\sqrt{\text{Hz}}$ that decreases when the bandwidth of the TIA is exceeded. No noise-gain peaking is observable. The rms voltage noise of the detector is calculated from the NSD spectrum by

$$V_{rms} = R_f \sqrt{\int_{f=100\,\text{kHz}}^{f=10\,\text{MHz}} i_N^2(f)\, df} = 95\,\mu\text{V} \tag{3.20}$$

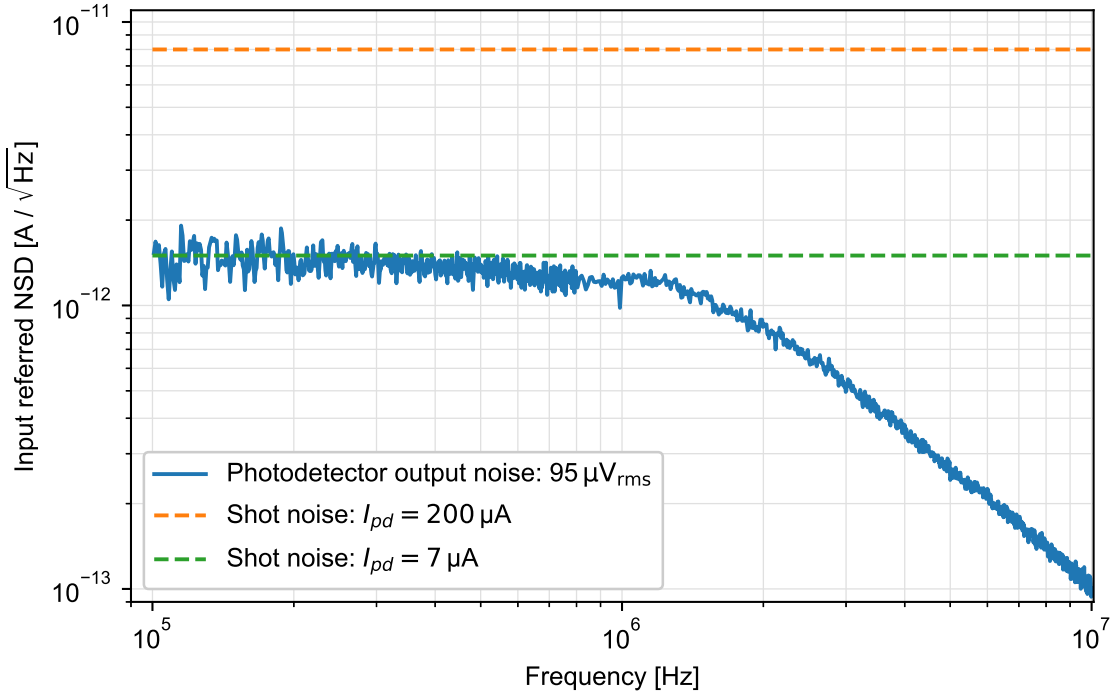

Fig. 3.17.: Input referred noise spectral density (NSD) of the photodetector depicted in Fig. 3.16 (blue). The output rms voltage noise stated in the legend is calculated from the spectrum. For comparison, the shot-noise level corresponding to the maximum photocurrent (orange) and the shot-noise level corresponding to the NSD of the photodetector (green) are shown.

Accounting for the maximum output voltage of $10\,\mathrm{V}$ this is equivalent to a signal-to-noise ration $SNR = 20\log_{10}(10\,\mathrm{V}/95\,\mu\mathrm{V}) \approx 100\,\mathrm{dB}$. Considering the shot noise level corresponding to the maximum photocurrent of $I_{pd} = 200\,\mu\mathrm{A}$ (orange) shows that the output noise is dominated by shot noise. This is the case for photocurrents exceeding $7\,\mu\mathrm{A}$ (green) corresponding to an optical power of approximately $19\,\mu\mathrm{W}$ at $780\,\mathrm{nm}$ which includes most applications.

The obtained bandwidth of the photodiode is analysed using the wideband current modulation technique described in Sec. 3.5. The described current source is implemented in an ECDL system emitting light at $780\,\mathrm{nm}$. The flat response and the low phase lag of the source allows for creating a well-known modulation of the laser intensity that is measured by the photodiode. The transfer function of the photodiode is recorded by an oscilloscope with a function generator (Keysight DSOX1102G) creating the intensity modulation via the wideband modulation input. The results depicted in Fig. 3.18 show that the photodetector exhibits no significant gain peaking. The transfer function is modelled using a generic second order transfer function

$$H(2\pi i f) = \frac{e^{-2\pi i f \tau_d}}{1 + 2\zeta\frac{f}{f_0} - \frac{f^2}{f_0^2}} \tag{3.21}$$

with the natural frequency f_0, the damping factor ζ, and an additional dead time τ_d. The fit depicted in Fig. 3.18 shows an excellent agreement with the measured data. Note, that the magnitude (top) is not affected by the dead time, while the phase behaviour is well

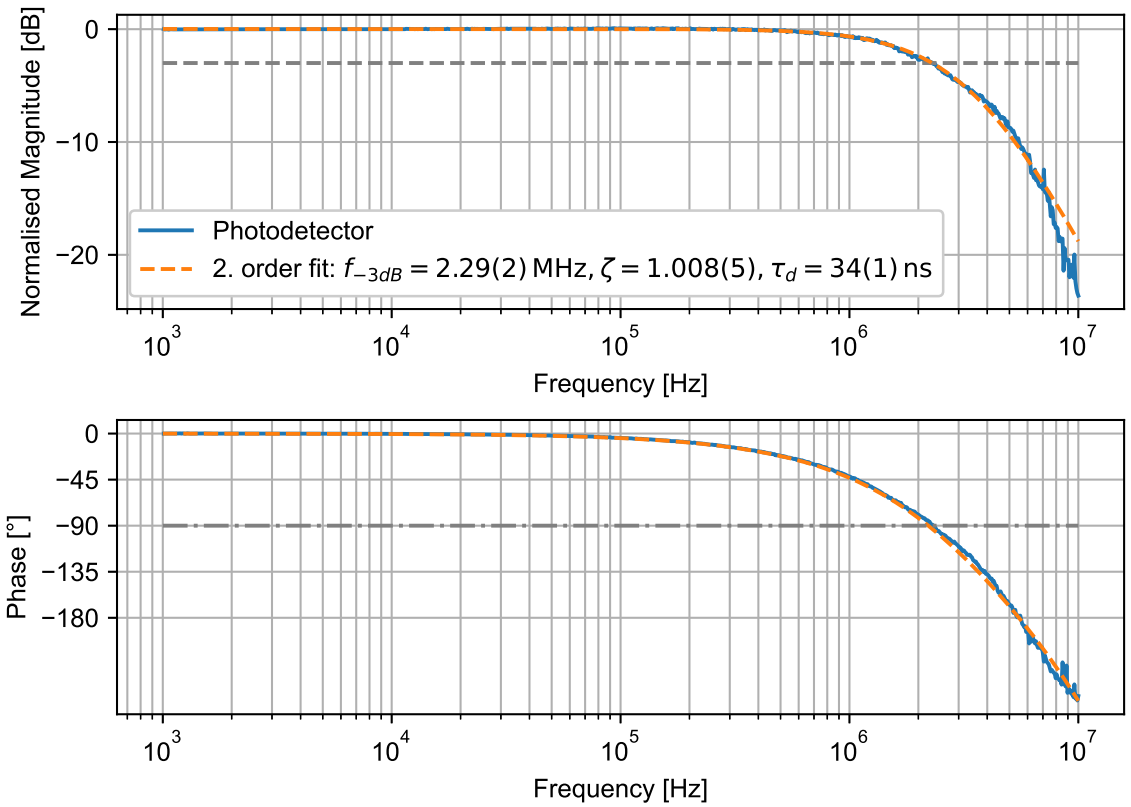

Fig. 3.18.: Bode plot of the transfer function of the photodetector described in this section. For the magnitude (top), the -3 dB-level is marked (dashed, grey). For the phase (bottom), a $90°$ phase lag is marked (dashed-dotted, grey). A generic second order transfer function is fitted to the data (dashed, orange). The resulting parameters are stated in the legend.

described by a small additional dead time accumulated over the entire measurement setup. The -3 dB-bandwidth f_{-3dB} is calculated from the fitted model by solving $|H(f)|^2 = 1/2$ yielding

$$f_{-3dB} = f_0\sqrt{1 + 2\zeta^2 + \sqrt{2 - 2\zeta^2 + 4\zeta^4}} = 2.29(2)\,\text{MHz}. \tag{3.22}$$

The obtained bandwidth is well above the maximum bandwidth of the intensity control loop of 1.25 MHz.

The developed photodetector is shot noise limited for the targeted application. It covers the entire input voltage range of the digital controller described in Sec. 3.6 and does not limit the bandwidth of the control loop. If a larger bandwidth is required for other applications, the transimpedance gain R_f can be reduced. Scaling up C_f by $\sqrt{R_f}$ according to Eq. 3.17 guarantees stability. According to Eq. 3.18 the bandwidth scales as $1/\sqrt{R_f}$.

3.8. Wideband photodetectors for Pound-Drever-Hall laser-frequency stabilisation

The Pound-Drever-Hall (PDH) scheme is commonly used for laser-frequency stabilisation. [99, 100] It relies on detection of a laser-phase modulation at typical frequencies between $10\,\mathrm{MHz}$ and $100\,\mathrm{MHz}$. Ideally, the detection should be shot noise limited putting high demands on the photodetector noise-level since typically only small intensities are available for detection. Hence, a low-noise photodetector with a high bandwidth is required for PDH stabilisation. A suitable design optimised for application at $780\,\mathrm{nm}$ and $960\,\mathrm{nm}$ is developed in this work. The design files are available as an open-source project. [114]

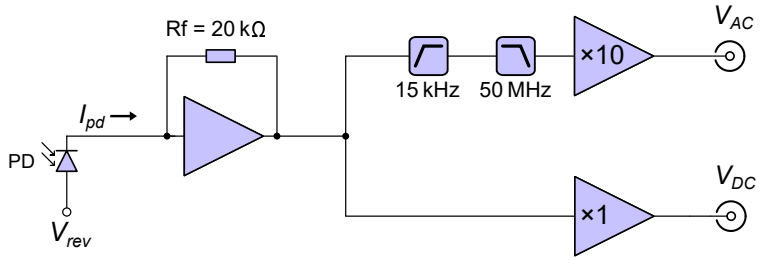

Fig. 3.19.: Simplified circuit of a wideband photodetector optimised for Pound-Drever-Hall frequency stabilisation. The detector is based on a transimpedance amplifier with gain $R_f = 20\,\mathrm{k\Omega}$ and features a DC-coupled (V_{DC}) and an amplified AC-coupled output (V_{AC}).

Figure 3.19 shows a simplified circuit of the photodetector. It is based on a high-speed TIA with gain $R_f = 20\,\mathrm{k\Omega}$ followed by an AC-coupled non-inverting amplifier stage with gain 10. This amplifier stage allows for achieving a large gain at the PDH frequency without saturating the detector at DC. A low-pass filter with a cut-off frequency of $50\,\mathrm{MHz}$ limits the bandwidth of the amplifier stage to our typical PDH frequencies thereby reducing noise and guaranteeing stability of the circuit. The output V_{AC} with a transimpedance gain of $200\,\mathrm{k\Omega}$ is used for PDH signal generation. Additionally, a buffered output (V_{DC}) is connected directly to the TIA stage. This feature realises a DC photodetector with a large bandwidth that is used to detect short transient times between intensity levels, e.g. for short laser pulses.

Noise level and bandwidth of the detector are predominantly determined by the design of the TIA. Details on the design of TIAs can be found in Sec. 3.7. In order to achieve a large bandwidth, a decompensated operational amplifier (Analog Devices LTC6269-10) is chosen. Furthermore, a low-capacitance photodiode is required (compare Eq. 3.16). For applications at $780\,\mathrm{nm}$ a silicon photodiode is chosen (Hamamatsu S9055-01). For applications at $960\,\mathrm{nm}$ an indium-gallium-arsenide photodiode (Excelitas C30617L-100) is more suitable due to an improved sensitivity. The photodiodes are biased with a voltage $V_{rev} = -2.5\,\mathrm{V}$. The total capacitance at the inverting input of the operational amplifier C_{in} is less than $1\,\mathrm{pF}$. In this circuit, a feedback capacity C_f as small as $50\,\mathrm{fF}$ is required for stability (see Eq. 3.17). A larger capacity limits the bandwidth of the TIA. Thus, stray capacitance in the feedback path is limited to a minimum by careful PCB design. The $-3\,\mathrm{dB}$-bandwidth of the TIA is estimated to $150\,\mathrm{MHz}$ by scanning a beat note between two lasers recorded with the photodetector.

The input referred NSD of the circuit is recorded using a spectrum analyser with an in-

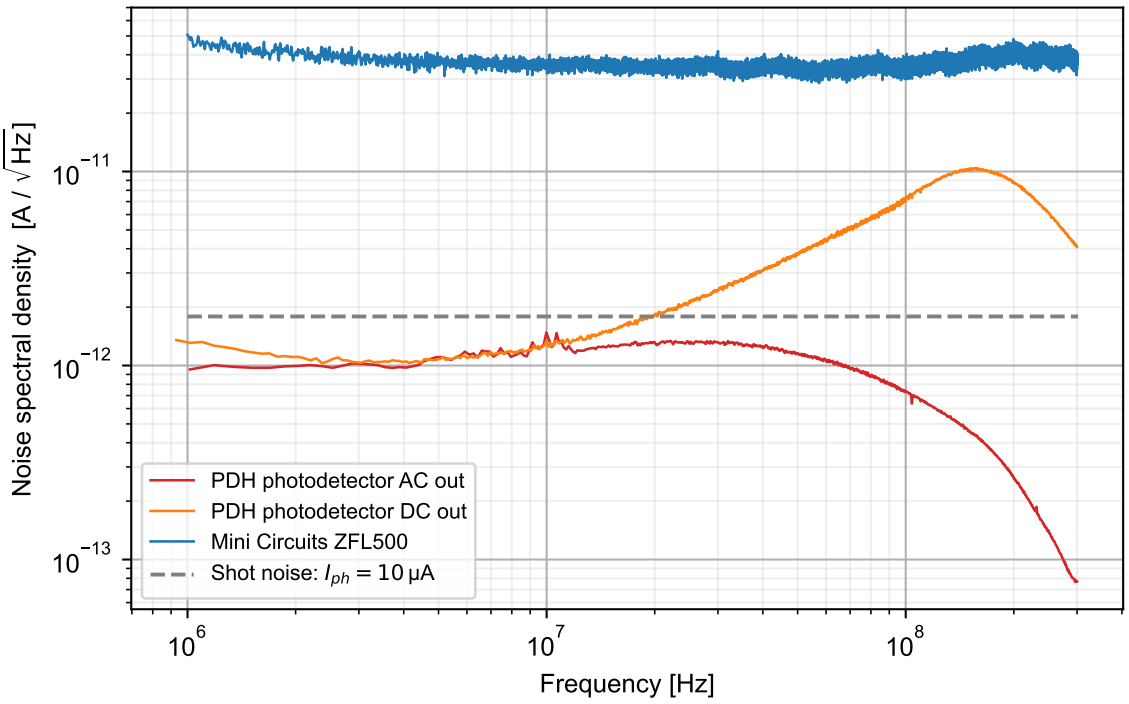

Fig. 3.20.: Input referred noise spectral density of Pound-Drever-Hall (PDH) photodetector presented in this section. For comparison, the calculated shot noise level of a typical photo current I_{ph} (grey, dashed) and the measured NSD of a fast photodiode connected to the HF amplifier Mini Circuits ZFL500 (blue) are depicted. The combination of photodiode and HF amplifier is used as an alternative to the PDH photodetector (see text for details).

tegrated preamplifier (Rhode & Schwarz FPC1500). Figure 3.20 shows the NSD of the AC output (red) and the DC output (orange). The unfiltered DC output shows a pronounced noise-gain peaking which is an attribute of the decompensated operational amplifier. The effect is efficiently suppressed by limiting the bandwidth to $50\,\mathrm{MHz}$ at the AC output. For this output, the NSD remains below the shot noise level of a photocurrent $I_{ph} = 10\,\mu\mathrm{A}$[4] typically used for PDH (grey, dashed line). Thus, this detector offers shot noise limited detection for PDH over its entire bandwidth. For comparison, the NSD of an alternative approach is recorded. A fast photodiode (Hamamatsu G4176-03) is reverse biased at $9\,\mathrm{V}$ using a bias tee. The AC output is amplified by a low-noise RR amplifier (Mini Circuits ZFL-500LN+). While offering a significantly larger bandwidth depending on the RF amplifier, the NSD is more than an order of magnitude larger as compared to out PDH photodetectors. Shot noise limited detection is not achieved using these detector, since the required photocurrent scaling quadratically with the NSD (Eq. 3.19) is above the damage threshold of the photodiode.

The DC output combines a large bandwidth with the inherently high precision of TIAs at DC, i.e. a low and stable offset and a high linearity. This feature opens possible applications beyond PDH. For instance, fast rise and fall times of approximately $2\,\mathrm{ns}$ allow for reliable detection of the pulse shape of short laser pulses.

[4]This photocurrent corresponds to an optical power of approximately $29\,\mu\mathrm{W}$ for the Si photodiode used at $780\,\mathrm{nm}$ and approximately $15\,\mu\mathrm{W}$ for the In-Ga-As photodiode used at $960\,\mathrm{nm}$.

3.9. Conclusion and discussion

A distinctive feature of the ECDL systems and TA modules presented here is their high mechanical stability directly related to an excellent passive frequency stability. As compared to earlier designs, the main advantage lies in the use of a mechanical lens mount making the adhesive based solution obsolete. Additional optimisation regarding stability and lifetime of ECDL systems is obtained by a careful choice of laser diodes in combination with interference filters and feedback levels and by a thorough analysis of the factors influencing the frequency stability of the systems. Besides the ECDL design, the current drivers and temperature controllers notably influence the frequency stability of the systems. While our latest current driver design already offers unprecedented performance, the commercial temperature controllers leave room for improvement. In particular, they exhibit strong drifts with a change of the ambient temperature. They will be replaced by an optimised custom design. Further substantial improvement of the ECDL design may in future be achieved by re-design. This design should include further miniaturisation of the external cavity in order to reduce the sensitivity to vibrational instabilities. The use of a simpler filter mount and a smaller piezo actuator offer the largest potential for miniaturisation. The remaining use of adhesives in the mount of the feedback mirror is believed to cause drifts that are not fully compensated by the piezo actuator. The feedback mirror and piezo mount should thus be replaced by an all mechanical solution. Also, an improved accessibility and positioning accuracy of the laser diode is required. However, all these improvements require a replacement of the existing ECDLs.

With the *Red Pitaya Lockbox* and the *Red Pitaya IntStab* versatile tools for laser-frequency stabilisation are presented on this chapter. The digital controllers allow for straightforward and reproducible gain settings covering several orders of magnitude. Complex stabilisation schemes can be implemented without hardware modifications. Thus, the controllers are suitable for a wide range of applications. The analog hardware developed in this work may be interpreted as an interface to the commercial STEMlab platform allowing for reliable use in a laboratory environment. Around the STEMlab platform an active community has evolved. In particular, new FPGA based software solutions are developed that may in future also extend the capabilities of the hardware presented here. Nevertheless, the noise and bandwidth performance of the controllers is defined by the Red Pitaya. If a faster controller or a higher ADC or DAC resolution is required, it is straightforward to replace the Red Pitaya by a different FPGA.

The laser-intensity controller is complemented by photodetectors that feature a gain, output-voltage range, and bandwidth specifically optimised for application in intensity control loops. For a typical application, the detectors are in principal shot noise limited. In a noisy laboratory environment however, this behaviour should be confirmed by separate measurements. Typically ground loops and long signal paths degrade the noise performance.

For high-performance laser-frequency locks, a large bandwidth is crucial. In this work, a novel technique for wideband laser-current modulation is presented. The resulting wideband, flat transfer function provides a predictable behaviour for frequency control loops. In a typical control loop, the phase-lag and non-linearity of this input will be negligible. Additionally, the performance at DC will not inflict the passive stability of the laser allowing for applications without control loops, such as frequency modulation or rapid frequency steps. The laser-current modulation is detected by the corresponding intensity modulation. However,

the transfer function relevant for laser-frequency modulation connects the control voltage applied to the modulation input with a change of the laser frequency. The resulting frequency modulation is dominated by two effects: The current modulation results in a modulation of the charge-carrier density of the gain material. At frequencies up to several MHz, this effect is masked, by the temperature modulation of the laser-diode junction also resulting in a modulation of the refractive index. [89] The transient regime of these effects [115] is typically found within the bandwidth of high-performance laser-frequency locks resulting in a reduced gain at high-frequencies, i.e. a reduced bandwidth. By analysing the beat spectrum of the modulated laser with a reference laser, it is straightforward to determine the transfer behaviour for each laser-diode type allowing for efficient compensation of the effect.

Low-noise detection is an often underestimated building block of laser-frequency stabilisation schemes. For low-bandwidth applications, it is convenient to use the photodetector optimised for intensity stabilisation due to its large area photodiode and the wide output-voltage range. The bandwidth can be extend to $\sim$7 MHz by reducing the TIA gain. Detection for schemes that require a large bandwidth and involve low intensities, such as the PDH scheme, is more challenging. In this chapter, a TIA based photodetector is presented that combines a large bandwidth with shot noise limited detection at low intensities. The detector can be equipped with a Si-photodiode or an InGaAs-photodiode thereby covering a large wavelength range of 320 nm to 1700 nm.

4. Laser systems for dissipative and coherent manipulation of rubidium at the D2 line

Laser cooling in a magneto-optical trap (MOT) relies on the dissipative interaction between light field and atoms. MOTs for alkali metals and alkaline earth metals have become a standard technique for experiments involving ensembles of cold atoms. Especially for rubidium, this technique is well understood on a fundamental level. However, the length of the MOT phase constitutes the experimental basis for the quantum computation and quantum simulation platform described in Chap. 2. This puts high demands on reliability, stability and quality of the MOT setup. The MOT phase predominantly defines the time required for an experimental cycle. Since the optical tweezer arrays are loaded directly from the MOT and no evaporative cooling is required, atom number and density play an subordinate role. So far, a simple 3D-MOT configuration with three counter propagating beam pairs is loaded directly from a rubidium dispenser. Due to its simple design, this configuration promises the best stability and retains a good optical access. For the laser system providing the MOT light fields, additional flexibility regarding frequency stabilisation and intensity control is required since the light fields are used in subsequent experimental phases, such as imaging or atom transport.

In this chapter, the MOT laser system is described and characterised. Techniques specifically suited for creating light fields close to an atomic resonance are presented. This includes a precision spectroscopic reference and frequency-offset lock techniques as well as intensity stabilisation and control schemes. The MOT laser system is based on a master-oscillator power-amplifier (MOPA) system described here. Furthermore, an optimised scheme for creating laser fields with a low relative phase noise employed for coherent coupling of the rubidium ground states is presented.

4.1. Multi-purpose master-oscillator power-amplifier (MOPA) system at 780 nm

For a stable and straightforward alignment of the MOT beams, large beam diameters are desirable. The optical power required for the optimal beam size and cooling light intensity typically exceeds the output power of a single diode laser. Hence, the MOT laser system described here is based on a high-power MOPA system. This system provides an output power that is significantly higher than the power required for the cooling light fields. The additional optical power is available for other light fields in the experiments near-resonant to the cooling transition. In the presented setup, two functions are realised: Firstly, a pushout laser field that removes atoms from the dipole traps state-selectively. This light field is also used for initial slowing of the atom discharged from the dispenser. Secondly, a light field is realised that is used to select one Talbot plane for experiments by removing atoms from all other planes (see Sec. 2.2 for details).

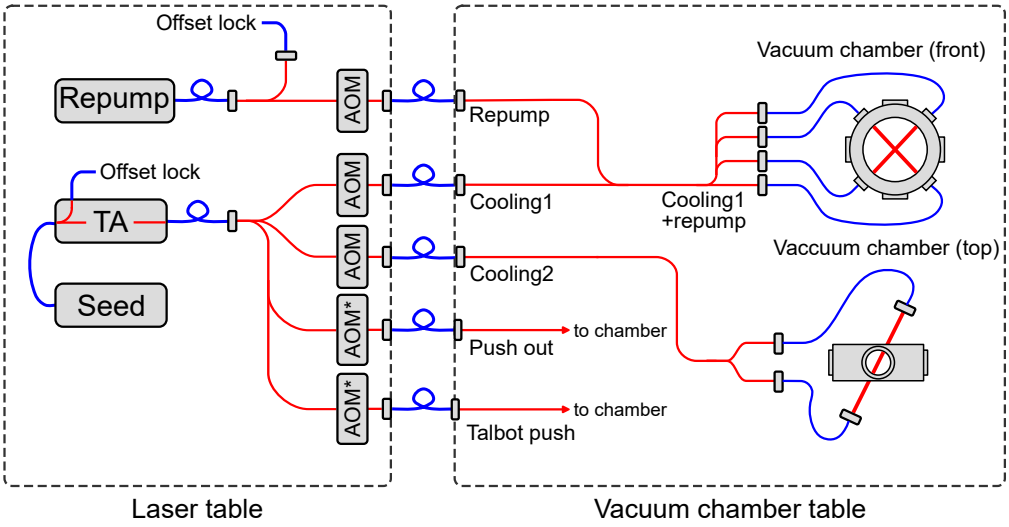

Fig. 4.1.: Simplified layout of the MOT laser system including key elements for switching and intensity stabilisation as well as light used for frequency stabilisation. Optical fiber connections are depicted in blue. Free-space setups are depicted in red. The dashed boxes indicate the physical location of the subsystems. Acousto-optic modulators (AOM) used in double-pass configuration are marked with a star.

Figure 4.1 shows an overview of the MOT laser system. All laser systems are realised using the external-cavity diode laser (ECDL) design presented in Sec. 3.1. The laser systems are located on one optical table (laser table). Different modules are connected by polarisation-maintaining single-mode optical (PM) fibers (blue). This modular design facilitates maintenance and improves the stability of the system by avoiding long free-space beam paths. The MOPA system consists of an ECDL system as a seed laser and a tapered amplifier (TA) system. At the input of the TA, a small portion of the seed light is forked for frequency stabilisation of the seed laser system. The output light of the TA is coupled directly into a PM fiber. The output of the fiber is distributed to four beam paths in a separate module. Each beam path involves an acousto-optical modulator (AOM) that is used as an actuator for intensity stabilisation and control (see Sec. 4.5 for details). The AOMs in the beam paths for the pushout light field and the Talbot-push light field are setup in double-pass configuration [116] as marked by a star (AOM*). This configuration allows for shifting the laser frequency within a range of twice the AOM bandwidth without affecting the alignment of the beam thereby allowing for dynamically shifting the laser frequency during an experimental cycle or to produce a variable frequency offset from the seed laser frequency. The cooling light is distributed to two beam paths (cooling1 and cooling2) that allow for separate intensity control. All AOM frequencies are chosen such that the four output light fields have a similar laser frequency within $20\,\mathrm{MHz}$. For the MOT, additional to the cooling light, repump light is required that transfers atoms from the $F = 2$ ground state manifold back to the $F = 3 \rightarrow F' = 4$ cooling cycle. This light field is offset from the cooling light field by a frequency of approximately $3.035\,\mathrm{GHz}$ (i.e. the hyperfine splitting of the ^{85}Rb ground states). A repump laser system is used that is frequency stabilised separately in order to realise the large frequency offset. The output of the ECDL is fiber coupled to a module that provides light for frequency stabilisation and an AOM for switching and intensity stabilisation. The five light fields generated on the laser table are transferred to the optical table holding the experimental vacuum chamber (vacuum chamber table) using PM fibers.

The experimental chamber is a custom stainless steel vacuum chamber with two CF100-type viewports providing the main optical access thereby defining the main optical axis normal to these viewports and orientated parallel to the surface of the optical table and $200\,\mathrm{mm}$ above the table surface. Perpendicular to this axis, optical access via twelve additional CF16-type and four CF40-type viewports is available. A simplified scheme of the experimental chamber is depicted in Fig.4.1. In order to improve the stability of the optical setup and facilitate the alignment, the six MOT beams are transferred to the vacuum chamber using separate PM fibers. For that purpose, a second distribution module is realised on the vacuum chamber table. In this module, the repump light is added to the first cooling light beam (cooling1). Subsequently, the combined light field is distributed to four PM fibers. The second light field (cooling2) containing cooling light only is distributed to two PM fibers. Using the light from the four PM fibers (cooling1+repump), two counter propagating MOT beam pairs are realised by attaching fiber couplers directly to the viewports. The third beam pair is realised by a short free-space beam path using the main optical access. This beam pair is switchable separately. This feature is used for instance in order to reduce stray light for imaging.

4.1.1. Tapered amplifier system

The TA module used for the MOT laser system is a prototype of the module discussed in Sec. 3.3.2. In contrast to the presented module, the collimation lenses in this prototype are mounted using a low expansion adhesive and the translation stage holding the cylindrical lens is not integrated in the TA module. Although the module is supplied by a standard current driver (Thorlabs LDC8040) and a standard temperature controller (Thorlabs TEC8040), the module uses custom connectors and cables. Seed light for the tapered amplifier is provided by one of our ECDL systems described in Sec. 3.1. The standard laser diode for $780\,\mathrm{nm}$ (Thorlabs LD785H1) is used with a $30\,\%$-feedback level. Feedback of the TA to the seed laser is suppressed by more than $60\,\mathrm{dB}$ using a tandem Faraday isolators at the output of the seed laser. A second Faraday isolator with a transmission of $T = 0.85$ and an isolation above $30\,\mathrm{dB}$ is used to protect the TA chip (DILAS TA-0780-2000 , serial number 44828) from feedback. The astigmatism of the tapered amplifier is characterised by the residual divergence $\theta'_x = 38(3)\,\mathrm{mrad}$ (see Sec. 3.3.2 for details). The focal length of the cylindrical lens is chosen to $f_{CL} = 40\,\mathrm{mm}$ according to Eq. 3.12 using the nominal beam waist calculated with Eq. 3.11 applying the beam divergence θ_y stated in the datasheet of the TA chip [117]. The value for θ'_x depends strongly on the operation current I. The quoted value has been determined at $I = 3\,\mathrm{A}$. The output of the TA module is coupled into a PM fiber (Thorlabs P3-780PM-FC) using an aspheric lens with a focal length of $f_{coup} = 7.5\,\mathrm{mm}$. Note, that the optimal value for f_{coup} is typically significantly smaller than expected from the numerical aperture of the fiber and the beam waist since the beam quality factor $M^2 > 1$. In Table 4.1, the specification and operating parameters for the TA module presented in this section are summarised. The maximum operating current I_{max} is stated in the datasheet of the TA chip. [117] Figure 4.2 shows the typical output power versus operating current characteristics as measured directly at the output of the TA module. The optimal seed power saturates the amplifier chip such that the maximal output power is vastly independent of the seed power. This is the case for the seed-power level during this measurement. The power characteristics are well represented by the linear function obtained by a fit to the data points (dashed). Typically, the optimal MOT intensities are reached at a current of $2\,\mathrm{A}$ corresponding to an output power of approximately $800\,\mathrm{mW}$. Thus, the system offers a large headroom guaranteeing stable operation of the MOT.

Specification	Value	Conditions
Wavelength	780 nm	777 nm to 797 nm
Maximum output power	2.45 W	$I = 3.5$ A, $P_{seed} = 12$ mW
Typical seed power	15 mW	10 mW to 30 mW
TA mount temperature	18.5 °C	
Nominal beam waist	1.45 mm	$f_{AL} = 3.1$ mm, $\theta_y = 25°$
Astigmatism θ'_x	38(3) mrad	$I = 3$ A
Cylindrical lens f_{CL}	40 mm	
Typical fiber coupling	45 %	$I = 3.5$ A , $f_{coup} = 7.5$ mm
Maximum fiber output	0.93 W	$I = 3.5$ A , including all losses

Tab. 4.1.: Specifications of the TA module used in the MOT laser system. TA chip: DILAS TA-0780-2000-CM, serial number 44828. I: operating current. P_{seed}: seed power. f_{coup}: Focal length of the lens used for fiber coupling. f_{AL}: Focal length of the output-collimation lens. θ_y: output divergence in y-dimension. θ'_x: Residual divergence in x-dimension (compare Fig. 3.4).

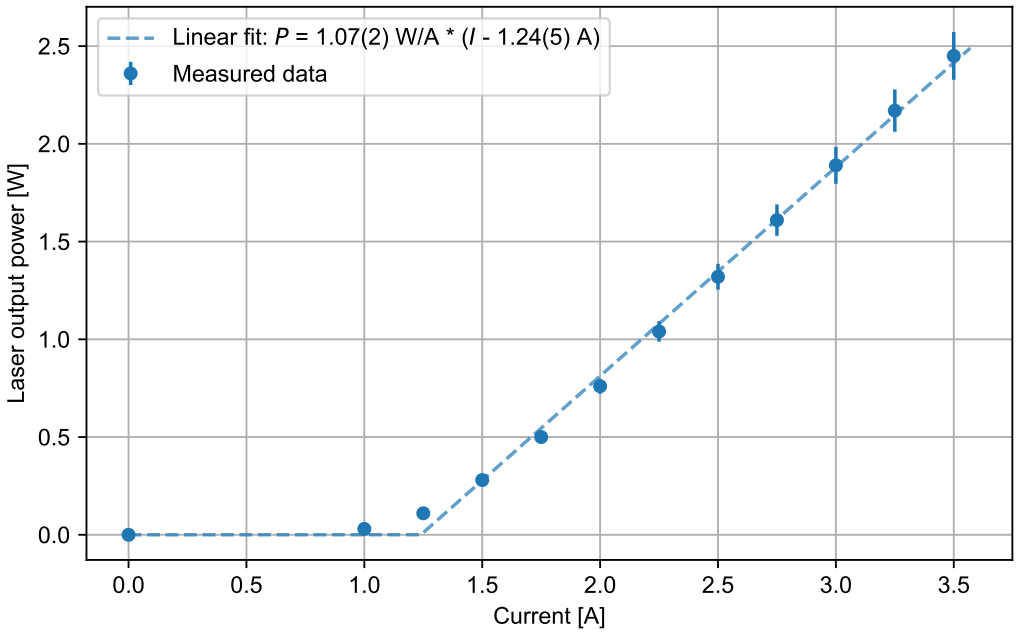

Fig. 4.2.: Typical output power versus operating current characteristics of the TA system discussed in this section. The dashed line shows the linear function stated in the legend as obtained by a fit to the data points. The maximum operating current of the chip is 3.5 A.

4.2. Precision spectroscopic reference

In order to achieve a predictable and controllable interaction between atoms and light fields, all laser systems generating light fields near-resonant to an atomic transition are required to exhibit a linewidth and long-term frequency fluctuations negligible as compared to the natural linewidth Γ of the transition. In this work, this is realised by implementing a suitable reference laser system that provides light for frequency-offset locks of the laser systems used in the experiment (see Sec. 4.3). The reference laser system is stabilised to a spectroscopic feature of ^{85}Rb detected by modulation transfer spectroscopy (MTS). [118, 119] The results concerning optimisation of the MTS technique presented in this section haven been published in [120].

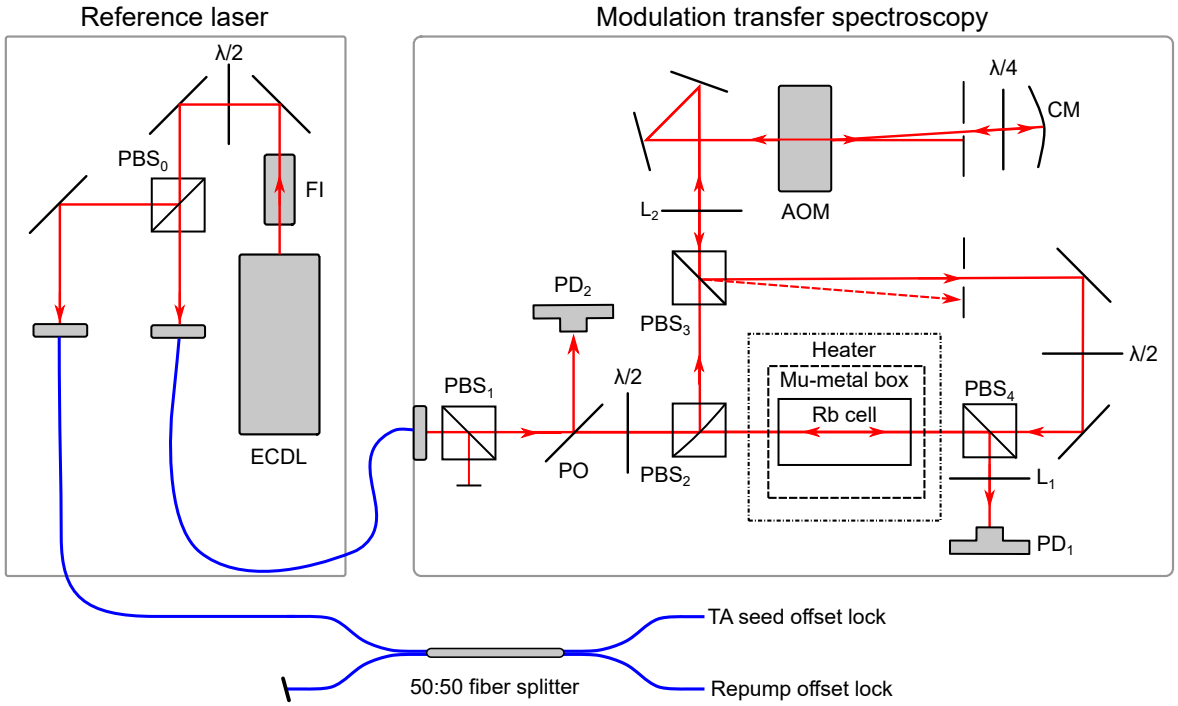

Fig. 4.3.: Optical setup of the reference laser system including modulation transfer spectroscopy. PM optical fibers are depicted in blue. Free-space beam paths are depicted in red. PBS: polarising beam splitter. FI: Faraday isolator. PD: photodetector. PO: pick-off. L: plano-convex lens. CM: curved mirror. $\lambda/2$: half-wave plate. $\lambda/4$: quarter-wave plate.

MTS is a Doppler-free frequency modulation spectroscopy scheme [121] that is characterised by a non-linear modulation transfer process. The MTS signal offers a high sensitivity due to its steep slope at the atomic resonance and a high accuracy due to its flat baseline. Thus, the MTS technique is specifically suitable for generating an error signal for laser-frequency stabilisation. Figure 4.3 shows the MTS setup (right) that is connected to the reference laser system (left) by a PM fiber. The fiber output is split into a probe beam and a pump beam. The required frequency modulation is imprinted on the pump beam using an AOM with a center frequency of $f_{AOM} = 110\,\text{MHz}$ (Crystal Technology 3110-120) in double-pass configuration in -1.-order. For that purpose, the RF signal of the AOM is frequency modulated with a modulation frequency f_m and a modulation index M. In this configuration, the pump beam field is given by

$$E_{pump}(t) = E_{pump,0}\,\cos\big(2\pi\,(f_{probe} - 2f_{AOM})t + 2M\,\sin(2\pi\,f_m t)\big). \tag{4.1}$$

Where f_{probe} is the laser frequency of the probe beam, i.e. the frequency of the reference laser. Note, that the factor of two in the frequency shift and in the modulation index result from the AOM double-pass configuration. A standard representation of the pump light field can be derived using the Jacobi-Anger expansion [122]

$$E_{pump}(t) = E_{pump,0} \sum_{n=-\infty}^{\infty} J_n(M)\,\cos\big(2\pi\,(f_{probe} - 2f_{AOM} + nf_m)t\big) \tag{4.2}$$

where J_n is the n-th Bessel function of the first kind. This representation shows that the frequency modulated pump spectrum consists of a carrier at the center frequency $f_{probe} - 2f_{AOM}$ and sidebands at an integer multiple of f_m. Pump beam and probe beam are aligned counter-propagating in a rubidium glass cell (TRIAD Technology TT-RB-75-V-P) with optimal perpendicular polarisation [123] and an intensity ratio of approximately 2:1. For an improved shielding against electro-magnetic fields, the cell is placed in a mu-metal box. Optimal absorption [124] is achieved by placing the shielded cell in an isolated enclosure with a heater that allows us to heat the cell to a temperature of approximately $40\,^{\circ}$C by applying a current of $300\,$mA. In the medium, the non-linear degenerate four-wave-mixing process leads to a transfer of the frequency components generated by frequency modulation to the probe field, if f_{probe} is close to resonance with an atomic transition. [125, 126] After passing the rubidium cell, the probe beam is detected using the low-noise photodetector presented in Sec. 3.7 (PD_1). In order to achieve, an optimal signal-to-noise ratio, the maximum optical power of $P_{pd} = 300\,\mu$W is used for detection. Applying Eq. 3.14 and Eq. 3.15 to Eq. 3.19 yields the corresponding voltage shot-noise spectral density of

$$e_{MTS} = R_f\sqrt{2e\eta P_{pd}} = 0.4\,\mu\text{V}/\sqrt{\text{Hz}} \tag{4.3}$$

using $R_f = 50\,\text{k}\Omega$ and $\eta = 0.62\,$A/W. The power level is achieved using a total fiber-output power of approximately $3\,$mW. Distribution, overlap, and separation of the described beam paths are realised using polarising beam splitters (PBS) and suitable polarisation rotations. A well defined linear polarisation is obtained by filtering the fiber output with an additional PBS (PBS_1). A pick-off and an additional photodetector (PD_2) allow for monitoring of the optical power used for spectroscopy.

4.2.1. Electronic module for modulation transfer spectroscopy

The MTS signal is generated by phase sensitive demodulation of the photodetector signal. Our theoretical analysis [120] shows, that optimal error signal amplitude and slope are achieved by setting the modulation parameters to a modulation frequency of $f_m = 2.5\,$MHz and a modulation index of $3 \leq 2M \leq 10$. Generating the required RF signal for application at the AOM is challenging due to the large modulation index in combination with the high modulation frequency. The signal can be generated by external frequency modulation of a high-performance synthesiser by a multi-channel direct digital synthesiser (DDS). [120] This solution requires additional buffer amplifiers and active filters. Due to the synthesiser, high costs are invoked. In this work, a compact and cost-efficient module for AOM based MTS is developed. [127]

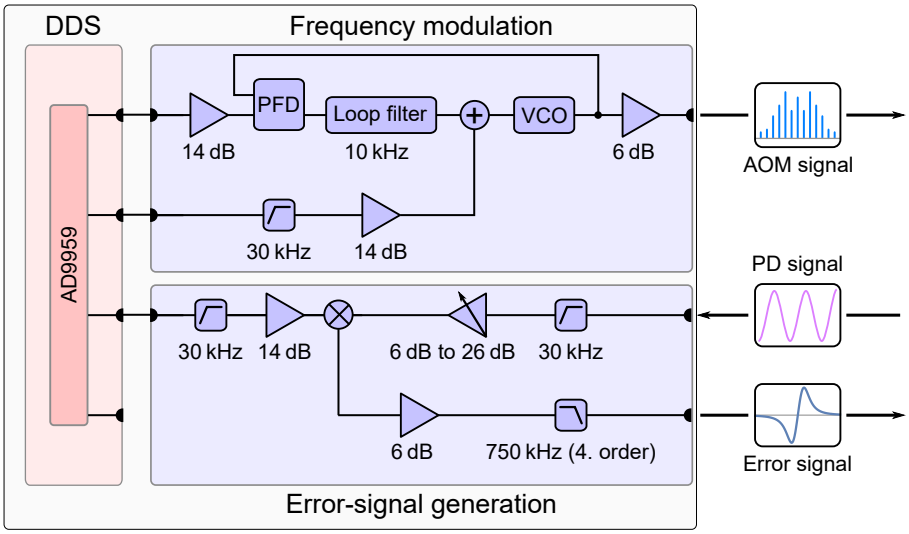

Fig. 4.4.: Block diagram of a module for MTS signal generation with a frequency-modulated AOM. The module is based on a 4-channel DDS (Analog Devices AD9959). It produces a frequency modulated RF signal that is applied to the AOM. An MTS error signal is generated by phase-sensitive demodulation of a MTS photodetector (PD) signal. Relevant amplifications and cut-off frequencies are denoted under the components. PFD: phase-frequency detector. VCO: voltage-controlled oscillator.

Figure 4.4 shows a block diagram of the MTS module. The module includes a commercial DDS board (Gra&Afch DDS AD9959 Arduino Shield) that provides the required RF signals. The module consist of two parts: a sub-module that produces the frequency modulated RF signal for the AOM and a sub-module that generates the error signal using the photodetector signal as an input. The AOM signal is produced by an voltage controlled oscillator (VCO, Crystek CVCO45CL-0100-0140). The VCO center frequency is locked to one channel of the DDS using a phase-frequency detector (Analog Devices HMC1031) and a passive loop filter with a bandwidth of $10\,\mathrm{kHz}$ in a phase-locked loop (PLL). A second DDS signal is added directly to the tuning port of the VCO. This signal allows for applying a frequency modulation beyond the bandwidth of the PLL. Input and output signal levels are optimised by suitable amplification. The modulation index is limited by the stability of the PLL. Proper function of the PLL is indicated by an LED in the front panel connected to a status pin of the PFD. The maximum modulation index is determined experimentally by increasing the amplitude of the modulation signal successively. Figure 4.5 shows the typical frequency modulation spectrum used for MTS recorded with a spectrum analyser (Rhode & Schwarz FPC1500) with a resolution bandwidth of $200\,\mathrm{kHz}$ (blue). The modulation frequency is set to $f_m = 2.5\,\mathrm{MHz}$ and the modulation index is set to the maximum value. The index M is extracted from the depicted spectrum by fitting the sideband amplitudes given by Eq. 4.2 to the spectrum (orange). The obtained value of $2M = 3.6$ is slightly below the value of 4.14 achieved using the synthesiser. [120] Varying the modulation frequency and adapting the modulation signal amplitude proportionally shows that the maximum modulation index can be considered constant for $100\,\mathrm{kHz} \leq f_m \leq 10\,\mathrm{MHz}$. The lower cut-off is defined by the bandwidth of the loop filter while the upper cut-off is determined by the input capacity of the VCO ($100\,\mathrm{pF}$) and the input series resistance required for stable operation ($100\,\Omega$).

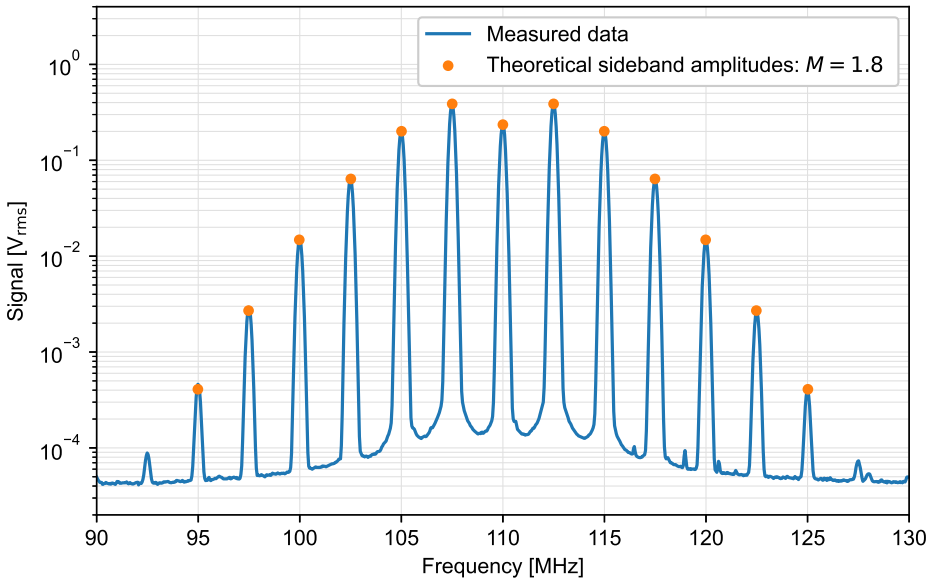

Fig. 4.5.: Typical frequency modulation spectrum of an RF signal applied to an AOM for MTS (blue). The spectrum is generated by the MTS module depicted in Fig. 4.4. The modulation index is set to the maximum value. The index is determined by comparison of the sideband amplitudes with a calculated frequency modulation spectrum.

The error signal sub-module depicted in Fig. 4.4 is based on a double-balanced frequency mixer (Mini Circuits SYPD-1+) used for phase sensitive demodulation of the photodetector signal. A demodulation signal at the modulation frequency f_m is generated by the DDS. The DDS allows for tuning of the phase between modulation and demodulation signal thereby allowing us to set the optimal demodulation phase. [120] The demodulation signal is applied to the first input of the frequency mixer. The photodetector signal is connected to the second input. The photodetector input features a variable amplifier that is used to optimise the signal amplitude. The output of the frequency mixer contains the MTS error signal at DC and the signal at $2f_m$. Additionally, a parasitic signal at f_m is expected due to the finite isolation of the mixer input to the output. In order to obtain an error signal suitable for frequency stabilisation, a low-pass filter suppressing the signals at f_m and $2f_m$ is applied. The low-pass filter defines the bandwidth of the error signal. In the presented MTS module, a 4th order Chebyshev filter is used as implemented by a low-noise active filter building block (Analog Devices LT1568). The measured -3 dB-cut-off frequency of the realisation is 850 kHz. The phase-lag induced by the filter is less than $90°$ below 400 kHz. A suppression of 47 dB at 2.5 MHz and larger than 60 dB at 5 MHz is achieved. The output voltage-noise spectral density (NSD) of the error signal sub-module is analysed using a spectrum analyser (Rhode & Schwarz FPC1500). For frequencies below 1 MHz, additionally a low-noise pre-amplifier (Stanfort Research Systems SR560) is used. The results are depicted in Fig. 4.6 (blue). For this measurement, no input signal is applied while the photodetector gain and the amplitude of demodulation signal are set to their maximum value. The noise-gain peaking and the cut-off of the filter are visible. Additional peaks appear at the modulation frequency and its harmonics due to the finite isolation of the frequency mixer. These peaks are well suppressed. The output NSD is compared to the fundamental noise level given by amplified photodiode shot noise. For this purpose, the gain of the demodulation including the photodetector amplifier is determined to 17 dB. The resulting

shot-noise level as calculated in Eq. 4.3 is plotted for comparison in Fig. 4.6 showing that the error signal noise is dominated by photodetector shot noise.

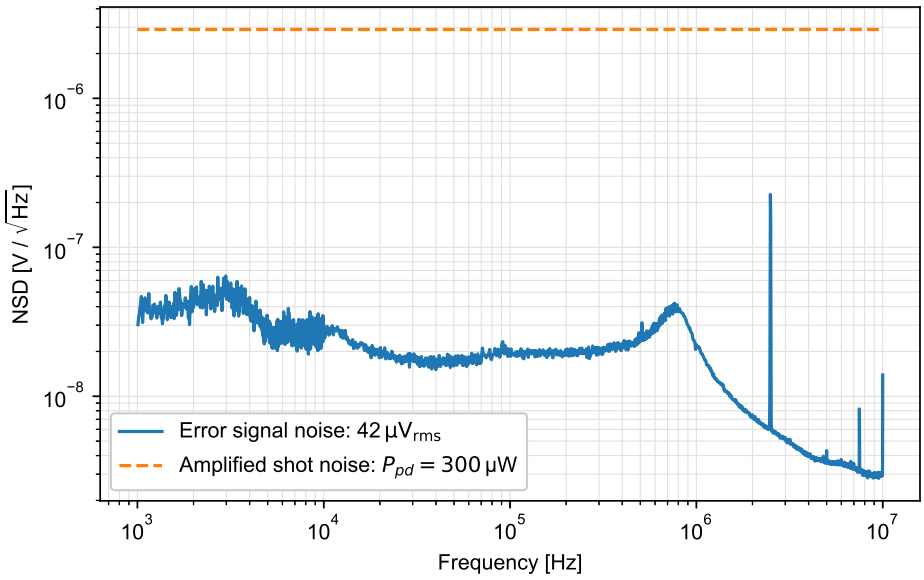

Fig. 4.6.: Voltage-noise spectral density (NSD) of the error-signal output of the MTS module depicted in Fig. 4.4. The rms noise value stated in the legend is calculated from the depicted spectrum. The amplified shot noise of the photodetector in the MTS setup using an optical power of P_{pd} is shown for comparison.

4.2.2. Long-term frequency stability and linewidth

The MTS technique provides the strongest signal for closed atomic transitions. [128] For the ^{85}Rb D2-line this is the $|5S_{1/2}, F = 3\rangle \rightarrow |5P_{3/2}, F' = 4\rangle$ transition. The AOM that imprints the frequency modulation to the pump field reduces its frequency by $2f_{AOM} = 220\,\text{MHz}$. This shift is compensated by the Doppler shift of the atoms in the rubidium cell. Pump and probe beam are resonant to the same velocity class if the probe beam is detuned by $-f_{AOM}$ from the transition and the pump field is detuned by $+f_{AOM}$. Hence, the reference laser is stabilised to a frequency $110\,\text{MHz}$ above the transition frequency. Figure 4.7 shows the typical error signal (top) and the Doppler-free absorption spectrum (bottom) of the MTS setup when scanning the laser over the atomic resonance. The absorption spectrum is recorded using the DC signal of the photodetector. The frequency scale is derived from the position of the strongest Lamb dips that are attributed to the $F' = 2, 4$ (co(2,4)) and $F' = 3, 4$ (co(3,4)) crossover transitions. [129] The features of these transitions are strongly suppressed in the error signal. The frequency calibration allows us to determine the error signal slope as stated in the legend by a linear fit to the data points close to the zero crossing (orange). The slope links an in-loop deviation of the error signal to a frequency deviation of the laser system. The error signal is used for frequency stabilisation with a digital controller employing the locking technique described in Sec. 3.4. The locking parameters are optimised for the lowest rms deviation of the error signal.

In order to evaluate the performance of the frequency lock, a laser linewidth characterising stochastic frequency fluctuations on sub-second time scales and the long-term stability

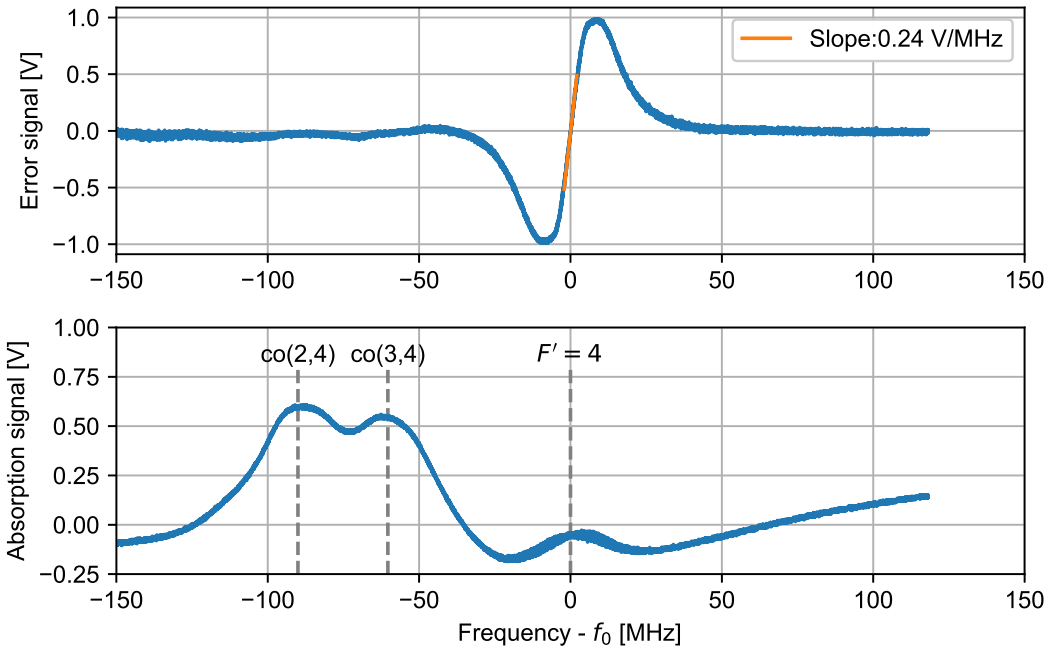

Fig. 4.7.: Typical error signal (top, blue) and Doppler-free absorption signal (bottom, blue) produced by the MTS setup depicted in Fig. 4.3. The slope of the error signal is determined by a linear fit (orange). The frequency calibration has been derived from the positions of the Lamb dips in the absorption spectrum relative to the error-signal zero crossing (f_0) as indicated by the dashed lines. The strongest lamp dips are attributed to the $F = 3 \rightarrow F' = 2, 4$ (co(2,4)) and the $F = 3 \rightarrow F' = 3, 4$ (co(3,4)) crossover transitions.

considering frequency drifts are determined. For most linewidth measurement methods, the experimentally accessible observable is the power spectral density (PSD) of the laser field. [130] Linking the PSD to an unknown laser-frequency noise spectrum is a challenging task. [131] In this section, we restrict the discussion to the simpler case of Lorentzian line shapes indicating pre-dominantly white frequency noise. [130] The PSD of the reference laser system is determined by recording the PSD of the beat note with another laser system stabilised independently. The beat-note PSD is given by the convolution of the PSD of both laser fields. In the case of Lorentzian line shapes the convolution yields a Lorentzian beat spectrum where the width is given by the sum of the contributing linewidths. Thus, the result yields an upper bound as it contains the linewidth of the second system as well. Ideally, this linewidth is negligible. Hence, the laser system described in Sec. 6.1 featuring a linewidth well below 10 kHz (FWHM) is used as a reference for this measurement. The beat note spectrum is depicted in Fig. 4.8 (blue). The laser linewidth is determined by fitting a Lorentzian function

$$L(f) = \frac{A}{1 + \left(\frac{f - f_0}{\gamma_L/2}\right)^2} \tag{4.4}$$

with amplitude A, center frequency f_0, and full width at half maximum (FWHM) γ_L to the central data points within a frequency range of $f_0 \pm 50$ kHz (orange). The central region of the laser line is described by the Lorentzian function while there are significant deviations in the line wings. The shape of the line wings is determined by the control loop parameters. [131]

The Lorentzian portion of the spectrum with a FWHM of

$$\gamma_L = 58(1)\,\mathrm{kHz} \tag{4.5}$$

contains $83.5\,\%$ of the integrated beat-note signal power. Neglecting the linewidth of the second laser system, this is equivalent to the fraction of the optical power of the reference laser system emitted with a Lorentzian line shape with width γ_L. The remaining PSD of the reference laser system accumulates within a frequency range of $f_0 \pm 400\,\mathrm{kHz}$. Thus, the central linewidth of the reference laser is two orders of magnitude below the natural linewidth of ^{85}Rb of $\Gamma = 2\pi \times 6\,\mathrm{MHz}$ [35] and also the spectral width of the line wings is negligible as compared to Γ.

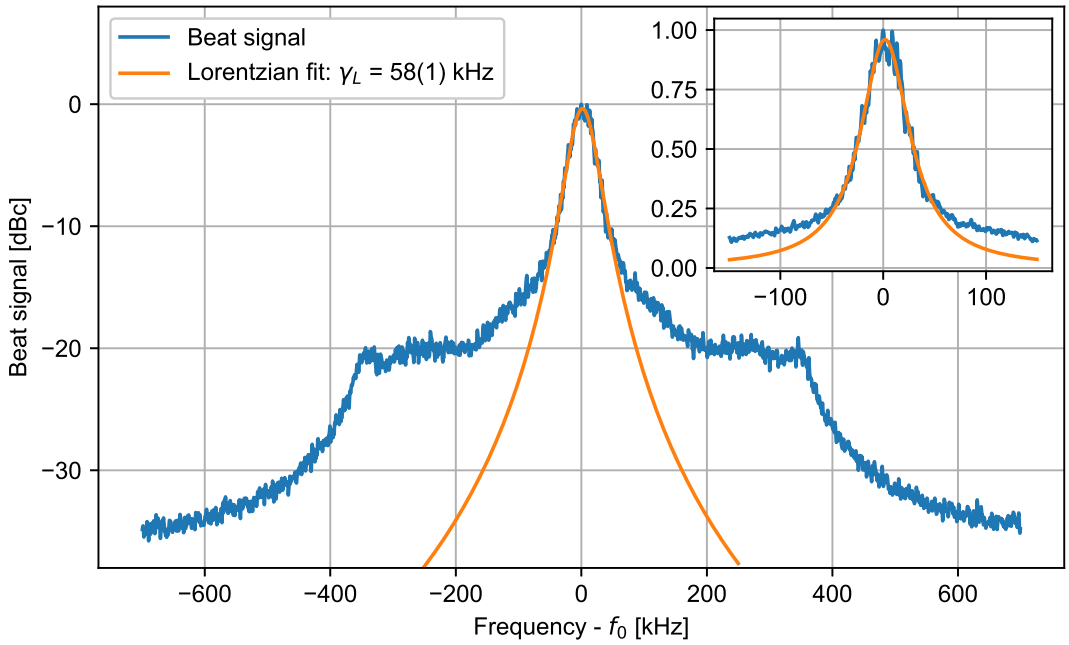

Fig. 4.8.: Beat-note spectrum of the reference laser system and the Rydberg laser system described in Sec. 6.1 normalised to the maximum amplitude. The frequency scale is shifted by the center beat frequency f_0. A Lorentzian function with FWHM γ_L is fitted to the data in the frequency range $-50\,\mathrm{kHz}$ to $50\,\mathrm{kHz}$ (orange). The inset shows a detail with a linear scale.

The long-term stability of the reference laser system is evaluated by comparison with a second laser system stabilised to an independent MTS setup. For that purpose, the beat note of the two laser systems is recorded using a frequency counter. This measurement neglects unlikely correlations between the setups which are located in different laboratories. Otherwise, it gives an upper bound to frequency fluctuations since it is not possible to attribute the measured frequency drifts to one of the setups unambiguously. Figure 4.9 shows the typical frequency fluctuations over a period of approximately $240\,\mathrm{h}$. A peak-to-peak fluctuation of $130\,\mathrm{kHz}$ and an rms deviation of $28\,\mathrm{kHz}$ are observed. These fluctuations are more than an order of magnitude below the natural linewidth of rubidium. The main origin of the frequency fluctuations is residual amplitude modulation (RAM) induced by the AOM. [132, 133] RAM renders the error signal asymmetric. Although RAM has been reduced significantly by a suitable

adjustment routine [120], the effect is still observable. Thus, fluctuations of the laser intensity used for spectroscopy resulting in a change of the error signal amplitude induce a fluctuating offset. In Fig. 4.9, the relative intensity fluctuations $\Delta I/I_0$ of the respective laser systems are plotted. A strong correlation between the frequency deviation and the intensity fluctuation in the second spectroscopy is observable. The measurement allows for an estimate of the RAM induced frequency shift of the reference laser system presented here to $\Delta I/I_0 \times 0.5\,\mathrm{MHz}$. Thus, the effect may be suppressed below the linewidth of the reference laser by maintaining an intensity stability better than $10\,\%$. The excellent long-term stability of both systems is also illustrated by the fact that both laser systems could be stabilised simultaneously over a time of 10 days.

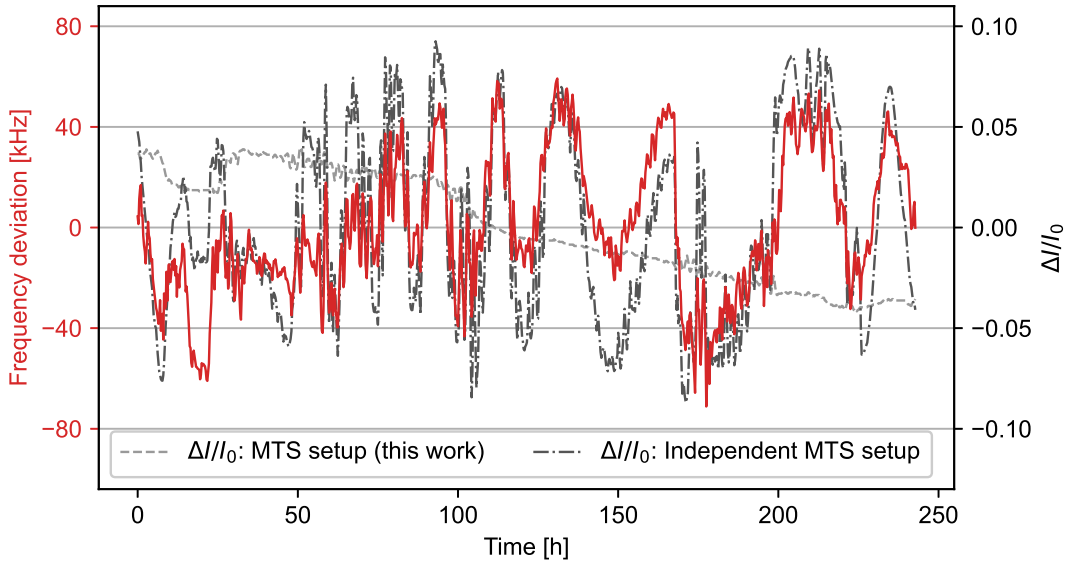

Fig. 4.9.: Frequency deviation of the beat note between two laser systems stabilised to two independent MTS setups (red). For comparison, the change in the laser intensity ΔI normalised to the average intensity (I_0) used for each spectroscopy is plotted for each setup.

4.3. Phase and frequency-offset locks

For applications using several laser fields with a similar frequency, a frequency-offset lock to a stable reference laser is realised. For that purpose, the beat note between the laser system to be stabilised and the reference laser is detected with a fast photodetector. The measured offset frequency is used to create a suitable error signal for frequency stabilisation. This technique is used to create cooling and repump light for the magneto-optical trap in this experiment. By varying the frequency-offset setpoint it is also possible to realise laser-frequency changes during the experiment. In this section, a simple photodetector for beat notes and two methods for error-signal generation from a beat signal are discussed.

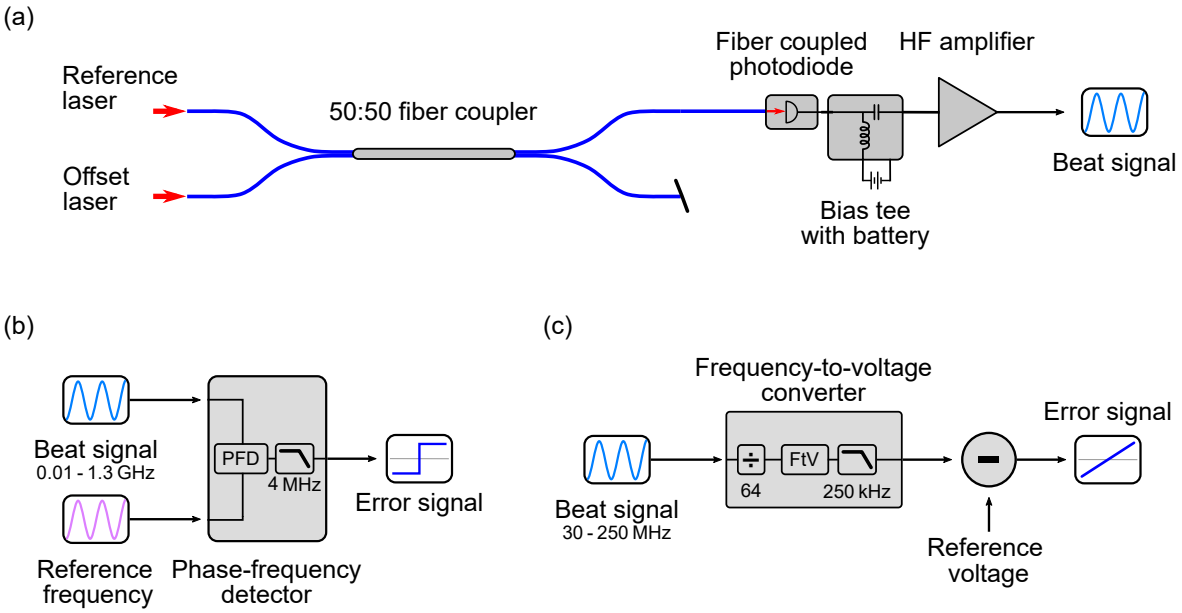

Fig. 4.10.: Block diagrams of different components for frequency-offset stabilisation. (a) Fiber-based photodetector for a beat note between two laser fields. (b) Error signal generation for frequency-offset stabilisation based on a phase-frequency detector (PFD). (c) Error signal generation for frequency-offset stabilisation based on a frequency-to-voltage converter (FtV).

4.3.1. Beat-note photodetector

For detection of beat notes, the simple photodetector depicted in Fig. 4.10 (a) is used. A small fraction (typically between 0.1 mW to 1 mW) of the output of the laser to be stabilised (offset laser) and of the reference laser are coupled into a single-mode optical-fiber combiner with a splitting ratio of 1:1 (Thorlabs TN785R5A2) such that the beat note of the two light fields can be detected at both outputs of the combiner. One of the outputs is connected directly to a fast silicon photodiode with a bulkhead fiber connector (Thorlabs FDS02). In order to achieve a maximal bandwidth, the junction capacitance of the photodiode is reduced by applying a reverse voltage of $9\,\mathrm{V}$ provided by a battery over a bias tee. The photodiode is soldered directly to the input of the bias tee. Its AC output is connected to a suitable high-frequency (HF) amplifier. The input voltage of the amplifier is generated by the alternating photocurrent through the $50\,\Omega$ input resistor of the amplifier. If necessary, the signal is amplified to the required level by additional HF amplifiers. This photodetector is a compact, robust and cost efficient solution since no free-space optics are involved. Its modular design allows for adaption to different applications.

If a suitable HF amplifier is chosen, the bandwidth of the detector is limited by the capacitance at the input of the amplifier C_{in}, i.e. the capacitance of the photodiode and stray capacitance. The capacitance of the photodiode is rated to $0.94\,\mathrm{pF}$ at a reverse voltage of $5\,\mathrm{V}$. However, the stray capacitance of the diode package and the bias tee can be significantly larger. The bandwidth of the detector is estimated by varying the beat frequency and recording the output signal level. Figure 4.11 shows the typical behaviour of the photodetector using light at $780\,\mathrm{nm}$. A steep roll-off for frequencies above $2\,\mathrm{GHz}$ is observable. For this measurement, an amplifier with a bandwidth of $14\,\mathrm{GHz}$ is used. Note, that for frequencies above $1\,\mathrm{GHz}$ also

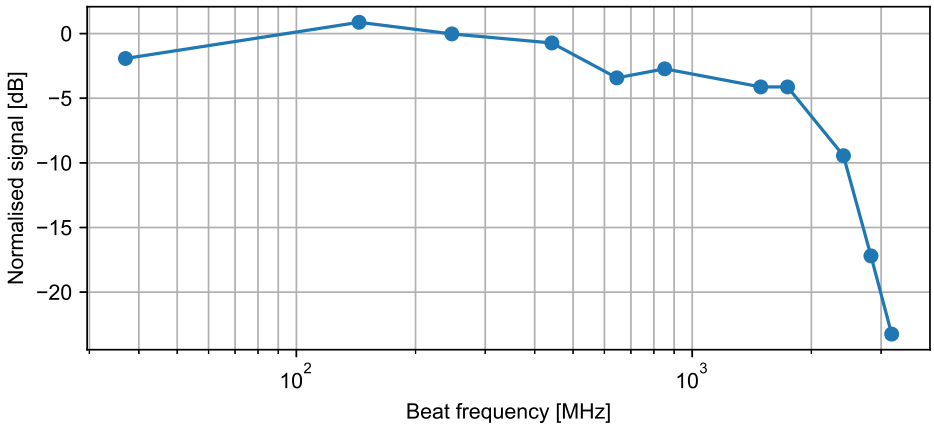

Fig. 4.11.: The bandwidth of the photodetector depicted in Fig. 4.10 (a) is estimated by varying the beat frequency.

considerable damping in the cables of the signal path is observable.

The noise level of this detector type is typically limited by electronic noise of the HF amplifiers. The Johnson–Nyquist noise [134] of the $R = 50\,\Omega$ input impedance of the amplifier at $T = 300\,\mathrm{K}$ is given by

$$e_I = \sqrt{\frac{4k_B T}{R}} \approx 18\,\mathrm{pA}/\sqrt{\mathrm{Hz}} \tag{4.6}$$

with the Boltzmann constant k_B. Thus, even for an ideal amplifier, the detector is not shot-noise limited at realistic photocurrents below $30\,\mathrm{mA}$. However, for a typical application the signal-to-noise ratio is sufficient.

4.3.2. Frequency-to-voltage converter

A frequency-to-voltage converter produces a voltage proportional to the frequency of the input signal. Using this device is a straightforward way of creating an error signal from a beat-note signal. By subtracting a setpoint voltage provided from the experimental control system from the output of the frequency-to-voltage converter an error signal with a variable zero crossing is created. The locking scheme employing the digital controller presented in Sec. 3.4 is used to stabilise the offset frequency. This technique is currently used to stabilise the seed laser of the MOPA system and the repump laser. A simplified block diagram of the custom frequency-to-voltage converter developed in this group is depicted in Fig. 4.10 (c). The input signal is divided by 64 using a prescaler (Fujitsu MB504). A frequency-to-voltage chip (Texas Instruments VFC110AD) with a bandwidth of $4\,\mathrm{MHz}$ is used to create the output signal. The signal is filtered by an active second-order low-pass filter with a cut-off frequency of $250\,\mathrm{kHz}$. This filter defines the bandwidth of the device. The input frequency range is limited by the prescaler at the lower end to $30\,\mathrm{MHz}$ and upwards to $250\,\mathrm{MHz}$ by the bandwidth of the frequency-to-voltage chip. An error signal is created using an external analog subtracting circuit. The main advantage of this technique is the linear response over the entire operating range. In combination with the fast digital controllers, this feature allows for the implementation of large frequency steps with transit times below $10\,\mu\mathrm{s}$. The maximum frequency step size is given by the frequency range of

the fast actuator employed in the lock (see Sec. 3.4 for details) to a typical value of $50\,\mathrm{MHz}$. Note that the device used here requires precise calibration since it exhibits non-linearities equivalent to several MHz within its operating range. Figure 4.12 shows the typical beat note between the stabilised laser and its reference laser obtained by using this technique. The Lorentzian function stated in Eq. 4.4 is fitted to the data. The beat note is well described by a Lorentzian function with a width of $\gamma_L = 145(1)\,\mathrm{kHz}$ with small deviations in the line wings. This linewidth is attributed to the minimum frequency deviation detectable by the frequency-to-voltage converter as estimated by

$$\Delta f_{FtV} = K_{FtV} \Delta V_{FtV} \approx 0.13\,\mathrm{MHz} \tag{4.7}$$

using the typical sensitivity $K_{FtV} = 0.04\,\mathrm{MHz/V}$ and the output voltage noise $\Delta V_{FtV} = 5\,\mathrm{mV}$. The linewidth determined here represents remaining frequency fluctuations as compared to the reference laser system. The resulting linewidth of the stabilised laser system is determined by a combination of the linewidths of the reference laser system and the beat note. Since the linewidth of the reference system is significantly smaller than the linewidth of the beat note (see Sec. 4.2), this locking technique limits the performance of the frequency lock. However, the resulting linewidth is still well below the natural linewidth of ^{85}Rb.

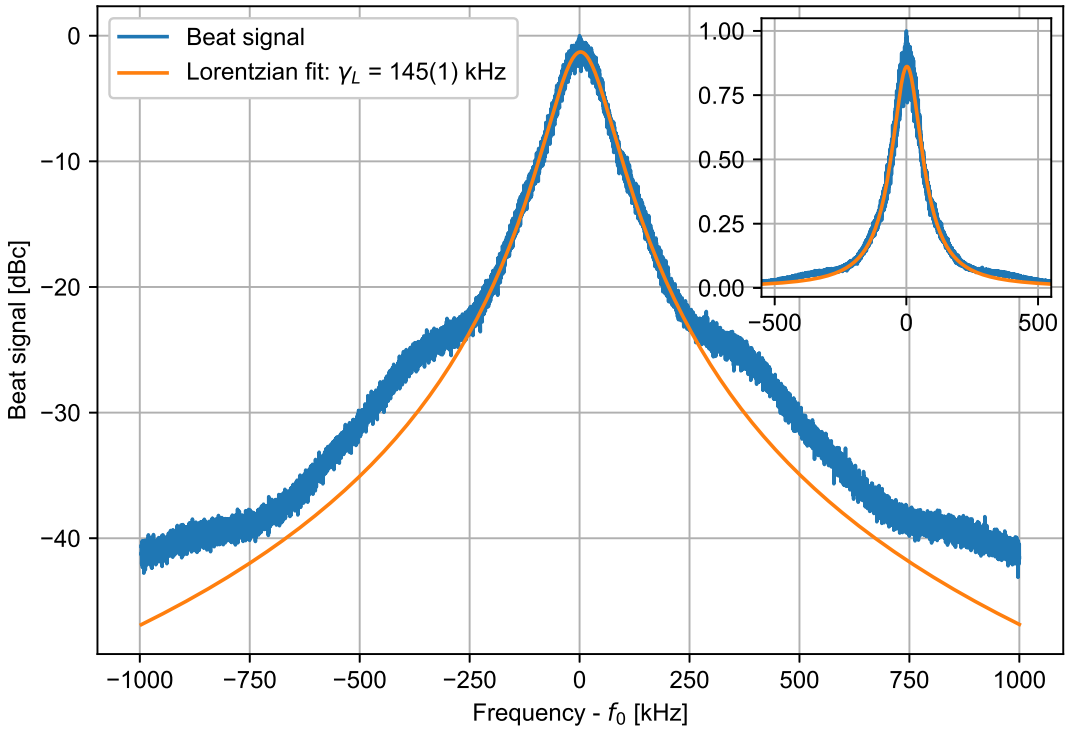

Fig. 4.12.: Beat-note spectrum of a frequency-offset lock using a frequency-to-voltage converter. The spectrum is normalised to the maximum amplitude. The frequency scale is shifted by the center beat frequency f_0. A Lorentzian function with FWHM γ_L is fitted to the data in the frequency range $-200\,\mathrm{kHz}$ to $200\,\mathrm{kHz}$ (orange). The inset shows a detail with a linear scale.

4.3.3. Phase-frequency detector

Phase-frequency detectors (PFD) are commonly used in electronic circuits such as phase-locked loops to lock a noisy oscillator to a stable frequency reference. In this work, a PFD module is developed that is designed to be used for laser frequency-offset locks. [135] Figure 4.10 (b) shows a simplified block diagram of the 19”-rack mount unit. The PFD (Analog Devices HMC439) compares the beat signal to a reference signal featuring a wide input frequency range of $10\,\mathrm{MHz}$ to $1.3\,\mathrm{GHz}$. The reference signal is provided by a custom DDS board based on a fast DDS chip (Analog Devices AD9910) and a microcontroller (Arduino Mega) that is programmed and triggered by the experimental control system. The DDS offers a maximum reference frequency of $350\,\mathrm{MHz}$ and allows for rapid frequency changes. If a larger reference frequency is required, a suitable synthesiser (e.g. Siglent SSG3021X) can be used instead. The output signal of the PFD is proportional to the phase difference between the two input signals. For a non-zero frequency deviation between the two input signals, the PFD will accumulate the phase difference modulo π at a rate of the frequency difference. The sign of this periodic signal gives the sign of the frequency deviation. In order to suppress intrinsic high frequency noise of the PFD, the output signal of the PFD module is low-pass filtered with a cut-off frequency of $4\,\mathrm{MHz}$. This filter also suppresses the periodic signal for large frequency differences, such that the the error signal produced by the PFD module when scanning the laser rapidly has the approximate shape of a step function as depicted in Fig. 4.10 (b). Using the digital controllers and the locking scheme described in Sec. 3.4, this error signal allows for locking the phase of the beat note to the reference oscillator. Thus, noise and accuracy of the laser offset-frequency are determined by the frequency reference up to remaining phase noise that is not compensated by the control loop. A typical beat-note spectrum between a phase-locked ECDL system and its reference laser system is depicted in Fig. 4.13. This spectrum is recorded using a spectrum analyser (Tektronix RSA306) set to a resolution bandwidth of $16\,\mathrm{Hz}$. Most of the signal power is accumulated in a sharp peak at the reference frequency (carrier). The width of the carrier is not resolved by the spectrum analyser. The depicted spectrum is normalised to the carrier power. For low phase-noise levels, the phase noise of the beat note is characterised by the PSD at a given offset frequency from the carrier under the assumption that intensity noise is negligible. [136, Sec. 3.4.3] Normalising the spectrum for positive offset frequencies to the resolution bandwidth of the measurement yields the standard phase-noise measure for HF oscillators $\mathcal{L}(f)$. [137] The phase-noise spectrum is mainly determined by the passive linewidth of the laser and the achieved control bandwidth. The control bandwidth is indicated by a broad gain-bandwidth peaking. The depicted spectrum allows us to determine the rms phase noise by [137]

$$\sqrt{\langle \Phi^2 \rangle} = \sqrt{2 \int_0^\infty \mathcal{L}(f)\, dx} \approx \sqrt{2 \int_{f_{min}}^{f_{max}} \mathcal{L}(f)\, dx} \tag{4.8}$$

where f_{min} represents the minimal offset frequency allowing for distinguishing between $\mathcal{L}(f)$ and the carrier. The upper bound f_{max} is chosen such that the frequency range contains all relevant contributions. The beat-note spectrum depicted in Fig. 4.13 yields the typical phase-noise level of approximately $300\,\mathrm{mrad}$ achievable with the locking technique described here. In this case, the laser linewidth is entirely determined by the linewidth of the reference laser system. Additional phase fluctuations at high frequencies can be neglected for most applications. The non-linear error signal limits the transient times for frequency steps to $100\,\mu\mathrm{s}$.

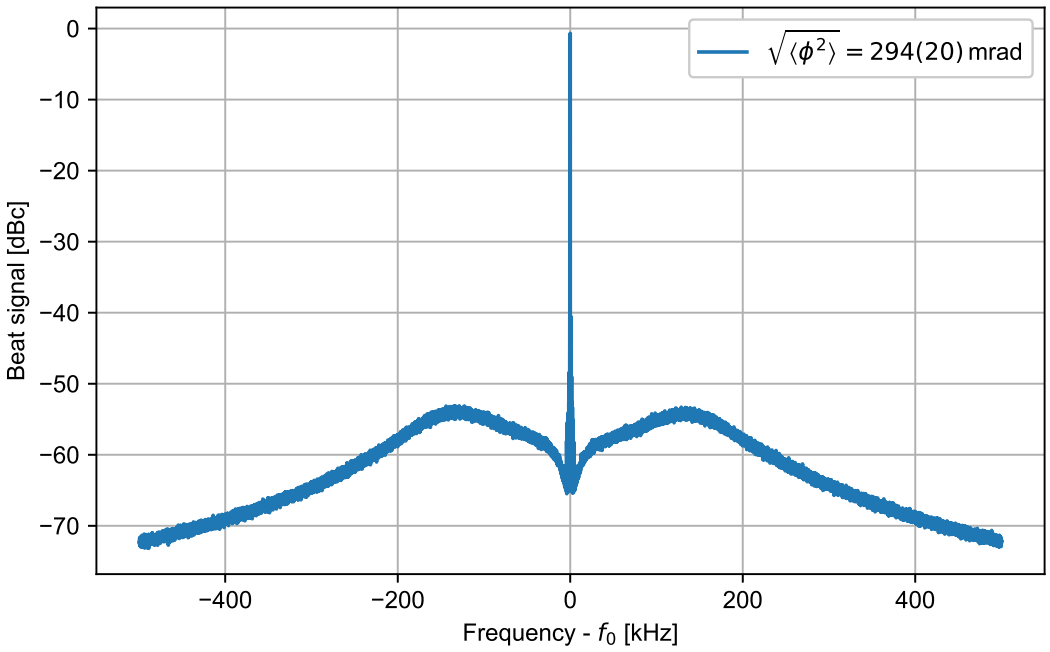

Fig. 4.13.: Typical beat-note spectrum between a phase-locked ECDL system and its reference laser system. The resolution bandwidth of this measurement is 16 Hz. The rms phase noise $\sqrt{\langle \Phi^2 \rangle}$ stated in the legend is calculated from the measured spectrum.

4.4. A low-noise phase lock for two-photon Raman coupling

The standard qubit in ^{85}Rb is the long-lived hyperfine qubit $|0\rangle := |5S_{1/2}, F = 2\rangle$ and $|1\rangle := |5S_{1/2}, F = 3\rangle$ with a precisely known transition frequency of $\Delta_{HFS} \approx 3.035\,\text{GHz}$. [35, 138] Coherent coupling of the qubit states is realised in a two-photon process similar to the Rydberg excitation schemes described in Sec. 2.3.2. Replacing the ladder scheme by a lambda scheme, a pair of Raman lasers detuned by Δ_{HFS} is employed. [139] Either the $|5P_{1/2}\rangle$ or $|5P_{3/2}\rangle$ state is used as an intermediate state by choosing laser frequencies off-resonant from the respective transition. In this configuration, an effective coupling of $|0\rangle$ and $|1\rangle$ according to Eq. 2.37 is achieved. As compared to direct coupling with a microwave field, the laser fields offer single-site resolution. The spectral properties relevant for decoherence effects are determined by the phase-noise spectral density of the difference frequency conveniently characterised by the beat note of the laser systems. [102] The required noise level is achieved by an optical phase-locked loop (OPLL). [101, 102] In this section, an optimised phase-lock scheme is presented that relies on a phase-frequency detector module developed in this work and utilises the fast current modulation technique presented in Sec. 3.5. Parts of the results presented here have been published in [103].

The OPLL is realised with a test system consisting of two 780 nm ECDL systems. The frequency of the reference laser (ADL-78901TX laser diode) is not stabilised. The phase lock is applied to the ECDL system employed for tests of the fast current modulation input (Sec. 3.5). The beat note between the Raman lasers is detected by a fast photodetector similar to the detector presented in Sec. 4.3.1. At large beat frequencies, the fiber coupled photodiode is

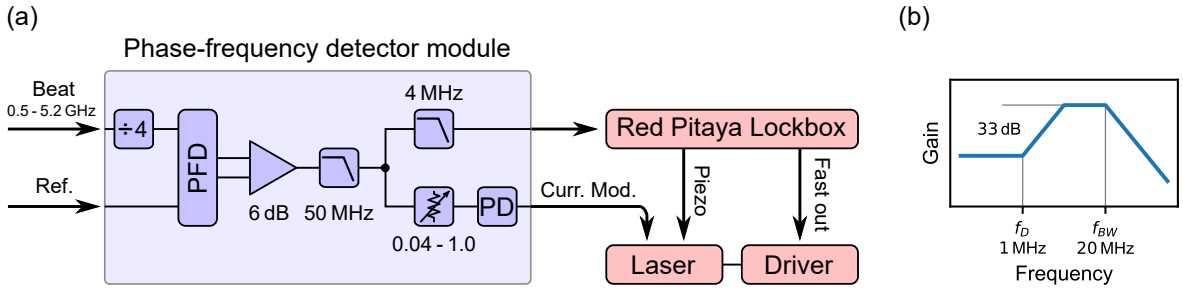

Fig. 4.14.: (a) Block diagram of the phase-frequency detector (PFD) module developed in this work (blue). The module is employed in a phase-lock scheme (red) utilising the digital controller (*Red Pitaya Lockbox*) presented in Sec. 3.4. (b) Schematic transfer function of the fast proportional-derivative (PD) controller integrated in the PFD module. The PD corner frequency f_D is set to $1\,\mathrm{MHz}$. The derivative gain is limited to $33\,\mathrm{dB}$.

replaced by a fast metal-semiconductor-metal photodetector (Hamamatsu G4176-03) offering a larger bandwidth due to its lower capacitance. The detected signal is amplified to a signal level between $-10\,\mathrm{dBm}$ and $10\,\mathrm{dBm}$ by two HF amplifiers (Mini Circuits ZX60-3018). Figure 4.14 (a) shows a block diagram of the phase-frequency detector (PFD) module developed in this work (blue) based on a digital PFD chip (Analog Devices HMC439). The beat frequency is divided by four in order to match the input frequency range of the PFD. The PFD compares the divided signal to a reference signal generated by a synthesiser. A suitable error signal is generated by an analog output stage including a $50\,\mathrm{MHz}$ low-pass filter. The error signal is filtered by an active second-order low-pass filter at $4\,\mathrm{MHz}$. The filtered signal is a buffered output. In a second signal path, a fast analog proportional-derivative (PD) controller is realised. The gain of the PD controller is set by an adjustable input attenuator. Detailed schematics and production files are available in [135]. Note, that the circuit is used for frequency-offset locks (Sec. 4.3) without the divider and the fast PD controller.

Contribution	**Estimation method**	**Estimated delay**
Free space beam paths	Length $1\,\mathrm{m}$, $v_{prop} = c$	$3\,\mathrm{ns}$
Coaxial cables	Length $1\,\mathrm{m}$, $v_{prop} = c/1.5$	$5\,\mathrm{ns}$
Optical fiber	Length $1.6\,\mathrm{m}$, $v_{prop} = c/1.45$	$7\,\mathrm{ns}$
Modulation input	Phase lag $\pi/2$ at $25\,\mathrm{MHz}$	$10\,\mathrm{ns}$
Phase detector	Separate measurement	$30\,\mathrm{ns}$

Tab. 4.2.: Record of contributions to the total delay of approximately $55\,\mathrm{ns}$ in the feedback path of the fast PD controller discussed in this section. The speed of propagation in the respective medium assumed for calculation of the delay is denoted with v_{prop}.

Figure 4.14 (a) includes a schematic overview of the locking scheme employed here (red). The error signal output of the PFD module is connected to the digital laser-frequency controller presented in Sec. 3.4. The fast output of the controller acts on the modulation input of the laser-current driver applying an suitable attenuation (typ. $20\,\mathrm{dB}$) such that quantisation noise of the digital output is negligible. An integral (I) controller in this feedback path realises a frequency lock, i.e. any frequency fluctuations of the beat note relative to the synthesiser resolved by the PFD are compensated. A drift compensation applied to the laser piezo prevents the I controller from overflow as detailed in Sec. 3.4. In a second feedback path, the PD

controller of the PFD module is applied to the fast current modulation input of the laser. This feedback path defines the performance of the OPLL. The requirement of the derivative term originates from the fact that the controller acts on the laser frequency while phase fluctuations are detected. Hence, the error signal has an integrating effect that is compensated by the derivative controller. For optimal performance, a large bandwidth is required. In the test setup, the delay in the feedback path without controller is estimated to 55 ns. A detailed record of the individual contributions can be found in Tab. 4.2.

A schematic transfer function of the PD controller is depicted in Fig. 4.14 (b). An optimal corner frequency of $f_D = 1$ MHz is found empirically. As detailed in Sec. 3.5, the optimal corner frequency may depend on the laser diode type (Thorlabs L785H1) due to its complex frequency response. In order to guarantee stability, the derivative gain is limited. Due to the integrating behaviour of the PFD signal, a large derivative gain (33 dB) is required. The cut-off frequency $f_{bw} \approx 20$ MHz is defined by the bandwidth of the high-speed operational amplifier (Analog Devices LTC6228) used for implementing the controller.

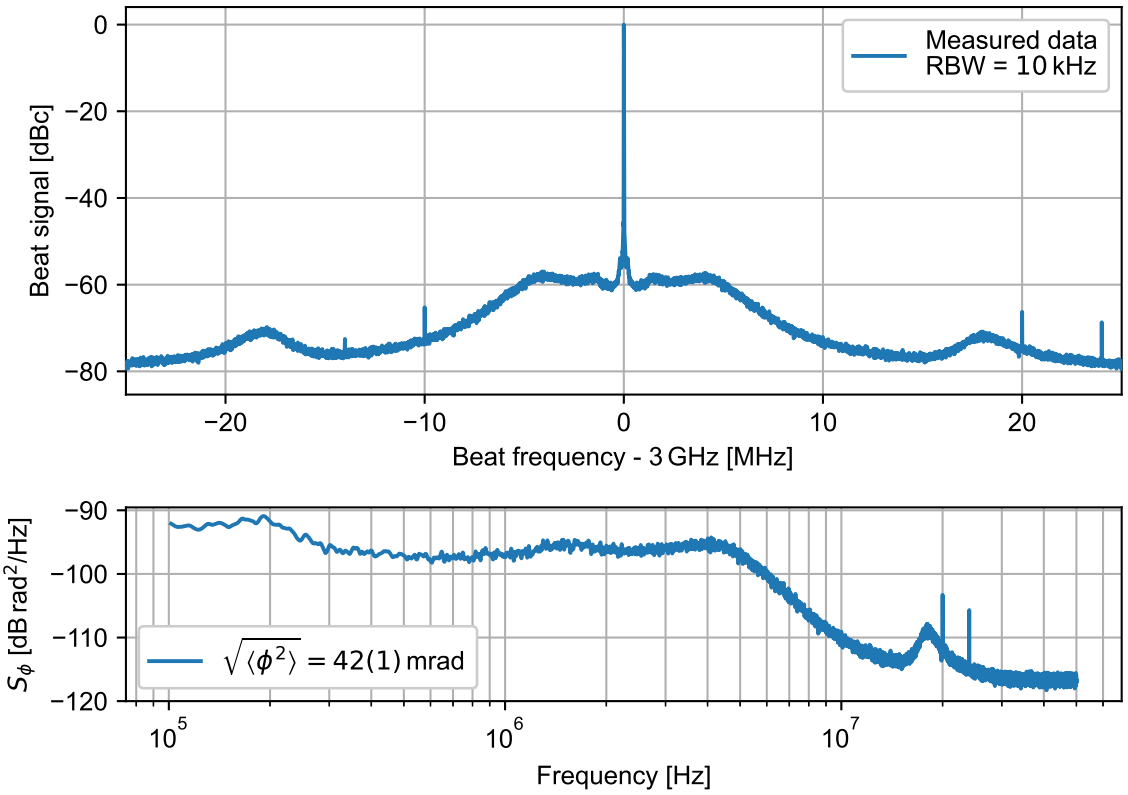

Fig. 4.15.: (top) Beat-note spectrum of the optimised OPLL discussed in this section. (bottom) Phase-noise spectral density S_ϕ calculated from the data depicted above. The rms phase noise $\sqrt{\langle \Phi^2 \rangle}$ stated in the legend is calculated from the depicted data set.

Figure 4.15 (top) shows the beat spectrum of the OPLL as recorded with a spectrum analyser (Tektronix RSA306) with a resolution bandwidth (RBW) of 10 kHz. The beat is centred at 3 GHz. The power of the beat signal is accumulated in a central feature at the beat frequency. The plateaus of the power spectral density at offset frequencies up to ± 4 MHz with a well-

defined roll-off indicate a flat, wideband response of the controller. A separate measurement shows that the gain bandwidth peak indicating the bandwidth of the feedback loop is located at $4.5\,$MHz. This result is in a good agreement with the estimated delay of $55\,$ns suggesting that the delay induced by the PD controller is negligible. Figure 4.15 (bottom) shows the phase-noise spectral density calculated from the measured data depicted above. The phase-noise spectral density is given by $S_\phi = 2\mathcal{L}$ where $\mathcal{L}$ is the single sided spectrum normalised to the RBW. A rms phase noise $\sqrt{\langle\Phi^2\rangle} = 42(2)\,$mrad is determined according to Eq. 4.8. The uncertainty is attributed to the identification of the carrier. The contributions of the broad peaks at $\sim$18 MHz originating from the control loop are negligible. Even though substantially lower S_ϕ at frequencies $\ll 1\,$MHz have been reported [102], an unprecedented rms phase noise is achieved due to the high bandwidth of the feedback loop. Note, that S_ϕ for offset frequencies below $100\,$kHz is not resolved by the spectrum analyser due its internal phase noise.

4.5. Intensity stabilisation and control

The targeted quantum information experiments require precise simultaneous real-time control of all light fields involved. The intensities of light fields generated by the laser systems discussed in this chapter are subject to thermal drifts and acoustic noise, e.g. due to a change in the fiber coupling efficiency or small polarisation rotations. The laser powers used in the experiment are measured using photodetectors optimised for this application (Sec. 3.7). An active intensity stabilisation employing the digital controller characterised in Sec. 3.6 compensates for intensity fluctuations. Real-time control of the laser intensities is achieved by varying the set point of the intensity stabilisation via the experimental control system. The timing resolution of applicable wave forms is determined by the control bandwidth of the feedback loop. In order to achieve a large bandwidth, an AOM is used as an actuator by controlling the RF power applied to it. In this section, the typical implementation and performance of an intensity stabilisation are discussed.

Figure 4.16 (a) shows an AOM driver module that produces a high-power RF signal. The module features fast switching and analog amplitude control of the RF power applied to the AOM. A DDS board based on the DDS chip Analog Devices AD9910 is used as a signal source. Alternatively, a board based on the chip Analog Devices AD9959 can be used if more than one channel is required. The DDS output typically exhibits a DC offset that is eliminated using a suitable DC block. Analog amplitude control is realised using a double-balanced frequency mixer (Mini Circuits ZAD-3+). The RF signal is applied to the local oscillator (LO) port of the mixer. A DC voltage provided by the digital controller is applied to the intermediate port (I) thereby controlling the output level of the mixer at the radio frequency (RF) port. The output of the mixer is amplified to the power level required by the AOM using a power amplifier with maximum output power of up to $3.5\,$W. Depending on the maximum output power of the DDS and losses induced by the mixer, a pre-amplifier is necessary in order to achieve the required gain. Placing an fast RF switch with integrated TTL driver (Mini Circuits ZYSWA-2-50DR+) at the input of the power amplifier allows for switching of the RF signal with transient times specified to $6\,$ns. This feature is used to create short light pulses in combination with the sample-and-hold feature of the controller (see Sec. 3.6 for detail) and to optimise the suppression of the RF signal when switching off light fields. The achievable transient times for the light fields are determined by the beam diameter at the position of the AOM and the speed of sound in the AOM crystal. Using a focused beam in a TeO_2-AOM with a small active aperture

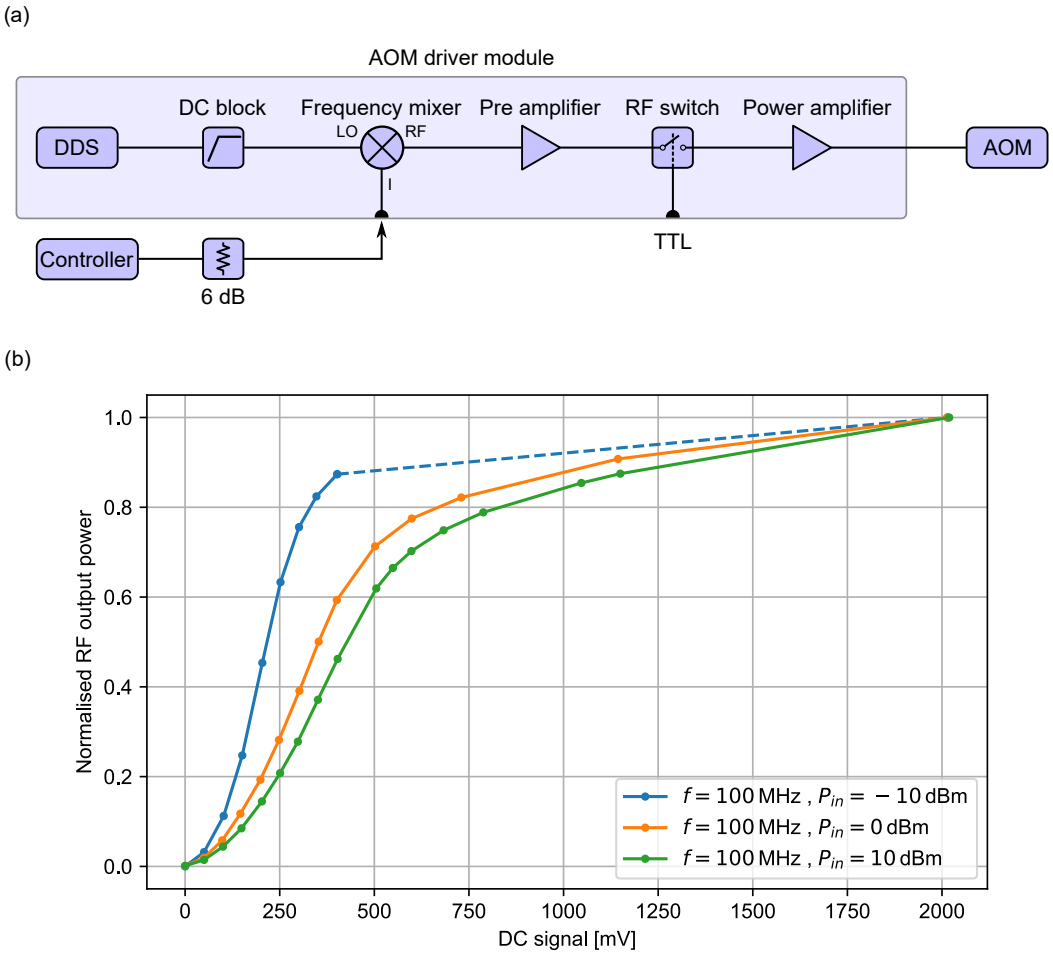

Fig. 4.16.: (a) Block diagram of an AOM driver module featuring analog amplitude control via a double-balanced frequency mixer and fast switching of the RF signal. (b) Typical amplitude control characteristics of the frequency mixer as employed in (a) (Mini Circuits ZAD-3+) for different input powers P_{in} at $f = 100\,\mathrm{MHz}$.

(e.g. Crystal Technologies 3200-121), transient times of $20\,\mathrm{ns}$ have been demonstrated using this system.

The diffraction efficiency of the AOM is proportional to the intensity of the sound wave and thus over a wide range proportional to the RF power applied to the AOM. [140, Chap. 20] Hence, the RF output power of the AOM driver module is required to depend linearly on the control voltage applied to the frequency mixer. The typical characteristics of the implemented amplitude control is depicted in Figure 4.16 (b) for different input power levels P_{in} over the entire specified input voltage range. The output power is normalised to the maximum value of each curve in order to facilitate comparison. A non-linear behaviour is observable. This behaviour can be attributed to the characteristics of the diode ring based frequency mixer. The gain of the actuator's transfer function is given by the derivative of the depicted curves at the operating point. Thus, it will decrease significantly for operating points close to the minimum or maximum output power as compared to intermediate levels. Comparing the depicted characteristics for different input powers shows that this effect increases with increasing power

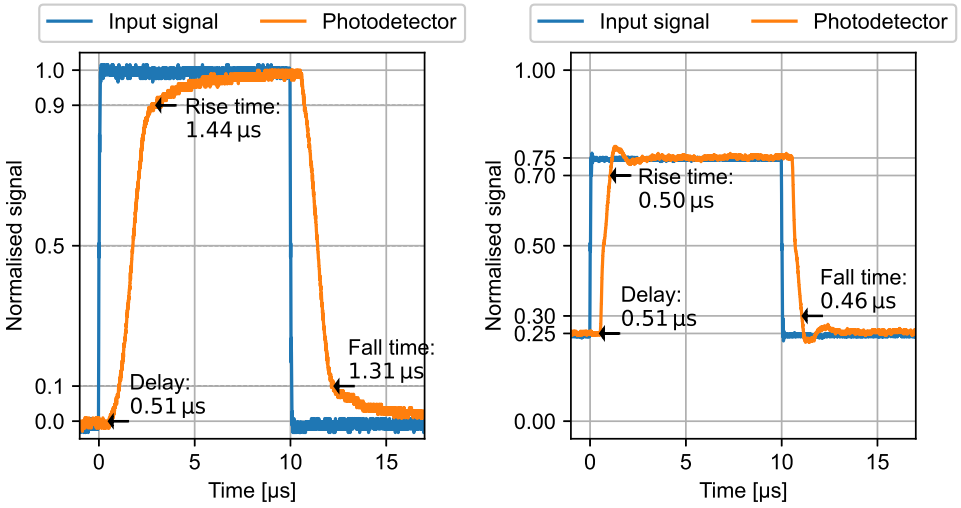

Fig. 4.17.: Typical transient performance of the implemented intensity stabilisation for an intensity change over the full range (left) and a selected intermediate range (right). With activated stabilisation, the input signal (blue) is applied to the reference input of the controller. The orange curves show the resulting intensity change. The uncertainties of the stated transient times are given by the last significant digit.

levels applied to the mixer. Hence, the frequency mixer is placed close to the signal source where the lowest RF power is applied (compare Fig. 4.16 (a)). In order to avoid oscillatory behaviour, the control parameters of the feedback loop are optimised for the maximum gain., i.e. the operating point that requires approximately $50\,\%$ of the maximum RF power. In order to reduce the effect of digital quantisation noise, the output of the controller is attenuated by $6\,\mathrm{dB}$ such that its output voltage range is restricted to the relevant input voltage range of the mixer of 0–$0.5\,\mathrm{V}$. For best performance, the output power of the signal source is tuned to reach the maximum AOM diffraction efficiency for the maximum output voltage of the controller. Figure 4.17 illustrates the typical performance of this technique as implemented for the light field “cooling 2” depicted in Fig. 4.1. A voltage pulse (blue) is applied to the reference input of the controller (see Sec. 3.6) and the resulting light pulse is recorded with an independent photodetector (orange). All data are normalised to the levels corresponding to $90\,\%$ of the maximum diffraction efficiency of the AOM (Crystal Technology 3200-121). The input signal depicted in the left plot results in a light pulse with this amplitude. As expected, the transient behaviour is degraded by the non-linearity of the AOM amplitude control in regions of high and low intensities. However, transient times below $1.5\,\mu\mathrm{s}$ are achieved which are sufficient for most applications. The pulse covering the linear region of Fig. 4.16 (b) used for optimisation of the PI parameters (right) shows enhanced transient times below $0.5\,\mu\mathrm{s}$. Both measurements show a short delay of $0.51\,\mu\mathrm{s}$ between the rising edge of the input signal and the first intensity change recorded by the photodetector. This delay is independent of the transient behaviour. It can be attributed to the delays in the control loop, such as the intrinsic delay of the digital controller, delays due to beam and signal paths, or the propagation time of the sound wave in the AOM crystal.

4.6. Conclusion and discussion

This chapter demonstrates relevant applications of the laser technologies presented in the previous chapter. All laser systems used in this chapter are based on the presented ECDL design. The MOT laser system additionally relies on the TA module.

For applications requiring light fields close to resonance with an atomic transition, such as laser cooling, a special emphasis is put on reliable laser-frequency stabilisation. The *Red Pitaya Lockbox* is employed for that purpose. The standard locking scheme used here significantly enhances the long-term stability of the system by introducing a drift compensation stage and reduces the linewidth by offering a large bandwidth and optimal gain settings. The controllers are complemented by optimised techniques for laser-frequency measurement, i.e. a highly stable spectroscopic reference and frequency-offset locks based on optical phase-locked loops (OPLL). An spectroscopic signal with an optimised signal-to-noise ratio is obtained by applying modulation transfer spectroscopy (MTS) in the regime of large modulation indices. An all-in-one MTS module is available for a straightforward and cost-efficient signal generation. The MTS signal inherently offers a large bandwidth and a high accuracy. This allows for creating a spectroscopic reference with long-term drifts and a linewidth negligible as compared to the natural linewidth of rubidium. If necessary, the long-term drifts of the reference system, mainly caused by residual amplitude modulation, can be reduced by active stabilisation of the optical power used for spectroscopy.

The application of OPLLs based on a phase-frequency detector module presented in this chapter allows for creating frequency-offset locks relative to the spectroscopic reference with negligible additional frequency noise. As compared to the earlier frequency-to-voltage scheme, the phase-frequency detectors offer a wide input frequency range of $0.01\,\mathrm{GHz}$ to $1.3\,\mathrm{GHz}$ as well as a high accuracy and stability of the offset frequency provided by the reference signal source. However, within a typical experimental sequence, frequency-offset locks are also used for dynamic frequency shifts. For this application, the transient times are limited by the non-linear response of the phase-frequency detector. These limitations are expected to be partly compensated when adding a derivative controller in the OPLL. In order to utilise the full potential of the technique, a signal source that allows for rapid frequency changes programmable by the experimental control system covering the entire input frequency range is needed. A fast direct digital synthesis (DDS) chip (e.g. Analog Devices AD9914) is an ideal candidate.

In this chapter, a OPLL of two ECDL systems with a rms phase-noise level unprecedented for diode laser systems is presented. This is achieved by a combination of techniques developed in this work. The fast proportional-derivative controller integrated in the phase-frequency detector module is the key component determining the performance of the system. The fast current source guarantees a sufficient bandwidth. The fast control loop is complemented by an integral controller with drift compensation implemented using the versatile features of the *Red Pitaya Lockbox*.

Using the *Red Pitaya IntStab* controllers in combination with the modular AOM driver unit, complex experimental sequences involving a multitude of different light fields are orchestrated. The microsecond transient times allow us to implement versatile intensity waveforms on rele-

vant experimental time scales by altering the setpoint of the intensity stabilisation accordingly. In contrast, for a conventional intensity stabilisation a significantly lower bandwidth is required since intensity fluctuations are typically dominated by long-term drifts. The response behaviour of the AOM-based control loop implemented here can be improved by using an AOM driver with a linear amplitude control input. For the present AOM driver, the linearity is expected to be improved by applying a voltage controlled current source to the frequency mixer input. A distinctive feature of the *Red Pitaya IntStab* controller is the sample-and-hold capability that can be used if intensity changes on sub-microsecond time scales are required. The digital accuracy and response time is unprecedented.

ECDL systems with a suitable current driver offer a remarkably low intensity-noise level. The intensity control loops implemented in this work are not capable of reducing the baseline noise level of the laser system. This can be achieved by using a significantly higher power levels for detection in combination with low-noise analog controllers. [141] However, this is not required for the typical application addressed here.

5. Micro-optical realisation of optical tweezer arrays

A unique feature of the experimental platform described in this work is the generation of large-scale tweezer arrays based on micro-optical elements. A microlens array (MLA) is illuminated with a Gaussian beam. The resulting focal spots are re-imaged into the experimental chamber using a high numerical aperture (NA) lens system. As compared to approaches using spatial light modulators [22, 24, 142] or acousto-optic deflectors [45–47], this approach offers an unprecedented scalability since there are MLAs with tens of thousands of lenslets commercially available. Furthermore, the simple optical setup inherently features an excellent stability and a high optical quality of the focal spots. In this chapter, advancements of tweezer arrays based on MLAs and required properties of the employed laser sources are discussed.

5.1. Large-scale tweezer arrays produced by an optimised lens system

In the current setup, the number of traps is technically limited by the maximally available laser power. The efficiency of the system can be enhanced by reducing the waist of the tweezers thereby reducing the required laser power per trap. Furthermore, a reduced waist allows for working with a smaller trap distance. This results in a smaller array for a given number of traps which is beneficial for realising strong Rydberg-Rydberg interactions and lifts constraints set by the size of the magneto-optical trap. Smaller trap waists are achieved by using an optimised high-NA lens system designed by *Lens Optics*. The custom lens system is characterised in this section.

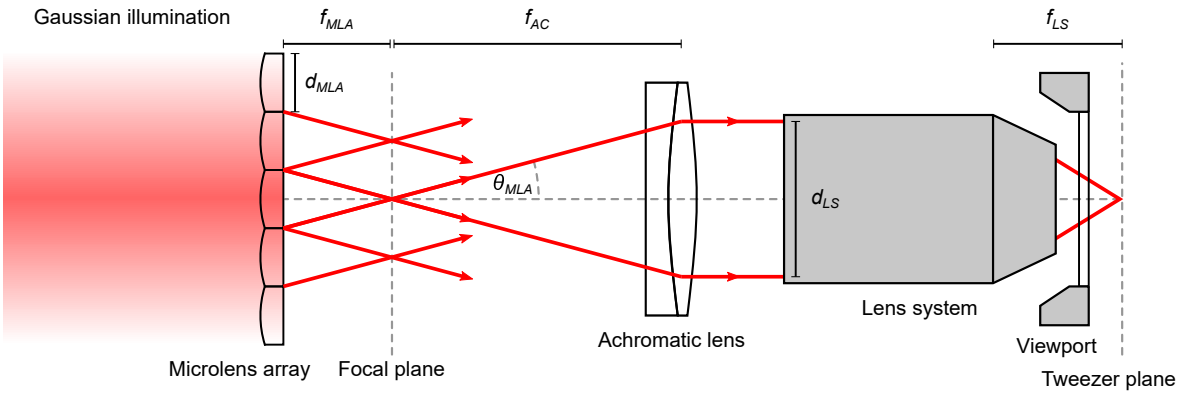

Fig. 5.1.: Simplified optical setup for generating a tweezer array based on a microlens array (MLA) using an achromatic lens (AC) and a high-NA lens system (LS).

Figure 5.1 shows a schematic view of the imaging setup employed for generating a tweezer array using an MLA. Typical MLAs consist of a regular quadratic or hexagonal pattern of

spherical lenses with a high filling factor, i.e. the distance of the lenslets matches their diameter. The MLA is illuminated with a Gaussian beam. The diameter of the lenslets is small as compared to the waist of the illuminating beam such that a nearly uniform illumination of each microlens is achieved. The MLA produces an array of focussed beams. The divergence of each beam θ_{MLA} is given by the NA of the microlenses obtained from their clear aperture d_{MLA} and focal length f_{MLA}. For simplicity, diffraction at the aperture of the microlens is neglected in the following discussion. If necessary, diffraction effects can be described as a reduction of f_{MLA} [143]. The focal shift is below $10\,\%$ for the microlenses used in this work. Typical specifications define the geometric properties MLAs. For a purely refractive lens, the divergence is determined by the radius of curvature *ROC* using lensmaker's equation for a thin lens [140, Chap. 2]

$$\theta_{MLA} \approx \tan\theta_{MLA} = \frac{(n_{MLA}-1)\,d_{MLA}}{2\,ROC} \tag{5.1}$$

where n_{MLA} is the refractive index of the MLA material at the trapping wavelength. The divergent beam is collimated with an achromatic doublet with focal length f_{AC}. The value of f_{AC} is matched to the effective aperture of the lens system d_{LS} such that the lens system generates a diffraction limited spot in the experimental chamber. This imaging system realises a re-imaging of the MLA focal plane with a demagification of f_{LS}/f_{AC}. Hence, the distance between the traps s_{trap} is determined by the demagnification of the imaging optics and the pitch of the microlenses s_{MLA}

$$s_{trap} = s_{MLA}\,\frac{f_{LS}}{f_{AC}}. \tag{5.2}$$

The lens system characterised here is specified with an effective focal length of $f_{LS} = 52.88\,\text{mm}$ and a clear aperture of $d_{LS} = 40\,\text{mm}$ (NA = 0.35)[1]. A first estimate of the minimal spot size achievable with the lens system is obtained by calculating the waist of an ideal Gaussian beam diverging with the maximum opening angle of the lens system $\tan\theta = d_{LS}/(2f_{LS})$ the corresponding beam waist is given by [41, Chap. 13.1]

$$w_{min} = \frac{\lambda}{\pi\theta} = \frac{\lambda}{\pi\,\arctan\left(\frac{d_{LS}}{2f_{LS}}\right)} \tag{5.3}$$

at a given wavelength λ. In practise, this ideal behaviour is typically not achieved due to imperfections of the lens system and the input mode. The lens system is compensated for the fused silica vacuum viewport with a thickness of $6.35\,\text{mm}$. The parameters of MLAs compatible with this lens system are defined by the intended trap distance defining the pitch of the microlenses and the NA required for diffraction limited imaging. The achromatic lens is chosen accordingly:

$$f_{AC} = \frac{d_{LS}}{2\theta_{MLA}}. \tag{5.4}$$

With Eq. 5.2 this yields an optimal trap distance

$$s_{trap} = s_{MLA}\theta_{MLA}\,\frac{2f_{LS}}{d_{LS}}. \tag{5.5}$$

However, a different trap distance can be achieved by either choosing a larger or a smaller value for f_{AC} accepting either losses at the lens system or larger trap waists. The achromatic

[1] Note, that the small-angle approximation is not valid for this NA.

lenses considered here are spherical. Spherical aberrations significantly degrade the imaging quality for focal lengths f_{AC} below $300\,\mathrm{mm}$.

5.1.1. An automatic evaluation routine for tweezer arrays

A high optical quality of the tweezer array is crucial for effective trapping of individual atoms. Typically, the focal plane of the tweezer array is inspected using a CCD camera with a suitable imaging system. For large scale arrays, an automatic evaluation routine of the camera image is required. In this work, a Python based automatic fitting routine is developed that allows for time efficient evaluation of large-scale tweezer arrays. The software is extended and maintained in a GitHub repository [144]. It is based on concepts developed in [145] and [146]. Several functionalities have been added in [147].

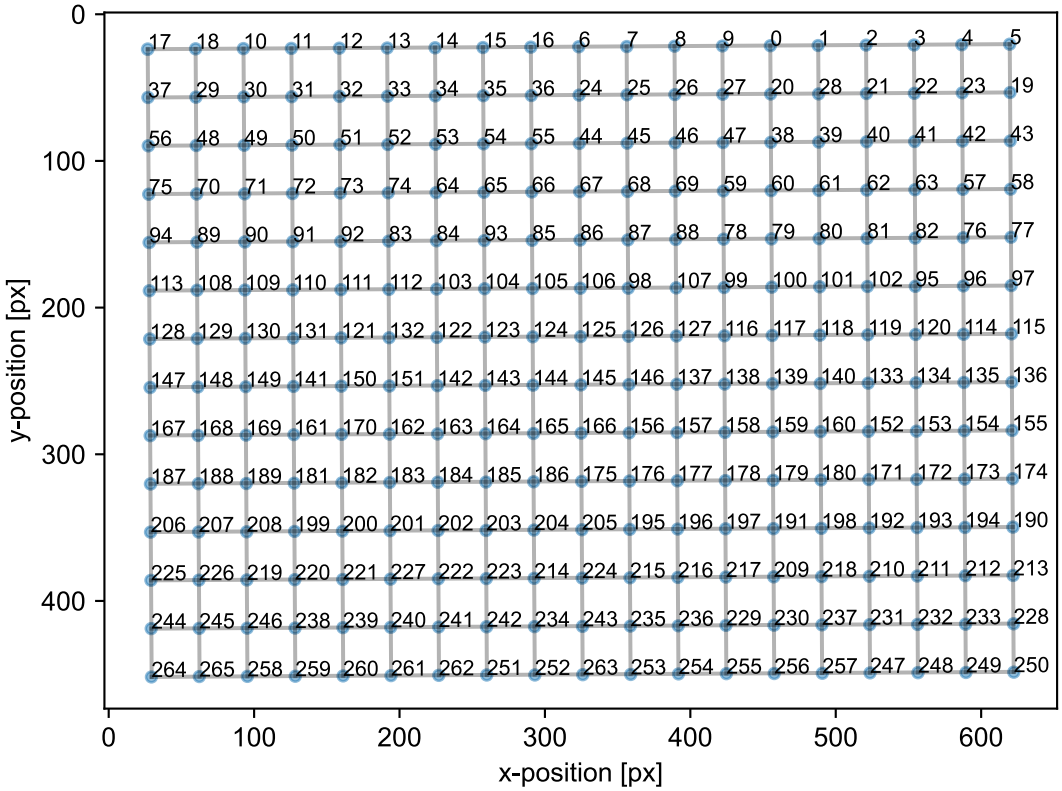

Fig. 5.2.: Output of the software used for illustration of the results of the automatic fitting routine described in this section. Position and size of the markers (blue) represent fitted positions and waists of the spots. The software assigns an unique number to each spot which is displayed in this output.

The routine allows for detecting spots based on an initial guess for global parameters such as pitch and minimum intensity of the spots. The spot detection is realised using a time efficient 2D image filter implemented with the Python function *scipy.ndimage.filters.maximum_filter*. A 2D-Gaussian intensity distribution is fitted to each detected spot. Reliable starting parameters for the fits are generated by calculating statistical moments of the data. This approach yields robust fits converging rapidly. Live evaluation of arrays with several hundreds of spots is feasible. Based on the fit data, a regular quadratic or hexagonal grid is calculated. The routine returns a

list of spot waists and positions. Figure 5.2 shows the standard output of the software used for inspection of the array. The image depicted in Fig. 5.3 is used as an input. Size and position of the blue markers represent the fitted waist and position of the detected spots. The grey grid is a regular pattern resulting from average base vectors connecting next neighbours. The numbers can be used for detailed inspection of the spots as described in the next section. They are assigned by the filter function in a non-regular fashion.

5.1.2. A large-scale quadratic tweezer array

A quadratic MLA with $s_{MLA} = 75\,\mu\text{m}$, $d_{MLA} = 72\,\mu\text{m}$, and $ROC = 0.5\,\text{mm}$ (Süss 19-00021) is used for characterisation. This MLA features chrome apertures covering the area in between the microlenses. The clear aperture of the mounted MLA with a diameter of $6\,\text{mm}$ contains approximately 5000 microlenses that are illuminated with a Gaussian beam with a waist of approximately $2.5\,\text{mm}$ produced by a fiber collimator (Thorlabs F810APC-780) at a wavelength of $\lambda = 795\,\text{nm}$. For the test setup, an achromatic doublet with a focal length of $f_{AC} = 750\,\text{mm}$ (Thorlabs AC508-750-B) that guarantees diffraction limited re-imagining is chosen. The vacuum viewport is mimicked by a laser-quality AR-coated fused silica substrate with a thickness of $6\,\text{mm}$ (Edmund Optics 36956) such that the tweezer array is accessible with a commercial microscope objective (Linos, $40\times$, NA = 0.65) that is mounted on a CCD camera (Flir DR2-BW or Flir CM3-U3-13Y3M). The magnification of the assembled imaging system is calibrated using a standard 1951 USAF resolution test target with an uncertainty of $\pm 3\,\%$.

Quantity	Experimental	Ideal	Calculation parameters
Number of traps	266		
Achromatic lens f_{AC}	$750(8)\,\text{mm}$	$612\,\text{mm}$	$ROC = 0.5\,\text{mm}, n = 1.454$
Pitch s_{trap}	$5.402(10)\,\mu\text{m}$	$5.288\,\mu\text{m}$	$f_{AC} = 750\,\text{mm}, s_{MLA} = 75\,\mu\text{m}$
Horizontal waist w_x	$0.888(7)\,\mu\text{m}$	$0.700\,\mu\text{m}$	$\lambda = 795\,\text{nm}$
Vertical waist w_y	$0.867(7)\,\mu\text{m}$	$0.700\,\mu\text{m}$	$\lambda = 795\,\text{nm}$
Side structure contrast	0.105		

Tab. 5.1.: Parameters of the tweezer array depicted in Fig. 5.3 as evaluated by the software developed in this work. For comparison, the ideal values are calculated. For all calculations, the parameters of the high-NA lens system, $f_{LS} = 52.88\,\text{mm}$ and $d_{LS} = 40\,\text{mm}$, are used.

Figure 5.3 shows an image of the central region of the tweezer array. A total number of 266 traps are observable. Relevant metrics of the tweezer array are evaluated using the software presented in Sec. 5.1.1. The results are summarised in Tab. 5.1. The quoted uncertainties are the standard deviation over the array yielding a measure for the scattering of the spot sizes and distances. For comparison, the ideal values are calculated. Choosing a slightly larger f_{AC} guarantees optimal spot sizes while maintaining a sufficient efficiency. The deviation for s_{MLA} are attributed to the uncertainties of f_{AC} and of the magnification of the re-imaging system. The optimal waists w_{min} set a lower bound for the achievable waists. In practise, waists below $0.86\,\mu\text{m}$ are not achievable which is in good agreement with detailed optical simulations of the lens system. [148] Beam waists below $1\,\mu\text{m}$ are achieved over the entire clear aperture of the MLA. The trap distance is constant within the uncertainty of the measurement. The results strongly depend on the alignment of the lens system relative to the beam and the viewport. Tilts as small as 0.2° degrade the imaging quality significantly. For the measurement

presented here, the vertical and horizontal tilt of the viewport is adjusted for best results in order to demonstrate the capabilities of the lens system. This is not possible in the experimental setup. Nevertheless, the parameters chosen for the test setup represent realistic experimental conditions. A similar performance is achieved by mounting the lens system on a precision tip/tilt/rotation stage. [147]

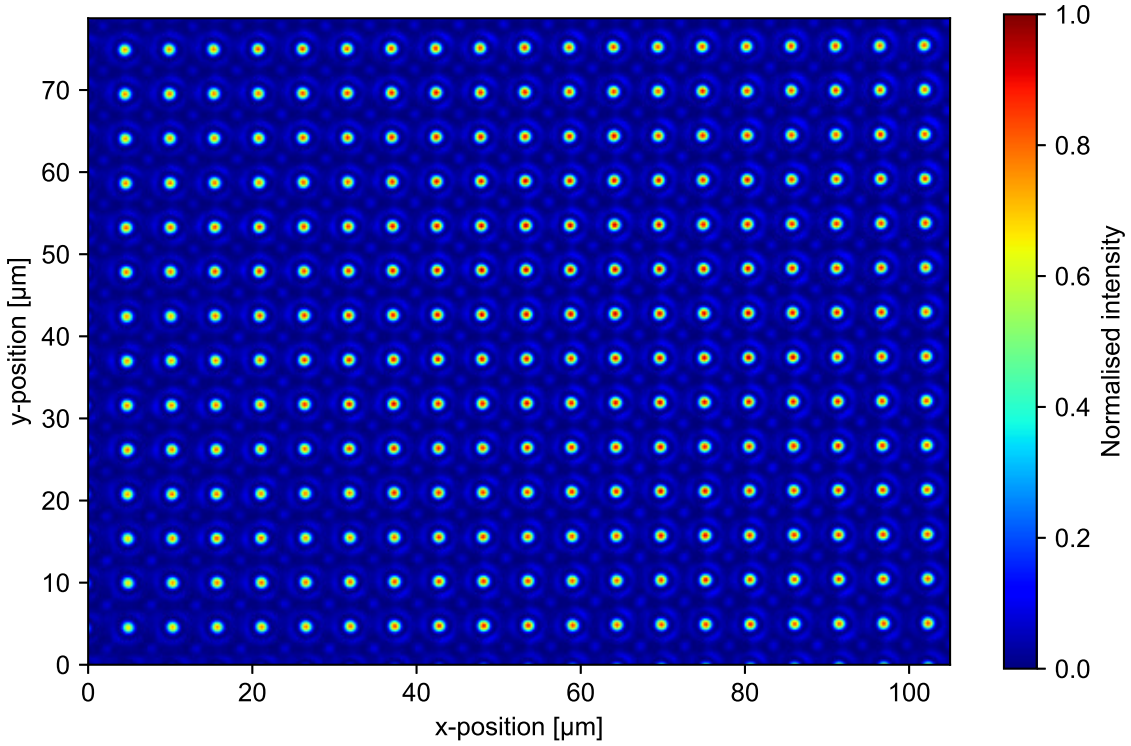

Fig. 5.3.: A tweezer array generated with the setup depicted in Fig. 5.1 using the microlens array Süss 19-00021. The y-axis points upwards (against gravity) perpendicularly to the optical table. The camera view is counter propagating to the illuminating laser beam.

A detail of the brightest (central) spot in Fig. 5.3 is shown in Fig. 5.4. A round spot with symmetric side structures is observable. These structures originate from diffraction at the aperture of the microlenses and the lens system in combination with interference effects between neighbouring spots. Neglecting the side structures a 2D-Gaussian intensity distribution

$$G_{2d}(x,y) = I_0 \exp\left(-\frac{2(x-x_0)^2}{w_x^2} - \frac{2(y-y_0)^2}{w_y^2}\right) \tag{5.6}$$

at position (x_0, y_0) with horizontal waist w_x, vertical waist w_y, and maximum intensity I_0 is fitted to the displayed data using all parameters. Cross sections through the brightest pixel in horizontal direction (bottom, left) and vertical direction (bottom, right) are displayed. The cross section of a diffraction limited focal spot is given by the radial distribution of an Airy ring [41, Sec. 10.2.5]

$$Ai(r) = I_0 \left[\frac{2J_1\left(z_0 \frac{r}{\zeta_0}\right)}{\frac{r}{\zeta_0}}\right]^2 \tag{5.7}$$

where J_1 is the first Bessel function of the first kind with its first zero $z_0 \approx 1.22\pi$. The radius of the dark Airy ring is given by the scaling factor ζ_0. Fitting $Ai(r)$ to the data points of the cross sections in Fig. 5.4 (green) shows that the focal spot is well approximated by this function. Also the radius of the dark Airy ring is in a good agreement with the theoretical description, whereas the intensity of the bright Airy ring is significantly underestimated (see inset). A 1D-Gaussian distribution is fitted to the data points (orange). For a better comparability, the $1/e^2$-radius of $Ai(r)$ is calculated numerically yielding $\sim 0.67\zeta_0$. The deviations between $Ai(r)$ and the 1D-Gaussian distributions are negligible. The resulting waists may vary slightly depending on the fitted model (2D-Gaussian, 1D-Gaussian, or Airy disk). This is considered as an additional measurement uncertainty.

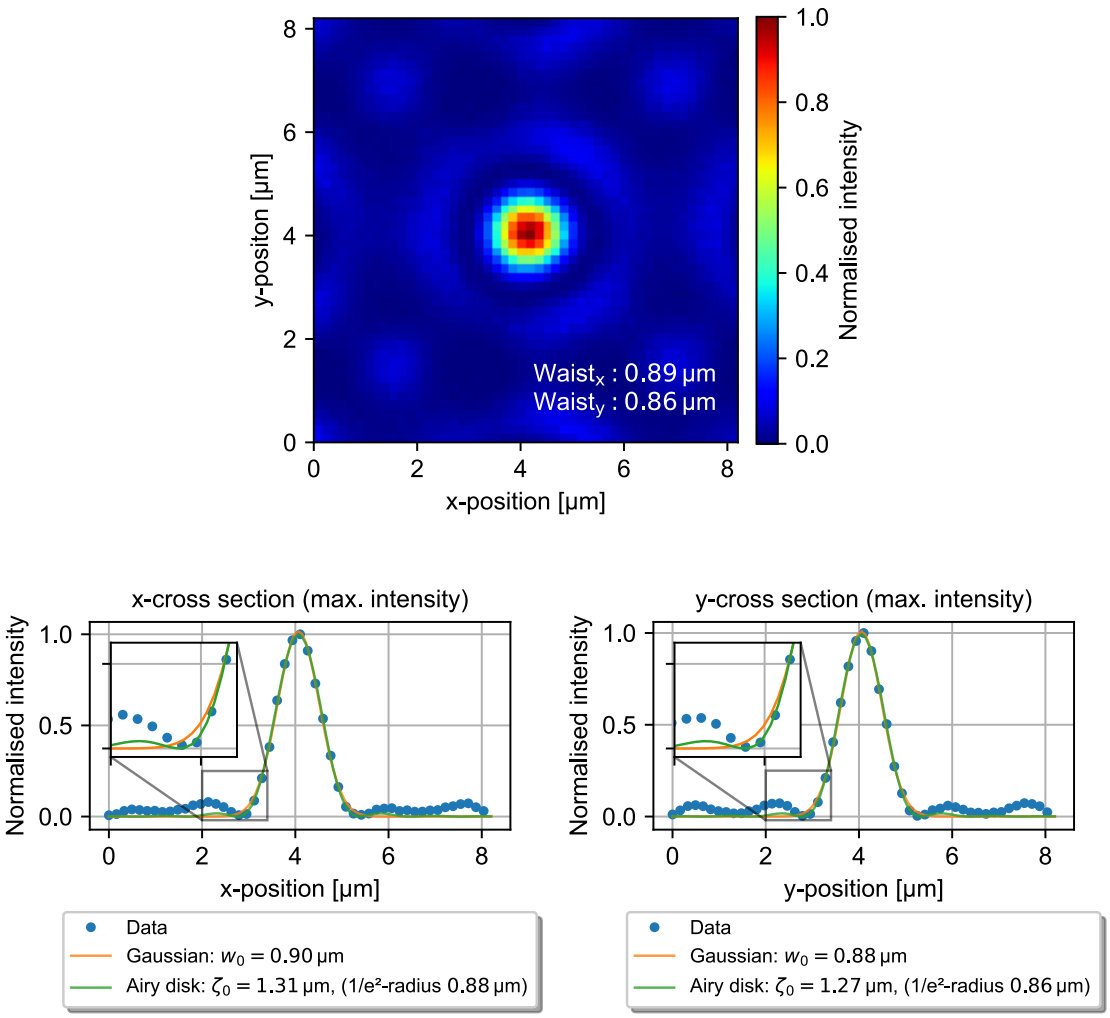

Fig. 5.4.: Detail of the brightest spot in Fig. 5.3 (top). The quoted waists are obtained by a 2D-Gaussian fit. On the bottom, cross-sections through the brightest pixel in horizontal (left) and vertical (right) direction are plotted. A 1D-Gaussian function and the cross-section of an Airy disk are fitted to the data points.

The obtained waists characterise the central region of the spot, i.e. the trapping region. Strong side structures affect the quality of the tweezer array, e.g. due to weakly trapped atoms in these structures. Hence, the maximum intensity of the side structures relative to the intensity

of the spot is used as an additional metric that allows us to characterise these structures. Based on the 2D-Gaussian fit (Fig. 5.4), the area outside the first dark Airy disk is identified. For the tweezer array depicted in Fig. 5.3, the side structure contrast is better than 0.105 for all spots.

5.1.3. Performance at 480 nm

For the experimental setup presented in this work, the main optical access via the custom lens system is also used for two-photon Rydberg excitations, as described in Sec. 2.3.2. For that purpose, the lens system is optimised for a low chromatic focus shift between the trapping wavelength and the Rydberg excitation wavelength of 480 nm and a suitable imaging quality at this wavelength.

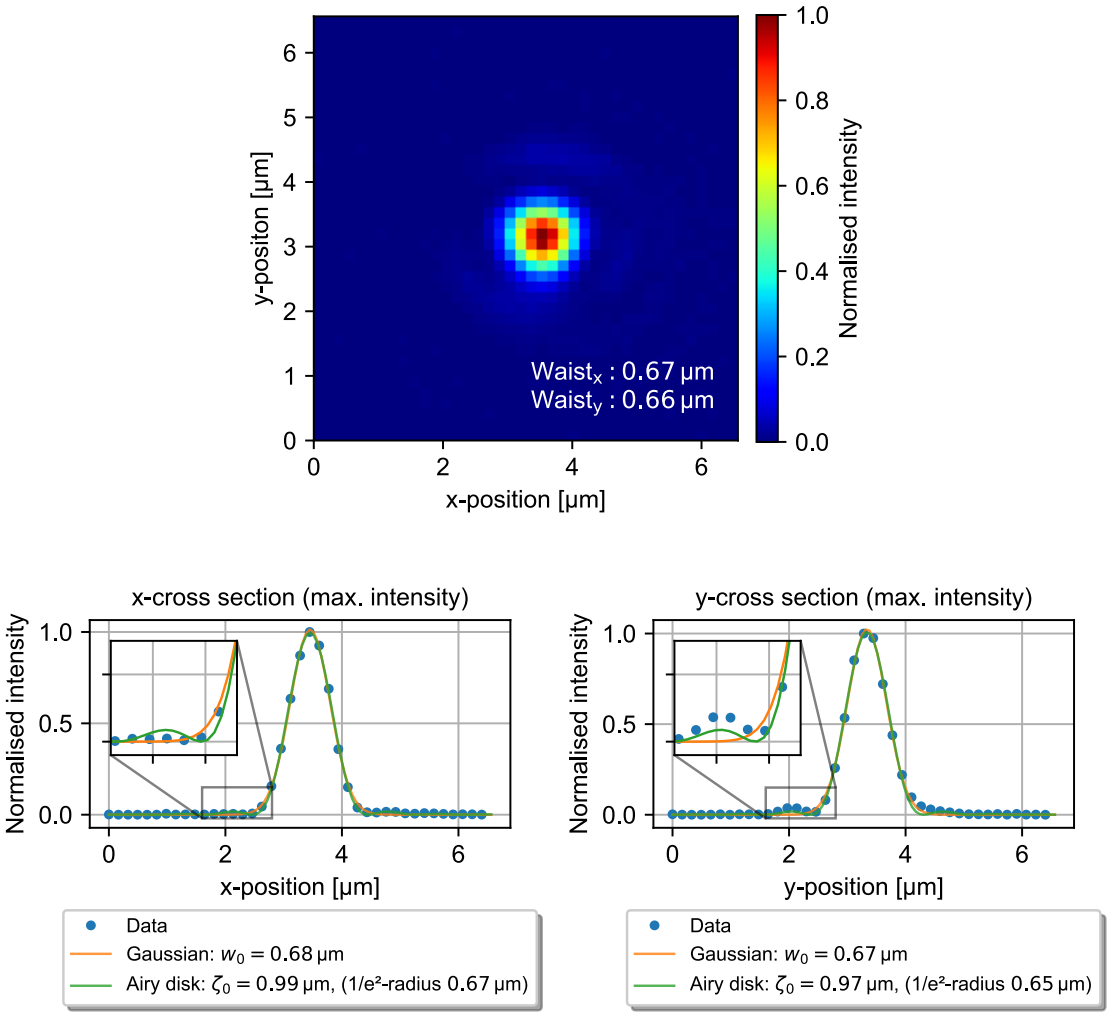

Fig. 5.5.: Detail of a single spot produced by the custom lens system at a wavelength of 480 nm (top) as discussed in this section. The quoted waists are obtained by a 2D-Gaussian fit. On the bottom, cross-sections through the brightest pixel in horizontal (left) and vertical (right) direction are plotted. A 1D-Gaussian function and the cross-section of an Airy disk are fitted to the data points.

The imaging quality at 480 nm is characterised by inspecting a single spot at this wavelength.

The spot is generated by focussing a large diameter beam produced by collimating the output of a single mode optical fiber (Thorlabs P3-488PM-FC) with a $300\,\text{mm}$ focal length achromatic lens (Thorlabs AC508-300-B). The beam diameter is larger than the aperture of the lens system. Figure 5.5 shows a round spot with an average waist $0.67\,\mu\text{m}$ which is significantly larger than the optimal waist according to Eq. 5.3 of $w_{min,480nm} = 0.42\,\mu\text{m}$.

The test setup also allows for obtaining an estimate of the focal shift between $480\,\text{nm}$ and $795\,\text{nm}$. For that purpose, the setup is adjusted for light at $480\,\text{nm}$. The fiber based beam generation allows for replacing the input fiber without notable misalignment. The shift of the lens system required for refocussing can be attributed to the chromatic shift of the lens system. This shift is measured by the precision translation stage used for mounting the lens system yielding a chromatic shift of

$$\Delta z_{chrom} = 35(5)\,\mu\text{m}. \tag{5.8}$$

It is straightforward to compensate this shift by slightly tuning the divergence of lens system input beam.

5.2. Realisation of arbitrary trap geometries by 3D direct laser writing

Realising atom patterns with exotic geometries is of great interest for state-of-the art quantum simulation experiments. [20, 149] Commercially available MLAs have been restricted to quadratic and hexagonal geometries so far. In order to extend our approach of micro-optical trap generation to almost arbitrary geometries, an additive manufacturing process is employed to produce custom MLAs on demand. This work is conducted in collaboration with S. Ristock and H. Gießen.[2] Part of the results in this section have been published in [150, 151].

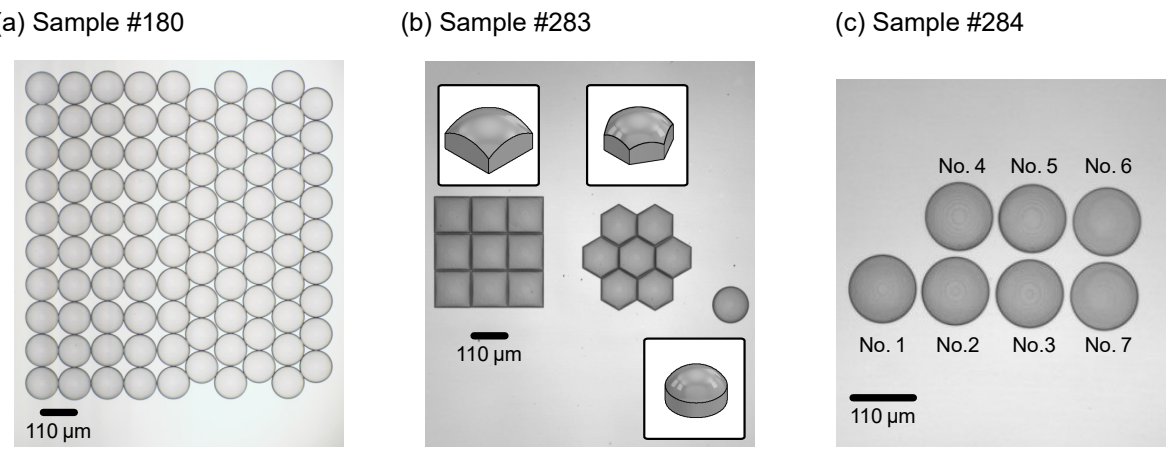

Fig. 5.6.: Overview of 3D-printed structures manufactured in this work using a two-photon polymerisation process. (a) MLA with a domain boundary between quadratic (left) and hexagonal (right) pattern. (b) Microlenses with quadratic (left), hexagonal (center), and round footprint. The insets show a schematic 3D model of each lens type (not to scale). (c) Microlenses with different design parameters (see text for details).

[2] 4th Physics Institute, University of Stuttgart, Pfaffenwaldring 57, 70569 Stuttgart, Germany

Two-photon polymerisation is an additive manufacturing process for microdevices with a wide range of applications in optics and photonics. [152, 153] The employed commercial solution *Photonic Professional GT2* (Nanoscribe GmbH) is based on a femto-second laser system focussed with a high-NA microscope objective into a photoresist (Nanoscribe IP-S). [153] Due to the non-linear two-photon polymerisation process, a sub diffraction limited resolution is achieved. Spatial control is realised by using a galvanometer scanner for steering the laser beam in combination with a precision piezo positioning system for the substrate. The microlenses are written subsequently on a fused silica substrate with a thickness of $0.7\,\mathrm{mm}$. Each lens consists of 50 to 100 layers with a thickness of $100\,\mathrm{nm}$ as defined by the spatial resolution in this dimension. After each layer, a settling time of $\sim 1\,\mathrm{s}$ is introduced in order to minimise shrinking effects. Accounting for uncertainties of the surface detection of the *Nanoscribe* system, the design contains a socket with a height of $5\,\mu\mathrm{m}$ to $10\,\mu\mathrm{m}$ under each lens. In order to achieve a reliable connection to the substrate, the initial plane of the writing process is placed purposely in the substrate such that the real height of the socket may vary with the uncertainty of the surface detection, while the lens profile is not affected. The considerations presented in Sec. 5.1 suggest an optimal parameter regime $ROC \gg d_{MLA}$, i.e. the lenses are shallow as compared to their diameter. Hence, the socket has a significant influence on the writing speed.

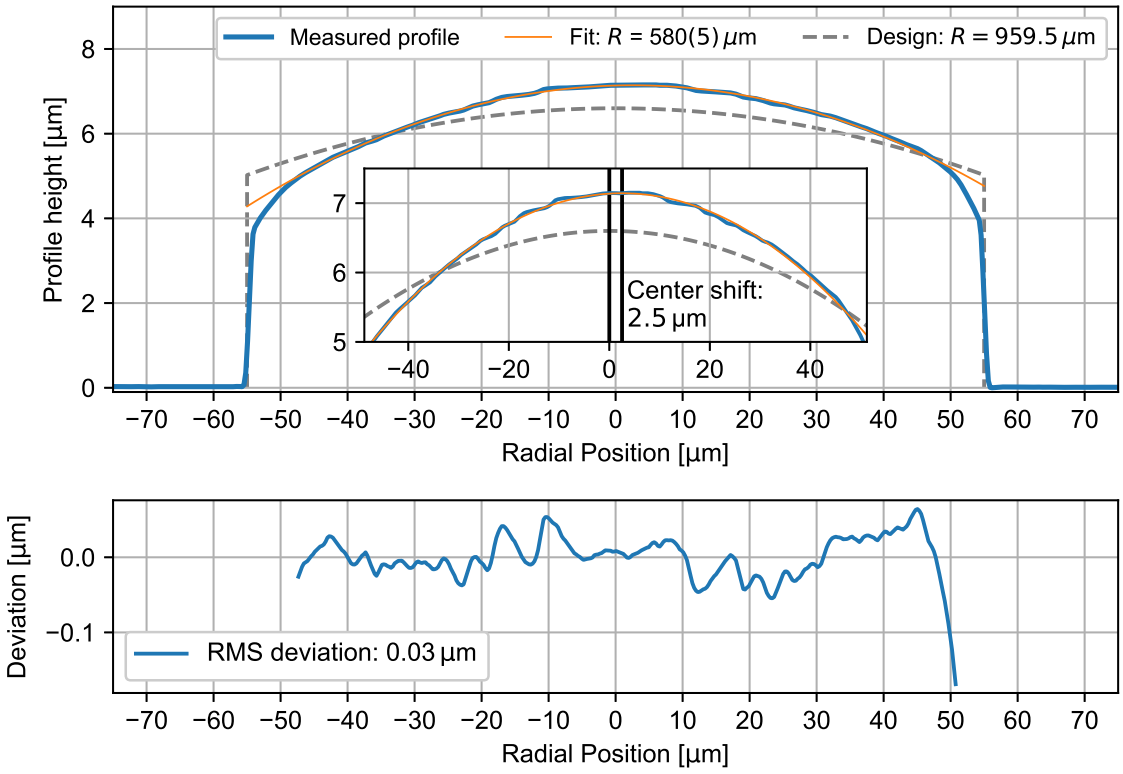

Fig. 5.7.: Cross section of a typical 3D-printed microlens of sample #180 (top). For comparison, the design parameters of the surface are plotted (grey, dashed). A circular arc with radius of curvature R (orange) is fitted to the center region of the profile. The inset shows this region and the center shift obtained by the fit. The deviations of the measured profile from the fitted arc are depicted in the bottom graph.

Figure 5.6 shows white light microscopy images of the samples manufactured in this work. Sample #180 is a MLA with a domain boundary between quadratic and hexagonal pattern consisting of 97 lenslets. This sample is also characterised in [151]. Diameter and ROC of the microlenses are chosen similarly to the quadratic MLA that has proven optimal experimental performance in our recent work (Suess 11-1401-101-111). [29] Considering the index of refraction $n = 1.505$ of the photoresist at a wavelength of 796 nm [154], $d_{MLA} = 110$ µm and $ROC = 959.5$ µm are chosen. The resulting (spherical) lens profile has a height of 1.6 µm. Thus, the required number of layers is mainly determined by the height of the socket. Typically, a writing speed of 10 lenses per hour is achieved. Optimising the socket height offers potential for a significant speed-up. Sample #283 and sample #284 are design studies used for optimising the design parameters of the microlenses in sample #180. In sample #283, lenslets with quadratic, hexagonal, and round footprint are compared. A schematic view of each lens type is depicted in the insets (not to scale). The inner diameter of each footprint is 110 µm such that a packing with an pitch identical to the pattern in sample #180 is achieved. The edges of the lenses are separated by a small spacing of ~ 1 µm in order to guarantee independent writing of each lens. Sample #284 holds single lenses with different ROCs and writing parameters as listed in Table 5.2.

The surfaces of all samples are inspected with a confocal microscope (NanoFocus μsurf expert). A typical profile of a lens in the quadratic region of sample #180 is depicted in Figure 5.7 (top). The diagonal cross section shows the socket with a spherical surface (blue). For comparison, the design parameters centred to the socket are shown (grey, dashed). The significant deviation from the design can be attributed to shrinking of the photoresist during the writing process in combination with the shallow structure. A circular arc (orange) is fitted to the inner region containing 90 % of the lens diameter (see inset). The fit yields the radius of curvature and the center of the profile. Due to asymmetric shrinking, the center of this lens is shifted slightly as compared to the design (socket position). Calculating the deviation from the fitted profile shape in the center region (bottom) shows that a spherical surface with a low rms deviation of 0.03 µm is obtained in this region. Note, that the deviations are below the spatial resolution of the 3D-printing system (0.1 µm) due to the shrinking process smoothening the surface.

Sample	**Shape**	**ROC**		**Writing parameters**
		Design	Measured	
#180	round	959.5 µm	580(2) µm	standard
#283 quadratic	quadratic	959.5 µm	652(25) µm	standard
#283 hexagonal	hexagonal	959.5 µm	585(5) µm	standard
#283 round	round	959.5 µm	522(5) µm	standard
#284 No. 1	round	959.5 µm	520(5) µm	standard
#284 No. 2	round	1334 µm	651(5) µm	standard
#284 No. 3	round	1474 µm	-	standard
#284 No. 4	round	1564 µm	730(5) µm	standard
#284 No. 5	round	1664 µm	844(5) µm	standard
#284 No. 6	round	959.5 µm	-	long settling time
#284 No. 7	round	959.5 µm	807(5) µm	long settling time, random offset

Tab. 5.2.: Design parameters and measured *ROC* of the 3D-printed microlenses developed in this work.

The *ROC* of the microlenses in sample #283 and #284 are determined applying a similar analysis of the lens profile. The results and design parameters are summarised in Tab. 5.2. Comparing the three lens types in sample #283 shows that the footprint has a significant influence on the shrinking process. The round lenses used in sample #180 are reproduced twice with identical parameters (#283 round and #284 No. 1) yielding a smaller *ROC*. This effect can be attributed to the contact of the lenses in sample #180 also resulting in a altered shrinking behaviour. The *ROCs* of lenlets No. 1 to No. 5 show that it is not possible to linearly compensate the shrinking process by choosing a larger design ROC. Even for the largest design parameter (lens No. 5), the resulting *ROC* is still significantly lower than intended. The design of lens No. 5 corresponds to a number of only 9 layers. Hence, it is not possible to realise the targeted radius of curvature in a reproducible fashion. For the manufacturing process discussed here, MLAs with a smaller pitch and a higher NA are more suitable. For the lenses No. 6 and No. 7 the settling time is increased to $10\,\mathrm{s}$. For lens No. 7, small random offsets of the piezo positioning stage are applied during the writing process. The offsets are compensated by the beam steering system such that an additional smoothening of the surface is achieved by averaging out systematic errors of the beam steering. The combination of increased settling time and random offset reduces the shrinking effect significantly (compare lens No. 1). However, the large settling time reduces the writing speed to approximately 4 lenses per hour.

The imaging quality of the microlenses is analysed using our high-NA lens system in combination with a $f_{AC} = 750\,\mathrm{mm}$ achromatic lens as described in Sec. 5.1. The resulting focal spots are depicted in Fig. 5.8 for sample #180 (a) and the quadratic part (b) as well as the hexagonal part (c) of sample #283. In Fig. 5.8 (a), structures in between the focal spots at an intensity level of up to $25\,\%$ of the maximum intensities are observable for sample #180. In general, the intensity of the parasitic structures is higher in the quadratic part. These structures originate from light passing through the spaces between the microlenses. The effect is strongly suppressed by using a digital mirror device (DMD) as a spatial light modulator for controlled illumination of the microlenses as demonstrated for this array in [151]. For detailed metrics, the spots depicted in Fig. 5.8 are evaluated using the software discussed in Sec. 5.1.1. The results are summarised in Tab. 5.3. Accounting for measurement uncertainties, the values for the pitch are in a good agreement with the calculated values. When compared to the tweezer array produced by the commercial MLA used in Sec. 5.1, the imaging quality of the 3D-printed lenses is slightly lower as the waists are larger and more asymmetric. Also, the variations of waists and pitches are larger. However, the imaging quality presented here is suitable for atom trapping. This substantial improvement as compared to our previous work without selective illumination [146] is attributed to the improved optical setup, especially the high-NA lens system. The remaining side structures observed with sample #180 are not desirable. As an alternative to selective illumination, the light fields generated with the small quadratic and hexagonal arrays (sample #283) presented in Fig. 5.8 (b) and Fig. 5.8 (c) respectively show that it is possible to reduce the contribution of side structures generated by the spacing of the lenses to a negligible level by eliminating the spaces using lenses with a suitable footprint (compare Fig. 5.6 (b)). The side structure contrast of the depicted light fields is determined by the imaging quality of the spots and not by the spaces between the lenslets.

The imaging quality of the single lenses in sample #284 are also analysed using the $f_{AC} = 750\,\mathrm{mm}$ achromatic lens with the high-NA lens system. Since the optimal *ROC* for this combination according to Eq. 5.1 is $1040\,\mu\mathrm{m}$, the NA of all lenses is significantly larger than the optimal NA. Thus, all samples produce a similar beam waist below $0.95\,\mu\mathrm{m}$ limited by the

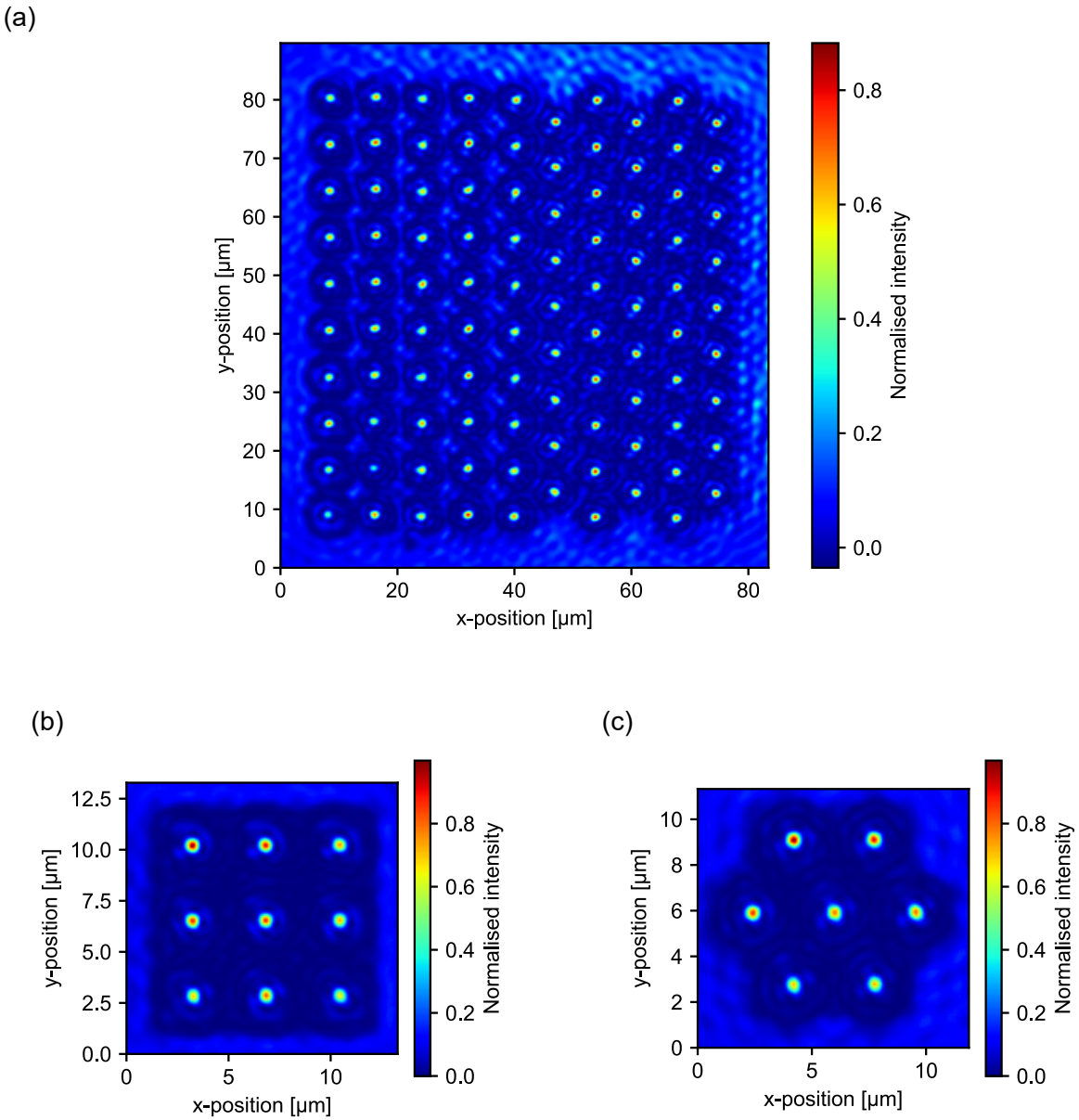

Fig. 5.8.: Tweezer arrays generated with the custom MLAs developed in this work as depicted in Fig. 5.6. (a) MLA #180 with a domain boundary between quadratic and hexagonal structures. (b) Using lenses with an optimised quadratic footprint (#283 left) eliminates side structures. In (c), microlenses with a hexagonal footprint (#283 center) are used.

imaging system and the beam quality, independent of the *ROC*, while the maximum intensity varies with the realised *ROC*. The focal shift between different microlenses is estimated by the shift of the high-NA lens system required for refocussing. The observed shifts as indicated by the precision translation stage of the lens system are in a good agreement with the measured *ROC*.

Quantity	Experimental	Optimal	Calculation parameters
Sample #180 quadratic			
Number of traps	50		
Achromatic lens f_{AC}	$750(8)$ mm	418 mm	$ROC = 0.58$ mm, $n = 1.505$
Pitch s_{trap}	$7.924(95)$ µm	7.76 µm	$f_{AC} = 750$ mm, $s_{MLA} = 110$ µm
Horizontal waist w_x	$1.006(67)$ µm	0.700 µm	$\lambda = 795$ nm
Vertical waist w_y	$0.885(67)$ µm	0.700 µm	$\lambda = 795$ nm
Side structure contrast	0.23		
Sample #180 hexagonal			
Number of traps	47		
Achromatic lens f_{AC}	$750(8)$ mm	418 mm	$ROC = 0.58$ mm, $n = 1.505$
Pitch s_{trap}	$7.928(187)$ µm	7.76 µm	$f_{AC} = 750$ mm, $s_{MLA} = 110$ µm
Horizontal waist w_x	$0.921(47)$ µm	0.700 µm	$\lambda = 795$ nm
Vertical waist w_y	$0.857(46)$ µm	0.700 µm	$\lambda = 795$ nm
Side structure contrast	0.25		
Sample #283 quadratic			
Number of traps	9		
Achromatic lens f_{AC}	$750(8)$ mm	468 mm	$ROC = 0.65$ mm, $n = 1.505$
Pitch s_{trap}	$7.612(95)$ µm	7.76 µm	$f_{AC} = 750$ mm, $s_{MLA} = 110$ µm
Horizontal waist w_x	$0.912(11)$ µm	0.700 µm	$\lambda = 795$ nm
Vertical waist w_y	$0.955(11)$ µm	0.700 µm	$\lambda = 795$ nm
Side structure contrast	0.11		Central spot only
Sample #283 hexagonal			
Number of traps	7		
Achromatic lens f_{AC}	$750(8)$ mm	428 mm	$ROC = 0.59$ mm, $n = 1.505$
Pitch s_{trap}	$7.538(84)$ µm	7.76 µm	$f_{AC} = 750$ mm, $s_{MLA} = 110$ µm
Horizontal waist w_x	$0.886(20)$ µm	0.700 µm	$\lambda = 795$ nm
Vertical waist w_y	$0.952(20)$ µm	0.700 µm	$\lambda = 795$ nm
Side structure contrast	0.10		Central spot only

Tab. 5.3.: Parameters of the tweezer arrays depicted in Fig. 5.8 as evaluated by the software developed in this work. For comparison, the ideal values are calculated. For all calculations, the parameters of the high-NA lens system, $f_{LF} = 52.88$ mm and $d_{LF} = 40$ mm, are used.

5.3. Laser sources for optical dipole traps

Micro-optical dipole trap generation offers an unprecedented scalability. For optical tweezer arrays employing this approach, the maximum number of traps available is typically limited by the laser power of the trapping laser. It is common practise to use titanium-sapphire lasers as trapping lasers [24, 28] since they offer excellent tuneability, spectral properties and beam profiles. Nevertheless, their large laser cavity with various tuning elements involves a high complexity and regular readjustment. Additionally, they are resource intensive. Hence, trap generation based on the tapered amplifier (TA) modules presented in Sec. 3.3.2 is explored in this work. This solution is more cost efficient and involves a significantly simpler optical and electronic setup.

Figure 5.9 shows a simplified optical setup of the master-oscillator power-amplifier (MOPA) system employed for generating trapping light. The system consists of a separate seed laser

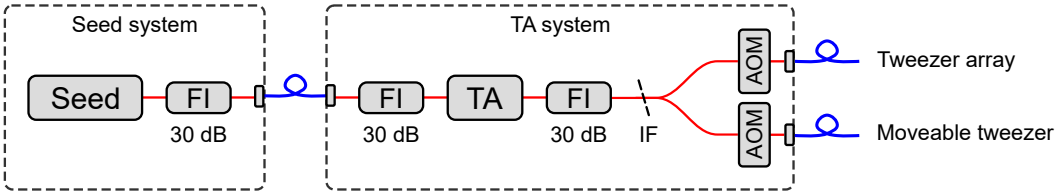

Fig. 5.9.: Simplified optical setup of the MOPA system used for generating trapping light at 795 nm to 800 nm. FI: Faraday isolator, TA: Tapered amplifier, IF: interference filter.

Specification	**Value**	**Conditions**
Wavelength	796.5 nm	785 nm to 803 nm
Maximum output power	2.6 W	$I = 4.5$ A, $P_{seed} = 23$ mW
Typical seed power	20 mW	20 mW to 60 mW
TA mount temperature	18.5 °C	
Nominal beam waist	1.45 mm	$f_{AL} = 3.1$ mm, $\theta_y = 25°$
Astigmatism θ'_x	35(3) mrad	$I = 4$ A
Cylindrical lens f_{CL}	40 mm	
Typical fiber coupling	49 %	$I = 4$ A , $f_{coup} = 7.5$ mm
Typical fiber coupling with AOM	58 %	$I = 4$ A , $f_{coup} = 7.5$ mm
Typical AOM efficiency	78 %	
Maximum fiber output	0.86 W	$I = 4.5$ A, with AOM, including all losses

Tab. 5.4.: Specifications of the MOPA system optimised for generating dipole traps. TA chip: DILAS TA-0795-3000-CM, serial number 39584. I: operating current. P_{seed}: seed power. f_{coup}: Focal length of the lens used for fiber coupling. f_{AL}: Focal length of the output-collimation lens. θ_y: output divergence in y-dimension. θ'_x: Residual divergence in x-dimension. (compare Fig. 3.4)

system and a TA system connected by a single-mode polarisation-maintaining (PM) fiber (Thorlabs P3-780PM-FC). One of our external-cavity diode laser systems (ECDL) equipped with a JDSU SDL-5431-G1 laser diode generates seed light for the TA system (see Sec. 3.1 for details) at a wavelength of 796.5 nm. In combination with a suitable interference filter (Laser Optik 798 nm / 6°), the ECDL system can be tuned to emission at wavelengths between 795 nm and 800 nm. If a larger detuning from the rubidium D1-line is required, the seed laser system can be replaced requiring minimal readjustment due to the modular setup. The TA chip (DILAS TA-0795-3000-CM, serial number 39584) is placed in a prototype of the TA module presented in Sec. 3.3.2. In contrast to the latest version, in this prototype the collimation lenses are mounted using adhesives and the cylindrical lens is mounted on an external translation stage. Faraday isolators (FI) before and after the optical fiber provide an isolation larger than 60 dB between seed laser and TA. An additional 30 dB-FI is used to protect the TA chip. In order to reduce the effect of amplified spontaneous emission (ASE) of the TA chip, optionally an interference (Laser Optik 804 nm / 6°) can be placed in the beam path. The TA output is distributed to two identical beam paths with a variable ratio. The beam paths are dedicated to be used for the tweezer array and an additional moveable tweezer for atom sorting. Acousto-optic modulators (AOM)) allow for independent switching and intensity stabilisation of each beam path. The employed AOM model (AA Opto-Electronic MT110-B50A1,5-IR-Hk) features a large active aperture and is placed in the collimated TA beam. The first order diffracted

beam is coupled into a PM fiber. The system is optimised for maximum fiber output. For that purpose, the transversal beam profile of the output field is analysed using a CCD camera (Flir CM3-U3-13Y3M) and suitable attenuation by a polarising beam splitter and neutral density filters. The results are depicted in Fig. 5.10 at the approximate position of the beam waist at a distance of $2.7\,\mathrm{m}$ from the TA chip (a) and at the position of the fiber coupler at a distance of $1.3\,\mathrm{m}$ (b). The typical behaviour of a TA beam profile is observable. The focus shows deviations from an ideal Gaussian mode in the line wings that evolve to pronounced side lopes closer to the TA chip containing a significant fraction of the output power. Additionally, the non-ideal matching of the cylindrical lens ($f_{CL} = 40\,\mathrm{mm}$) results in a small residual astigmatism. A standard measure for the beam diameter is obtained by the D4σ method. [155] This method is applicable to non-Gaussian beams. Based on the statistical second moments of the intensity distribution, the horizontal beam diameter $d_{4\sigma,x}$ and vertical beam diameter $d_{4\sigma,y}$ are calculated. Based on these values, an aspheric lens with an focal length of $f_{coupl} = 7.5\,\mathrm{mm}$ (Thorlabs A375TM-B) is chosen for fiber coupling accounting for the NA ≈ 0.075 of the PM fiber and the beam quality factor $M^2 = 1.5$ as measured for the chip in use by the manufacturer.

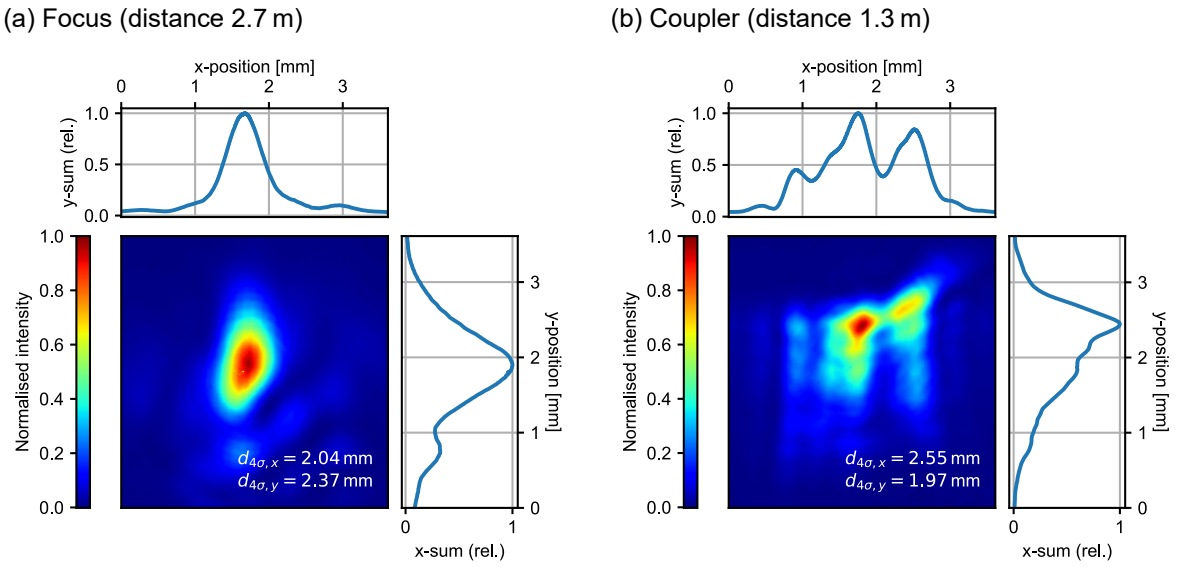

Fig. 5.10.: Transversal beam profile of the TA module presented in this section at the position of the beam waist (a) and at the position of the fiber coupler (b). The x-dimension (y-dimension) is orientated parallel (perpendicularly) to the tapered dimension of the TA chip. (compare Fig. 3.4)

Figure 5.11 shows the typical output power versus current characteristics of the TA (blue) and the maximum output power for different seed-power levels (red). All power levels are measured directly at the output or input of the TA system. At the stated maximum current, the output power is below the specified value of $3\,\mathrm{W}$. The red curve shows that the amplifier is saturated at the typical operation point of $P_{seed} = 20\,\mathrm{mW}$. A slightly higher output power is possible using a higher seed-power level. However, additional test shows that a higher seed power also degrades the transversal mode of the output resulting in a lower fiber coupling efficiency. The typical performance of the MOPA system is summarised in Tab. 5.4. The stated values may vary with the operating conditions of the system. The TA chip is supplied by a current driver with a maximum output of $8\,\mathrm{A}$ (Thorlabs LDC8080). Temperature stabilisation is

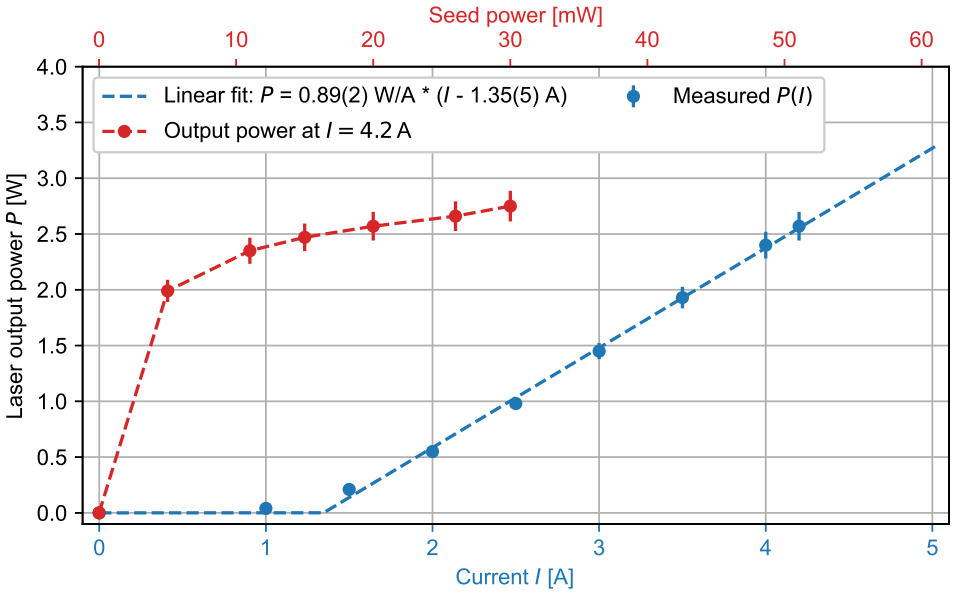

Fig. 5.11.: Output power versus current characteristic of the TA module (blue) with a linear fit (blue, dashed). The maximum output power of the system is plotted in red for different input-power levels (seed power). TA chip: DILAS TA-0795-3000-CM, serial number 39584.

realised using a Thorlabs TEC8040 controller. The diffraction efficiency of the AOM is limited to $78\,\%$ since the active aperture of the device is significantly smaller than the beam diameter. In this configuration, the transversal mode of the diffracted beam is optimised such that a higher fiber coupling efficiency is achieved as compared to the setup without AOM. Due to the improved coupling efficiency, the AOM induced loss is reduced to $1 - 0.78 \cdot 0.58/0.49 \approx 0.08$ of the fiber output.

5.4. Analysis of dipole-trap scattering rates

Scattering of trapping light is a major source of decoherence and heating effects for individual atoms trapped in optical tweezers. [28, 156] Typically, the scattering rates are calculated using Eq. 2.24. This expression is derived by assuming an ideal monochromatic laser field with a detuning $\Delta = \omega_L - \omega_0$ between the frequency of the optical transition ω_0 and the laser frequency ω_L. The approximation is valid for

$$\Gamma \ll |\Delta| \ll \omega_0 \tag{5.9}$$

where Γ is the natural linewidth of the transition. In practise, the emission of a laser is not monochromatic. The laser source may emit a suppressed background with a bandwidth much larger than the detuning. In this case, the background intensity causes resonant scattering not described by Eq. 2.24. In this section, a theoretical analysis of this resonant scattering effect is presented. The results are compared to the intensity spectra of our trapping laser thereby illustrating the relevance of the effect.

Figure 5.12 gives an overview of the quantities and assumptions relevant for the following

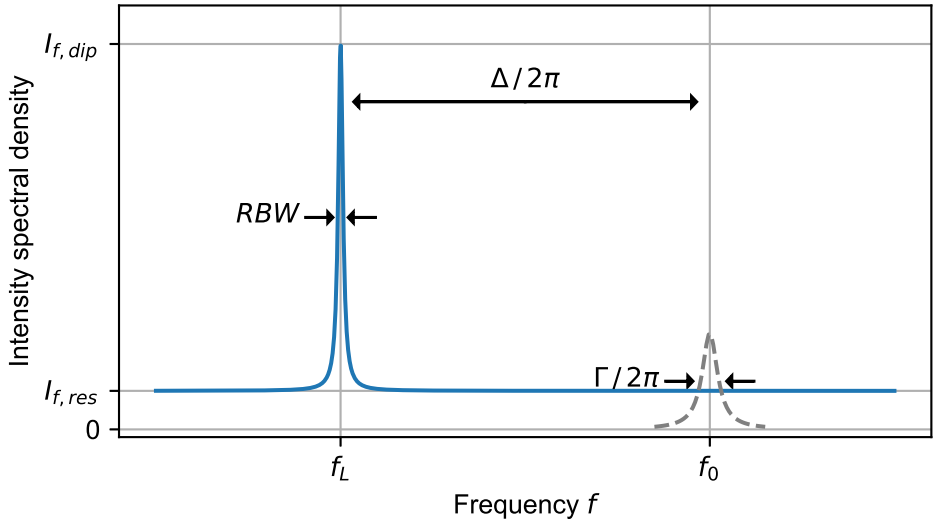

Fig. 5.12.: Schematic spectral intensity distribution at the center of a dipole trap providing an overview of the quantities and assumptions relevant for the calculations in this section (blue). For illustration, the atomic line is depicted (dashed, grey). Peak intensity density: $I_{f,dip}$. Constant background intensity density: $I_{f,res}$. Laser frequency: f_L. Atomic transition frequency: f_0. Natural linewidth: Γ. Resolution bandwidth: *RBW*.

calculations. We consider the spectral density of the intensity at the center of a dipole trap. The intensity is accumulated at the laser frequency $f_L = \omega_L/(2\pi)$. A constant background spectral density $I_{f,res}$ is assumed for simplicity. This approximation is justified as long as the level varies negligibly around the resonance frequency $f_0 = \omega_0/(2\pi)$. Note, that we have chosen the conventional representation referring the spectral density to the frequency f. In the following, the expression $I_{\omega,res} = I_{f,res}\,/\,(2\pi)$ is used for the spectral density as referred to the angular frequency ω. The laser frequency is far detuned from the atomic resonance such that $|\Delta| \gg \Gamma$. The scattering rate of a resonant light field is given by Eq. 2.23. Efficient atom trapping is only possible, if saturation effects can be neglected. We calculate the background scattering rate $\Gamma_{sc,res}$ by integrating over the intensity distribution

$$\Gamma_{sc,res} = \int_{-\infty}^{\infty} \frac{\Gamma}{2} \frac{\frac{I_{\omega,res}}{I_{sat}}}{1+\left(\frac{2\Delta}{\Gamma}\right)^2}\, d\Delta \tag{5.10}$$

$$\underset{x:=2\Delta/\Gamma}{=} \frac{\Gamma^2}{4}\frac{I_{\omega,res}}{I_{sat}} \int_{-\infty}^{\infty} \frac{1}{1+x^2}\, dx \tag{5.11}$$

$$= \frac{\Gamma^2}{4}\frac{I_{\omega,res}}{I_{sat}} \arctan(x)\Big|_{-\infty}^{\infty} \tag{5.12}$$

$$= \frac{\pi\Gamma^2}{4}\frac{I_{\omega,res}}{I_{sat}} = \frac{\Gamma^2}{8}\frac{I_{f,res}}{I_{sat}} \tag{5.13}$$

where $I_{sat} = 4.4876\,\mathrm{mW/cm^2}$ [35] is the saturation intensity of the transition. The quantity $I_{\omega,res}$ is a property of the laser field scaling with the trapping intensity. The power spectral density of the laser field defines the suppression $\eta = I_{\omega,res}/I_{\omega,dip}$ of the resonant background

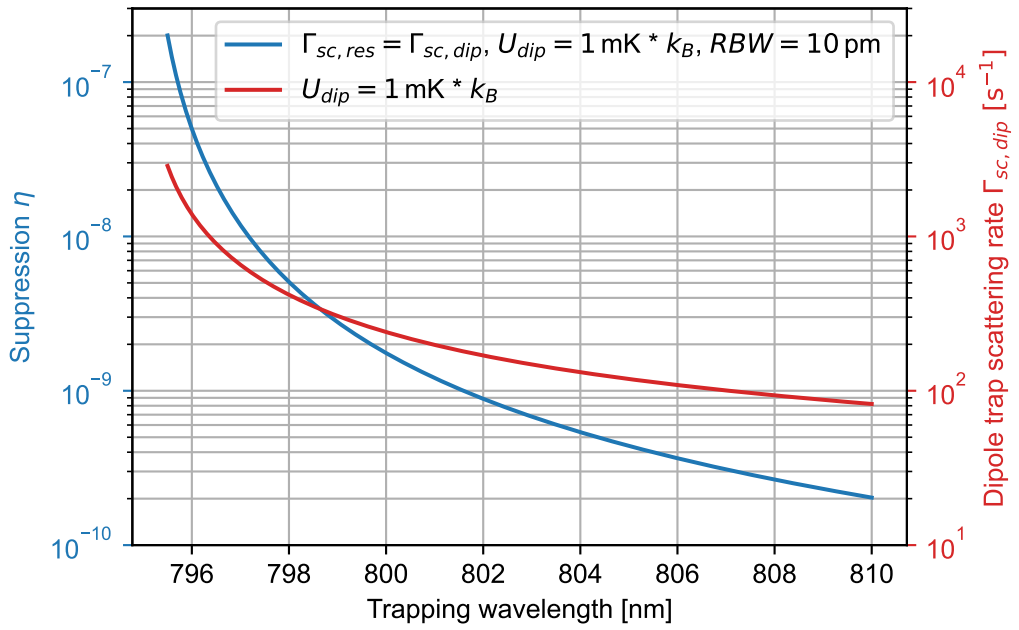

Fig. 5.13.: Suppression η of resonant light required for achieving a scattering rate $\Gamma_{sc,res} = \Gamma_{sc,dip}$ depending on the trapping wavelength for a typical trap depth (blue). This calculation considers resonant scattering on the D1 line only. The scattering rates of the trapping light $\Gamma_{sc,dip}$ are depicted in red.

as compared to the laser line. In practise, the peak intensity density $I_{f,dip}$ will either depend on the linewidth of the laser system or the finite resolution of the measurement. In the following, we will assume the latter, making the results comparable to the typical measurement obtained by an optical spectrum analyser (OSA). Thus,

$$I_{f,res} = \eta \frac{I_{dip}}{RBW} \tag{5.14}$$

where I_{dip} is the maximum intensity of the dipole trap defining its depth and *RBW* is the resolution bandwidth of the measurement. The required peak intensity I_{dip} of the trap is linked to the targeted trap depths by Eq. 2.17 depending on the effective detuning Δ_{eff} (Eq. 2.18). Figure 5.13 illustrates the relevance of resonant scattering. The suppression η required to achieve a scattering rate $\Gamma_{sc,res}$ equal to the scattering rate of the dipole trap is depicted in blue for a typical trap depth of $U_{dip} = 1\,\mathrm{mK} \times k_B$. Remarkably, a large suppression of 7 to 10 orders of magnitude is required. It increases with the trapping wavelength since a larger intensity is used and a lower $\Gamma_{sc,dip}$ is achieved. However, typically the resonant background scales favourably with the detuning.

The power spectral density (PSD) of a light field at a certain offset frequency from the laser line is measured using an optical spectrum analyser (Yokogawa AQ6373). The suppression of resonant light η is derived from the spectrum by normalising it to the measured carrier PSD. Note, that the obtained value of η depends on the *RBW* set for the measurement since the laser linewidth is typically not resolved. Choosing an *RBW* of $10\,\mathrm{pm}$ allows for direct comparison of the measured values to the calculated values for η in Fig. 5.13. In Figure 5.14, the optical spectra of the MOPA system characterised in Sec. 5.3 (blue) and its seed laser system (orange)

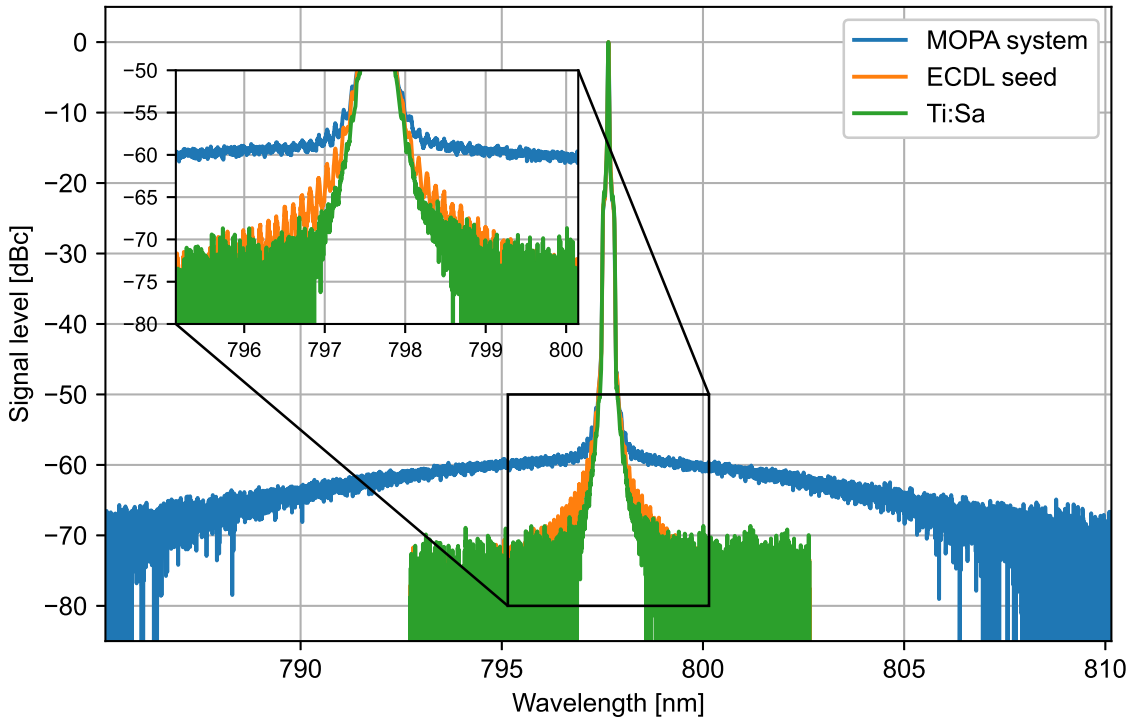

Fig. 5.14.: Power spectral density of different light sources employed for optical dipole traps as obtained by an optical spectrum analyser. The resolution bandwidth of the measurement is $0.01\,\mathrm{nm}$. The central line shapes are determined by the window function of the spectrum analyser. The inset shows a detail of the line wings.

are depicted. For comparison, the spectrum of a titanium-sapphire laser (Coherent 899) also used for dipole trap generation is recorded (green). The carrier spectra are not resolved and thus identical for both laser systems. For the MOPA system (blue), a broadband background with a suppression of $\eta \approx 1 \times 10^{-6}$ is observable. This is a typical behaviour originating from amplified spontaneous emission. [157] The background suppression is not sufficient for efficient atom trapping. Additional suppression of resonant light of more than three orders of magnitude has to be applied using an optical filter (e.g. Semrock 808 RE). For the seed laser and the titanium-sapphire laser, the sensitivity of the OSA is not sufficient to resolve the PSD level at the rubidium D1 line ($\lambda = 794.98\,\mathrm{nm}$). However, the line wings of the ECDL laser are resolved, whereas it is not possible to distinguish between the titanium-sapphire line wings and spurious effects due to the limited dynamic range of the OSA (compare inset). For both laser systems, the noise floor of the OSA sets an upper bound of 1×10^{-7} for η. Based on these results, a sufficient suppression can be guaranteed for all practical purposes by using a suitable optical filter.

5.5. Conclusion and discussion

Two key features of micro-optical tweezer arrays are addressed in this chapter. On the one hand, the superior scalability of the system size enhanced by an optimised lens system is demonstrated. On the other hand, the novel approach of microlens arrays produced in an additive manufacturing process widely resolves limitations concerning available geometries of

the tweezer array.

For micro-optical tweezer arrays, the system size is typically limited by the available laser power. In this situation, smaller spot sizes increase the system size. Tweezer arrays with spot sizes below $1\,\mu$m (waist) are demonstrated. Remarkably, this is achieved by using a lens system with a large focal length of $52.88\,$mm allowing for placing the dielectric surface of the vacuum viewport at a distance of $\sim 20\,$mm from the tweezer plane. Thereby, the undesired effects of charges accumulated on the surface acting on particularly sensitive Rydberg atoms are reduced significantly. The results obtained for large-scale tweezer arrays mainly rely on the method of inspecting the tweezer focal plane with a microscope objective that features a higher resolution than the imaging system. This system is significantly more robust against misalignment than the imaging system such that aberration of the tweezer spots can be uniquely attributed to the imaging system. However, the method is only applicable for test setups due to the short focal length of the microscope objective prohibiting application with the experimental chamber at place. A high-quality re-imaging system for live inspection of the tweezer arrays is still work in progress. For large scale arrays, the automatic software routine developed in this work is a powerful tool allowing for simultaneous inspection and optimisation of all tweezer spots. Due to its high performance, it is also possible to use the routine on a regular basis in the experiment which also requires a suitable re-imaging system.

The feasibility of producing microlens arrays with an additive manufacturing process is demonstrated. This approach allows us to achieve almost arbitrary array geometries. An imaging quality suitable for efficient trapping of individual atoms is achieved using the manufactured arrays. The side structure contrast is improved significantly by filling the spaces in the array using lenslets with a suitable footprint. For the test array produced in this work, there are significant deviations from the design parameters of the lenslets. In future, microlenses with a higher NA and an optimised footprint should be used.

The results on micro-optical tweezer arrays are complemented by a characterisation of suitable light sources. A simple and cost-efficient system based on the master-oscillator power-amplifier systems developed in this work is presented. Theoretical analysis of the scattering rates of trapped atoms shows the relevance of resonant scattering. Intensity close to resonance with an atomic transition is required to be suppressed be several orders of magnitude.

6. Laser systems for coherent Rydberg excitation and spectroscopy on highly-charged bismuth

Coherent Rydberg excitation of rubidium atoms at large Rabi rates is realised in a two-photon scheme as discussed in Sec. 2.3. In this work, the scheme is implemented using the $|5P_{3/2}\rangle$-state as an intermediate state. At the lower $|5S_{1/2}\rangle \rightarrow |5P_{3/2}\rangle$ transition our standard diode lasers (see Sec. 3.1) are employed. For the second transition, all S- and D-Rydberg states $|r\rangle$ with principal quantum number $n > 30$ are accessible using laser light within a wavelength range of $479\,\text{nm}$ to $483\,\text{nm}$. A suitable light source is implemented via second-harmonic generation of a high-power infrared laser system. When considering coherent excitation dynamics, the combined phase noise of both light fields constitutes a major decoherence effect [61]. The requirement of long coherence times puts high demands on the frequency stability of the employed laser systems. A suitable frequency reference is realised using a high finesse reference cavity. Both laser systems are stabilised to this reference via the Pound-Drever-Hall (PDH) scheme. [99, 100]

In this chapter, the setup of the $780\,\text{nm}$ laser system and the setup of the $480\,\text{nm}$ Rydberg laser system are discussed. The reference cavity is characterised and the Pound-Drever-Hall locks are optimised involving custom electronic modules for signal generation and photodetectors developed in this work. Analysing the effect of laser phase and frequency noise on coherent excitation dynamics allows us to assess the achieved laser linewidths also characterised in this chapter. With minor modifications, the laser system can be applied to spectroscopy of highly-charged bismuth [158] at $244\,\text{nm}$ utilising an additional frequency-doubling stage. This application relying on the laser technology presented in this work is also discussed here.

6.1. Rydberg laser system

For two-photon Rydberg excitations, the minimal one-photon scattering rates are achieved by choosing equal Rabi rates on both transitions (see Sec. 2.3 for details). Since the dipole coupling on the $|n, S_{1/2}\rangle \rightarrow |n, P_{3/2}\rangle$ transition is orders of magnitude stronger as compared to the coupling on the second $|5P_{3/2}\rangle \rightarrow |r\rangle$ transition [57], a moderate laser power of several mW is used for the $780\,\text{nm}$ transition in the experiment, whereas the achievable Rabi rate is determined by the laser power available at the $|5, P_{3/2}\rangle \rightarrow |r\rangle$ transition. The Rydberg laser system consists of an external-cavity diode laser (ECDL) system emitting light at $780\,\text{nm}$ and a high-power multi-stage laser system providing light at $480\,\text{nm}$. Both systems are characterised in this section.

Figure 6.1 (a) shows a schematic overview of the optical setup of the $780\,\text{nm}$-Rydberg system. The ECDL system is equipped with a high-power $785\,\text{nm}$-laser diode (Sharp GH0782RA2C)

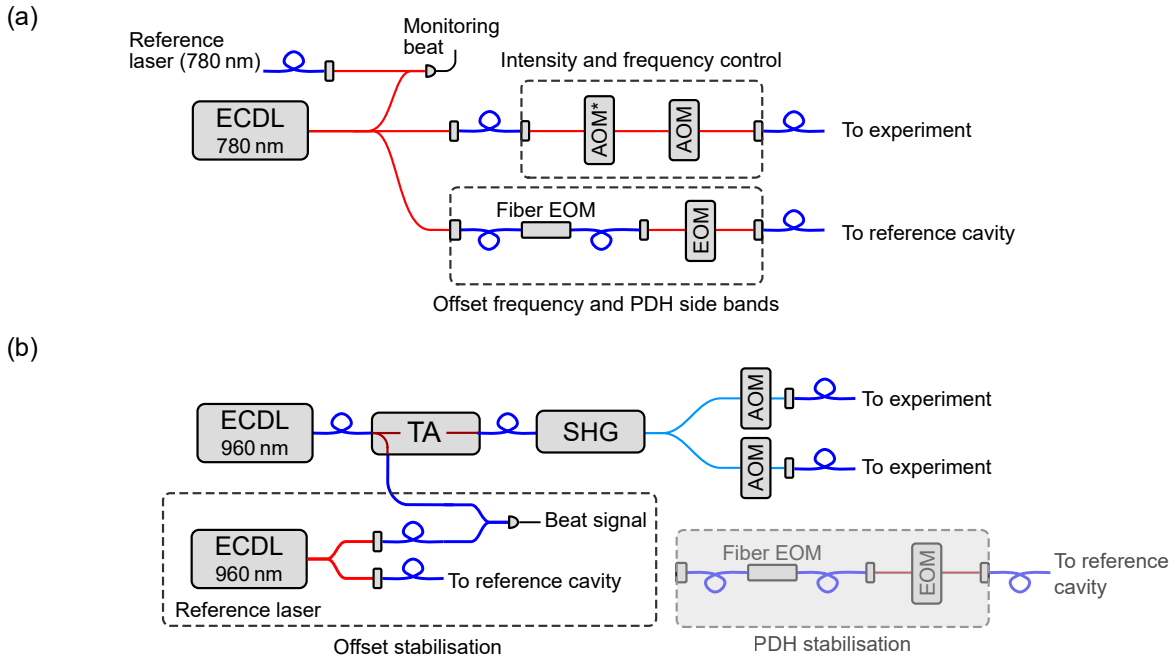

Fig. 6.1.: Schematic overview of the Rydberg laser system consisting of laser systems emitting light at 780 nm (a) and 480 nm (b). Free-space beam paths are marked in red (780 nm) or light blue (480 nm) depending on the wavelength. Optical fiber connections are marked in blue. External-cavity diode laser (ECDL) systems are employed as laser sources. In (b), the ECDL light is amplified by a tapered amplifier (TA) and frequency-doubled in a second-harmonic generation (SHG) module. A commercial reference laser system (Toptica DL100) is used for offset-frequency stabilisation. Alternative parts of the setup that are currently not used are greyed out. Acousto-optic modulators (AOM) marked with a star are used in double-pass configuration. EOM: electro optic modulator.

using a 30 %-feedback mirror. For fast electronic feedback on the laser current, a JFET-circuit similar to the circuit used in [101] is included in the laser head. For better performance, this current-modulation technique will be replaced by the technique presented in Sec. 3.5 in the future. The ECDL output is distributed to three beam paths. Two paths are coupled into polarisation-maintaining single-mode optical fibers (PM fibers) where the first part, connected to a module for fast frequency and intensity control, provides light for the experiment and the second path is used for frequency stabilisation. With the third beam path a beat note with a reference laser stabilised to a rubidium spectroscopy is realised. The beat note is used for monitoring the absolute frequency of the laser system with a high accuracy. Frequency shifts on µs-time scales are realised using an AOM (Crystal Technology 3110-120) in double-pass configuration in combination with fast signal generation based on direct digital synthesis (DDS). Independent intensity control is implemented with the digital controller developed in this work and a single-pass AOM (Crystal Technology 3110-120). Both functionalities are integrated in a compact fiber coupled module. The module providing light suitable for PDH frequency stabilisation with a variable frequency offset consists of a fiber electro-optic modulator (EOM) and a free-space EOM (see Sec. 6.3 for details). Typically, a small portion of the ECDL output ($\sim$3 mW) is used for frequency stabilisation.

A schematic overview of the Rydberg laser system emitting light at $480\,\mathrm{nm}$ is depicted in Fig. 6.1 (b). The laser system consists of a master-oscillator power-amplifier (MOPA) system emitting light at $960\,\mathrm{nm}$ and a commercial frequency-doubling unit (Toptica SHG pro) generating light at $480\,\mathrm{nm}$ by second-harmonic generation (SHG) in a non-linear crystal. Seed light for the MOPA system is provided by an ECDL system equipped with a high-power laser diode (JDSU SDL-6531-J1) and a $15\,\%$-feedback mirror. For fast feedback on the laser current, the current-modulation technique presented in Sec. 3.5 is implemented in this ECDL system. The ECDL output is fiber coupled to a tapered amplifier (TA) module providing an optical output power of approximately $2\,\mathrm{W}$. At the input of the TA, an additional beam path allows for using a small portion of the seed light for frequency stabilisation. Currently, frequency stabilisation is realised by a frequency-offset lock employing the phase-lock technique described in Sec. 4.3. A commercial reference laser system (Toptica DL100) is stabilised to a high-finesse reference cavity. Due to the modular setup, this locking scheme can be replaced by a direct PDH lock to the reference cavity in a straightforward fashion by introducing a fiber EOM and a free-space EOM (greyed out) similar to the setup depicted in Fig. 6.1 (a). The output of the TA is coupled directly into a PM fiber connected to a commercial frequency-doubling unit (Toptica SHG pro). The output of the unit is distributed to two identical beam paths coupled to a PM fiber providing light for two experiments simultaneously. Both beam paths include an AOM (Crystal Technology 3080-125) for switching and intensity stabilisation using our digital controllers as described in Sec. 4.5. This type of AOM offers a large active aperture. It is placed in the collimated beam and achieves high diffraction efficiencies above $90\,\%$.

6.1.1. MOPA system at 960 nm

MOPA systems combine the excellent spectral properties of an actively stabilised ECDL with a high output power. Hence, they are an ideal choice for driving the $|5, P_{3/2}\rangle \rightarrow |r\rangle$ transition since the achievable Rabi rate will be limited by the optical power available at this transition. In this section, a MOPA system optimised for maximum output power from a PM fiber at a wavelength of $960\,\mathrm{nm}$ is characterised.

Specification	**Value**	**Conditions**
Wavelength	$960\,\mathrm{nm}$	$950\,\mathrm{nm}$ to $970\,\mathrm{nm}$
Maximum output power	$2.0\,\mathrm{W}$	$I = 2.75\,\mathrm{A}$, $P_{seed} = 13\,\mathrm{mW}$
Typical seed power	$13\,\mathrm{mW}$	$10\,\mathrm{mW}$ to $50\,\mathrm{mW}$
TA mount temperature	$18.5\,^{\circ}\mathrm{C}$	
Nominal beam waist	$1.04\,\mathrm{mm}$	$f_{AL} = 3.1\,\mathrm{mm}, \theta_y = 18.5^{\circ}$
Astigmatism θ'_x	$35(3)\,\mathrm{mrad}$	$I = 2.75\,\mathrm{A}$
Cylindrical lens f_{CL}	$38\,\mathrm{mm}$	
Typical fiber coupling	$55\,\%$	$I = 2.75\,\mathrm{A}$, $f_{coup} = 4.51\,\mathrm{mm}$
Maximum fiber output	$1.10\,\mathrm{W}$	$I = 2.75\,\mathrm{A}$

Tab. 6.1.: Specifications of the MOPA system employed in the Rydberg laser system. TA chip: eagleyard EYP-TPA-0960-02000, serial number EC-07964. I: operating current. P_{seed}: seed power. f_{coup}: Focal length of the lens used for fiber coupling. f_{AL}: Focal length of the output-collimation lens. θ_y: output divergence in y-dimension. θ'_x: Residual divergence in x-dimension (compare Fig. 3.4).

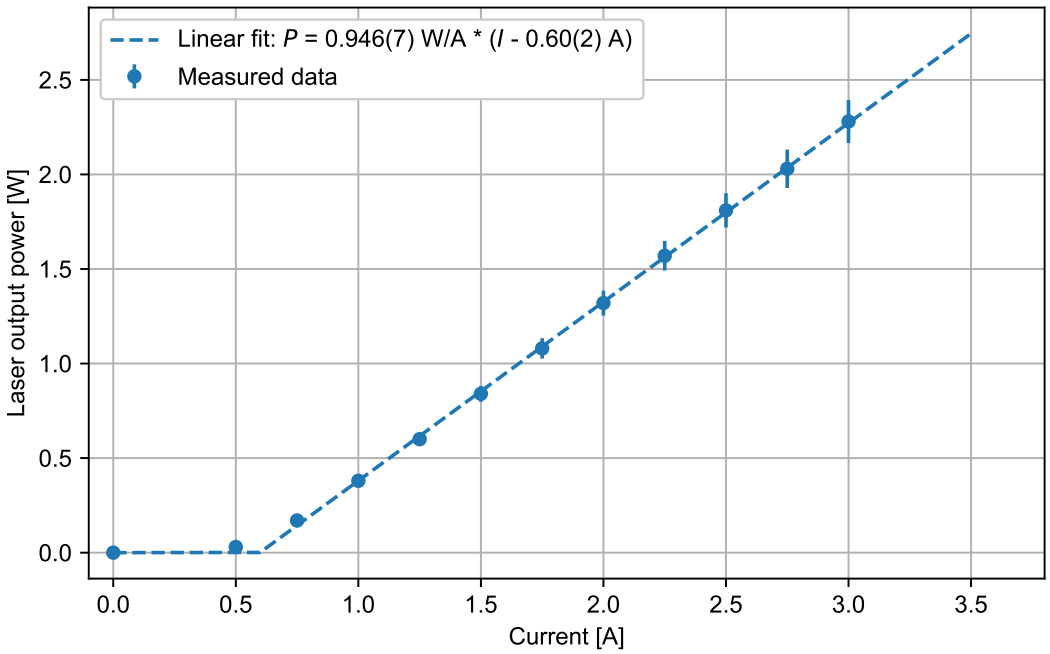

Fig. 6.2.: Power versus current characteristics of a tapered amplifier (eagleyard EYP-TPA-0960-02000, serial number EC-07964) measured directly after the TA and before the optical isolator (blue markers). A linear fit is applied to the measured data points (dashed line).

The optical setup of the MOPA system is similar to the setup employed for the magneto optical trap as described in Sec. 4.1. The ECDL seed laser is connected to the TA system by a PM fiber. The TA module is implemented using the design presented in Sec. 3.3.2. For this TA system, an *eagleyard EYP-TPA-0960-02000* TA chip is chosen. The TA module is operated with our standard 4 A-current drivers (Thorlabs LDC8040) and temperature controllers (TEC8040). At the input of the TA an optical isolation of 60 dB is provided by 30 dB-Faraday isolators at the input and output of the optical fiber. A third Faraday isolator (30 dB) protects the output of the TA chip. For that purpose, an isolator with a high transmission > 90 % is chosen (Linos FI-930-5SC). Figure 6.2 shows the typical power versus current characteristics as measured directly at the output of the TA module (blue markers), i.e. before the optical isolator. The measured data are well represented by the linear fit (dashed line). The maximum output power of 2 W stated in the datasheet is achieved at a current well below the maximum current of 3.5 A. The linear fit suggest that the output power at 3.5 A would be 2.76 W. If the maximum output power may be exceeded without damaging the chip, is still an open question.

The output of the TA system is coupled into a PM fiber specialised for high-power applications (Toptica OE-000796). The numerical aperture (NA) of the fiber is measured by analysing the beam profile emitted from the fiber without collimation optics using a CCD camera. The measurement yields an asymmetric NA of $NA_x = 0.076(3)$ perpendicular to the polarisation key at the fiber connector and $NA_y = 0.088(3)$ parallel to the key. In order to optimise the fiber coupling efficiency, the beam profile of the TA system is inspected with a CCD camera. Figure 6.3 shows the beam profile at the position of the fiber coupler at a distance of approximately 0.6 m from the TA chip. The chip is operated at a current of $I = 2.75$ A. When compared to the beam profile of the 795 nm MOPA system depicted in Fig. 5.10, a significantly higher beam

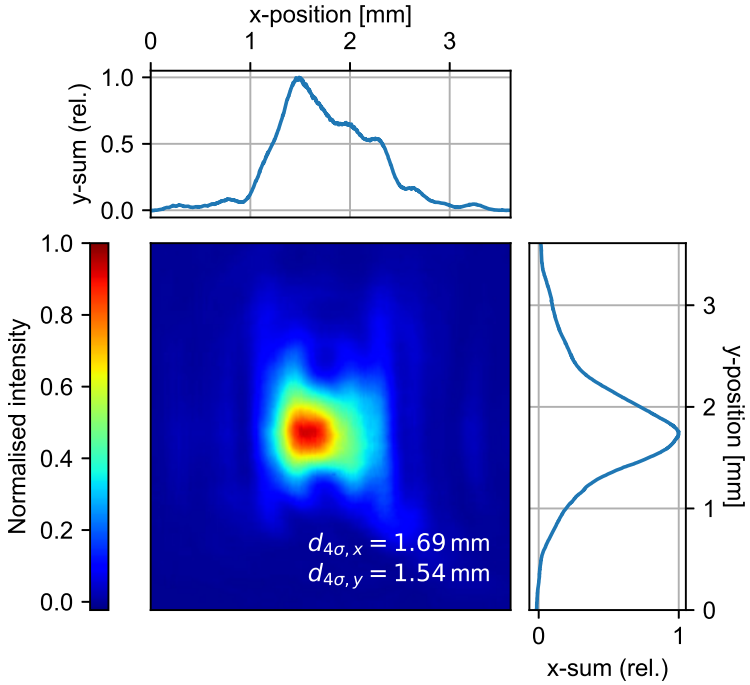

Fig. 6.3.: Transversal beam profile of the TA system described in this section at the position of the fiber coupler (distance to TA chip: $\sim 0.6\,\mathrm{m}$). The x-dimension (y-dimension) is orientated parallel (perpendicularly) to the tapered dimension of the TA chip (compare Fig. 3.4).

quality is achieved since the side lopes in the horizontal dimension (x-dimension) are less pronounced, the intensity distribution in vertical dimension (y-dimension) is symmetric, and the aspect ratio is closer to unity. This enhancement is mainly a consequence of choosing a TA chip from a different manufacturer. Partly, it can also be attributed to the improved collimation optics. Note, that for this type of TA chips, it is essential to adapt the axis of the cylindrical lens (see Sec. 3.3.2 for details) to the orientation of the emitter, which may be tilted as referred to its mount. The aspheric lens used for fiber coupling is matched to the measured $D4\sigma$ values and the *NA* of the fiber considering that $M^2 > 1$. Additionally, the orientation of the fiber is adapted such that the asymmetric *NA* of the fiber matches the asymmetry of the beam profile.

The specifications of the MOPA system are summarised in Tab. 6.1. As compared to the MOPA systems characterised in Sec. 4.1 and Sec. 5.3, a higher fiber coupling efficiency is achieved due to the improved beam quality. Also, the nominal beam diameter is significantly smaller due to the larger vertical size of the TA output facet. This MOPA system is competitive with state-of-the-art commercial TA systems while being available at lower costs and offering significantly more flexibility.

6.1.2. Second-harmonic generation

The frequency-doubling unit used in this work is a commercial system (Toptica SHG pro) with a fiber-dock input and free-space output. Second-harmonic generation is realised based on a critically phase-matched non-linear crystal in a bow-tie ring cavity. The optical cavity length is controlled by shifting two cavity mirrors with piezo actuators. The PDH scheme is employed in order to lock the resonance frequency of the cavity to the laser frequency of the fundamental light field. PDH sidebands are created using a free-space EOM placed in front of the input of

the cavity. The system achieves a typical conversion efficiency of 70 % with an input-power level of 1.1 W. Due to the non-linear conversion process, the efficiency increases with increasing input power. A characterisation of the output beam quality of the system and optimisation strategies for the fiber coupling efficiency are presented in this section.

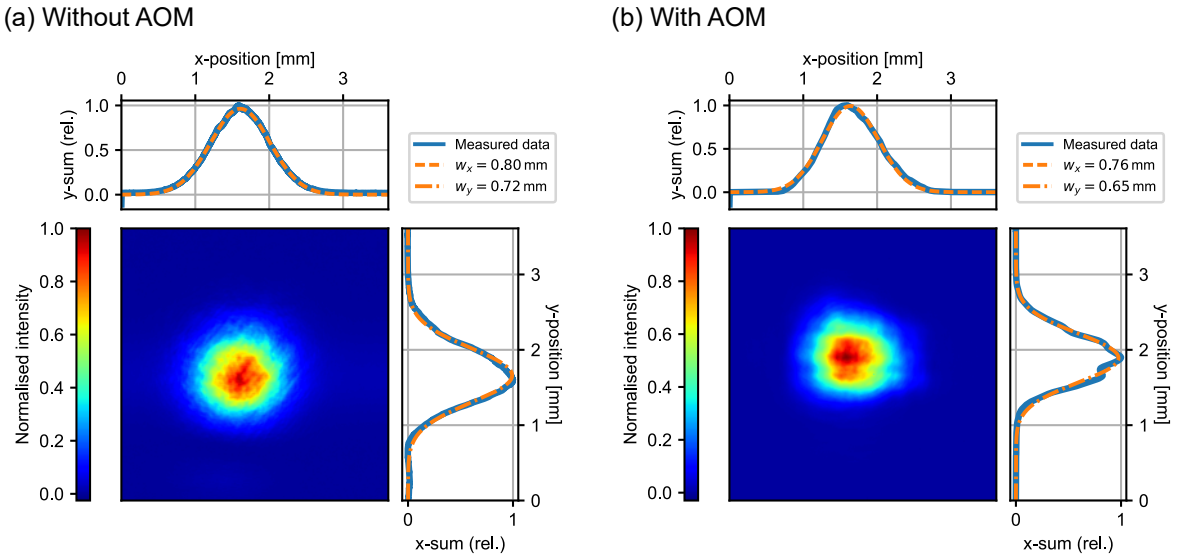

Fig. 6.4.: Transversal beam profile of the frequency-doubling unit characterised in this section without AOM (a) and with AOM (b) for intensity control. Distance to the output aperture: ~ 0.5 m. The x-dimension (y-dimension) is orientated parallel (perpendicularly) to the base plate of the frequency-doubling unit.

The beam profile of the SHG output is inspected at the position of the fiber coupler with a CCD camera and suitable neutral density filters. The distance to the output aperture of the SHG unit is approximately 0.5 m. For comparison, the beam profile without AOM and with AOM are imaged (compare Fig. 6.1 (b)). The results are depicted in Fig. 6.4 (a) and Fig. 6.4 (b). The beam waist is determined by fitting a 1D Gaussian distribution (orange) to the depicted summed intensity distributions (blue). For beam profiles with approximately Gaussian intensity distribution, this method is more accurate as compared to the D4σ method. [155] The resulting beam waists w_x and w_y are stated in the legend. The measured transversal beam profile are in excellent agreement with an ideal Gaussian mode in both cases, with and without AOM. The high quality of the output beam can be deduced to the high quality of the fundamental mode decoupled from a PM fiber. The beam waist with AOM (Crystal Technology 3080-125) is smaller and the aspect ratio is slightly larger. Substructures of the beam profiles can be attributed to interference effects induced by the neutral density filters used for this characterisation only. The output of the frequency-doubling unit is coupled into a PM fiber for high-power applications at 480 nm (Toptica OE-001075). The NA of the fiber is determined analogously the NA of to the input fiber of the SHG unit yielding $NA_x = 0.061(5)$ in the dimension perpendicular to the polarisation alignment key and $NA_y = 0.054(5)$ parallel to the key. Based on this measurement and the obtained values for the beam waists a $f = 11$ mm aspheric lens (Thorlabs A397TM-A) is chosen for fiber coupling. Adapting the asymmetric *NA* of the fiber to the asymmetry of the beam increases the coupling efficiency by 3 % to 5 %. Without AOM, a fiber coupling efficiency of 60 % is obtained. The coupling efficiency decreases to 56 % when the AOM is used for unknown reasons. The effect could be reproduced using

this AOM type with another laser system. The laser system generates a maximum fiber output power of $600\,\mathrm{mW}$. Inspecting the output of the SHG with a fast photodiode shows that a rms intensity stability better than 3×10^{-3} in the frequency range $1\,\mathrm{Hz}$ to $100\,\mathrm{kHz}$ is achieved. The residual amplitude modulation induced by the PDH modulator is not resolved in this measurement indicating a relative level below 1×10^{-3}.

6.2. A laser system for spectroscopy of highly-charged bismuth

Highly-charged heavy ions are an ideal test bed for quantum electrodynamics (QED). The bound electron experiences QED effects in the strong electric field of the highly-charged nucleus. In standard QED, the behaviour of the bound electron is predicted by perturbation expansion in αZ where α is the fine structure constant and Z is the nuclear charge number. For highly-charged heavy ions the perturbative theory is not applicable since αZ is large. QED effects are treated in terms of non-perturbative strong-field QED. [159] For large Z, the hyperfine splitting of the ground state is resolvable by optical spectroscopy allowing for precise measurement of QED effects. However, the effects are masked by non-QED effects such as shifts due to the finite size of the nucleus, the Bohr-Weisskopf effect, [160] or due to the inhomogeneous nuclear charge distribution, the Breit-Rosenthal effect [161]. These effects are cancelled by comparison between the hyperfine splitting of hydrogen-like bismuth and lithium-like bismuth. [158] The *Artemis* experiment at the HITRAP facility of the GSI Helmholtz centre for heavy ion research is a cryogenic Penning trap experiment that is capable of working with a wide range of heavy and light highly-charged ions, among them hydrogen-like bismuth $^{209}\mathrm{Bi}^{82+}$ and lithium-like $^{209}\mathrm{Bi}^{80+}$. [162, 163] At the HITRAP facility, the relevant M1 hyperfine transition $|1S_{1/2}, F = 4\rangle \rightarrow |1S_{1/2}, F = 5\rangle$ of $^{209}\mathrm{Bi}^{82+}$ has been determined from spectroscopy at $0.7c$ to $\lambda = 243.822(8)\,\mathrm{nm}$ in the rest frame of the ion. These measurements already show significant deviations from the theoretical QED predictions. [164] The uncertainty of $40\,\mathrm{GHz}$ is expected to be reduced significantly by spectroscopy of cold ions in a Penning trap. Thus, spectroscopy of highly-charged hydrogen-like bismuth is promising to gain further insights in bound-state strong-field QED.

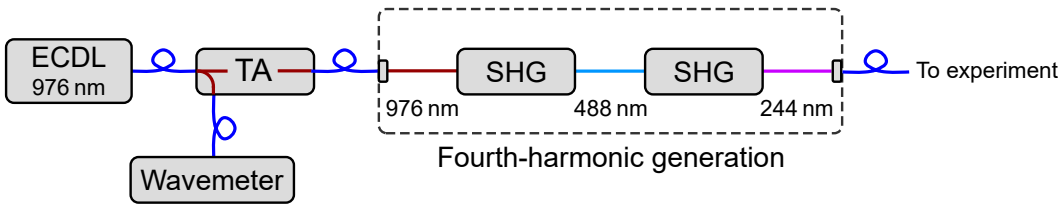

Fig. 6.5.: Schematic overview of a laser system used for spectroscopy of highly-charged bismuth. Optical fiber connections are marked in blue. TA: Tapered amplifier. SHG: Second-harmonic generation.

Light at the target wavelength of $244\,\mathrm{nm}$ is generated using fourth harmonic generation (FHG) in two frequency-doubling stages. Accordingly, the fundamental wavelength is $976\,\mathrm{nm}$ which is frequency doubled to $488\,\mathrm{nm}$. These wavelengths are within the tuning range of the frequency-doubling unit of the Rydberg laser system. Hence, this system is applicable to spectroscopy of highly-charged bismuth as well. Thus, the characterisation presented in the previous section is also valid for this application. The subsequent frequency-doubling stage

to 244 nm has already been described previously. [165] However, the target wavelength of 976 nm exceeds the tuning range of the tapered amplifier in the Rydberg laser system. In this section, a MOPA system is characterised that provides fundamental light at 976 nm. The spectral properties of this system define the quality of the light field used for spectroscopy. For the *Artemis* experiment a Doppler-broadened linewidth of 30 MHz is expected. [165]

Figure 6.5 shows an schematic overview of the laser system applicable to spectroscopy of highly-charged bismuth. The fundamental light at 976 nm is produced by a MOPA system developed in this work. The system consist of an ECDL system connected to the a TA system by an optical fiber. At the input of the TA module, an auxiliary output is available that is used to stabilise the seed laser frequency with a high-resolution wavelength meter (High Finesse WS8-2). The output of the TA system is coupled to a single mode optical fiber. Fourth-harmonic generation will be realised using a commercial system (Toptica FHG) consisting of two subsequent SHG stages. Both stages are based on frequency-doubling in a critically phase-matched crystal placed in a bow-tie ring cavity. While in the first stage the standard PDH scheme is used for stabilisation, the second stage is stabilised applying the Hänsch-Couillaud scheme that does not require phase modulation of the blue beam. [166] Replacing the Hänsch-Couillaud scheme with the PDH scheme is expected to further improve the overall system performance.

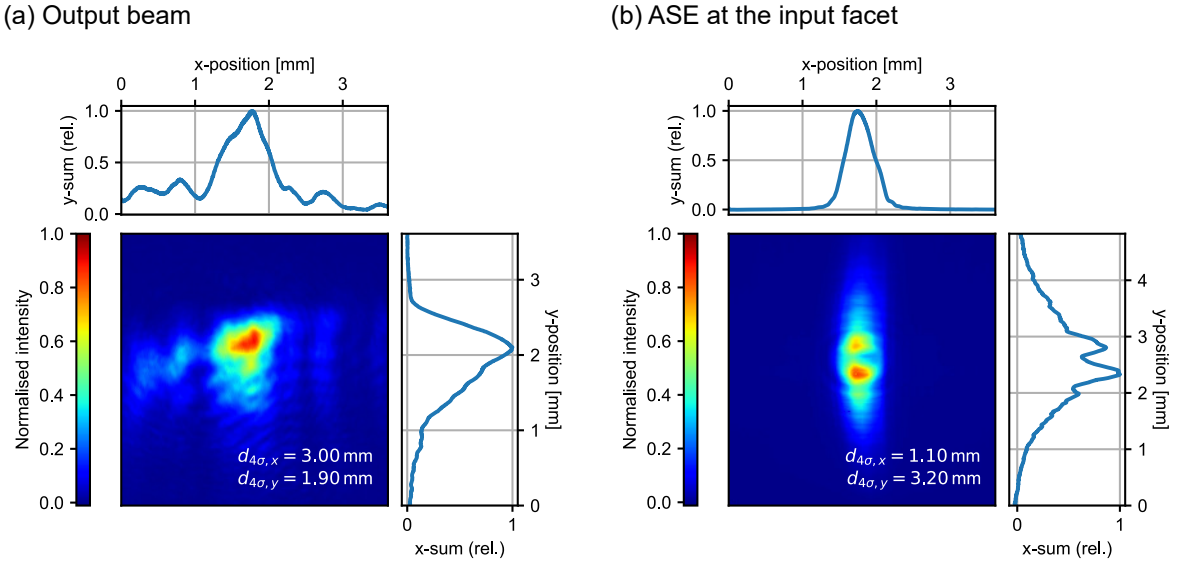

Fig. 6.6.: (a) Transverse beam profile of the MOPA system described in this section at the position of the fiber coupler. (b) ASE emitted at the input facet of the TA. The x-dimension (y-dimension) is orientated parallel (perpendicularly) to the tapered dimension of the TA chip (compare Fig. 3.4).

The ECDL seed system for the high-power MOPA system is identical to the ECDL system described in Sec. 6.1.1 except for omitting the fast current control that is not required for this laser system. Operation at 976 nm is more efficient for this laser diode type (JDSU SDL-6531-J1) as compared to operation at 960 nm. In the TA system, a high-power TA chip with a nominal output power of 4 W (DILAS TA-0975-4000-CM, serial number 101508) is used. The chip is placed in a prototype of our TA module (see Sec. 3.3.2) identical to the module used in Sec. 5.3. Figure 6.6 (a) shows the beam profile of the output of the TA module at the position

of the fiber coupler. For this measurement, the TA chip is operated at maximum operating current $I = 5.75\,\mathrm{A}$. The beam diameters in vertical and horizontal direction are calculated using the D4σ-method. Strong side structures and an asymmetric aspect ratio are observed. In Figure 6.6 (b), the output of ASE at the input facet of the TA chip as collimated by the input coupling lens is depicted. The beam profile shows an strongly asymmetric beam profile with an aspect ratio of ∼3:1. The input beam is matched to this beam profile using a 3:1 cylindrical-lens telescope thereby improving the stability and input-power requirements. The specifications of this TA module are summarised in Tab. 6.2. The highest output power of all TA modules presented in this work is achieved while a good fiber coupling efficiency is maintained.

Estimating the FHG efficiencies from previous work [165], an output power $> 10\,\mathrm{mW}$ at $244\,\mathrm{nm}$ will be available for the spectroscopy of highly-charged bismuth. Linewidth measurements of the TA system presented in detail in Sec. 6.6 show that a linewidth of $25\,\mathrm{kHz}$ is achieved at $960\,\mathrm{nm}$ corresponding to a linewidth of $\sim 100\,\mathrm{kHz}$ at $244\,\mathrm{nm}$. By compensating for long-term drifts, e.g. by stabilisation to a calibrated high-precision wavelength meter, the linewidth of the laser system is more than two orders of magnitude below the linewidth of Doppler-broadened bismuth line. A state-of-the-art wavelength meter (HighFinesse WS8-2) provides an absolute frequency accuracy of $2\,\mathrm{MHz}$ at $488\,\mathrm{nm}$ corresponding to an accuracy of $4\,\mathrm{MHz}$ at $244\,\mathrm{nm}$. A suitable calibration of the wavelength meter is derived from tellurium spectroscopy. [165]

Specification	**Value**	**Conditions**
Wavelength	$976\,\mathrm{nm}$	
Maximum output power	$3.96\,\mathrm{W}$	$I = 5.75\,\mathrm{A}$, $P_{seed} = 18\,\mathrm{mW}$
Typical seed power	$18\,\mathrm{mW}$	$10\,\mathrm{mW}$ to $50\,\mathrm{mW}$
TA mount temperature	$18.5\,^{\circ}\mathrm{C}$	
Nominal beam waist	$1.45\,\mathrm{mm}$	$f_{AL} = 3.1\,\mathrm{mm}, \theta_y = 25^{\circ}$
Astigmatism θ'_x	$45(3)\,\mathrm{mrad}$	$I = 5.75\,\mathrm{A}$
Cylindrical lens f_{CL}	$30\,\mathrm{mm}$	
Typical fiber coupling	$47\,\%$	$I = 5.75\,\mathrm{A}$, $f_{coup} = 6.24\,\mathrm{mm}$
Maximum fiber output	$1.55\,\mathrm{W}$	$I = 5.75\,\mathrm{A}$

Tab. 6.2.: Specifications of the MOPA system employed for the spectroscopy of highly-charged bismuth. TA chip: DILAS TA-0975-4000-CM, serial number 101508. I: operating current. P_{seed}: seed power. f_{coup}: Focal length of the lens used for fiber coupling. f_{AL}: Focal length of the output-collimation lens. θ_y: output divergence in y-dimension. θ'_x: Residual divergence in x-dimension (compare Fig. 3.4).

6.3. High-finesse reference cavity for laser-frequency stabilisation

In order to reduce laser linewidths by active frequency stabilisation, a frequency reference is required, that allows for detection of small frequency deviations at a high bandwidth. At the same time a high long-term stability of the frequency reference is required. In this work, a suitable reference is realised by a commercial high-finesse cavity (Stable Laser Systems). In this section, the cavity is characterised and the optical setup used for two-colour laser stabilisation is discussed.

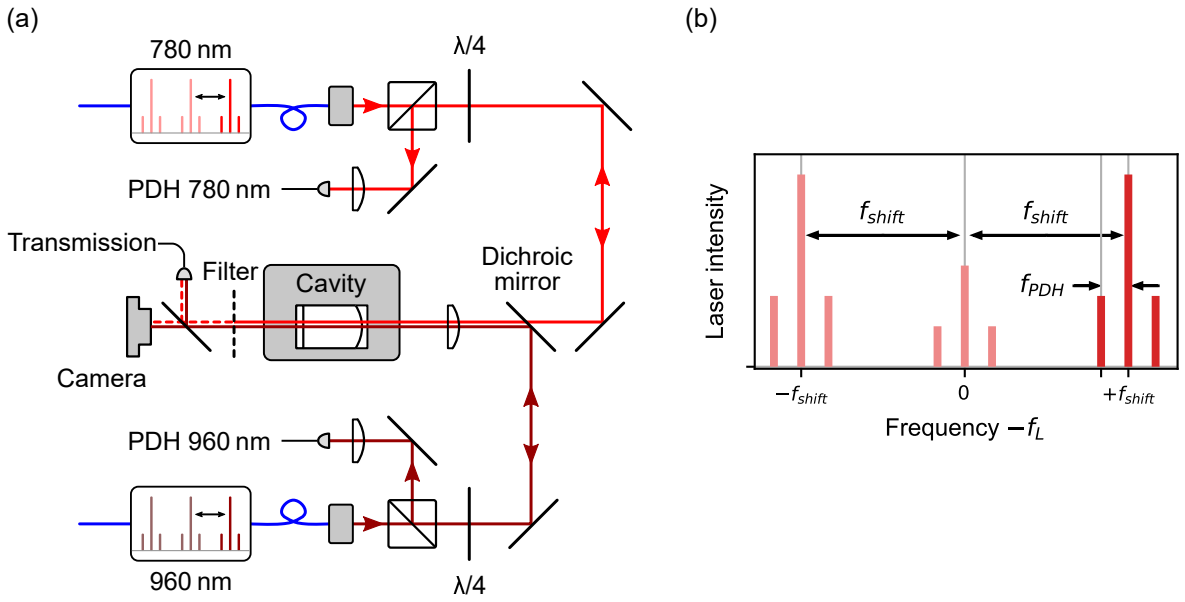

Fig. 6.7.: (a) Optical setup for two-colour laser stabilisation to a high-finesse cavity. (b) Scheme of the sideband spectrum used for Pound-Drever-Hall (PDH) frequency stabilisation at the frequency f_{PDH}. The laser is stabilised to a frequency $f_L + f_{shift}$ with the variable offset f_{shift}.

The cavity consists of mirrors with a highly-reflective dielectric coating placed on an ultra-low expansion (ULE) glass spacer. The mirrors form a cavity with a spectral width dependent on their reflectivity R and their distance L. The ULE glass spacer is manufactured such that a zero crossing of its temperature expansion coefficient can be found close to room temperature. At this operating temperature, a high long-term stability of the resonance frequency of the cavity is guaranteed. Additionally, the cavity is placed in a temperature controlled vacuum housing for insulation from environmental influences, such as vibrations and variations of the barometric pressure. The mirror coating is tailored to the targeted wavelengths of $780\,\text{nm}$ and $960\,\text{nm}$. Additionally, there are other wavelength ranges available that are not used in this work. A detailed measurement of the reflectivity provided by the manufacturer can be found in Appendix A.2. Figure 6.7 (a) shows the optical setup used for two-colour laser stabilisation on the cavity. Light at $960\,\text{nm}$ and $780\,\text{nm}$ is emitted from PM fibers. The optical setup consists of identical beam paths for both wavelengths overlapped by a dichroic mirror. The combined beams are coupled into the cavity using an achromatic mode matching lens (focal length $300\,\text{mm}$). The focal length of the lens is adapted to the radius of curvature of the input mirror ($0.5\,\text{m}$) and the beam diameter ($\sim 1.1\,\text{mm}$). For each beam path, the counter propagating beams reflected from the cavity are separated using quarter-wave plates in double-pass and polarising beam splitters. The reflected beams are focused on photodetectors optimised for PDH frequency stabilisation. The phase modulation required for PDH frequency stabilisation (see Sec. 6.1 for details) is applied by a separate optical module. The transmission of the cavity is analysed using a CCD camera and a photodetector. The camera is used to identify the fundamental TEM_{00} mode of the cavity. The photodetector evaluates the quality of the lock. The wavelengths are discriminated by an optical filter placed on a flip mount.

For optimal flexibility, it should be possible to stabilise the Rydberg laser systems to an

arbitrary frequency within their tuning range. Since the resonance frequencies of the cavity are not tunable, a variable frequency offset f_{shift} between laser frequency and cavity resonance is required. The frequency range of f_{shift} is required to cover the free spectral range (FSR) of the cavity. Figure 6.7 (b) shows a simplified scheme of the sideband spectrum used for PDH stabilisation. A fiber EOM (Jenoptik PM785 / Jenoptik PM980) is used to generate sidebands at an offset frequency f_{shift}. The fiber EOM is driven by a synthesiser (Siglent SSG3021X) connected to the experimental control system. A resonant free-space EOM (Qubig PM7-NIR) is used to imprint sidebands at the PDH frequency f_{PDH} to each frequency component of the light field. In this configuration, it is possible to apply PDH stabilisation to one of the sidebands generated by the fiber EOM thereby allowing for shifting the lock point by tuning f_{shift}. Choosing $f_{PDH} = 20\,\text{MHz}$ at $780\,\text{nm}$ and $f_{PDH} = 25\,\text{MHz}$ reduces crosstalk between the PDH locks at $780\,\text{nm}$ and $960\,\text{nm}$. Due to the large bandwidth of the fiber EOM, it is possible to set f_{shift} between $200\,\text{MHz}$ and $>1.7\,\text{GHz}$ such that more than one FSR ($1.5\,\text{GHz}$) is covered . The lower bound is chosen such that the PDH sideband manifolds are well separated. The modulation index for modulation at f_{PDH} is set to the optimal value of $M = 1.08$ [100] corresponding to an power ratio of $J_1(M)^2/J_0(M)^2 \approx 0.41$ between first sideband and carrier (Eq. 4.2). The optimal modulation index for the modulation at f_{shift} maximises the optical power of the first-order sidebands. This is the case for $M = 1.84$ corresponding to a fraction of $J_1(M)^2 \approx 0.34$ of the total power in each first-order sideband. Note, that only this fraction contributes to the signal while the shot noise level is determined by the total power incident to the photodetector.

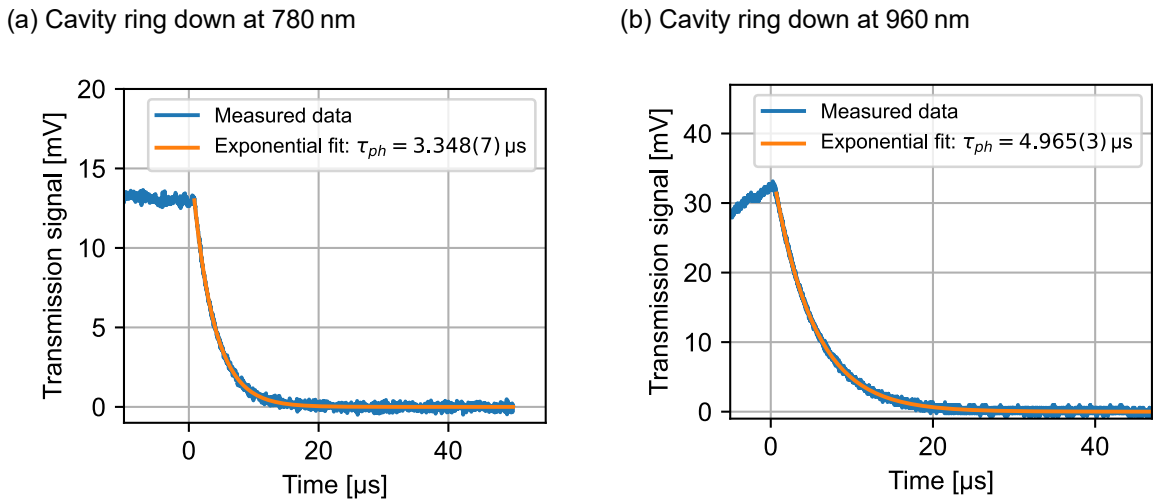

Fig. 6.8.: Cavity ring down measurements at $780\,\text{nm}$ (a) and $960\,\text{nm}$ (b). An exponential decay (orange) is fitted to the measured data (blue). The plot range indicates the data points used for the fit. The 1/e-decay time τ_{ph} obtained from the fit is stated in the legend.

The finesse of an optical cavity is defined as the ratio of its FSR and its spectral full width at half maximum (FWHM) Δf_{FWHM}. It is related to the reflectivity of the cavity mirrors R by [140, Chap. 11]

$$\mathcal{F} := \frac{FSR}{\Delta f_{FWHM}} = \frac{\pi\sqrt{R}}{1-R} \tag{6.1}$$

assuming identical R for both mirrors for simplicity. The photon decay rate in the cavity

τ_{ph} is related to the reflectivity of the mirrors by [140, Chap. 11]

$$R = e^{-\frac{1}{2\,FSR\,\tau_{ph}}}. \tag{6.2}$$

The photon decay rate is measured by stabilising a laser system to the cavity and switching off the incident beam rapidly while recording the transmission of the cavity with a photodetector. For switching, AOMs are employed achieving fall times below 50 ns. Figure 6.8 (a) shows the results of this *ring-down measurement* at a wavelength of 780 nm and Figure 6.8 (b) at 960 nm, respectively. An exponential decay is fitted to the data points in order to determine τ_{ph}. The plot range of the fit (orange) indicates the data points used for exponential fitting. The results and other specifications of the cavity are summarised in Tab. 6.3. The stated finesse values are calculated according to Eq. 6.1 using the specified value for R or calculating R using Eq. 6.2 and the measured values for τ_{ph}. The measured finesse at 780 nm is in good agreement with the coating specifications while the measured finesse at 960 nm is significantly higher than expected. The free spectral range of the cavity is measured with high accuracy using the monitoring beat signal of the 780 nm laser system depicted in Fig. 6.1. This beat signal is also used to determine the value of the zero crossing temperature which has been determined previously. [62]

Quantity	**Specification**	**Measured**	**Conditions**
Free spectral range (FSR)	1500 MHz	$1496.923(10)$ MHz	$\lambda = 780$ nm
Long-term frequency drift	<10 kHz/d		
Finesse at 780 nm	$34\,180$	$31\,600(500)$	Spec. calculated from R
Finesse at 960 nm	$30\,610$	$46\,700(300)$	Spec. calculated from R
Zero crossing temperature	<50 °C	$29.47(7)$ °C	At vacuum housing

Tab. 6.3.: Overview of the specifications of the high-finesse cavity used in this work. The manufacturer's specification are compared to our measurements.

6.4. Pound-Drever-Hall frequency stabilisation of the Rydberg laser system

The Pound-Drever-Hall (PDH) technique is commonly used for laser-frequency stabilisation. [99, 100] It offers a frequency resolution enhanced by up to several orders of magnitude as compared to the linewidth of the optical reference cavity and a feedback bandwidth up to tens of MHz. [100] The PDH scheme relies on phase modulation of the light coupled into the cavity at a modulation frequency f_m. As discussed in detail in Sec. 4.2, the phase modulation imprints sidebands on the light field. The frequency offset of the sidebands is given by an integer multiple of f_m . The amplitudes are determined by the modulation index M according to Eq. 4.2. By choosing $f_m \gg \Delta f_{FWHM}$, the sidebands are reflected from the cavity if the carrier frequency is close to a cavity resonance. In this case, the amplitude of the beat note between carrier and sidebands is proportional to the frequency deviation. A suitable error signal is obtained by phase sensitive demodulation of the beat signal. In this work, a module for PDH error-signal generation is developed. The device is characterised in this section. Furthermore, an electronic setup for PDH stabilisation of the Rydberg laser system is described. Note, that there exist two alternative approaches for the stabilisation of the 960 nm system (compare

Sec. 6.1). Currently, a commercial reference laser (Toptica DL100) is locked to the cavity and a phase lock between the reference laser and the Rydberg system is implemented as described in Sec. 4.3. This scheme does not involve EOMs which were not available when the system has been installed. For optimal performance, the locking scheme will be upgraded to a direct lock similar to the scheme used for the 780 nm system. In this section, the current implementation is described.

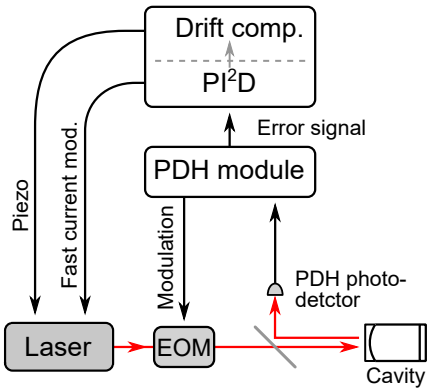

Fig. 6.9.: Simplified scheme of PDH laser stabilisation to a reference cavity. The EOM based phase modulation may be replaced by direct modulation of the laser current using a bias tee.

Figure 6.9 shows the scheme applied to lock the Rydberg laser systems to a resonance of the high-finesse cavity. The intensity reflected from the cavity is detected using the PDH photodetectors characterised in Sec. 3.8. The PDH error signal is generated by a PDH module developed in this work (see Sec. 6.5 for details). The required phase modulation is generated using a free-space EOM (QUBIG PM7-NIR) or direct modulation of the laser current via a bias tee. The PDH module also provides a suitable modulation signals. Frequency stabilisation is realised by a fast analog controller. Different controllers are used for the 780 nm-system (Vescent D2-125) and for the 960 nm system (Toptica FALC110). The functionalities of both controllers used in this work and their performance are similar. Both controllers feature a proportional (P), two integral (I), and a derivative (D) part with adjustable corner frequencies. The controller acts on the laser current via a fast modulation input in the laser head, e.g. as realised via the current-modulation technique discussed in Sec. 3.5. A drift compensation holds the average output of the fast controller at zero by controlling the laser piezo voltage with a slow I controller.

The analog controllers used in this work offer a multitude of different configurations affecting their transfer function. Optimal control parameters are determined empirically within the parameter tuning range of the controllers by minimising the in-loop error-signal noise. Figure 6.10 shows schematic transfer functions of the controllers for the 780 nm system (a) and the 960 nm system (b). Settings for the adjustable integral corner frequencies f_{I1}, f_{I2}, and derivative corner frequencies f_D as well as the -3 dB-bandwidth are marked in the plot f_{BW}. For the 780 nm system (a), a PI^{2}D controller is implemented. While the gain of the D controller is limited, the I controllers are not limited. In contrast, two limited I controllers are used for the 960 nm system (b). Identical derivative controllers are chosen for both systems. The main gain setting of both controllers shifts the gain of the entire transfer function. This setting is adjusted for a minimum residual noise and reduced gain-bandwidth peaking.

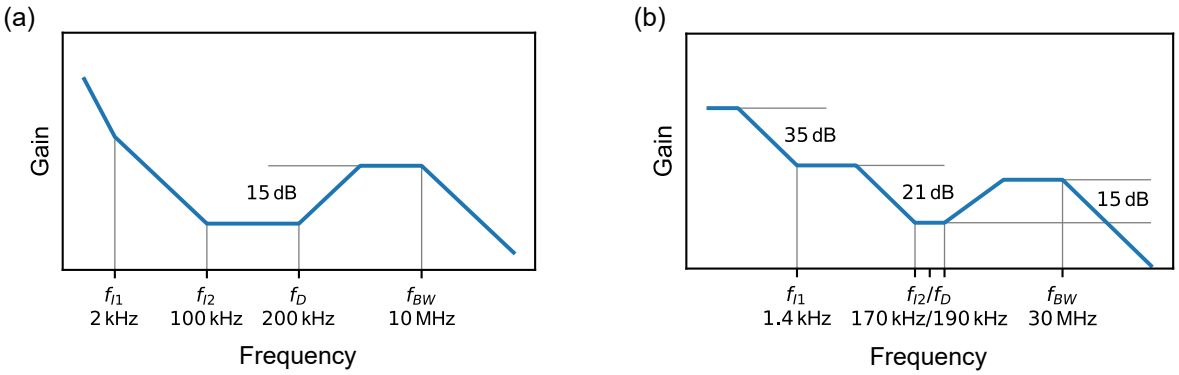

Fig. 6.10.: Schematic transfer functions of the controllers configured for the 780 nm Rydberg laser system (a) and the 960 nm Rydberg laser system (b).

6.5. Pound-Drever-Hall module based on direct digital synthesis

Error signal generation in the PDH scheme relies on phase sensitive demodulation of a photodetector signal at a frequency between 10 MHz and 100 MHz. In this section, an electronic PDH module is presented that provides a suitable modulation signal and generates a low-noise error signal from a photodetector signal. The module is available in a GitHub repository. [167]

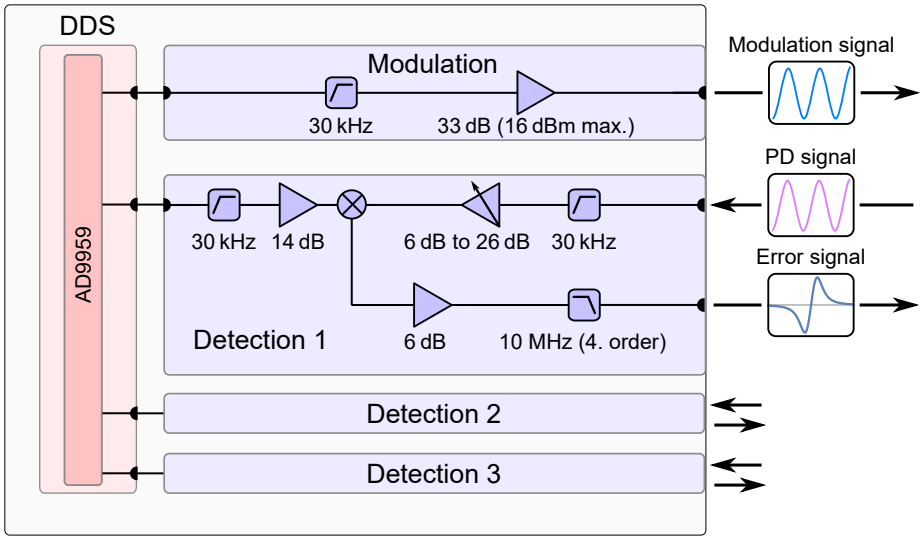

Fig. 6.11.: Block diagram of the PDH module developed in this work. Based on a DDS board, a modulation signal is amplified to the required signal level. A detection sub-module generates the error signal by phase-sensitive demodulation of a photodetector (PD) signal. The module offers up to three PDH signals from the same phase modulation. Relevant cut-off frequencies, gains and maximum output powers are denoted under the respective components.

The signal generation is based on direct digital synthesis (DDS) with a 4-channel chip (Analog Devices AD9959). This method offers a high frequency accuracy and excellent phase stability between all channels while allowing for straightforward tuning of frequency and phase. Low-cost, stand-alone DDS boards (Gra&Afch DDS AD9959 Arduino Shield) are used. However, it is also possible to equip the PDH module with a different type of DDS board. The

PDH module is implemented as a standard size PCB. The PCB and the DDS board are combined in a compact 19”-rack mount unit. Figure 6.11 shows a block diagram of the PDH module. The modulation signal at the PDH frequency f_{PDH} is provided by one channel of the DDS board. The signal is amplified using a high-gain amplifier with a maximum output power suitable for driving a typical resonant EOM at the optimal modulation index. When modulating the laser current via a bias tee, the amplifier is not used. The error signal is generated by a detection sub-module using a second channel of the DDS for demodulation. The modulation is realised using an analog diode-ring frequency mixer (Mini Circuits SYPD-1+). Both input signals are amplified to the optimal signal level of the mixer. For that purpose, a variable amplifier stage for the photodetector input is available. The output of the frequency mixer is amplified to cover a voltage range of approximately $\pm 1\,\mathrm{V}$ at $50\,\Omega$. The signal contains the demodulated signal and undesired signals at the sum frequency $2f_{PDH}$ as well as at f_{PDH} due to the finite isolation of the mixer. In order to suppress these signals, a low-pass filter at the output of the mixer is required. This filter sets the bandwidth of the error-signal generation. A 4th-order Chebyshev filter realised with a low-noise filter building block (Analog Devices LT1568) offers the required suppression while maintaining a large bandwidth. In the default configuration, the filter exhibits a cut-off frequency of $10\,\mathrm{MHz}$ and a phase-lag less than $90°$ for frequencies below $5\,\mathrm{MHz}$. If the application offers a limited bandwidth only, e.g. due to a low-bandwidth actuator, the cut-off frequency ($-3\,\mathrm{dB}$) can be adjusted between $200\,\mathrm{kHz}$ and $10\,\mathrm{MHz}$. Since there are two additional DDS channels available, it is possible to use up to three demodulation modules to derive different PDH stabilisations from the same phase modulation. A possible class of applications includes stabilising the modulated laser to a reference cavity and stabilising tunable cavities, such as frequency-doubling systems or transfer cavities, to the stabilised laser system.

6.6. Laser-linewidth measurements

The frequency stabilisation scheme of the Rydberg laser systems discussed previously is optimised for minimising decoherence effects in coherent Rydberg excitations due to laser frequency and phase noise, where the first term refers to the frequency noise constituting the line shape of the laser field while the latter refers to laser phase fluctuations contributing to the line wings. [130, 131] In order to evaluate the performance of the stabilisation schemes, suitable figures characterising decoherence effects are determined in this section. Laser-frequency noise is evaluated in terms of an in-loop measurement using the PDH error signal as a frequency discriminator. For the $960\,\mathrm{nm}$ laser systems presented in Sec. 6.1, the delayed self-heterodyne method is applied in order to obtain a linewidth measurement independent of the reference cavity. The reference laser is compared to the Rydberg laser system. The linewidth of both systems without active frequency stabilisation is determined.

A well established method for determining laser linewidths is the delayed self-heterodyne method (DSH). The method has been proposed for the first time in [168]. The output of the laser is split in two parts. One part is shifted by a constant frequency while the other part is delayed by a time τ_d that is ideally much larger than the coherence time of the laser. Combining the two parts on a photodetector allows for detection of a beat note at the shift frequency. Due to the long delay time, both laser fields are uncorrelated. The observed beat note is treated as a beat note between two laser exhibiting equal frequency noise. Typically, laser-frequency noise is well described by considering a white noise component and a $1/f$ noise component. [169]

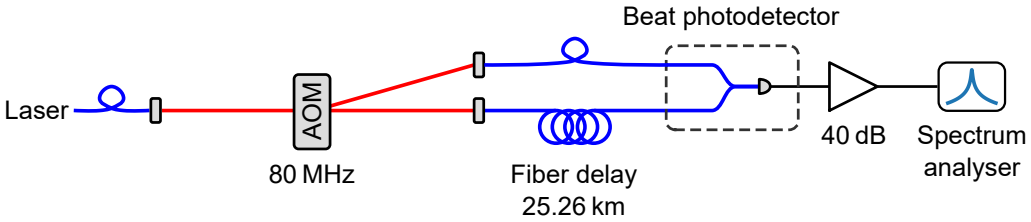

Fig. 6.12.: Simplified setup for delayed self-heterodyne linewidth measurements. The application of the setup is limited to wavelengths above $960\,\mathrm{nm}$ due to losses in the fiber delay line.

In this case, the line shape is given by a Voigt function [170] defined as the convolution

$$V_{\gamma_G,\gamma_L}(f) = \int_{-\infty}^{\infty} G_{\gamma_G}(f')L_{\gamma_L}(f-f')\,df \tag{6.3}$$

between a Gaussian function G_{γ_G} with width γ_G (FWHM) and a Lorentzian function L_{γ_L} with width (FWHM) γ_L. From this definition follows that the line shape is Gaussian, if $\gamma_G \gg \gamma_L$ and Lorentzian if $\gamma_L \gg \gamma_G$. The width γ_V of V_{γ_L,γ_G} is well approximated by [171]

$$\gamma_V = \frac{\gamma_L}{2} + \sqrt{\frac{\gamma_L^2}{4} + \gamma_G^2}. \tag{6.4}$$

The beat of two Lorentzian lines exhibits a width of $2\gamma_L$ while the beat of two Gaussian lines yield a width of $\sqrt{2}\gamma_G$. The noise contributions of the Voigt function derived from the beat-note spectrum are rescaled accordingly. Especially for narrow linewidth laser systems, the delay required for sufficiently uncorrelated measurements is not feasible. Thus, the delay may be below or on the order of the coherence time. Due to the cut-off for frequencies below $1/\tau_d$, DSH systematically underestimates strong $1/f$ noise [170] while white noise effects are overestimated by coherence in the DSH interferometer. [172] We are mainly interested the latter since $1/f$ noise is compensated by the laser-frequency control loop.

Figure 6.12 shows a simplified scheme of the optical setup employed for the DSH in this work. The light field under test is delivered by an optical fiber. The frequency shift is realised by an AOM (Isomet IMD80DH-780) driven by a synthesiser at its central frequency of $80\,\mathrm{MHz}$. A single-mode fiber (Corning SMF-28) with a length of $25.26\,\mathrm{km}$ is used as a delay line for the zeroth order beam of the AOM. This fiber type is optimised for telecom wavelengths of $1310\,\mathrm{nm}$ and $1550\,\mathrm{nm}$. However, a linewidth measurement with a loss of approximately $30\,\mathrm{dB}$ at $960\,\mathrm{nm}$ is still feasible, if a sufficient amount of laser power ($> 10\,\mathrm{mW}$) is available. Application to a wavelength of $780\,\mathrm{nm}$ is not possible due to significantly larger losses. As estimated from the data sheet [173], the fiber features an effective index of refraction of $1.47(1)$ at $960\,\mathrm{nm}$ resulting in $\tau_d = 124(1)\,\mu\mathrm{s}$. For detection of the beat note, the fiber-based beat-note photodetector described in Sec. 4.3 is used. The detector is optimised for infrared wavelengths by employing an InGaAs photodiode (Thorlabs FGA01FC). Suitable amplification is applied to the photodetector signal. The beat-note spectrum is obtained by a spectrum analyser (Tektronix RSA306). The commercial reference laser system (Toptica DL100) and the Rydberg laser system based on our ECDL design (see Sec. 6.1 for details) are operated at a wavelength of $960\,\mathrm{nm}$ suitable for the DSH setup.

The performance of an active frequency stabilisation is strongly affected by the passive stability of the laser system. Hence, the linewidth of the reference system and the Rydberg

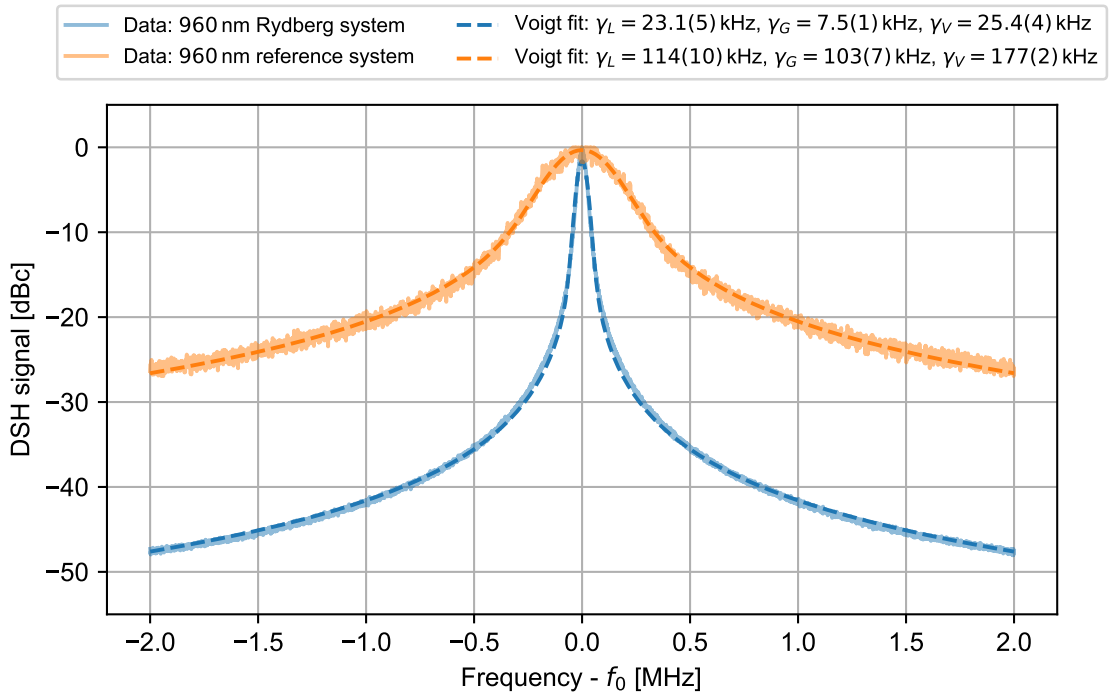

Fig. 6.13.: Line shapes of the 960 nm Rydberg laser system (blue) and the reference laser system (orange) as obtained by DSH measurements. The frequency of both laser systems is not stabilised. The Rydberg laser system is based on the ECDL design presented in Sec. 3.1 while the reference laser is a commercial system (Toptica DL100). Voigt functions are fitted to the data points (dashed). The resulting parameters γ_L and γ_G are stated in the legend. The values are rescaled to represent the laser linewidths. The linewidth (FWHM) γ_V is calculated from the fitted values.

system are analysed without active frequency stabilisation. Figure 6.13 shows the results of the measurement. The spectra are shifted by the AOM frequency (80 MHz) and normalised to their maximum for convenience. The Gaussian contribution and the Lorentzian contribution of the line are determined by fitting V_{γ_G,γ_L} to the measured spectra. An efficient Voigt fit is realised exploiting the relation to the Faddeeva function [174] and their powerful Python implementation *scipy.special.wofz()* (see Appendix B.1 for details). The stated values are rescaled to represent the linewidth of the laser. Both spectra are in excellent agreement with the fitted Voigt functions. The passive linewidth of the Rydberg system (blue) is substantially smaller than the linewidth of the reference system (orange). This can be attributed to our superior ECDL design optimised for passive stability as discussed in Sec. 3.1. For the Rydberg system, the line shape is predominantly Lorentzian indicating a low level of $1/f$ noise above the cut-off frequency $1/\tau_d \approx 8$ kHz. In contrast, for the reference laser the $1/f$ contribution leads to a significant broadening. As described in Sec. 6.1, the frequency of Rydberg laser system is stabilised relative to the reference laser system using a phase lock. The DSH line center of both laser systems are depicted in Figure 6.14 in a linear scale. Both spectra are not distinguishable in this frequency range. This behaviour is expected due to the properties of the phase lock and the fact that the Rydberg laser features a significantly smaller passive linewidth. The Voigt fits yield a linewidth of 1 kHz dominated by the Lorentzian line shape for both lasers. The PDH lock of the reference laser defining the linewidth is able to reduce the passive linewidth of the

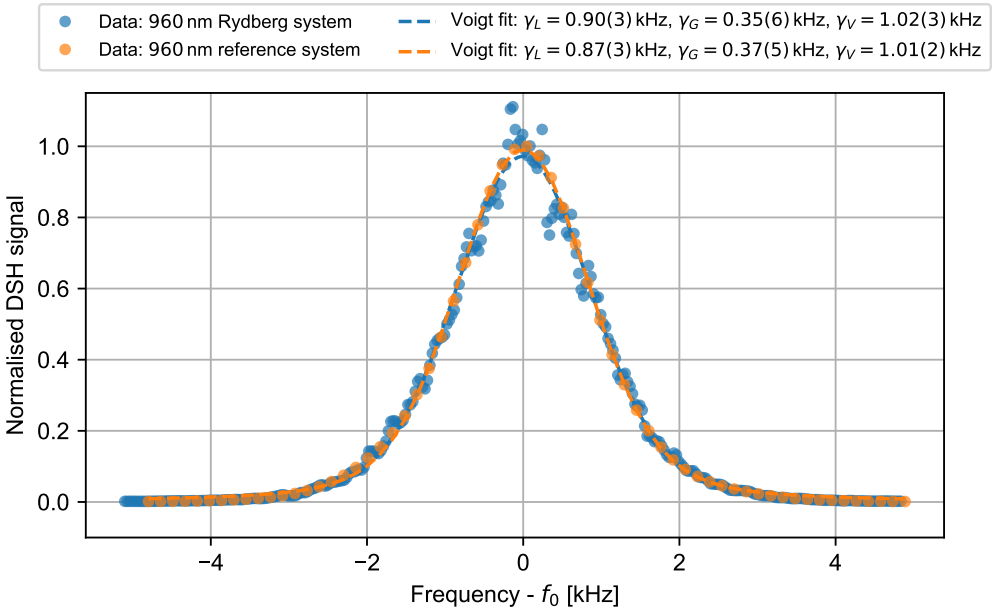

Fig. 6.14.: Line center of the DSH spectra for the $960\,\mathrm{nm}$ Rydberg laser (blue) and reference laser (orange). The reference laser is locked to a high-finesse cavity and the Rydberg laser is phase locked to the reference laser. Voigt profiles are fitted to the measured data (dashed lines). The resulting parameters γ_L and γ_G are stated in the legend. The values are rescaled to represent the laser linewidths. The linewidth (FWHM) γ_V is calculated from the fitted values.

reference laser by more than two order of magnitude. The $1/f$ noise contribution is reduced to a negligible level. This measurement also shows that the linewidth contribution added by the phase-lock scheme described in Sec. 4.3 is negligible, even for high-performance locking schemes, justifying the assumption that the linewidth of the phase-locked Rydberg laser system is given by the linewidth of the reference laser.

The sensitivity of coherent Rydberg excitation to laser phase and frequency noise is high at frequencies comparable to the Rabi rate which is expected to be in the MHz region. [61] Figure 6.15 shows the single sideband spectrum of the DSH signal for the stabilised Rydberg laser system (blue) and the stabilised reference laser system (orange) in the relevant frequency range. Due to the frequency control loops, both spectra deviate significantly from the line wings predicted by the Voigt profile describing the line center. A similar profile with pronounced side lopes is derived in [131] using an heuristic frequency-noise model predicting a reduction of the frequency noise within the bandwidth of the control loop only. The phase lock of the Rydberg laser system (blue) constitutes a non-negligible noise contribution for frequencies within its bandwidth. The performance of the lock may be enhanced by reducing the gain bandwidth peaking by adapting the control parameters or by increasing the bandwidth using our laser-current modulation technique (Sec. 3.5). However, even for an optimal phase lock, the Rydberg system is expected to exhibit the noise level of the reference system. For the locked laser systems, the coherence time $\tau_c = 1/\gamma_V \approx 1\,\mathrm{ms}$ is larger than the fiber delay τ_d. In this case, the interpretation of the DSH spectrum is complex since the laser fields are correlated leading to coherent effects in the DSH interferometer. However, the ratio between coherence time and

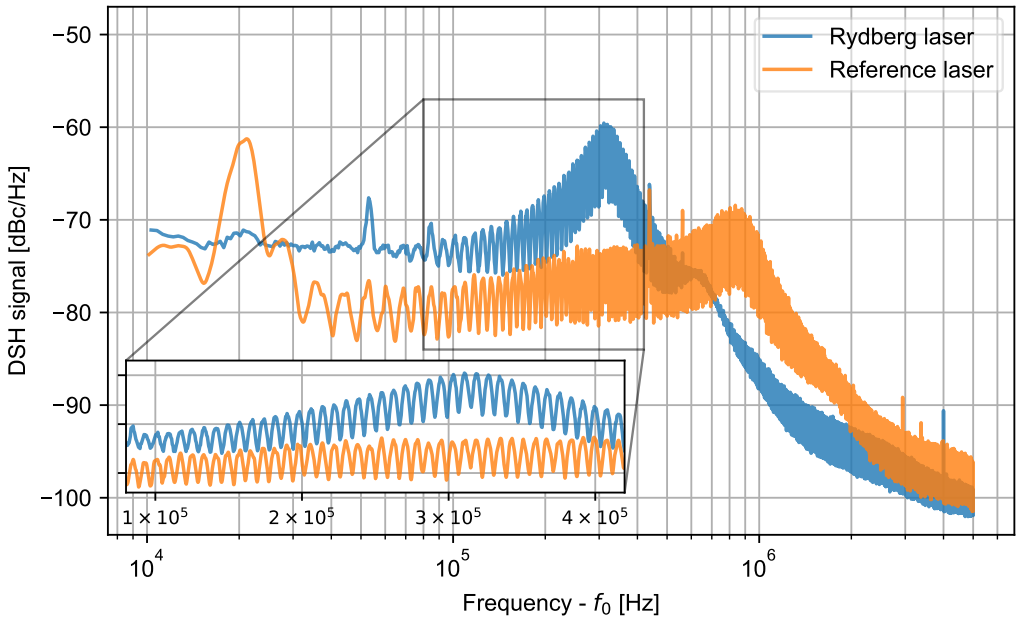

Fig. 6.15.: DSH-sideband spectra describing the line wings of the 960 nm Rydberg laser (blue) and the 960 nm reference laser (orange). The reference laser is locked to a high-finesse cavity and the Rydberg laser is phase locked to the reference laser. The inset reveals fringes of DSH interferometer observable due to the high coherence of the laser system.

fiber delay is still in a region where the laser-line shape dominates the DSH signal. [175] As expected, the spectrum shows pronounced fringes with a distance $1/\tau_d \approx 8$ kHz throughout the entire spectrum depicted here (compare inset). This effect confirms that the coherence time of both lasers is significantly larger than the fiber delay of 124 µs.

An estimate for the frequency-noise spectral density is obtained by analysing the error signal while the laser is locked. This methods allows for a direct measurement of the remaining frequency fluctuations using the high-finesse cavity as a frequency discriminator. Frequency noise induced by the cavity and the error-signal generation is neglected due to the in-loop character of the measurement. The method is applied to the 780 nm Rydberg laser system that cannot be analysed using our DSH setup.

The slope of the error signal D in the linear region close to its zero crossing is estimated from the error signal peak-to-peak amplitude V_{error} and the bandwidth of the cavity $\Delta f_{FWHM} = \frac{FSR}{\mathcal{F}}$ by [100]

$$|D| = 4\frac{V_{error}}{\Delta f_{FWHM}}. \tag{6.5}$$

The voltage-noise spectral density of the error signal is linked to the frequency-noise spectral density by D. The voltage-noise spectral density is obtained by fast Fourier transform of an oscilloscope signal (Rigol MSO7014). For an optimal amplitude resolution, Welch's method is employed as implemented by the Python function *scipy.signal.welch()*. Figure 6.16 shows the frequency-noise spectral density obtained by this method for the 780 nm Rydberg laser system

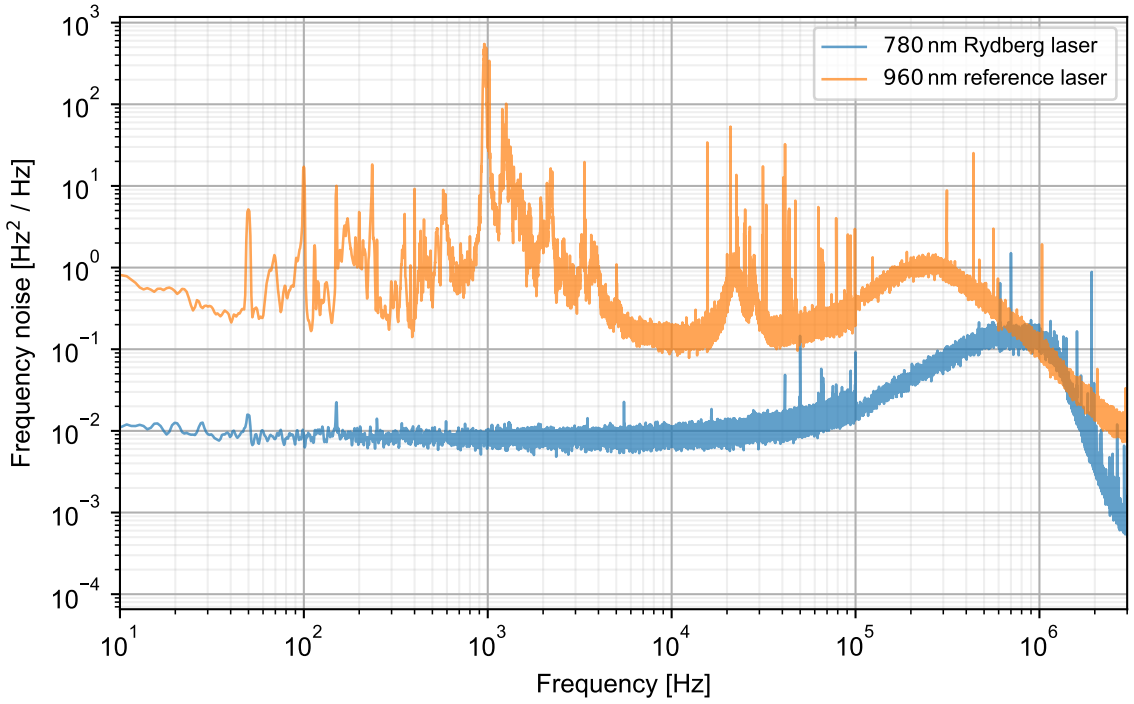

Fig. 6.16.: Frequency-noise spectral density of two laser systems stabilised to a high-finesse cavity. The noise spectrum is derived from the in-loop error signal.

(blue) and the 960 nm reference laser system (orange). Both systems exhibit a remarkably low frequency-noise level. For white frequency noise at a level h_0 the line shape is Lorentzian with linewidth πh_0. [131] Thus, the baseline obtained for both lasers in this measurement corresponds to a linewidth below 10 Hz. These results shows that a tight lock to the cavity is established. The commercial reference laser system shows several sharp noise peaks in the acoustic frequency range while a flat frequency-noise spectrum is observed for the 780 nm system. The enhanced performance can be attributed to the superior passive stability of our ECDL design as well as the robust signal generation based on EOMs. Furthermore, for the 960 nm reference laser system, a prototype of the PDH module is used that is less compact and does not feature the filter and amplifier stages at the output of the mixer (see Sec. 6.5 for details). However, for the 960 nm reference laser system, the obtained values tremendously underestimate the linewidths as compared to the independent DSH method.

Measurement	**Laser system**		
	Rydberg (960 nm)	Reference (960 nm)	Rydberg (780 nm)
DSH unlocked γ_V	25.4(4) kHz	177(2) kHz	
DSH locked γ_V	1.02(3) kHz	1.01(2) kHz	
In-loop frequency noise		$\sim$1 Hz^2/Hz	0.01 Hz^2/Hz (typ.)

Tab. 6.4.: Overview of all linewidths and frequency-noise values determined in this section.

All linewidths and noise values determined in this section are listed in Table 6.4. For the

780 nm system, only the in-loop measurement is available. This measurement suggests a noise level below the level of the 960 nm system. The noise contributions neglected by the measurement can be assumed to be similar for both laser systems such that the linewidth of the 960 nm reference laser system may be used as an upper bound for the linewidth of the 780 nm Rydberg system.

6.7. Decoherence effects due to laser phase and frequency noise

When considering coherent atom-light interactions, phase and frequency noise of the light field constitute serve decoherence effects. Quantifying these effects is a challenging task since a highly non-trivial sensitivity function connecting the phase-noise spectral density and decoherence of the system is involved. [176] The exact shape of this function strongly depends on the system under investigation. In this work, we follow the simpler numerical approach presented in [61]. Random samples of noisy light fields are generated. Solving the time-dependent Schrödinger equation numerically and averaging over a large number of realisations allows us to evaluate the effects of a given noise model. This approach links the measured laser-frequency noise to an expected decay of the Rabi oscillations observed in our system.

We consider a two-level atom system in a classical light field. The laser phase noise is described by a stochastic process $\phi(t)$. The time dependence of the classical laser field with angular frequency ω_L is given by

$$E(t) = E_0 \cos(\omega_L t + \phi(t)). \tag{6.6}$$

Applying the standard derivation and approximations describing Rabi oscillations (see e.g. [32, Sec. 2.3.2]) yields the time-dependent interaction Hamiltonian

$$\hat{H}_{int}(t) = \frac{\hbar}{2} \begin{pmatrix} \Delta & \Omega e^{i\phi(t)} \\ \Omega e^{-i\phi(t)} & -\Delta \end{pmatrix} \tag{6.7}$$

governing the dynamics of the system with Rabi rate Ω and detuning $\Delta = \omega_L - \omega_0$ where $\hbar\omega_0$ is the energy spacing of the two-level system. The Hamiltonian is denoted in the standard basis. The Python package *QuTiP* [177] is used to solve the time-dependent Schrödinger equation for a given sample of $\phi(t)$. Damped Rabi oscillations are observed when averaging over 100 to 1000 realisations. A description of the damping is derived by introducing a heuristic decay rate γ to the optical Bloch equations yielding damped Rabi oscillations [178, Sec. 2.8]

$$P_{|e\rangle}(t) = \frac{\Omega^2}{\gamma^2 + 2\Omega^2} \left[1 - \left(\cos(\tilde{\Omega} t) + \frac{3\gamma}{4\tilde{\Omega}} \sin(\tilde{\Omega} t) \right) e^{-\frac{3}{4}\gamma t} \right] \tag{6.8}$$

with modified Rabi frequency $\tilde{\Omega} = \sqrt{\Omega^2 - \frac{\gamma^2}{16}}$. In the following discussion, the rate γ is used as a measure for the decoherence of the system. The phase-noise process inducing the decoherence in the system is defined by its power spectral density. The following strategy is employed to create a random sample of $\phi(t)$ with a defined PSD in each realisation. A noise model describing the PSD is derived either from measured data, if available, or from calculations. An uncorrelated sample of normal distributed random numbers is produced. The sample is Fourier transformed via fast Fourier transform (FFT). Weighting each data point with the amplitude of the noise model at the given Fourier frequency introduces suitable correlations. The correlated sample is obtained by inverse FFT. The corresponding Python code can be found

in Appendix. B.2. Figure 6.17 (top) shows a typical random sample of the correlated noise obtained using this scheme. The PSD of the noise sample (bottom, blue) approximates the noise model (bottom, orange) accurately over a large frequency range.

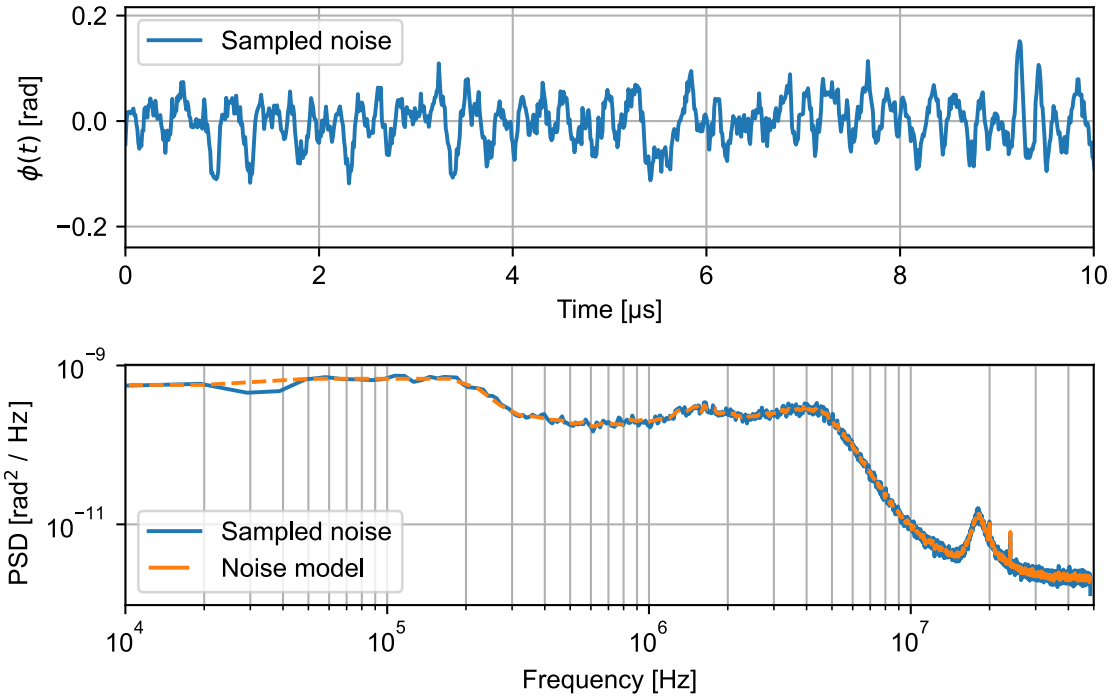

Fig. 6.17.: Illustration of a scheme for generating correlated noise. (top) Detail of a random sample of correlated phase noise with 1×10^6 data points and a sampling rate of $1 \times 10^8\,1/\mathrm{s}$. (bottom) The correlations are designed such that the power spectral density (PSD) of the noise sample (blue) approximates a noise model derived from measured data (orange).

6.7.1. Rydberg laser system

The Rydberg lasers employed in the two-photon excitation scheme are assumed to be uncorrelated, such that the relevant phase-noise PSD is given by

$$S_\phi = S_{\phi,780} + 4S_{\phi,960} \tag{6.9}$$

where $S_{\phi,780}$ is the contribution of the $780\,\mathrm{nm}$ Rydberg laser and $S_{\phi,960}$ of the $960\,\mathrm{nm}$ Rydberg laser respectively. The factor of four originates from the frequency doubling stage and the quadratic scaling of the PSD. For simplicity, we assume $S_{\phi,780} = S_{\phi,960}$. This assumption overestimates the phase noise slightly. In this case, the effective phase noise contribution of both laser systems will be dominated by the frequency doubled $960\,\mathrm{nm}$ system. Determining $S_f(f)$ for a narrow linewidth laser system is a challenging task. The in-loop measurements presented in Sec. 6.6 underestimate the frequency noise drastically. Thus, we will rely on the DSH measurements. Relating the results of a DSH measurement to S_f requires a model for S_f due to the complex form of the laser field autocorrelation function. For the Rydberg laser system, a heuristic model for servo controlled system is used [131]

$$S_f(f) = \begin{cases} h_0 & \text{for } f \leq f_{bw} \\ h_1 & \text{for } f > f_{bw} \end{cases}. \tag{6.10}$$

Within the servo bandwidth f_{bw}, the frequency noise is suppressed to a level h_0, while the level h_1 of the laser without stabilisation is approached beyond the bandwidth. The levels h_i are derived from the DSH linewidths γ_i by $\gamma_i = \pi h_i$ assuming pre-dominantly white frequency noise. This results in $h_0 \approx 1.6 \times 10^3\,\mathrm{Hz}^2/\mathrm{Hz}$ and $h_1 \approx 4.0 \times 10^4\,\mathrm{Hz}^2/\mathrm{Hz}$. The bandwidth is set to $f_{bw} = 300\,\mathrm{kHz}$ as suggested by the DSH side lopes observed in Sec. 6.6.

The relevant PSD S_ϕ of the phase-noise process $\phi(t)$ is related the frequency-noise PSD S_f by [136]

$$S_\phi(f) = \frac{S_f(f)}{f^2}. \tag{6.11}$$

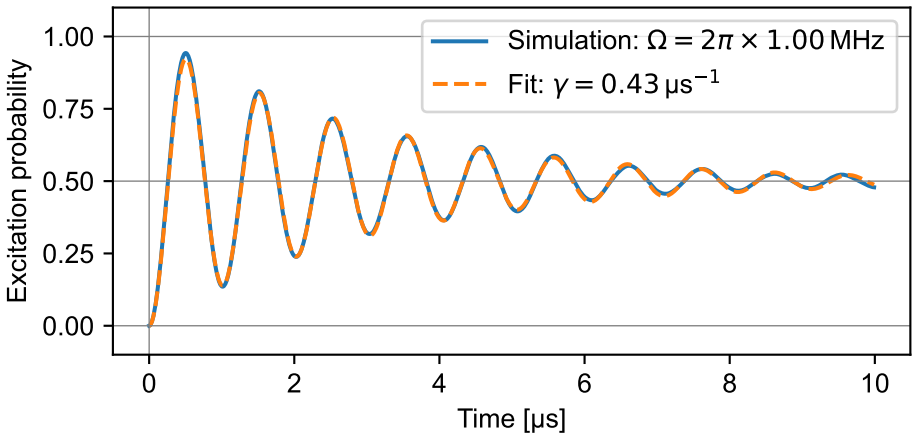

Fig. 6.18.: Simulation of Rabi oscillations with a noisy laser field (blue). The frequency noise is chosen according to measurements determining the linewidths of the Rydberg laser system. The model given by Eq. 6.8 is fitted to the simulation results (orange, dashed). The obtained value of γ as stated in the legend yields a measure for the decoherence of the system: $2\pi\gamma/\Omega = 0.43$.

Figure 6.18 shows a typical result of the simulation with a Rabi frequency $\Omega = 2\pi \times 1\,\mathrm{MHz}$. The model stated in Eq. 6.8 is fitted to the data obtained by the simulation yielding a value for γ. The model is in an excellent agreement with the simulation results. As a measure for decoherence, the dimensionless value $2\pi\,\gamma/\Omega$ is introduced. This value can be interpreted as decays per Rabi cycle. Since a notable damping of the Rabi oscillations is observable, this simulation shows that the decoherence effect discussed here is relevant at the present noise level of the laser system. Thus, the fidelity of coherent Rydberg excitations is expected to benefit from further improvements of the system. Note, that there are other decoherence effects with a similar strength that have been studied previously. [62] Namely, spontaneous emission from the intermediate state and Doppler broadening due to the finite temperature of the trapped atoms.

Due to the $1/f^2$-scaling of S_ϕ induced by constant frequency noise, the noise model is strongly frequency dependent. Phase noise at frequencies $f \ll \Omega/(2\pi)$ is approximately constant during

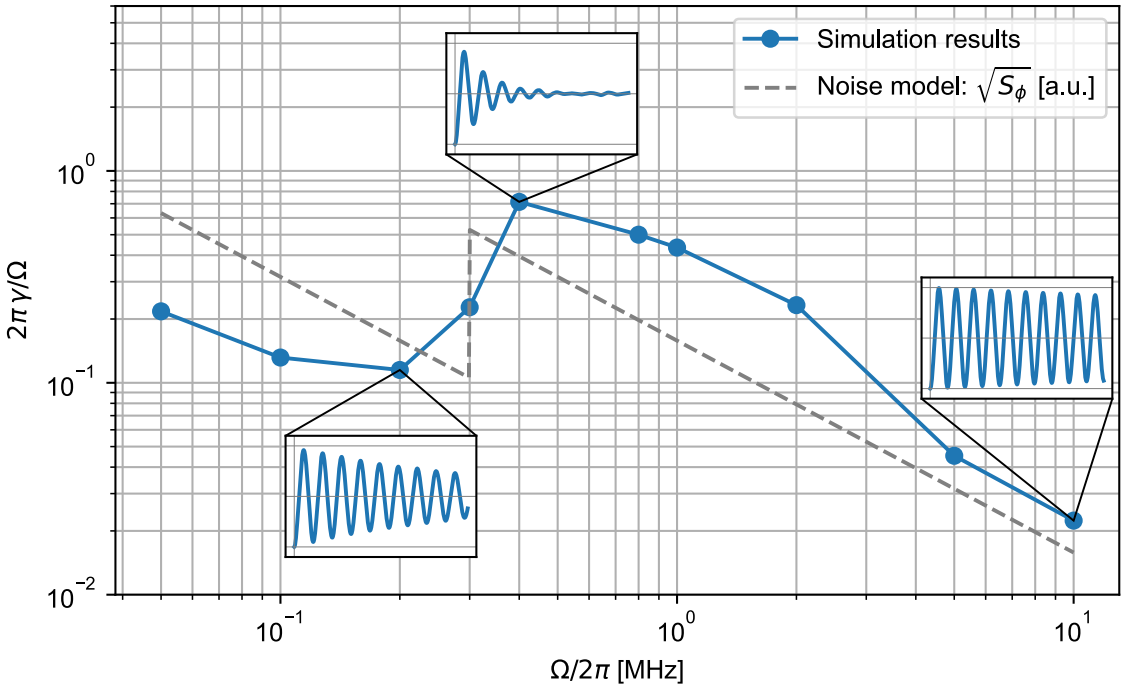

Fig. 6.19.: Simulated decoherence quantified by $2\pi\gamma/\Omega$ for different Rabi frequencies (blue). The simulation results for the marked data points are displayed in the insets. For comparison, the spectral density of the noise model used for simulation is depicted in arbitrary units (a.u.).

a Rabi cycle and can thus be neglected while phase noise at $f \gg \Omega/(2\pi)$ is averaged during a Rabi cycle. Hence, the decoherence of the system is expected to depend pre-dominantly on the phase-noise PSD at the Rabi frequency. Figure 6.19 shows the decoherence measure $2\pi\,\gamma/\Omega$ for different Rabi frequencies. Pictograms of the simulation results corresponding to characteristic data points are depicted in insets. For comparison, the spectral density of the noise model ($\sqrt{S_\phi}$) is shown rescaled by a constant factor to fit the plotting range. As expected, the decoherence in the system is correlated to $\sqrt{S_\phi}$. The general trend shows that decoherence is reduced for larger Rabi rates due to the underlying f^{-2}-scaling of S_ϕ. For Rabi frequencies close to the servo bandwidth, undesirable decoherence effects are observable. In this region unexpected effects may occur when tuning the Rabi frequency. However, the local behaviour of the noise model used here is oversimplified since there will be a transient regime from servo controlled frequency range to the unlocked region. Hence, the decoherence effects for Rabi frequencies close to the control bandwidth are likely to be overestimated by the simulation.

6.7.2. Raman laser system

The results presented in Sec. 4.4 provide an accurate model for S_ϕ relevant for coherent coupling of the rubidium hyperfine ground-states realised by a pair of phase-locked Raman lasers. As compared to the optical Rydberg transition, the microwave field allows for direct measurement of the phase-noise level. Figure 6.17 (bottom) shows the obtained phase-noise model used for simulation.

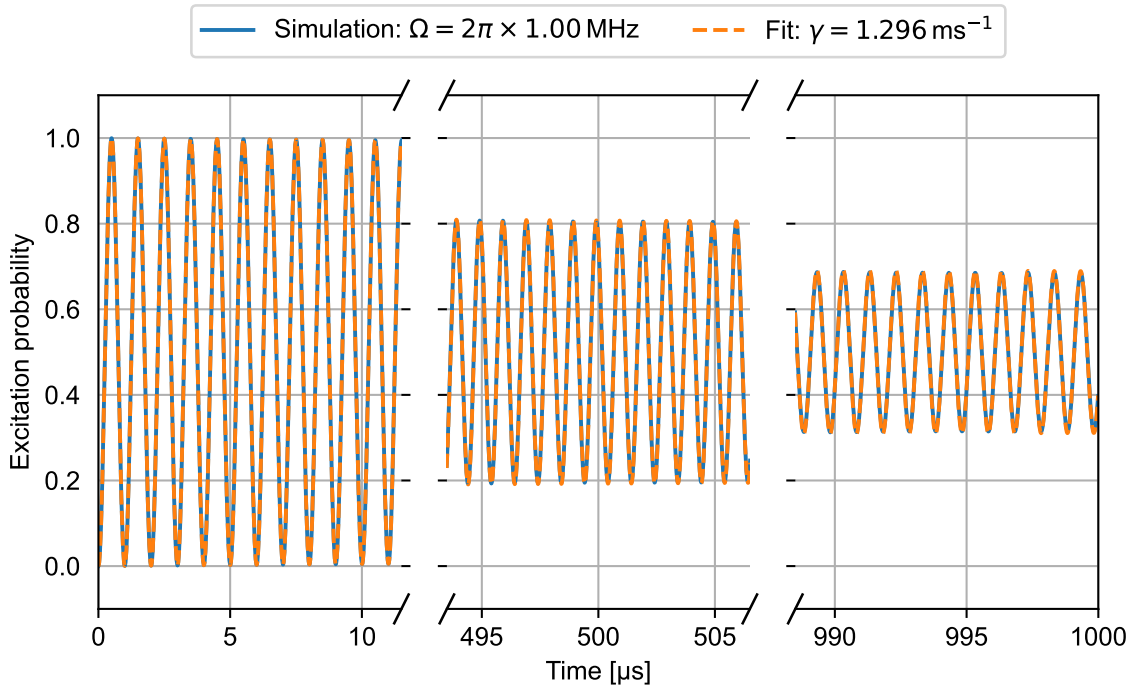

Fig. 6.20.: Simulation of Rabi oscillations with a noisy laser field (blue). The phase-noise spectral density of the Raman laser system presented in Sec. 4.4 is used for the simulation. The model given by Eq. 6.8 is fitted to the simulation results (orange, dashed). The obtained value of γ as stated in the legend yields a measure for the decoherence of the system: $2\pi\gamma/\Omega = 1.296 \times 10^{-3}$. The time axis is broken for better visibility of the Rabi oscillations.

Figure 6.20 shows the results of a simulation with $\Omega = 2\pi \times 1\,\text{MHz}$ over 1000 cycles (blue). The model described by Eq. 6.8 is fitted to the data points. An excellent agreement between model and data is achieved by allowing for a slightly smaller Rabi frequency ($\sim 0.999 \times \Omega$). If Ω is not included in the fit, the damping is overestimated due to de-phasing of model and data. Thus, the heuristic model does not describe the decoherence process accurately, if the observation time is long as compared to $1/\Omega$. However, the observable decoherence effect characterised by $2\pi\,\gamma/\Omega = 1.296 \times 10^{-3}$ is negligible for most experiments. Hence, phase noise of the Raman laser system is not expected to induce serve decoherence effects.

6.8. Conclusion and outlook

This chapter presents a characterisation of a high-power laser system at $480\,\text{nm}$. The main advantage of the system lies in its high output power from a single mode fiber in combination with excellent spectral properties. The system is relevant for coherent Rydberg excitation and the field of spectroscopy on highly-charged bismuth as a second application. This example illustrates the often surprising universality of the technologies developed in this work. Comparison between the TA system at $960\,\text{nm}$ and the $976\,\text{nm}$ TA systems shows that, especially for applications that require fiber coupling, a significantly lower output power is acceptable, if a high-quality beam profile is obtained.

The excellent spectral properties of the Rydberg laser system are achieved by PDH stabilisation to the high-finesse cavity. The PDH photodetectors and the PDH module are crucial for a reliable, low-noise error-signal generation that defines the achievable frequency-noise suppression relative to the cavity linewidth. In order to utilise the full potential of the PDH error signal, a fast controller in combination with a wideband actuator as provided by our novel current-modulation input is required. Comparison to the commercial $960\,\mathrm{nm}$ reference laser illustrates the relevance of basing the Rydberg systems on highly-stable ECDL systems. Over the course of this thesis, several PDH modulation schemes, such as direct laser-current modulation, or modulation based on a wideband EOM or a double-pass AOM, as well as AOM based frequency shifts have been tested. These schemes are not discussed extensively since the EOM based scheme presented here has proven to offer the highest performance and flexibility. Thus, also the PDH lock of the $960\,\mathrm{nm}$ system should be updated to a direct lock to the cavity based on this scheme.

For the $960\,\mathrm{nm}$ laser systems, tremendous deviations between the linewidth determined by in-loop measurements and the independent DSH method are observed. Since in-loop measurements neglect frequency noise associated with the reference cavity and the error signal, the DSH measurements are more reliable. Similar deviations are expected for the $780\,\mathrm{nm}$ system where DSH measurements are not available. In general, a DSH setup at $780\,\mathrm{nm}$ and $795\,\mathrm{nm}$ would provide an independent linewidth measurement for most laser systems used in this work. The linewidth expected for the Rydberg laser system requires a long delay line. Thus, correlated DSH [172, 175] with short delay lines may be applied. Alternatively, a beat note can be used requiring a second laser with a similar or smaller linewidth.

The linewidth obtained by DSH for the $960\,\mathrm{nm}$ laser system is a factor of 50 below the typical linewidth of the laser systems employed in the laser cooling setup. However, numerical simulations show that the decoherence effects induced by the finite linewidth are still utterly relevant when considering coherent Rydberg-ground state dynamics although the simulations tent to overestimate their influence. The accuracy of the simulations can be improved by introducing a more realistic noise model based on the DSH spectra. Furthermore, the strategy for producing correlated noise with a well defined power spectral density as included in the simulation code is applicable to a wide range of simulations involving random processes with a known spectral density.

7. Discussion and future perspective

Quantum information processing with Rydberg atoms in optical tweezer arrays predominantly relies on optical methods such as laser cooling, optical dipole traps, and coherent quantum state manipulation. Due to the micrometer spacing of array sites, single-site access is necessarily optical. Progress in state-of-the-art experiments is closely related to technological advances. For instance, system sizes are often defined by the laser power available for generation of the tweezer arrays and coherence times are limited by the spectral quality of the excitation laser system. Furthermore, with the latest advances, experiments grow increasingly complex. In combination with the large statistics inherently involved in evaluating quantum mechanical effects, reliability and stability of the system becomes a crucial factor. This thesis contains a versatile tool box tailored to optical tweezer platforms including optimised diode laser systems, advanced schemes and electronics for laser frequency and intensity stabilisation, as well as techniques facilitating the generation of tweezer arrays at large-scale or with versatile geometry. For most of the techniques developed here, the strategy of rapid prototyping is applied, i.e. first prototypes are integrated into the experiment as soon as possibles. This strategy allows for rapid implementation of novel techniques and tests under realistic operating conditions. Systems permanently in use provide a proven reliability and performance.

The following account illustrates versatile applications of the technologies presented in this thesis. More than 40 ECDL systems have been equipped with the optimised mechanical lens mount. The tapered-amplifier (TA) module utilising similar lens mounts profits from the experience gained with ECDL systems. Five master-oscillator power-amplifier (MOPA) systems have been constructed in this work. The latest version of the TA module utilises all-mechanical lens mounts. For an improved stability, all modules in use will be updated to this version in near future. This includes the $780\,\mathrm{nm}$ system providing light for the magneto optical trap (MOT), the $795\,\mathrm{nm}$ system for dipole trap generation, and the $976\,\mathrm{nm}$ system for spectroscopy on highly charged bismuth.

The *Red Pitaya Lockbox* and *Red Pitaya IntStab* controllers are foreseen for stabilisation of the lasers for the bismuth experiment. They are already widely used for two quantum information experiments based on optical tweezers and a Bose-Einstein condensate experiment. This involves the permanent use of more than ten units of each type. Thus, the reliability and performance as well as the interface with our Python-based experimental control system has been evaluated for various different applications and systems including non-standard applications such as the realisation of a chirp-laser system and the lock of a high-finesse optical filter cavity. By using the *Red Pitaya Lockbox* in combination with the optimised locking scheme, a typical long-term stability of several days is achieved. This long-term stability is particularly relevant since it allows for long measurements involving several laser systems without requiring manual intervention. By employing optimised modulation transfer spectroscopy conveniently implemented using a custom signal generation module, the linewidth and frequency accuracy of the spectroscopic reference laser system is improved significantly.

In combination with frequency-offset locks realised as optical phase-locked loops (OPLL), the linewidth, frequency accuracy, and frequency long-term stability of the laser systems used in fundamental experimental phases, such as laser cooling, optical pumping or imaging, is more than one order of magnitude below the natural linewidth of rubidium. MTS spectroscopy is employed for all spectroscopic references used in the experiments mentioned above. The integration of OPLL frequency-offset locks is an on-going process. Even though the alternative frequency-to-voltage scheme is sufficient for most applications, the OPLL offers potential for significant improvement concerning offset-frequency range and accuracy. In this context, it should be noted that the application of over ten simple beat-note photodetectors reduces the complexity of the optical setup significantly. For intensity stabilisation, the combination of the *Red Pitaya IntStab*, the modular AOM driver, and the optimised photodetector is established as a technological standard guaranteeing proven performance.

Two types of high-performance laser frequency locks are implemented. The Pound-Drever-Hall (PDH) stabilisation of the Rydberg laser system and the phase lock of the Raman laser system. Both locks define the phase and frequency-noise level of the light fields employed for coherent coupling of atomic states. This application is particularly sensitive to decoherence induced by phase and frequency noise. Numerical simulations show that the obtained noise levels constitute a relevant source of decoherence in the present Rydberg setup. The decoherence level is predominantly determined by the phase-noise spectral density S_ϕ at the Rabi frequency. For Rydberg excitations, a large Rabi rate is advantageous in two respects: The influence of laser-frequency noise decreases since $S_\phi \propto f^{-2}$ for phase noise originating from the laser linewidth. Additionally, the observation time becomes large as compared to the period of the Rabi oscillations. Recently, extended coherence times and Rabi frequencies have been demonstrated for rubidium using Rydberg-ground state coupling via the $|6P_{3/2}\rangle$ state. [22] The underlying setup is based on titanium-sapphire laser systems that feature an inherently low phase noise at high frequencies. When stabilised to a high-finesse reference cavity, substantially smaller linewidths as compared to diode laser systems are achieved. The $|5S_{1/2}\rangle \rightarrow |6P_{3/2}\rangle$ coupling at $420\,\mathrm{nm}$ is realised by a frequency doubled $840\,\mathrm{nm}$ titanium-sapphire laser. A $\sim 1010\,\mathrm{nm}$ titanium-sapphire laser amplified by a Raman fiber amplifier provides a large optical power for coupling to the Rydberg state. In future, a similar system may replace the Rydberg system presented here. Its superior spectral properties are expected to increase the coherence times obtained for Rydberg-ground state coupling significantly. The larger output power also offers additional flexibility. Single-photon scattering rates can be reduced by increasing the detuning from the intermediate state while maintaining a constant Rabi frequency. In the context of quantum simulation, where global Rydberg excitation is applied, a higher power allows for increasing the system size. The proposed laser system is significantly more complex and resource intensive as compared to the present system since the diode laser systems are replaced by titanium-sapphire lasers. However, the frequency and intensity stabilisation techniques implemented in this work, such has the PDH module and photodetectors, EOM-based frequency shifts and phase modulation, as well as intensity stabilisation and pulse shaping, are also applicable to titanium-sapphire laser systems.

The decoherence effects corresponding to the phase-noise level obtained for the Raman laser system is negligible for most applications. However, if required, the phase-noise level may be reduced significantly by deriving both light fields from the same laser source. This can be realised by phase modulation at the hyperfine splitting frequency and optical filtering [138], by application of a wideband fiber-based electro-optical amplitude modulator [179], or by

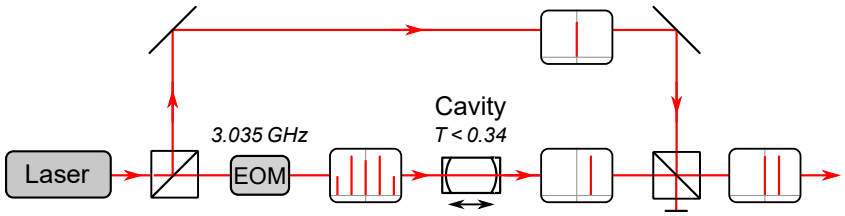

Fig. 7.1.: Generation of Raman laser fields based on a resonant free-space electro-optical phase modulator (EOM) and an optical filter cavity. The pictograms show spectra of the laser field at characteristic positions. The offset of the side bands corresponds to the hyperfine splitting of ^{85}Rb.

a resonant free-space electro-optical phase modulator (EOM) in combination with an highly dispersive optical element converting phase modulation to amplitude modulation [180]. The latter scheme is applicable to high-power laser systems and offers a high efficiency. Limitations of the system presented here arise mainly from the limited output power of the diode laser systems. The available power limits the two-photon Rabi frequency and the possible detuning from the intermediate state. A higher output power is achieved by replacing the diode laser systems by titanium-sapphire lasers. The excellent spectral properties of titanium-sapphire lasers also promise a lower phase-noise level. An alternative approach, relies on phase modulation of a single titanium-sapphire laser with a resonant free-space EOM and subsequent optical filtering by a tunable high-finesse cavity. Only a single sideband is used and the carrier is added separately after the filter cavity. This scheme is depicted in Figure 7.1. At cost of efficiency, this scheme offers a strong suppression of the carrier and all other sidebands in combination with a low phase noise defined by the microwave signal applied to the EOM and differential phase fluctuations between the sideband transmitted by the filter cavity and the carrier. The efficiency is limited by the maximum transmission of the filter cavity $T_{max} = J_1(1.84)^2 \approx 0.34$ determined by the maximum intensity in the first side band (see Eq. 4.2).

State-of-the-art titanium-sapphire lasers provide output powers of several Watts from a single-mode optical fiber at wavelengths suitable for rubidium dipole traps. In combination with the high-quality micro-optical tweezer array generation presented here it is straightforward to implement registers with several thousand atoms. In this large system, the MOPA system dedicated to dipole trap generation is ideally suited for auxiliary functions, such as generation of multiple tweezers or reservoir arrays, due to is robust and simple setup. This approach, makes the full power of the trapping laser available for the main array and allows for using a smaller detuning for auxiliary traps where scattering rates play an subordinate role. In the context of quantum simulation, exotic array geometries enable engineering of specific interaction patterns between multiple sites. This becomes especially relevant for the implementation of models with topological features as demonstrated recently for the Su–Schrieffer–Heeger (SSH) model [20] and quantum spin liquids [149] in tweezer array platforms based on holographic trap generation. Geometries that are not based on a quadratic or triangular grid have not been accessible with micro-optical tweezer arrays so far. This limitation is resolved by additive manufacturing of microlens-arrays. Figure 7.2 (a) shows a relevant geometry used in [20] in order to implement the SSH model. The interaction on horizontal edges is suppressed by choosing an angle $\theta = 54.7°$ where the resonant dipole-dipole interaction between Rydberg atoms vanished. It is straightforward to implement the depicted geometry using a microlens array consisting of irregular hexagonal lenses. Figure 7.2 (b) shows a schematic outline of an array realising the geometry depicted in (a). The inset shows a 3D view of the corresponding

microlens design. This example illustrates the versatility induced by additively manufactured microlens arrays opening the field for applications that have not been possible so far.

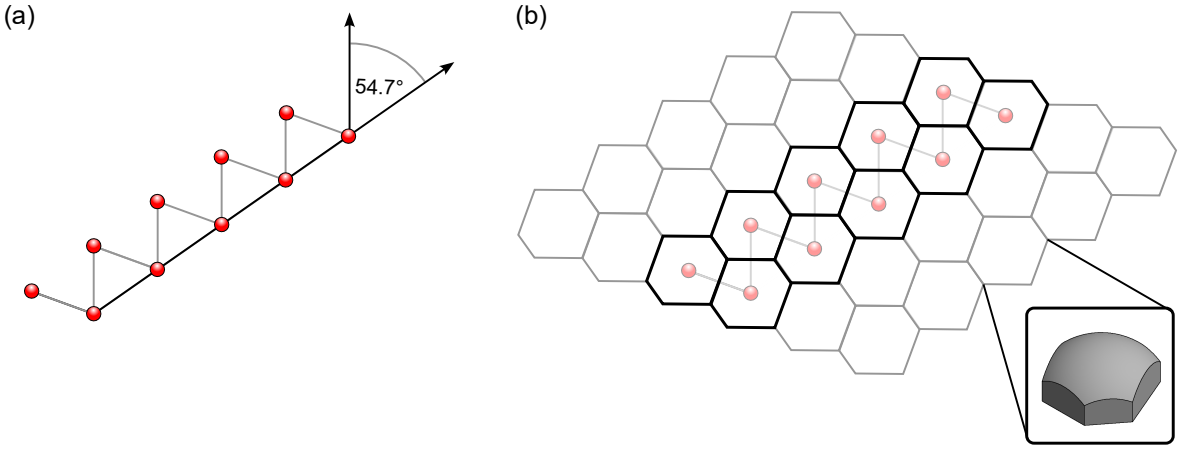

Fig. 7.2.: (a) Geometry used to implement an SSH model in a quantum simulation experiment based on holographic optical tweezers. [20] (b) Outline of a microlens array suitable for realisation of the geometry depicted in (a). The inset shows a 3D view of an individual lens (aspect ratios not to scale).

State-of-the-art experiments for quantum information processing with individual atoms in optical tweezers experience a rapid evolution. The concepts presented in this thesis constitute a sustainable basis for future development of this experimental platform. The achieved long-term stability and hands-off operation of laser systems is also essential for applications in high-resolution spectroscopy of highly-charged ions in the harsh environment of accelerator facilities. Even though the technologies are already widely established in state-of-the-art experiments, their versatility and flexibility offer great potential for future advances, not only for the targeted experimental platform. A special emphasis is put on making the solutions developed in this work available to a wide community by providing well documented open-source projects. These projects contain valuable information such as production files, components, requirements, and possible modifications. They are also subject to further development based on information gained by frequent application. The results on specific systems presented here also provide a characterisation of the applied techniques and devices in a general context.

References

[1] A. Einstein, B. Podolsky and N. Rosen, *Can Quantum-Mechanical Description of Physical Reality Be Considered Complete?*, Phys. Rev. **47,** 777–780 (1935).

[2] D. Deutsch and R. Penrose, *Quantum theory, the Church–Turing principle and the universal quantum computer*, Proceedings of the Royal Society of London. A. Mathematical and Physical Sciences **400,** 97–117 (1985).

[3] D. Deutsch and R. Jozsa, *Rapid solution of problems by quantum computation*, Proceedings of the Royal Society of London. Series A: Mathematical and Physical Sciences **439,** 553–558 (1992).

[4] L. K. Grover, *A Fast Quantum Mechanical Algorithm for Database Search*, In *Proceedings of the Twenty-eighth Annual ACM Symposium on Theory of Computing*, STOC '96 pp. 212–219 (ACM, New York, NY, USA, 1996).

[5] P. W. Shor, *Polynomial-Time Algorithms for Prime Factorization and Discrete Logarithms on a Quantum Computer*, SIAM J. Comput. **26,** 1484–1509 (1997).

[6] M. Saffman, T. G. Walker and K. Mølmer, *Quantum information with Rydberg atoms*, Rev. Mod. Phys. **82,** 2313–2363 (2010).

[7] F. Schmidt-Kaler, H. Häffner, M. Riebe, S. Gulde, G. P. T. Lancaster, T. Deuschle, C. Becher, C. F. Roos, J. Eschner and R. Blatt, *Realization of the Cirac–Zoller controlled-NOT quantum gate*, Nature **422,** 408–411 (2003).

[8] D. P. DiVincenzo, *Quantum Computation*, Science **270,** 255–261 (1995).

[9] F. Arute *et al.*, *Quantum supremacy using a programmable superconducting processor*, Nature **574,** 505–510 (2019).

[10] M. V. G. Dutt, L. Childress, L. Jiang, E. Togan, J. Maze, F. Jelezko, A. S. Zibrov, P. R. Hemmer and M. D. Lukin, *Quantum Register Based on Individual Electronic and Nuclear Spin Qubits in Diamond*, Science **316,** 1312–1316 (2007).

[11] D. Loss and D. P. DiVincenzo, *Quantum computation with quantum dots*, Phys. Rev. A **57,** 120–126 (1998).

[12] J. Preskill, *Quantum Computing in the NISQ era and beyond*, Quantum **2,** 79 (2018).

[13] D. P. Divincenzo, in *Mesoscopic Electron Transport*, L. L. Sohn, L. P. Kouwenhoven and G. Schön, eds., (Springer Netherlands, Dordrecht, 1997), pp. 657–677.

[14] L. Henriet, L. Beguin, A. Signoles, T. Lahaye, A. Browaeys, G.-O. Reymond and C. Jurczak, *Quantum computing with neutral atoms*, Quantum **4,** 327 (2020).

[15] L. Isenhower, E. Urban, X. L. Zhang, A. T. Gill, T. Henage, T. A. Johnson, T. G. Walker and M. Saffman, *Demonstration of a Neutral Atom Controlled-NOT Quantum Gate*, Phys. Rev. Lett. **104,** 010503 (2010).

[16] H. Levine, A. Keesling, A. Omran, H. Bernien, S. Schwartz, A. S. Zibrov, M. Endres, M. Greiner, V. Vuletić and M. D. Lukin, *High-Fidelity Control and Entanglement of Rydberg-Atom Qubits*, Phys. Rev. Lett. **121,** 123603 (2018).

[17] M. Saffman, *Quantum computing with atomic qubits and Rydberg interactions: progress and challenges*, Journal of Physics B: Atomic, Molecular and Optical Physics **49,** 202001 (2016).

[18] R. P. Feynman, *Quantum mechanical computers*, Foundations of Physics **16,** 507–531 (1986).

[19] V. Lienhard, S. de Léséleuc, D. Barredo, T. Lahaye, A. Browaeys, M. Schuler, L.-P. Henry and A. M. Läuchli, *Observing the Space- and Time-Dependent Growth of Correlations in Dynamically Tuned Synthetic Ising Models with Antiferromagnetic Interactions*, Phys. Rev. X **8,** 021070 (2018).

[20] S. de Léséleuc, V. Lienhard, P. Scholl, D. Barredo, S. Weber, N. Lang, H. P. Büchler, T. Lahaye and A. Browaeys, *Observation of a symmetry-protected topological phase of interacting bosons with Rydberg atoms*, Science **365,** 775–780 (2019).

[21] V. Lienhard *et al.*, *Realization of a Density-Dependent Peierls Phase in a Synthetic, Spin-Orbit Coupled Rydberg System*, Phys. Rev. X **10,** 021031 (2020).

[22] P. Scholl *et al.*, *Quantum simulation of 2D antiferromagnets with hundreds of Rydberg atoms*, Nature **595,** 233–238 (2021).

[23] D. Bluvstein *et al.*, *Controlling quantum many-body dynamics in driven Rydberg atom arrays*, Science **371,** 1355–1359 (2021).

[24] S. Ebadi *et al.*, *Quantum phases of matter on a 256-atom programmable quantum simulator*, Nature **595,** 227–232 (2021).

[25] P. Scholl *et al.*, *Microwave Engineering of Programmable XXZ Hamiltonians in Arrays of Rydberg Atoms*, PRX Quantum **3,** 020303 (2022).

[26] W. D. Phillips, *Nobel Lecture: Laser cooling and trapping of neutral atoms*, Rev. Mod. Phys. **70,** 721–741 (1998).

[27] A. Ashkin, *Applications of Laser Radiation Pressure*, Science **210,** 1081–1088 (1980).

[28] M. Schlosser, S. Tichelmann, J. Kruse and G. Birkl, *Scalable architecture for quantum information processing with atoms in optical micro-structures*, Quantum Information Processing **10,** 907 (2011).

[29] D. Ohl de Mello, D. Schäffner, J. Werkmann, T. Preuschoff, L. Kohfahl, M. Schlosser and G. Birkl, *Defect-Free Assembly of 2D Clusters of More Than 100 Single-Atom Quantum Systems*, Phys. Rev. Lett. **122,** 203601 (2019).

[30] M. Schlosser, S. Tichelmann, D. Schäffner, D. Ohl de Mello, M. Hambach and G. Birkl, *Large-scale multilayer architecture of single-atom arrays with individual addressability*, arXiv:1902.05424 [quant-ph] (2019).

[31] A. M. Kaufman and K.-K. Ni, *Quantum science with optical tweezer arrays of ultracold atoms and molecules*, Nature Physics **17,** 1324–1333 (2021).

[32] G. Grynberg, A. Aspect, C. Fabre and C. Cohen-Tannoudji, *Introduction to Quantum Optics: From the Semi-classical Approach to Quantized Light* (Cambridge University Press, 2010).

[33] D. A. Steck, *Quantum and Atom Optics* (https://atomoptics.uoregon.edu/∼dsteck/teaching/quantum-optics/, 2007).

[34] H. Metcalf and P. van der Straten, *Laser Cooling and Trapping*, *Graduate Texts in Contemporary Physics* (Springer New York, 2001).

[35] D. A. Steck, *Rubidium 85 D Line Data*, 2021, http://steck.us/alkalidata/rubidium85numbers.pdf.

[36] D. A. Steck, *Rubidium 87 D Line Data*, 2021, http://steck.us/alkalidata/rubidium87numbers.pdf.

[37] R. Grimm, M. Weidemüller and Y. B. Ovchinnikov, *Optical Dipole Traps for Neutral Atoms*, in *Optical Dipole Traps for Neutral Atoms*, Vol. 42 of *Advances In Atomic, Molecular, and Optical Physics*, B. Bederson and H. Walther, eds., (Academic Press, 2000), pp. 95 – 170.

[38] W. D. Phillips and H. Metcalf, *Laser Deceleration of an Atomic Beam*, Phys. Rev. Lett. **48,** 596–599 (1982).

[39] E. Riis, D. S. Weiss, K. A. Moler and S. Chu, *Atom funnel for the production of a slow, high-density atomic beam*, Phys. Rev. Lett. **64,** 1658–1661 (1990).

[40] J. V. Prodan and W. D. Phillips, *Chirping the light – fantastic? Recent NBS atom cooling experiments*, Progress in Quantum Electronics **8,** 231–235 (1984).

[41] E. Hecht, *Optik* (De Gruyter, 2018).

[42] F. Nogrette, H. Labuhn, S. Ravets, D. Barredo, L. Béguin, A. Vernier, T. Lahaye and A. Browaeys, *Single-Atom Trapping in Holographic 2D Arrays of Microtraps with Arbitrary Geometries*, Phys. Rev. X **4,** 021034 (2014).

[43] H. Kim, W. Lee, H.-g. Lee, H. Jo, Y. Song and J. Ahn, *In situ single-atom array synthesis using dynamic holographic optical tweezers*, Nature communications **7,** 13317 (2016).

[44] D. Kim, A. Keesling, A. Omran, H. Levine, H. Bernien, M. Greiner, M. D. Lukin and D. R. Englund, *Large-scale uniform optical focus array generation with a phase spatial light modulator*, Opt. Lett. **44,** 3178–3181 (2019).

[45] M. Endres, H. Bernien, A. Keesling, H. Levine, E. R. Anschuetz, A. Krajenbrink, C. Senko, V. Vuletić, M. Greiner and M. D. Lukin, *Atom-by-atom assembly of defect-free one-dimensional cold atom arrays*, Science **354,** 1024–1027 (2016).

[46] A. W. Young, W. J. Eckner, W. R. Milner, D. Kedar, M. A. Norcia, E. Oelker, N. Schine, J. Ye and A. M. Kaufman, *Half-minute-scale atomic coherence and high relative stability in a tweezer clock*, Nature **588,** 408–413 (2020).

[47] K. Singh, S. Anand, A. Pocklington, J. T. Kemp and H. Bernien, *Dual-Element, Two-Dimensional Atom Array with Continuous-Mode Operation*, Phys. Rev. X **12,** 011040 (2022).

[48] N. Schlosser, G. Reymond, I. Protsenko and P. Grangier, *Sub-poissonian loading of single atoms in a microscopic dipole trap*, Nature **411,** 1024–1027 (2001).

[49] M. O. Brown, T. Thiele, C. Kiehl, T.-W. Hsu and C. A. Regal, *Gray-Molasses Optical-Tweezer Loading: Controlling Collisions for Scaling Atom-Array Assembly*, Phys. Rev. X **9,** 011057 (2019).

[50] D. Barredo, S. de Léséleuc, V. Lienhard, T. Lahaye and A. Browaeys, *An atom-by-atom assembler of defect-free arbitrary two-dimensional atomic arrays*, Science **354,** 1021–1023 (2016).

[51] F. Mayer, *Design of Algorithms for Efficient Relocation of Atoms in a Quantum Register*, Master's thesis, TU Darmstadt, 2015.

[52] K.-N. Schymik, V. Lienhard, D. Barredo, P. Scholl, H. Williams, A. Browaeys and T. Lahaye, *Enhanced atom-by-atom assembly of arbitrary tweezer arrays*, Phys. Rev. A **102,** 063107 (2020).

[53] C. Sheng, J. Hou, X. He, P. Xu, K. Wang, J. Zhuang, X. Li, M. Liu, J. Wang and M. Zhan, *Efficient preparation of two-dimensional defect-free atom arrays with near-fewest sorting-atom moves*, Phys. Rev. Research **3,** 023008 (2021).

[54] T. F. Gallagher, *Rydberg Atoms*, *Cambridge Monographs on Atomic, Molecular and Chemical Physics* (Cambridge University Press, 1994).

[55] R. Cardman and G. Raithel, *Hyperfine Structure of $nP_{1/2}$ Rydberg States in ^{85}Rb*, 2022.

[56] N. Šibalić, J. D. Pritchard, C. S. Adams and K. J. Weatherill, *ARC: An open-source library for calculating properties of alkali Rydberg atoms*, Computer Physics Communications **220,** 319–331 (2017).

[57] I. I. Beterov, I. I. Ryabtsev, D. B. Tretyakov and V. M. Entin, *Quasiclassical calculations of blackbody-radiation-induced depopulation rates and effective lifetimes of Rydberg nS, nP, and nD alkali-metal atoms with $n \leq 80$*, Phys. Rev. A **79,** 052504 (2009).

[58] J. Zeiher, P. Schauß, S. Hild, T. Macrì, I. Bloch and C. Gross, *Microscopic Characterization of Scalable Coherent Rydberg Superatoms*, Phys. Rev. X **5,** 031015 (2015).

[59] S. Hollerith, J. Rui, A. Rubio-Abadal, K. Srakaew, D. Wei, J. Zeiher, C. Gross and I. Bloch, *Microscopic electronic structure tomography of Rydberg macrodimers*, Phys. Rev. Research **3,** 013252 (2021).

[60] A. F. Linskens, I. Holleman, N. Dam and J. Reuss, *Two-photon Rabi oscillations*, Phys. Rev. A **54,** 4854–4862 (1996).

[61] S. de Léséleuc, D. Barredo, V. Lienhard, A. Browaeys and T. Lahaye, *Analysis of imperfections in the coherent optical excitation of single atoms to Rydberg states*, Phys. Rev. A **97,** 053803 (2018).

[62] D. Ohl de Mello, *Rydberg interactions in a defect-free array of single-atom quantum systems*, Ph.D. thesis, TU Darmstadt, 2020.

[63] C. D. Herold, V. D. Vaidya, X. Li, S. L. Rolston, J. V. Porto and M. S. Safronova, *Precision Measurement of Transition Matrix Elements via Light Shift Cancellation*, Phys. Rev. Lett. **109,** 243003 (2012).

[64] M. Schlosser, D. O. de Mello, D. Schäffner, T. Preuschoff, L. Kohfahl and G. Birkl, *Assembled arrays of Rydberg-interacting atoms*, Journal of Physics B: Atomic, Molecular and Optical Physics **53,** 144001 (2020).

[65] M. Morgado and S. Whitlock, *Quantum simulation and computing with Rydberg-interacting qubits*, AVS Quantum Science **3,** 023501 (2021).

[66] T. G. Walker and M. Saffman, *Consequences of Zeeman degeneracy for the van der Waals blockade between Rydberg atoms*, Phys. Rev. A **77,** 032723 (2008).

[67] D. Jaksch, J. I. Cirac, P. Zoller, S. L. Rolston, R. Côté and M. D. Lukin, *Fast Quantum Gates for Neutral Atoms*, Phys. Rev. Lett. **85,** 2208–2211 (2000).

[68] A. Browaeys and T. Lahaye, *Many-body physics with individually controlled Rydberg atoms*, Nature Physics **16,** 132–142 (2020).

[69] P. Schauss, *Quantum simulation of transverse Ising models with Rydberg atoms*, Quantum Science and Technology **3,** 023001 (2018).

[70] I. I. Beterov and M. Saffman, *Rydberg blockade, Förster resonances, and quantum state measurements with different atomic species*, Phys. Rev. A **92,** 042710 (2015).

[71] S. K. Dutta, J. R. Guest, D. Feldbaum, A. Walz-Flannigan and G. Raithel, *Ponderomotive Optical Lattice for Rydberg Atoms,* Phys. Rev. Lett. **85,** 5551–5554 (2000).

[72] D. Barredo, V. Lienhard, P. Scholl, S. de Léséleuc, T. Boulier, A. Browaeys and T. Lahaye, *Three-Dimensional Trapping of Individual Rydberg Atoms in Ponderomotive Bottle Beam Traps*, Phys. Rev. Lett. **124,** 023201 (2020).

[73] P. Zorabedian and W. R. Trutna, *Interference-filter-tuned, alignment-stabilized, semiconductor external-cavity laser*, Opt. Lett. **13,** 826–828 (1988).

[74] K. Liu and M. G. Littman, *Novel geometry for single-mode scanning of tunable lasers*, Opt. Lett. **6,** 117–118 (1981).

[75] X. Baillard, A. Gauguet, S. Bize, P. Lemonde, P. Laurent, A. Clairon and P. Rosenbusch, *Interference-filter-stabilized external-cavity diode lasers*, Optics Communications **266,** 609 – 613 (2006).

[76] D. J. Thompson and R. E. Scholten, *Narrow linewidth tunable external cavity diode laser using wide bandwidth filter*, Review of Scientific Instruments **83,** 023107 (2012).

[77] V. Annovazzi-Lodi, S. Merlo and S. Moroni, *Power efficiency of a semiconductor laser with an external cavity*, Optical and Quantum Electronics **32,** 1343–1350 (2000).

[78] J. Osmundsen and N. Gade, *Influence of optical feedback on laser frequency spectrum and threshold conditions*, IEEE Journal of Quantum Electronics **19,** 465–469 (1983).

[79] A. Daffurn, R. F. Offer and A. S. Arnold, *A simple, powerful diode laser system for atomic physics*, Appl. Opt. **60,** 5832–5836 (2021).

[80] H. John, *Entwicklung eines Systems zum Fangen und Kühlen von atomarem Quecksilber*, Ph.D. thesis, TU Darmstadt, 2019.

[81] P. Baus and G. Birkl, *An Open-Source, Low Noise, High Stability Digital Laser Driver for the next Generation of Laser Diodes*, 2022, unpublished.

[82] P. Baus, *GitHub repository TU-Darmstadt-APQ/DgDrive*, https://github.com/TU-Darmstadt-APQ/DgDrive, 2022.

[83] K. G. Libbrecht and J. L. Hall, *A low-noise high-speed diode laser current controller*, Review of Scientific Instruments **64,** 2133–2135 (1993).

[84] Datasheet, *Aluminium EN AW-7020*, Batz+Burgel, 06-2020, https://batz-burgel.com/wp-content/uploads/data-de/BB_7020.pdf.

[85] N. I. Khan, S. H. Choudhury and A. A. Roni, *A comparative study of the temperature dependence of lasing wavelength of conventional edge emitting stripe laser and vertical cavity surface emitting laser*, In *Proceedings of the International Conference on Optical Communication Systems*, pp. 1–5 (2011).

[86] T. Numai, in *Fundamentals of Semiconductor Lasers* (Springer Japan, Tokyo, 2015), pp. 89–186.

[87] P. E. Ciddor and R. J. Hill, *Refractive index of air. 2. Group index*, Appl. Opt. **38,** 1663–1667 (1999).

[88] J. Stone and J. Zimmerman, *Index of Refraction of Air*, http://emtoolbox.nist.gov/Wavelength/Documentation.asp, 2001.

[89] K. Petermann, in *Laser Diode Modulation and Noise* (Springer Netherlands, Dordrecht, 1988), Chap. 5, pp. 119–144.

[90] J. N. Walpole, *Semiconductor amplifiers and lasers with tapered gain regions*, Optical and Quantum Electronics **28,** 623–645 (1996).

[91] M. Mikulla, in *Tapered High-Power, High-Brightness Diode Lasers: Design and Performance* (2000), Vol. 78, pp. 265–288.

[92] STEMlab, *RedPitaya STEMlab 125-14*, https://www.redpitaya.com/f130/STEMlab-board, 2013.

[93] T. Preuschoff, M. Schlosser and G. Birkl, *Digital laser frequency and intensity stabilization based on the STEMlab platform (originally Red Pitaya)*, Review of Scientific Instruments **91,** 083001 (2020).

[94] T. Preuschoff *et al.*, *GitHub repository TU-Darmstadt-APQ/RedPitaya-Lockbox*, https://github.com/TU-Darmstadt-APQ/RedPitaya-Lockbox, 2020.

[95] L. Neuhaus, *GitHub repository PyRPL project*, https://github.com/lneuhaus/pyrpl, 2017.

[96] L. Neuhaus, *Red Pitaya DAC performance*, https://ln1985blog.wordpress.com/2016/02/07/red-pitaya-dac-performance, 2016.

[97] A. C. Cárdenas Olaya *et al.*, *Noise characterization of analog to digital converters for amplitude and phase noise measurements*, Rev. Sci. Instrum. **88,** 065108 (2017).

[98] P. Welch, *The use of fast Fourier transform for the estimation of power spectra: A method based on time averaging over short, modified periodograms*, IEEE Transactions on Audio and Electroacoustics **15,** 70–73 (1967).

[99] R. W. P. Drever, J. L. Hall, F. V. Kowalski, J. Hough, G. M. Ford, A. J. Munley and H. Ward, *Laser phase and frequency stabilization using an optical resonator*, Applied Physics B: Lasers and Optics **31,** 97–105 (1983).

[100] E. D. Black, *An introduction to Pound–Drever–Hall laser frequency stabilization*, American Journal of Physics **69,** 79–87 (2001).

[101] J. Appel, A. MacRae and A. I. Lvovsky, *A versatile digital GHz phase lock for external cavity diode lasers*, Measurement Science and Technology **20,** 055302 (2009).

[102] S. H. Yim, S.-B. Lee, T. Y. Kwon and S. E. Park, *Optical phase locking of two extended-cavity diode lasers with ultra-low phase noise for atom interferometry*, Applied Physics B: Lasers and Optics **115,** 491–495 (2014).

[103] T. Preuschoff, P. Baus, M. Schlosser and G. Birkl, *Wideband current modulation of diode lasers for frequency stabilization*, Review of Scientific Instruments **93,** 063002 (2022).

[104] T. Preuschoff *et al.*, *GitHub repository TU-Darmstadt-APQ/Laser_Backplane_DVI*, https://github.com/TU-Darmstadt-APQ/Laser_Backplane_DVI, 2022.

[105] D. H. Sheingold, *Impedance & Admittance Transformations Using Operational Amplifiers*, Lightning Empiricist **12,** 1–8 (1964).

[106] L. T. Harrison, *Chapter 11 - Creating Precision Current Sources with Op Amps and Voltage References*, in *Current Sources and Voltage References*, L. T. Harrison, ed., (Newnes, Burlington, 2005), pp. 281–317.

[107] Datasheet, *ADA4807-2, 180 MHz,Rail-to-Rail Input/Output Dual Amplifiers*, Analog Devices, 09-2015, rev. B.

[108] C. J. Erickson, M. Van Zijll, G. Doermann and D. S. Durfee, *An ultrahigh stability, low-noise laser current driver with digital control*, Review of Scientific Instruments **79,** 073107 (2008).

[109] T. Preuschoff *et al.*, *GitHub repository TU-Darmstadt-APQ/RedPitaya-IntStab*, https://github.com/TU-Darmstadt-APQ/RedPitaya-IntStab, 2020.

[110] T. Preuschoff, *GitHub repository TU-Darmstadt-APQ/SFH203_photodetector*, https://github.com/TU-Darmstadt-APQ/SFH203_photodetector, 2022.

[111] Texas Instruments, *Transimpedance Amplifiers (TIA): Choosing the BestAmplifier for the Job*, 2017, https://www.tij.co.jp/jp/lit/an/snoa942a/snoa942a.pdf.

[112] Analog Devices, *Photodiode Wizard*, https://tools.analog.com/en/photodiode/.

[113] R. Lerch, *Elektrische Messtechnik: analoge, digitale und computergestützte Verfahren*, *Elektrische Messtechnik / Reinhard Lerch* (Springer, 2005).

[114] T. Preuschoff, *GitHub repository TU-Darmstadt-APQ/PDH_photodiode*, https://github.com/TU-Darmstadt-APQ/PDH_photodiode, 2022.

[115] S. Kobayashi, Y. Yamamoto, M. Ito and T. Kimura, *Direct Frequency Modulation In AlGaAs Semiconductor Lasers*, IEEE Transactions on Microwave Theory and Techniques **30,** 428–441 (1982).

[116] E. A. Donley, T. P. Heavner, F. Levi, M. O. Tataw and S. R. Jefferts, *Double-pass acousto-optic modulator system*, Review of Scientific Instruments **76,** 063112 (2005).

[117] Coherent, *Datasheet TA-0780-2000-CM*, 2017, https://www.coherent.com/resources/datasheet/components-and-accessories/DILAS_TA-0785-2000.pdf.

[118] J. H. Shirley, *Modulation transfer processes in optical heterodyne saturation spectroscopy*, Opt. Lett. **7,** 537–539 (1982).

[119] G. Camy, C. Bordé and M. Ducloy, *Heterodyne saturation spectroscopy through frequency modulation of the saturating beam*, Optics Communications **41,** 325 – 330 (1982).

[120] T. Preuschoff, M. Schlosser and G. Birkl, *Optimization strategies for modulation transfer spectroscopy applied to laser stabilization*, Opt. Express **26,** 24010–24019 (2018).

[121] W. Demtröder, *Laser Spectroscopy 2: Experimental Techniques* (Springer Berlin Heidelberg, 2015).

[122] M. Abramowitz and I. Stegun, *Handbook of Mathematical Functions: With Formulas, Graphs, and Mathematical Tables*, *Applied mathematics series* (Dover Publications, 1964).

[123] D. Sun, C. Zhou, L. Zhou, J. Wang and M. Zhan, *Modulation transfer spectroscopy in a lithium atomic vapor cell*, Opt. Express **24,** 10649–10662 (2016).

[124] C. Bing, W. Zhao-Ying, W. Bin, X. Ao-Peng, W. Qi-Yu, X. Yun-Fei and L. Qiang, *Laser frequency stabilization and shifting by using modulation transfer spectroscopy*, Chinese Physics B **23,** 104222 (2014).

[125] M. Ducloy and D. Bloch, *Theory of degenerate four-wave mixing in resonant Doppler-broadened systems - I. Angular dependence of intensity and lineshape of phase-conjugate emission*, J. Phys. France **42,** 711–721 (1981).

[126] M. Ducloy and D. Bloch, *Theory of degenerate four-wave mixing in resonant Doppler-broadened media. - II. Doppler-free heterodyne spectroscopy via collinear four-wave mixing in two- and three-level systems*, J. Phys. France **43,** 57–65 (1982).

[127] T. Preuschoff, *GitHub repository TU-Darmstadt-APQ/MTS_module*, https://github.com/TU-Darmstadt-APQ/MTS_module, 2022.

[128] E. Jaatinen, *Theoretical determination of maximum signal levels obtainable with modulation transfer spectroscopy*, Optics Communications **120,** 91 – 97 (1995).

[129] Z. Tan, X.-c. Zhao, Y. Cheng, X.-p. Sun, J. Luo, X. Zhou, J. Wang and M.-s. Zhan, *Doppler-free spectroscopy of rubidium atoms driven by a control laser*, Frontiers of Physics **7,** 311–314 (2011).

[130] Z. Fang, H. Cai, G. Chen and R. Qu, *Single Frequency Semiconductor Lasers* (Springer, Berlin, Heidelberg, 2017).

[131] G. D. Domenico, S. Schilt and P. Thomann, *Simple approach to the relation between laser frequency noise and laser line shape*, Appl. Opt. **49,** 4801–4807 (2010).

[132] E. Jaatinen and J.-M. Chartier, *Possible influence of residual amplitude modulation when using modulation transfer with iodine transitions at 543 nm*, Metrologia **35,** 75 (1998).

[133] E. Jaatinen and D. J. Hopper, *Compensating for frequency shifts in modulation transfer spectroscopy caused by residual amplitude modulation*, Optics and Lasers in Engineering **46,** 69 – 74 (2008).

[134] J. B. Johnson, *Thermal Agitation of Electricity in Conductors*, Phys. Rev. **32,** 97–109 (1928).

[135] T. Preuschoff, *GitHub repository TU-Darmstadt-APQ/HMC439_Phase-Frequency_Detector*, https://github.com/TU-Darmstadt-APQ/HMC439_Phase-Frequency_Detector, 2022.

[136] F. Riehle, *Frequency Standards: Basics and Applications* (Wiley-VCH, 2004).

[137] *IEEE Standard Definitions of Physical Quantities for Fundamental Frequency and Time Metrology-Random Instabilities*, IEEE Std 1139-1999 pp. 1–40 (1999).

[138] D. D. Yavuz, P. B. Kulatunga, E. Urban, T. A. Johnson, N. Proite, T. Henage, T. G. Walker and M. Saffman, *Fast Ground State Manipulation of Neutral Atoms in Microscopic Optical Traps*, Phys. Rev. Lett. **96,** 063001 (2006).

[139] M. Kasevich and S. Chu, *Atomic interferometry using stimulated Raman transitions*, Phys. Rev. Lett. **67,** 181–184 (1991).

[140] B. E. A. Saleh and M. C. Teich, *Grundlagen der Photonik*, *Lehrbuch Physik*, 1. aufl., [dt. übers. der] 2., vollst. überarb. und erw. aufl. ed. (Wiley-VCH, Weinheim, 2008), pp. XXIII, 1406 S., 3. Aufl. u.d.T.: Optik und Photonik.

[141] F. Tricot, D. H. Phung, M. Lours, S. Guérandel and E. de Clercq., *Power stabilization of a diode laser with an acousto-optic modulator*, Review of Scientific Instruments **89,** 113112 (2018).

[142] W. Lee, H. Kim and J. Ahn, *Defect-free atomic array formation using the Hungarian matching algorithm*, Phys. Rev. A **95,** 053424 (2017).

[143] Y. Li and E. Wolf, *Focal shifts in diffracted converging spherical waves*, Optics Communications **39,** 211–215 (1981).

[144] T. Preuschoff, S. Amann, L. Sturm, L. Brozio and J. Werkmann, *GitHub repository TU-Darmstadt-APQ/eval_MLA*, https://github.com/TU-Darmstadt-APQ/eval_MLA, 2022.

[145] J. Werkmann, *Control Systems and Optical Tweezers for Quantum Information Processing*, Master's thesis, TU Darmstadt, 2018.

[146] L. Brozio, *Micromirror-Based Manipulation of Dipole Traps Created by Microlens Arrays*, Master's thesis, TU Darmstadt, 2019.

[147] S. Amann, *Optical Setup for Interleaved Dipole Trap Arrays with Reduced Trap Waist and Pitch*, Master's thesis, TU Darmstadt, 2021.

[148] L. Günther, *Simulation der optischen Eigenschaften eines neuen Objektivs und eines neuen Mikrolinsenaufbaus*, Bachelor's thesis, TU Darmstadt, 2020.

[149] G. Semeghini *et al.*, *Probing topological spin liquids on a programmable quantum simulator*, Science **374,** 1242–1247 (2021).

[150] T. Preuschoff, S. Ristok, D. Schäffner, L. Brozio, D. Ohl de Mello, L. Kohfahl, M. Schlosser, H. Giessen and G. Birkl, *Micro-optical systems for quantum technologies with laser-trapped neutral atoms based on rapid prototyping by 3D direct laser writing*, In *DGaO-Proceedings 2019*, p. B016 (DGAO, 2019).

[151] D. Schäffner, T. Preuschoff, S. Ristok, L. Brozio, M. Schlosser, H. Giessen and G. Birkl, *Arrays of individually controllable optical tweezers based on 3D-printed microlens arrays*, Opt. Express **28,** 8640–8645 (2020).

[152] S. Kawata, H.-B. Sun, T. Tanaka and K. Takada, *Finer features for functional microdevices*, Nature **412,** 697–698 (2001).

[153] T. Gissibl, S. Thiele, A. Herkommer and H. Giessen, *Two-photon direct laser writing of ultracompact multi-lens objectives*, Nature Photonics **10,** 554 EP – (2016).

[154] M. Schmid, S. Thiele, A. Herkommer and H. Giessen, *Three-dimensional direct laser written achromatic axicons and multi-component microlenses*, Opt. Lett. **43,** 5837–5840 (2018).

[155] *Test methods for laser beam widths, divergence angles and beam propagation ratios*, Standard, International Organization for Standardization, Geneva, CH (2000) .

[156] K.-N. Schymik, S. Pancaldi, F. Nogrette, D. Barredo, J. Paris, A. Browaeys and T. Lahaye, *Single Atoms with 6000-Second Trapping Lifetimes in Optical-Tweezer Arrays at Cryogenic Temperatures*, Phys. Rev. Applied **16,** 034013 (2021).

[157] D. Voigt, E. C. Schilder, R. J. C. Spreeuw and H. B. van Linden van den Heuvell, *Characterization of a high-power tapered semiconductor amplifier system*, Applied Physics B **72,** 279–284 (2001).

[158] V. M. Shabaev, A. I. Bondarev, D. A. Glazov, M. Y. Kaygorodov, Y. S. Kozhedub, I. A. Maltsev, A. V. Malyshev, R. V. Popov, I. I. Tupitsyn and N. A. Zubova, *Stringent tests of QED using highly charged ions*, Hyperfine Interactions **239,** 60 (2018).

[159] T. Beier, *The gj factor of a bound electron and the hyperfine structure splitting in hydrogenlike ions*, Physics Reports **339,** 79–213 (2000).

[160] A. Bohr and V. F. Weisskopf, *The Influence of Nuclear Structure on the Hyperfine Structure of Heavy Elements*, Phys. Rev. **77,** 94–98 (1950).

[161] J. E. Rosenthal and G. Breit, *The Isotope Shift in Hyperfine Structure*, Phys. Rev. **41,** 459–470 (1932).

[162] H.-J. Kluge *et al.*, *Chapter 7 HITRAP: A Facility at GSI for Highly Charged Ions*, in *Current Trends in Atomic Physics*, Vol. 53 of *Advances in Quantum Chemistry*, S. Salomonson and E. Lindroth, eds., (Academic Press, 2008), pp. 83–98.

[163] Z. Andjelkovic, S. Bharadia, B. Sommer, M. Vogel and W. Nörtershäuser, *Towards high precision in-trap laser spectroscopy of highly charged ions*, Hyperfine Interactions **196,** 81–91 (2010).

[164] J. Ullmann *et al.*, *High precision hyperfine measurements in Bismuth challenge bound-state strong-field QED*, Nature Communications **8,** 15484 (2017).

[165] S. Albrecht, *Ein Lasersystem zur Spektroskopie von hochgeladenen Ionen, Tellurmolekülen und Rubidium-Rydberg-Zuständen*, Ph.D. thesis, TU Darmstadt, 2014.

[166] T. W. Hansch and B. Couillaud, *Laser frequency stabilization by polarization spectroscopy of a reflecting reference cavity*, Optics Communications **35,** 441–444 (1980).

[167] T. Preuschoff, *GitHub repository TU-Darmstadt-APQ/PDH-module*, https://github.com/TU-Darmstadt-APQ/PDH-module, 2021.

[168] T. Okoshi, K. Kikuchi and A. Nakayama, *Novel method for high resolution measurement of laser output spectrum*, Electronics Letters **16,** 630–631(1) (1980).

[169] D. S. Elliott, R. Roy and S. J. Smith, *Extracavity laser band-shape and bandwidth modification*, Phys. Rev. A **26,** 12–18 (1982).

[170] L. B. Mercer, *1/f frequency noise effects on self-heterodyne linewidth measurements*, Journal of Lightwave Technology **9,** 485–493 (1991).

[171] E. E. Whiting, *An empirical approximation to the Voigt profile*, Journal of Quantitative Spectroscopy and Radiative Transfer **8,** 1379–1384 (1968).

[172] Y. He, S. Hu, S. Liang and Y. Li, *High-precision narrow laser linewidth measurement based on coherent envelope demodulation*, Optical Fiber Technology **50,** 200–205 (2019).

[173] Datasheet, *Corning SMF-28 Ultra Optical Fiber*, Corning, 2021, https://www.corning.com/media/worldwide/coc/documents/Fiber/product-information-sheets/PI-1424-AEN.pdf.

[174] S. M. Abrarov and B. M. Quine, *Efficient algorithmic implementation of the Voigt/complex error function based on exponential series approximation*, Applied Mathematics and Computation **218,** 1894–1902 (2011).

[175] S. Huang, M. Wan, J. Wu, D. Lu, B. Zhang, Y. Zheng, C. Liu and X. Fang, *Precise laser linewidth measurement by feature extraction withshort-delay self-homodyne*, Appl. Opt. **61,** 1791–1796 (2022).

[176] P. Cheinet, B. Canuel, F. Pereira Dos Santos, A. Gauguet, F. Yver-Leduc and A. Landragin, *Measurement of the Sensitivity Function in a Time-Domain Atomic Interferometer*, IEEE Transactions on Instrumentation and Measurement **57,** 1141–1148 (2008).

[177] J. R. Johansson, P. D. Nation and F. Nori, *QuTiP 2: A Python framework for the dynamics of open quantum systems*, Computer Physics Communications **184,** 1234–1240 (2013).

[178] R. Loudon, *The Quantum Theory of Light* (Clarendon Press, Oxford, 1973).

[179] H. Levine *et al.*, *Parallel Implementation of High-Fidelity Multiqubit Gates with Neutral Atoms*, Phys. Rev. Lett. **123,** 170503 (2019).

[180] H. Levine, D. Bluvstein, A. Keesling, T. T. Wang, S. Ebadi, G. Semeghini, A. Omran, M. Greiner, V. Vuletić and M. D. Lukin, *Dispersive optical systems for scalable Raman driving of hyperfine qubits*, Phys. Rev. A **105,** 032618 (2022).

A. Optical coatings

A.1. Feedback mirrors for external-cavity diode lasers

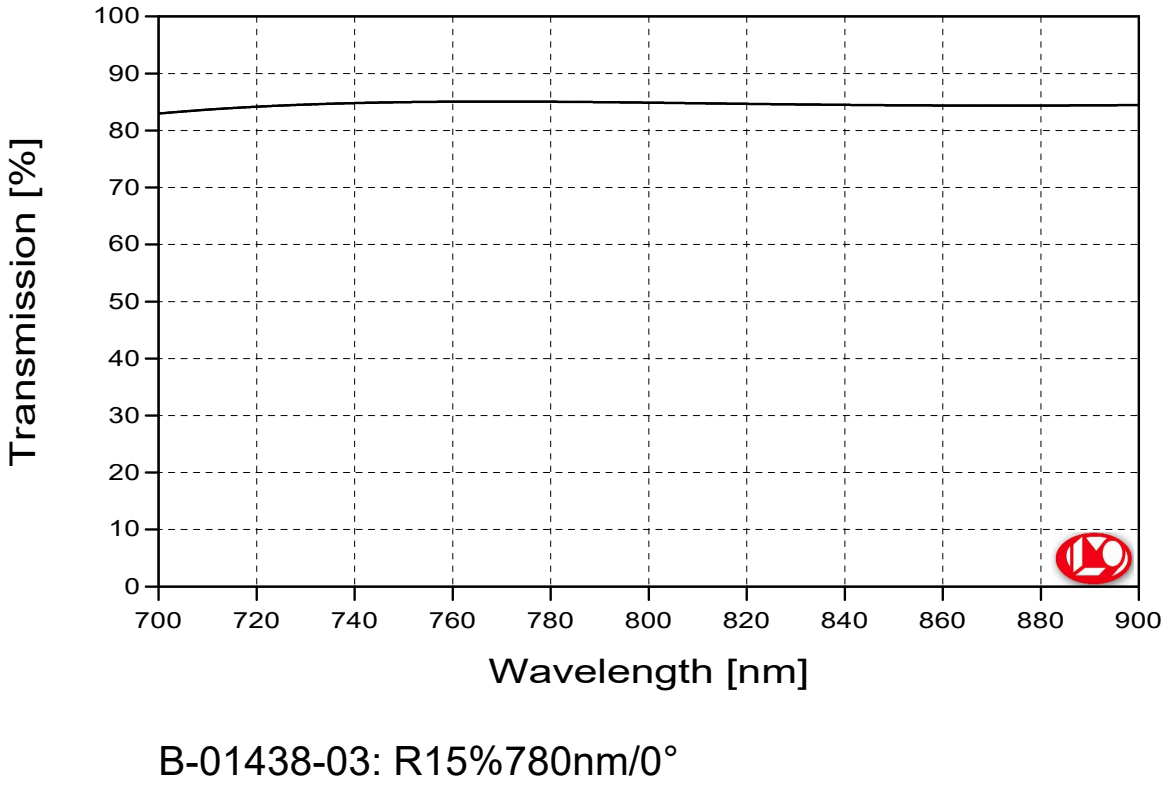

Fig. A.1.: Theoretical reflectivity versus wavelength for a partially reflective coating with a nominal reflectivity of $R = 15\%$. Manufacturer: Laseroptik.

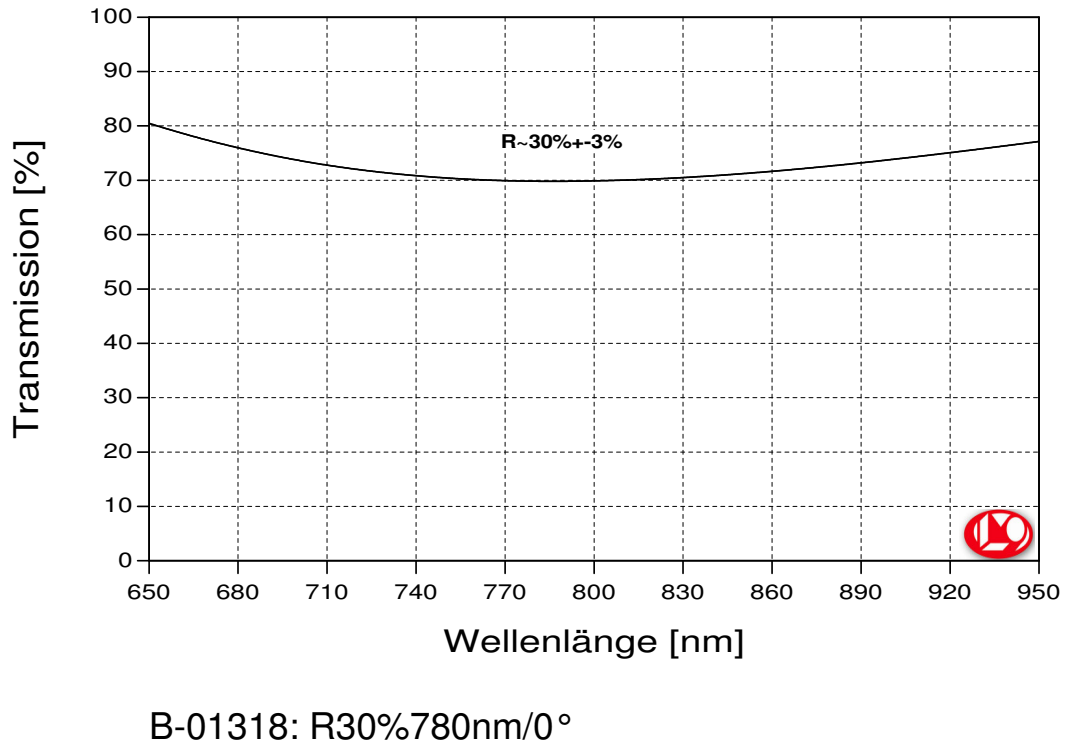

Fig. A.2.: Theoretical reflectivity versus wavelength for a partially reflective coating with a nominal reflectivity of $R = 30\%$. Manufacturer: Laseroptik.

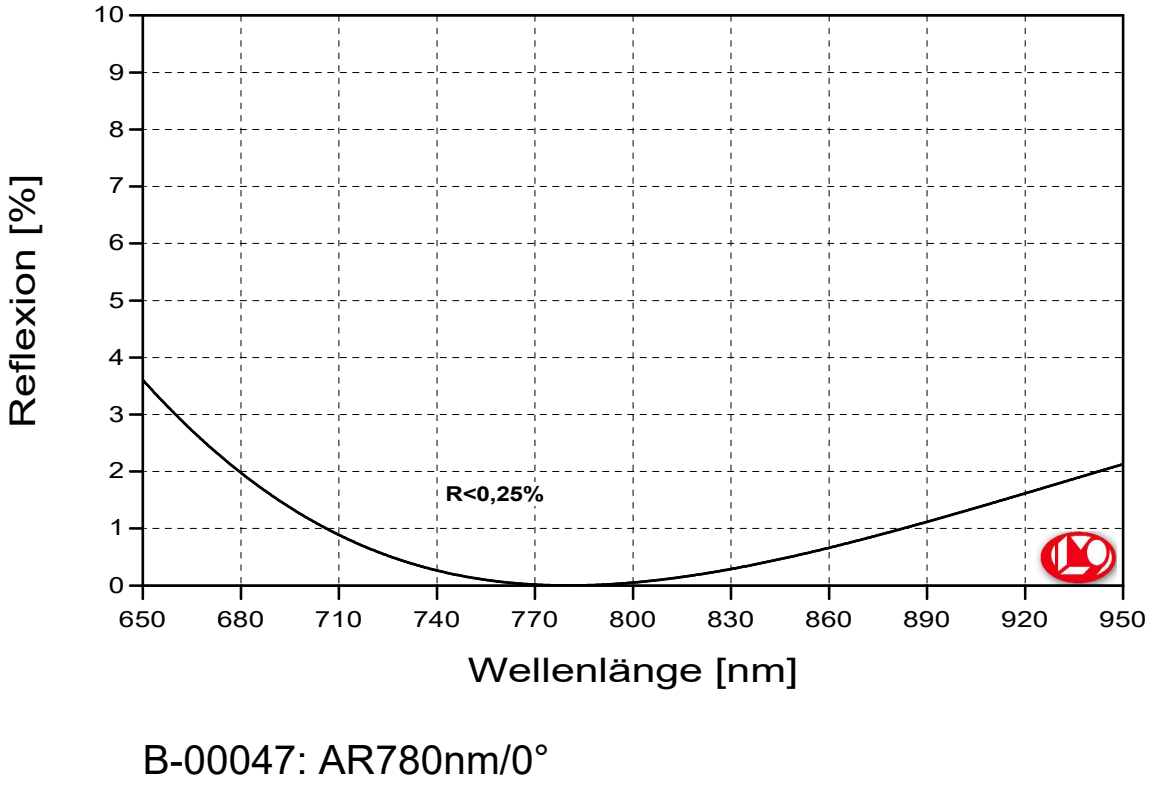

Fig. A.3.: Theoretical reflectivity verses wavelength for an anti-reflective coating centred at 780 nm. Manufacturer:Laseroptik.

A.2. High-finesse reference cavity

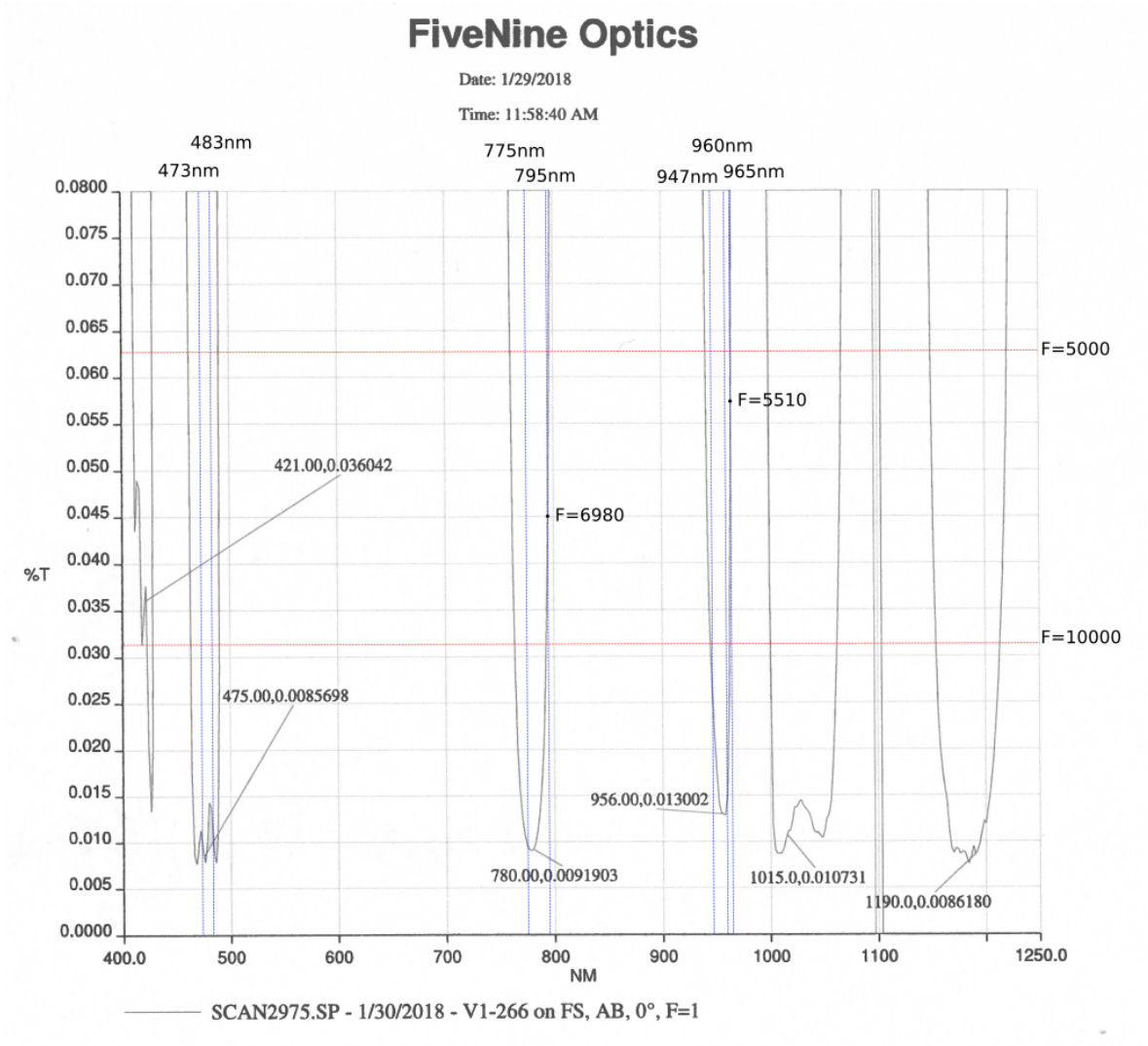

Fig. A.4.: Transmission of the cavity mirror as measured by the manufacturer. Relevant wavelengths are marked by vertical lines. Reflectivities equivalent to finesse 5000 and 10000 are indicated by horizontal red lines. Manufacturer: Stable Laser System / Five Nine Optics / Advanced Thin Films.

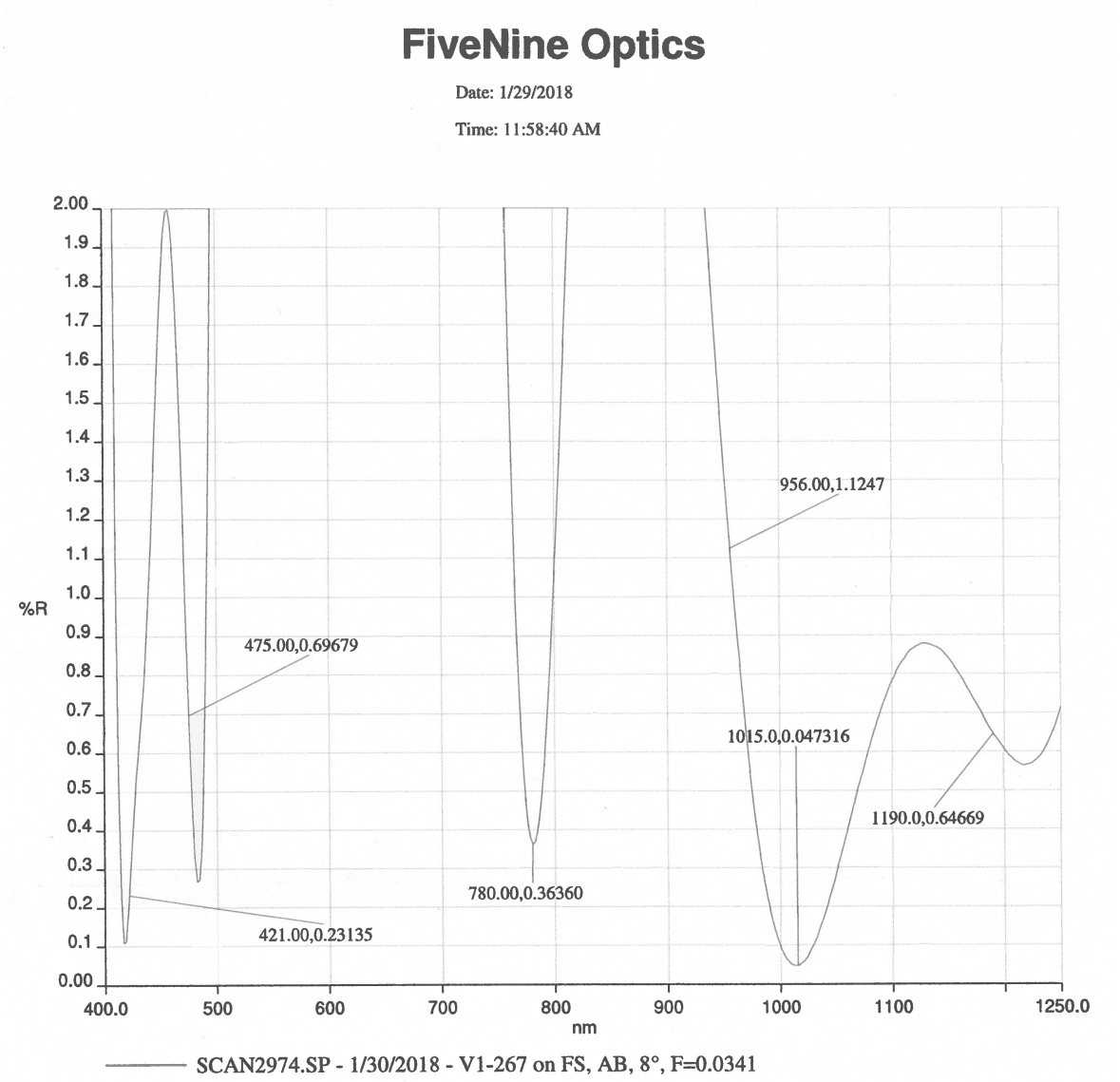

Fig. A.5.: Reflectivity of the rear surface of the cavity mirror as measured by the manufacturer. Manufacturer: Stable Laser System / Five Nine Optics / Advanced Thin Films.

B. Selected Python codes

B.1. Voigt fit

The code below shows a minimal working example of the code used for fitting a Voigt profile to a delayed self heterodyne (DSH) spectrum obtained by a spectrum analyser.

```
import numpy as np
import pandas as pd
from scipy.optimize import curve_fit
from scipy.special import wofz

def read_data(filename):
  data = pd.read_csv(filename, delimiter=",", names=['time', 'signal1','signal2',
    'signal3'])
  x = data['time'].astype(float)
  y = data['signal1'].astype(float)
  return np.array(x),np.array(y)

def voigt(x, alpha, gamma,x0,y0):
  """
  Return the Voigt line shape at x with Lorentzian component HWHM gamma
  and Gaussian component HWHM alpha.

  """
  sigma = alpha / np.sqrt(2 * np.log(2))

  return y0*np.real(wofz(((x-x0) + 1j*gamma)/sigma/np.sqrt(2))) / sigma / np.sqrt
    (2*np.pi)


########################################
# Read data and apply Voigt fit

f, mag = read_data('RSA_file.csv')
mag = mag / np.max(mag)
f = f - f[np.argmax(mag)]
popt, pcov = curve_fit(voigt, f,mag,p0=[1000,1000,0,1])
fwhm = popt[1]+np.sqrt(popt[1]**2+4*popt[0]**2)

#Print fit results
print('Gaussian linewidth (FWHM): ', 2*popt[0])
print('Lorentzian linewidth (FWHM): ', 2*popt[1])
print('Voigt linewidth: ', fwhm)
```

B.2. Generation of correlated noise

The code below shows a minimal working example of the code used to generated temporally correlated noise with a given power spectral density.

```
import numpy as np
import pandas as pd
from scipy.interpolate import CubicSpline

def read_data(filename):
  data = pd.read_csv(filename, delimiter=",", names=['time', 'signal1','signal2', 'signal3'])
  x = data['time'].astype(float)
  y = data['signal1'].astype(float)
  return np.array(x),np.array(y)

def sample_phase_noise(N, sampling_rate, noise_model):
  """
  Returns N samples of colored noise generated from a noise model.
  N: Number of samples
  sampling_rate: set the sampling rate, such that the Nyquist frequency is well above the noise psd cut-off
  noise_model: continous model for sqrt(psd) [rad/sqrt(Hz)] (e.g. use a cubic spline generated from measured data)
  """
  white_psd = np.fft.rfft(np.random.randn(N)) #FFT of uncorrelated sample
  freq = np.fft.rfftfreq(N, d = 1/sampling_rate)# Fourier frequencies of the sample
  weights = noise_model(freq) # Generate weights from the noise model avoid f= 0 for f**-x models
  # Normalize weighting function: ||noise_model||_2 / sqrt(mean_psd)
  # Attention: f**-x models are not integrable. Avoid freq[0] = 0 and rescale empirically.
  weights = weights/np.sqrt(np.mean(weights**2))*np.sqrt(np.trapz(noise_model(freq)**2,freq))
  shaped_psd = white_psd*weights
  t=np.arange(N)*1/sampling_rate
  shaped_noise = np.fft.irfft(shaped_psd) # obtain samples by inverse Fourier transform
  return t, np.real(shaped_noise)

### Get noise_model from measured data
f, noise = read_data('noise_models/phasenoise_Raman.csv')
sampling_rate = np.max(f)*2
noise_model = CubicSpline(f,np.sqrt(noise))

### Sample random noise
t, phase_noise = sample_phase_noise(int(1e6),sampling_rate,noise_model)

```

B.3. Simulation of Rabi oscillations with a noisy laser field

The code below shows a minimal working example of the code used to simulate Rabis oscillations with a noisy laser field. The laser phase noise is generated using the code in Appendix B.2.

```
from qutip import *
import numpy as np
import matplotlib.pyplot as plt
import pandas as pd
from scipy.optimize import curve_fit
from scipy.interpolate import CubicSpline
from scipy import signal
import time


def get_noise_model(filename, sampling_rate, noise_scale=1):
  ### Get noise_model from measured data
  f, noise = read_data(filename)
  #extrapolate noise data
  if 1.1*np.max(f) < sampling_rate/2:
    f0 = np.logspace(np.log10(f[-1]*1.2),np.log10(sampling_rate/2),100)
    f = np.append(f,f0)
    n0 = np.zeros(len(f0))+noise[-1]
    noise = np.append(noise,n0)
  noise = np.sqrt(noise_scale*noise)
  return CubicSpline(f,noise)


def simulate_phase_noise(omega_rabi,delta,noise_model, model_name=None,
    rabi_cycles=10, rabi_res = 100, avg = 1000, save_results=True, weight_scale
    =1):
  """
  Set simulation parameters:
  omega_rabi: (angular) Rabi frequency
  delta: detuning from resonance (exspectation value of the frequency
    distribution)
  noise_model: path to noise model csv-file. The model defines the phase noise
    PSD [rad**2/Hz].
  Data are interpolated -- make shure they cover the relevant frequency range.
  Extrapolation may lead to unexpected behaviour.
  noise_scale: scale noise with a factor, e.g. due to SHG or unit conversion
  rabi_cycles: run simulation over # rabi cycles
  avg: Average over # of realizations
  limit_bw: Set sampling rate, for low Rabi frequencies. If None, the sampling
    rate is chosen to cover the frequency range given by the noise model.
  random_delta: Include random frequency offset considered constant during the
    simulation time, e.g. caused by a finite laser lindwidth.
  save_results: save simultaion results as .csv
  """

  #calculate sampling rate and sample length
  sampling_rate = int(rabi_res*(omega_rabi/2/np.pi))
  N = rabi_res*rabi_cycles
  t=np.arange(N)*1/sampling_rate

  #Define Hamiltonian:
  g = Qobj([[1],[0]])#start in the ground state
```

```
  e = Qobj([[0],[1]])
  e_proj = Qobj([[0,0],[0,1]])
  H0 = -delta/2*sigmaz()
  H1 = omega_rabi/2*Qobj([[0,0],[1,0]])
  H2 = omega_rabi/2*Qobj([[0,1],[0,0]])

  output= []
  print('Start simulation: Omega_rabi = %.3f MHz'%(omega_rabi/(2*np.pi*1e6)))
  t0 = time.time()
  for i in range(avg):
    #Draw an instance of phase noise
    phase_noise = sample_phase_noise(N,sampling_rate,noise_model,weight_scale)
    S1 = Cubic_Spline(t[0], t[-1],np.exp(1j*phase_noise))#interpolate discrete
    random data
    S2 = Cubic_Spline(t[0], t[-1],np.exp(-1j*phase_noise))

    'solve Schroedinger equation'
    H = [H0,[H1,S1],[H2,S2]]
    result = sesolve(H,g,t,e_ops=[e_proj])
    output.append(result)

  'average over all realizations'
  mean_list = []
  for result in output:
    mean_list.append(np.abs(result.expect[0]))
    mean = np.mean(mean_list,axis=0)
  print('Done in %.0f s'%(time.time()-t0))

  'save data'
  if save_results:
    df = pd.DataFrame()
    df['Time'] = np.concatenate((np.array(['omega_rabi','delta','noise_model','
    rabi_cycles','res_t']),t),axis=None)
    df['Mean'] = np.concatenate((np.array([omega_rabi,delta,model_name,
    rabi_cycles,rabi_res]),mean),axis=None)
    df.to_csv('results_phase_noise_rabi_%.3fMHz_%.0f_cycles.csv'%(omega_rabi/(2*
    np.pi*1e6),rabi_cycles))
  return t,mean,omega_rabi

########################################

omega_rabi = 10e6
t_res = 100
noise_model = get_noise_model('phasenoise_Raman.csv', omega_rabi*t_res,
    noise_scale=1)
t,mean,omega_rabi = simulate_phase_noise(2*np.pi*omega_rabi,0,noise_model,
    model_name = 'Raman phase noise',
rabi_cycles=100, rabi_res = t_res, avg = 1000, save_results=True)
```

C. List of publications

T. Preuschoff, M. Schlosser and G. Birkl, *Optimization strategies for modulation transfer spectroscopy applied to laser stabilization*, Opt. Express **26,** 24010–24019 (2018).

T. Preuschoff, S. Ristok, D. Schäffner, L. Brozio, D. Ohl de Mello, L. Kohfahl, M. Schlosser, H. Giessen and G. Birkl, *Micro-optical systems for quantum technologies with laser-trapped neutral atoms based on rapid prototyping by 3D direct laser writing*, In *DGaO-Proceedings 2019*, p. B016 (DGAO, 2019).

D. Ohl de Mello, D. Schäffner, J. Werkmann, T. Preuschoff, L. Kohfahl, M. Schlosser and G. Birkl, *Defect-Free Assembly of 2D Clusters of More Than 100 Single-Atom Quantum Systems*, Phys. Rev. Lett. **122,** 203601 (2019).

D. Schäffner, T. Preuschoff, S. Ristok, L. Brozio, M. Schlosser, H. Giessen, and G. Birkl, *Arrays of individually controllable optical tweezers based on 3D-printed microlens arrays*, Opt. Express **28,** 8640–8645 (2020).

T. Preuschoff, M. Schlosser and G. Birkl, *Digital laser frequency and intensity stabilization based on the STEMlab platform (originally Red Pitaya)*, Review of Scientific Instruments **91,** 083001 (2020).

M. Schlosser, D. O. de Mello, D. Schäffner, T. Preuschoff, L. Kohfahl and G. Birkl, *Assembled arrays of Rydberg-interacting atoms*, Journal of Physics B: Atomic, Molecular and Optical Physics **53,** 144001 (2020).

T. Preuschoff, P. Baus, M. Schlosser and G. Birkl, *Wideband current modulation of diode lasers for frequency stabilization*, Review of Scientific Instruments **93,** 063002 (2022).

Acknowledgments

An dieser Stelle möchte ich mich bei all denjenigen bedanken, die mich während meiner Promotionszeit begleitet haben und ohne die diese Arbeit nicht möglich gewesen wäre.

An erster Stelle gilt mein Dank Herrn Prof. Birkl für die hervorragende Betreuung. Sie haben es immer verstanden, für ein fruchtbares Arbeitsumfeld zu sorgen. Viele konstruktive Diskussionen und Ihr echtes Interesse – auch an kleinen Details – haben maßgeblich zu dem Erfolg dieser Arbeit beigetragen.
Auch Herrn Prof. Walther möchte ich für die unkomplizierte Übernahme des Zweitgutachtens danken. Ebenso bedanke ich mich bei Herrn Prof. Walser und Frau Prof. Arcones für ihre Beteiligung an der Prüfungskommission.

Für das angenehme Arbeitsumfeld bedanke ich mich ebenso bei allen Mitgliedern der Arbeitsgruppe Atome-Photonen-Quanten. Insbesondere bei meinem Kollegen Lars, mit dem ich das QUIPS C Experiment aufbauen durfte. Der Schritt vom beinahe leeren Labor zu einer vielseitigen Plattform für viele spannende zukünftige Experimente ist zu einem großen Teil deiner effizienten und immer freundlichen Mentalität zu verdanken. Unsere erfolgreiche Arbeitsteilung beim Aufbau des Experiments hat nicht nur das Thema dieser Arbeit maßgeblich bestimmt, sondern auch viele Ergebnisse erst ermöglicht. Patrick hat mir immer mit Rat und Tat bei zahlreichen Elektronikentwicklungen zur Seite gestanden. Bei Malte möchte ich mich für sein jeder Zeit offenes Ohr bei physikalischen und organisatorischen Fragen bedanken. Auf deinen Rat konnte ich mich, auch schon bei der Betreuung meiner Masterarbeit, immer verlassen. Die enge, konstruktive Zusammenarbeit mit Daniel, Dominik und Tobias von QUIPS B, aber auch mit Felix und Dominik von ATOMICS hat mir sehr dabei geholfen, Anforderungen und Verbesserung der hier vorgestellten Systeme und Techniken zu finden. In diesem Zusammenhang seien auch die Beiträge in den Abschlussarbeiten zur Weiterentwicklung von Lasersystemen von Patrick Sauer, Simon Bickl und Leo Göttlicher sowie zur Spektroskopie von Fabian Christ und Erik Hinkelmann und auch die Simulationsarbeit von Florian Kroh erwähnt. Mein Dank gilt ebenso dem Sekretariat. Gabi und Nathalie haben es immer verstanden, Formalien und Organisatorisches möglichst unkompliziert zu erledigen.

Mein besonderer Dank gilt auch dem Team der Feinmechanikwerkstatt um Herrn Weick: Laura, Tim und Simon. Dank eurer zuverlässigen und hochwertigen Arbeit sind aus meinen Ideen funktionstüchtige Bauteile entstanden, die ihr teilweise sogar in kleinen Serien gefertigt habt. Eure Unterstützung bei der Umsetzung dieser Projekte ist alles andere als selbstverständlich.

Nicht zuletzt möchte ich mich bei meiner Familie und meinen Freunden für die Unterstützung bedanken. Vor allem bei meiner Frau Christiane und meinen Kindern Marietta, Aaron und Lasse. Ihr musstet – gerade in den letzten Monaten – viel meiner Zeit und Aufmerksamkeit entbehren.

Curriculum Vitae

Not included in the online version for reasons of data protection.

Erklärungen laut Promotionsordnung

§ 8 Abs. 1 lit. c PromO

Ich versichere hiermit, dass die elektronische Version meiner Dissertation mit der schriftlichen Version übereinstimmt.

§ 8 Abs. 1 lit. d PromO

Ich versichere hiermit, dass zu einem vorherigen Zeitpunkt noch keine Promotion versucht wurde. In diesem Fall sind nähere Angaben über Zeitpunkt, Hochschule, Dissertationsthema und Ergebnis dieses Versuchs mitzuteilen.

§ 9 Abs. 1 PromO

Ich versichere hiermit, dass die vorliegende Dissertation selbstständig und nur unter Verwendung der angegebenen Quellen verfasst wurde.

§ 9 Abs. 2 PromO

Die Arbeit hat bisher noch nicht zu Prüfungszwecken gedient.

Darmstadt, 24. Januar 2023

T. Preuschoff